CHEMICAL PROFILING OF DRUGS AND METABOLITES FROM COMPLEX BIOLOGICAL MATRICES BY ATMOSPHERIC PRESSURE AND AMBIENT IONIZATION MASS SPECTROMETRY

CONSUELO JAVIERA PEREZ

A DISSERTATION SUBMITTED TO
THE FACULTY OF GRADUATE STUDIES
IN PARTIAL FULLFILLMENT OF THE REQUIREMENTS
FOR THE DEGREE OF
DOCTOR OF PHILOSOPHY

GRADUATE PROGRAM IN CHEMISTRY
YORK UNIVERSITY
TORONTO, ONTARIO

September 2020

Abstract

Atmospheric pressure and ambient mass spectrometry (MS) techniques are powerful analytical tools for the “omics” technologies. Ambient MS techniques allow for the surface analysis of molecules directly from substrates and thin biological tissue sections with minimal to no sample pretreatment in the open environment. This dissertation describes the development and implementation of rapid and novel MS based methods for the analysis of targeted analytes such as drugs and metabolites from complex biological matrices in two main fields of application, drug development and phytometabolomics. We explored the potential of quantitative mass spectrometry imaging (MSI) by the ambient MS technique, desorption electrospray ionization-mass spectrometry (DESI-MS). The discovery of quantitation MSI methods were explored and evaluated based on its analytical figures of merit (precision, accuracy, linearity, and so forth). Triple threat methods covering the identification, quantification and mapping the spatial distribution of analytes from biological tissue sections opens new avenues in MSI. The development of targeted qualitative and quantitative ESI-MS, DESI-MS and multistage mass spectrometry, DESI-MS^n, methods for plant metabolomics were also investigated. DESI-MS and DESI-MS^n methods coupled offline to normal phase high performance thin layer chromatography (HPTLC) and C_{18} functionalized reverse phase (RPTLC) were created to identify and separate bioactive secondary metabolites from natural products such as seeds, roots, twigs, and leaves. The implementation of these rapid, robust and high-throughput methods allowed for the discovery of novel phytochemicals in the plant species under investigation.

Acknowledgements

I would like to thank my supervisor, Professor Demian Ifa, I'm forever grateful for the amazing opportunity, and the privilege, to be a part of your research group. Thank you for mentoring and guiding me during my time as a PhD student and giving me the chance to explore different research interests that organically turned into projects. To my supervisory committee, thank you to Professor Sylvie Morin and Professor Derek Wilson for great suggestions and feedback every year during evaluations to help improve the research. Thank you to my PhD examination committee, Professor Sylvie Morin, Derek Wilson, Andre Venter and Nikola Kovinich for accepting to be a part of the oral examination committee.

Dr. Alessandra Tata, thank you for taking me under your wing during my first year as a master student. Your passion and dedication towards science inspired and encouraged me to continue in academia after the master's degree. Working alongside you has helped me more than you can imagine, and I carry with me all the DESI lessons.

To past and current members of Professor Ifa's group: Rachel, Rogerio, Paulo, Bruna, Aafreen, Carol, Alessandro, Adriana, Mayara, and Maryam, thank you for the opportunity to work with you and learn from you all. Rodrigo, your love of nature and plants sparked my curiosity into the world of phytochemistry. Thanks for all the good times we spent working together, that flew by too quickly.

Thank you to the MS-ESE CREATE program, Professor Derek Wilson and Dr. David Tulumello for the opportunity to intern for 8 months in the biochemistry unit at Sanofi Pasteur. Ewa, thank you for being so patient and kind to me and teaching me your secrets on SDS-PAGE and Western Blots. Przemek, conversations with you were very helpful in working my way around Sanofi. Samaneh and Diana, thank you for the opportunity to work with you both on research projects using microcapillary immunoassay by Protein Simple Wes. Shakiba, Linda, Ruby and Jessie, you all made work feel like home. To the kindest manager on this earth, David Tulumello, thank you for the chance to intern in your group. You have made a huge impact in my scientific

development and I'm grateful for your career advice, and support to help me transition into industry.

To my best friend, Harpreet, thank you for your friendship for the past 13 years, you're an unbelievable soul. We somehow found each other in a lecture hall of 400+ students in first year chemistry. Thank you for all the support, kindness, laughter, and being there for me through the ups and downs that life brings, and for being someone I can turn to for absolutely anything.

To my family, thank you for your support and teaching me that no matter what, *family*, always comes first. Everything in life changes, health, jobs, wealth, boyfriends, it all seems to come and go for us throughout the years, but the bond we share has been my true constant, it doesn't bend or change over time. Connie, I can't believe when we were kids I'd tell you the horrible story that mama found you crying at the bottom of a dumpster and brought you home to raise as her own, and that's why you looked so different from me, with your red hair, green eyes and freckles, and you'd cry your eyes out and I'd get into so much trouble. Even though our troublemaking days together are long gone, I have nothing but gratitude in my heart that YOU are my sister. Thank you for the gift of a lifelong friendship, I can't imagine my life without you.

Mama, you are a phenomenal woman, ahead of your time. Thank you for all the sacrifices you've made so that we could live an amazing life. The greatest gift you have given me is the freedom and trust to let me find my own journey, without judgements or limitations on what I should or shouldn't be doing with my time on this earth. My inner warrior *(what you say is, stubbornness*) and my free spirit, *that you complain SO much about*, lets be honest with each other, I am who I am because of you. I love you both so much.

I'd like to thank absolutely *everyone,* that in one way or another, made this insane dream become my reality.

"Solo los peces muertos siguen la corriente del río"/ "Only dead fish follow the river's current"

- Unknown

Table of Contents

Abstract ..... **ii**

Acknowledgements ..... **iii**

Table of Contents ..... **v**

List of Tables ..... **x**

List of Abbreviations ..... **xvi**

List of Publications ..... **xviii**

Chapter One: General Introduction 1

1.1. The Foundation of Mass Spectrometry 2

1.2. Atmospheric Pressure Ionization Mass Spectrometry 2

1.2.1. Electrospray Ionization Mass Spectrometry (ESI-MS) 2

1.3. Ambient Ionization Mass Spectrometry 3

1.3.1. Desorption Electrospray Ionization-Mass Spectrometry 9

1.3.2. Principles of Ambient Mass Spectrometry Imaging 9

1.3.3. Tandem Mass Spectrometry and Multistage Mass Spectrometry 12

1.4. Mass Spectrometers 12

1.4.1. Thermo Finnigan™ LTQ™ Mass Spectrometer 13

1.4.2. Thermo Scientific™ LTQ-Orbitrap Elite™ Hybrid Mass Spectrometer 14

1.4.3. Thermo Scientific™ QExactive ™ Hybrid Mass Spectrometer 16

1.5. Principles of Thin layer Chromatography 17

1.5.1. Normal and Reverse Phase TLC 18

1.5.2. HPTLC Coupled to DESI-MS 19

1.6. Dissertation Research Objectives 20

Chapter Two: Internal Standard Application Strategies in Mass Spectrometry Imaging by Desorption Electrospray Ionization 21

2.1. Summary 22

2.2. Introduction 23

2.3. Experimental 25

2.3.1. Biological Tissue Sample Preparation 25

2.3.2. Sample Preparation and ESI-MS Analysis of Golden Apple Snail (*p. diffusa*) Tissue Extracts 25
2.3.3. DESI-MSI of the Golden Apple Snail (*p. diffusa*) Tissue Sections 26
2.3.4. The Targeted Method Development for Quantitative DESI-MSI 26
2.3.5. DESI-MSI Data Processing and Collection 26
2.3.6. DESI-MSI in the Absence of the Internal Standard 27
2.3.7. Internal Standard Application Strategies 27
2.3.8. Evaluation of Accuracy 28
2.4. Results and Discussion 28
2.4.1. Metabolomic Profiling of the Golden Apple Snail (*p.diffusa*) 28
2.4.2. The Spatial Distribution of Metabolites in the Golden Apple Snail (*p.diffusa*) 30
2.4.3. The Development of the Targeted Quantitative DESI-MSI Method 34
2.4.4. Phenobarbital 37
2.4.5. Selectivity 37
2.4.5. Specificity 39
2.4.6. Sensitivity 41
2.4.7. Dynamic range 41
2.4.8. DESI-MSI of Phenobarbital in the Absence of the Internal Standard 41
2.4.9. Tissue Homogeneity 43
2.4.10. Method III - The Internal Standard in the DESI Spray Solvent 43
2.4.11. Method II – Optimization of the IS Thin Film 43
2.4.12. Comparison of the Internal Standard Application Strategies 46
2.4.13. Statistical Analysis 52
2.4.14. Method Validation by Accuracy Assessment 53
2.5. Conclusions 54

Chapter Three: Chemical Profiling of Bioactive Secondary Metabolites from Maca (*Lepidium peruvianum)* by Normal and Reverse Phase TLC Coupled to DESI-MS 56
3.1. Summary 57
3.2. Introduction 58
3.3. Experimental 59
3.3.1. Materials and Reagents 59

3.3.2. The Extraction of Secondary Metabolites from Maca Seeds and Supplements 60
3.3.3. ESI-HRMS Analysis of Red and Black Maca (*L. peruvianum*) Seeds 60
3.3.4. The HPTLC/RPTLC-(-)DESI-MS Analysis of Secondary Metabolites 61
3.3.5. The HPTLC-(+)DESI-MS Analysis of Imidazole Alkaloids 61
3.4. Results and Discussion 62
3.4.1. Glucosinolates 62
3.4.2. MS^2 Fragmentation Pattern of Aromatic Glucosinolates 70
3.4.3. Comparison of Glucosinolates in Red and Black Maca (*L.peruvianum*) Seeds 73
3.4.4. Glycosylated Ascorbigens and Dihydroascorbigens 74
3.4.5. Brassicaceae Fatty Acids 76
3.4.6. Imidazole Alkaloids 79
3.4.7. MS^2 Fragmentation Pathway of Imidazole Alkaloids 82
3.5. Conclusion 86

Chapter Four: The Characterization and Spatial Distribution of Isoquinoline and Aporphine Alkaloids from *Sassafras Albidum* by HPTLC-DESI-MS^n and DESI-MS Imaging 87
4.1. Summary 88
4.2. Introduction 88
4.3. Experimental 90
4.3.1. *Sassafras albidum* Extract Preparation 90
4.3.2. ESI-MS and ESI-MS^n of the *Sassafras albidum* Extracts 90
4.3.3. The Separation of Alkaloids from *Sassafras albidum* by HPTLC 90
4.3.4. DESI-MS^n of Alkaloids in *Sassafras albidum* 91
4.3.5. DESI-MSI of TLC Imprints of *Sassafras albidum* Roots and Twigs 91
4.4. Results and Discussion 92
4.4.1. The Presence of Alkaloids in Extracts of Roots and Twigs by (+)ESI-MS 92
4.4.2. HPTLC-DESI-MS^n of *Sassafras albidum* Roots and Twigs 93
4.4.3. Benzylisoquinoline Alkaloids 96
4.4.4. Aporphine Alkaloids 99
4.4.5. The Spatial Distribution of Alkaloids in *S. albidum* by DESI-MSI 101
4.5. Conclusion 105

Chapter Five: The Fragmentation and Separation of Benzylisoquinoline and Aporphine Alkaloids from the Acaracide Extract of *Ocotea Spixiana* by HPTLC-DESI-MS^n 106

5.1. Summary 107

5.2. Introduction 107

5.3. Experimental 108

5.3.1. Plant Material and Preparation of the Extract 108

5.3.2. ESI-MS and Tandem MS of *O. spixiana* Extracts 109

5.3.3. The Separation of Alkaloids by HPTLC 109

5.3.4. DESI-MS^n Analysis of Alkaloids in *O. spixiana* 109

5.4. Results and Discussion 110

5.4.1. Alkaloids in Twigs of *O. spixiana* 110

5.4.2. Benzylisoquinoline Alkaloids 113

5.4.3. Aporphine Alkaloids 116

5.5. Conclusion 121

Chapter Six: A Quantitative Metabolomic Study of Novel *Coffea Canephora* Genotypes Across Stages of Maturity by High Resolution Mass Spectrometry 122

6.1. Summary 123

6.2. Introduction 123

6.3. Experimental 125

6.3.1. The Origin of Brazilian Green Coffee Beans 125

6.3.2. Extract Preparation of Green Coffee Beans 125

6.3.3. ESI-LTQ-Orbitrap: Sample Preparation 125

6.3.4. ESI-HRMS LTQ-Orbitrap Elite™ Analysis 126

6.3.4. mMass Data Calibration 126

6.4. Results and Discussion 127

6.4.1. Bioactive Metabolites Across Green Coffee Bean Species 127

6.4.2. Caffeine, Trigonelline and Total Sugar Content in Green Coffee Bean Species Across Stages of Maturity 133

6.4.3. Phenolic and Chlorogenic Acid Content in Green Coffee Bean Species Across Stages of Maturity 138

6.5. Conclusion 144

Chapter Seven: Conclusions and Future Work 145
7.1. Conclusions and Future Work 146

REFERENCES 149

APPENDICES 158
Appendix A. Supplementary Data for Chapter 2 158
Appendix B. Supplementary Data for Chapter 3 168

List of Tables

Table 1.1: Summary of selected ambient ionization imaging techniques showing the type of ionization, a schematic of the ion source, common imaging resolutions and references of the first report of the ambient ionization imaging techniques. Reproduced with permission from Perez et al.[8] 6

Table 1.2: Summary of the Principles of Normal and Reverse Phase TLC 19

Table 2.1: Probing the Sampling Depth of the DESI Sprayer from Drugs Deposited at Concentrations of 100 µM on Snail Tissues (*p.diffusa*) from Thicknesses of 10-30 µm. 36

Table 2.2: The application of the IS thin film on top of snail (*p.diffusa*) tissue sections..... 45

Table 2.3: Intra- and interday MSI linear regression analyses for method I and II. 51

Table 3.1: Bioactive Secondary Metabolites in Red and Black Maca (*L. peruvianum*) Seeds and Black Maca Root Powder analyzed by HPTLC and RPTLC-DESI-MS in Negative Ion Mode. 64

Table 3.2: The Separation of Glucosinolates in Red Maca (*L. peruvianum*) Seeds Analyzed by HPTLC-DESI-MS in Negative Ion Mode..... 69

Table 3.3: Imidazole Alkaloids in Black Maca (*L. meyenii*) Root Powder and Tinctures Analyzed by HPTLC-DESI-MS in Positive Ion Mode. 81

Table 4.1: Key fragment ions of isoquinoline alkaloids of *Sassafras albidum* from HPTLC-DESI-MS^n analyses. Reproduced with permission from Conceição et al.[165] 96

Table 4.2: Aporphine alkaloids of *Sassafras albidum* analyzed by DESI-MS^n. Reproduced with permission from Conceição et al.[165] 100

Table 5.1: Key fragment ions in the MS/MS spectra of Benzylisoquinoline type alkaloids. Reproduced with permission from Conceição et al.[122] 114

Table 5.2: Major fragment ions observed by DESI-MS^n analysis of aporphine alkaloids of *Ocotea spixiana*. Reproduced with permission from Conceição et al.[122] 117

Table 6.1: High-resolution MS/MS characterization of green coffee bean metabolites in Arabica (Catuai 81, Obata, Topazio), novel genotypes Diamante 101, 105 and 108 and Robusta Tropical at three stages of maturity. Reproduced with permission from Lemos et al.[229] 131

Table 6.2: Caffeine, trigonelline and sugar content (µM) in green coffee species by (+)ESI-HRMS. Reproduced with permission from Lemos et al.[229] 137

Table 6.3: Phenolic and chlorogenic acid content (µM) in different coffee species by (-)ESI-HRMS. Reproduced with permission from Lemos et al.[229] 141

List of Figures

Figure 1.1: A. Electrospray ionization (ESI). Adapted from Banjeree et al.[7] the summary of ESI mechanisms: IEM, CRM and CEM. Reproduced with permission from Konermann et al.[5] 3

Figure 1.2: Schematic of the general methodology in ambient mass spectrometry. Reproduced with permission from Li et al.[9] 4

Figure 1.3: A. Schematic of the Desorption Electrospray Ionization Source. B. DESI geometric parameters. Reproduced with permission from Takats et al.[67] 9

Figure 2.1: Schematic representation of quantitative DESI-MSI. 22

Figure 2.2: IS application strategies in MSI by DESI. a) Method I - IS microspots on top of the tissue. b) Method II – IS thin film using the DESI sprayer. c) Method III - adding the IS in the DESI solvent spray. 24

Figure 2.3: ESI-MS full scan spectra of the tissue extracts of the invasive freshwater golden apple snail (*p. diffusa*) from a) the $CHCl_3$ fraction. b) the MeOH fraction. The inset chemical structure on the top spectrum is glycerophosphoglycerol, PG(16:0/16:0), and the disaccharide, sucrose, in the bottom figure. 29

Figure 2.4: (-)DESI-MSI of golden apple snail (*p. diffusa*) tissues with MeOH 0.1% NH_4OH. Imaging dimensions of the snail head tissue section were 16000 µm x 10000 µm set to 150 µm for the lateral resolution. 31

Figure 2.5: (-)DESI-MSI of freshwater golden apple snail (*p. diffusa*) tissues inside the shell using imaging dimensions of 11000 µm x 14000 µm set to 200 µm for the lateral resolution using the solvent A. MeOH and B. ACN. a) Snail body inside the shell fixed in 5% CMC. b) CMC block during cryosectioning. c) Optical image of 20 µm tissue section. d) H&E stained tissue after MSI analysis. e) H&E stained tissue outlined in red. Panel A. MSI of the snail tissue section with MeOH 0.1% NH_4OH. Panel B. MSI of snail tissue section with ACN 0.1% NH_4OH. 33

Figure 2.6: (-)DESI-MS profiles of the invasive freshwater golden apple snail (*p.diffusa*) tissues. A. MEOH and B. ACN. 34

Figure 2.7: Evaluation of tissue sampling depth by the DESI sprayer. 100 µM of carbamazepine, fentanyl, verapamil and phenobarbital were deposited in 1 µL spots on snail tissues ranging from 10, 12, 15, 20, 25, and 30 µm in thickness. The figure displays the average intensity of the pharmaceuticals (n=2). Carbamazepine, fentanyl and verapamil are positively charged ions $[M+H]^+$ in the (+)DESI-MS analysis and phenobarbital is a negatively charged ion $[M-H]^-$ in the (-)DESI-MS analysis. 35

Figure 2.8: Average (-)DESI-MS/MS spectra of a) PB (*m/z* 231). b) The isotopically labelled IS, PB-D5 (*m/z* 236) on 10 µm snail tissue sections. c) MS/MS fragmentation pathway of Phenobarbital.

The MS/MS profiles were collected via CID from 1 µL spots of 100 ng/µL of each standard and fragmented with collision energies of 20 (manufacturer's unit). 38

Figure 2.9: (-)DESI-MS profiles of PB (*m/z* 231) and the isotopically labelled IS PB-D5 (*m/z* 236) deposited (100 ng/µL) directly on 10 µm snail (*p. diffusa*) tissue sections collected for 30 secs in a) Full scan MS mode (*m/z* 200-300) displaying the average intensity PB as 1.63E1 (100%) and PB-D5 as 1.62 E1 (99.5%). b) SIM mode (*m/z* 228.5-238.5) depicting the average intensity of PB and PB-D5 as 1.97 E2 (97.5%) and 2.02 E2 (100.0%). 40

Figure 2.10: (-)DESI-MSI analytical performance in the absence of the IS on 10 µm snail (*p. diffusa*) tissues. a) H&E stained 10 µm tissue section after MSI analysis. b) LOD study of PB (*m/z* 231). c) PB microspots of 1-100 ng/µL on the snail tissue section. d) Standard curve of PB from snail tissues in the absence of the IS from three separate (-)DESI-MS imaging analyses (n=3). e) Table of the overall analytical performance. 42

Figure 2.11: (+)DESI-MSI analysis of phospholipids in 10 µm rat brain tissue sections using MeOH. Panel A. Control rat brain tissue. Panel B. After the addition of the IS thin film using a Nitrogen gas pressure of 40 psi and a solvent flow rate of 1.5 µL/min. DESI-MS image dimensions of 16000 x 10000 µm set to a lateral resolution of 200 µm. The top image illustrates the brain substructures of a coronal rat brain tissue section adapted from Woods et al.[103] 44

Figure 2.12: Method II – The optimization of PB-D5 thin film on snail tissues by DESI-MSI. a) IS film of 1 ng/µL. b) IS film of 10 ng/µL. c) IS film of 100 ng/µL. d) Standard curves of the IS thin film of 1 ng/µL (0.34 ng/mm²) blue line, 10 ng/µL (3.4 ng/mm²) grey line, and 100 ng/µL (33.6 ng/mm²) green line. 46

Figure 2.13: Intra- and Interday (-)DESI-MSI study of PB and PB-D5 on snail (*p. diffusa*) tissues between 10-100 ng/µL. Panel A. Method I – Microspots on top of the tissue. a) Snail head tissue block during cryosectioning. b) Optical image. c) H&E stained tissue section after MSI analysis. d) f) & h) Day 1 –100 ng/µL of PB-D5 (*m/z* 236). e), g) & i) Day 1– PB (*m/z* 231). j), l) and n) Day 2 - 100 ng/µL of PB-D5 (*m/z* 236). k), m), o) Day 2– PB (*m/z* 231). Panel B. Method II – Application of the IS thin film with the DESI sprayer. a) Snail head tissue block during cryosectioning. b) Optical image. c) H&E stained tissue section after (-)DESI-MSI analysis. d), f), h) Day 1 – 10 ng/µL of PB-D5 (*m/z* 236) corresponding to (3.4 ng/mm²). e), g) & i) Day 1– PB (*m/z* 231). j), l) and n) Day 2 - PB-D5 (*m/z* 236). k), m), o) Day 2– PB (*m/z* 231). 48

Figure 2.14: Intra- and interday standard curves plotting PB (ng/µL) vs the ion intensity ratios of PB/PB-D5 for method I and II. Panel A. Method I and II intraday analyses. Panel B. Method I and II interday analyses. 50

Figure 2.15: a) A Bland-Altman plot with multiple measurements per subject (concentration) by plotting the differences between the methods against the averages of the methods as a comparison between IS application strategies. The horizontal line represents the mean difference (blue line) and the lower and upper limits of the SD (±1.96) of the mean (red dotted lines) and the upper and lower limits of the 95% CI (green error bars). The red hollow circles (10 ng/µL), red

squares (50 ng/µL), blue circles (75 ng/µL) and the green triangles (100 ng/µL). b) The Bland-Altman input and output data. 52

Figure 2.16: Method validation by assessing the accuracy of method I and II from PB QCs (75 ng/µL) on 10 µm snail tissue sections. a) PB-D5 (*m/z* 236) QC microspots of 100 ng/µL (n=3). b) PB (*m/z* 231) QC microspots of 75 ng/µL (n=3). c) PB-D5 thin film (10 ng/µL) in the DESI solvent spray corresponding to 3.4 ng/mm² on tissues (*m/z* 236). d) PB (m/z 231) QC microspots of 75 ng/µL (n=3). 53

Figure 3.1: Schematic representation of HPTLC coupled to DESI-MS for phytometabolomics. 57

Figure 3.2: HPTLC-(-)DESI-MS profiles of glucosinolates from the hydromethanolic extracts of Maca (*L. peruvianum*) using ACN. a) Red Maca seeds. b) Black Maca seeds. c) Black Maca root lyophilized powder. The inset MS spectra illustrates glycosylated ascorbigens and dihydroascorbigens in the mass range of *m/z* 460-600. 63

Figure 3.3: Aromatic, indoyl, and aliphatic glucosinolates in red and black Maca (*L. peruvianum*) seeds. 67

Figure 3.4: The separation of intact glucosinolates from the hydromethanolic extract of red Maca (*L. peruvianum*) seeds with BnOH:EtOH (7:3) v/v and ACN as the DESI solvent. a) The superimposed extracted ion chromatograms of indoyl (4-hydroxy-Glucobrassicin), aromatic (Glucolepigramin/Glucosinalbin) and aliphatic (n-hexyl glucosinolate) glucosinolates. b) 4-hydroxy-Glucobrassicin (*m/z* 463) and hydroxy-methoxy Glucobrassicin (*m/z* 493). c) 3-hydroxy-4-methoxy glucosinolate (*m/z* 454). d) Glucolepigramin/Glucosinalbin (*m/z* 424). e) Glucotropaeolin (*m/z* 408). f) Glucolimnanthin/Glucoaubrietin (*m/z* 438). 68

Figure 3.5: HPTLC-(-)DESI-MS^2 profiles of intact glucosinolates from the hydromethanolic extract of red Maca (*L. peruvianum*) seeds via CID. a) Glucotropaeolin (*m/z* 408) using 30 as the collision energy. b) Glucolepigramin/Glucosinalbin (*m/z* 424) using 30 as the collision energy. c) Glucolimnanthin/Glucoaubrietin (*m/z* 438) using 30 as the collision energy. 71

Figure 3.6: The DESI-MS^2 fragmentation pathway of bioactive secondary metabolites in Maca (*L.peruvianum*). A. Aromatic Glucosinolates. B. Glycosylated Ascorbigens/Dihydroascorbigens.. 72

Figure 3.7: Glycosylated ABGs/dABGs in red and black Maca (*L. peruvianum*) seeds. 74

Figure 3.8: Glycosylated ABGs/dABGs fragmented by HPTLC-(-)DESI-MS/MS via CID from the hydromethanolic extracts of red Maca (*L. peruvianum*) seeds. a) β-D-glucose-ABG and Glucolepigramin/Glucosinalbin adduct (*m/z* 482) using 20 as the collision energy. b) Glucolepigramin/Glucosinalbin adduct and an unknown glycosylated ABG/dABG (*m/z* 508) using 20 as the collision energy. 75

Figure 3.9: C_{18} functionalized RPTLC coupled to (-)DESI-MS for the analysis of Brassicaceae fatty acids from the $CHCl_3$ extract of Maca (*L. meyenii*) using ACN:H_2O (8:2) v/v as the DESI solvent from a) Black Maca seeds. b) Black Maca root lyophilized powder. 78

Figure 3.10: The HPTLC-(+)DESI-MS spectra of imidazole alkaloids using ACN as the solvent in the mass range of *m/z* 240-600 extracted from a) The $CHCl_3$ extract of black Maca (*L. meyenii*) root lyophilized powder and b) Directly from Maca root tinctures. 80

Figure 3.11: The separation of Lepidiline A-D and three minor imidazole alkaloids from the $CHCl_3$ extract of black Maca (*L. meyenii*) lyophilized root powder with Ace:Ben:H_2O (7:2:1) v/v. 82

Figure 3.12: Imidazole alkaloids in Maca (*L. meyenii*) health supplements such as black Maca root lyophilized powder and Maca root tincture. B. MS^2 fragmentation pathway. 84

Figure 3.13: Imidazole alkaloids, Lepidiline A, B, C and D fragmented by HPTLC-(+)DESI-MS/MS via CID from $CHCl_3$ extracts of black Maca (*L. meyenii*) lyophilized root powder. a) Lepidiline A (*m/z* 277) using 30 as the collision energy. b) Lepidiline B (*m/z* 291) using 30 as the collision energy. c) Lepidiline C (*m/z* 307) using 25 as the collision energy. d) Lepidiline D (*m/z* 321) using 25 as the collision energy. 85

Figure 4.1: Full scan (+)ESI-MS spectra of *Sassafras albidum* extracts from A. Roots, B. Twigs, and C. Leaves. Reproduced with permission from Conceição et al.[165] 93

Figure 4.2: SIM mode extracted ion chromatograms of *Sassafras albidum* root extract by HPTLC-DESI-MS separated with Ben:EtOH (7:3 v/v). Reproduced with permission from Conceição et al.[165] 94

Figure 4.3: Alkaloids from *Sassafras albidum*. A) Isoquinoline and B) Aporphine. Reproduced with permission from Conceição et al.[165] 95

Figure 4.4: MS^n fragmentation pattern of the Benzylisoquinoline alkaloids and their characteristic fragment ions. Reproduced with permission from Conceição et al.[165] 98

Figure 4.5: 2D-DESI-MS image of *Sassafras albidum* root with imaging dimensions of 13000 µm x 13000 µm and a spatial resolution of 200 µm showing the spatial distribution of benzylisoquinoline and aporphine alkaloids. Reproduced with permission from Conceição et al.[165] 102

Figure 4.6: 2D-DESI-MS image of *S. albidum* twig with imaging dimensions of 13000 µm x 13000 µm and a spatial resolution of 200 µm showing the spatial distribution of benzylisoquinoline and aporphine alkaloids. B) Superimposed image of the distribution of cinammoralurine (*m/z* 298) and boldine (*m/z* 328). Reproduced with permission from Conceição et al.[165] 104

Figure 5.1: Full scan (+)ESI-MS spectrum of the ethyl acetate extract from *Ocotea spixiana* twigs. Reproduced with permission from Conceição et al.[122] 111

Figure 5.2: HPTLC-DESI-MS SIM extracted ion chromatograms of the ethyl acetate extract with acaricide activity of *O. spixiana* twigs. Reproduced with permission from Conceição et al.[122] ... 112

Figure 5.3: Alkaloids in ethyl acetate extract of twigs of *O. spixiana*. A) Benzylisoquinoline alkaloids. B) Aporphine alkaloids. Reproduced with permission from Conceição et al.[122] 113

Figure 5.4: Proposed fragmentation pathway and MS^n spectra of Reticuline (1). Reproduced with permission from Conceição et al.[122] 115

Figure 5.5: Fragmentation pathway of aporphine alkaloids from *Ocotea spixiana*. (A) Compounds with hydroxy and methoxy groups in vicinal positions represented by boldine (5). (B) Compounds with two vicinal methoxy groups represented by glaucine (10). (C) Compounds with a methylenedioxy group represented by isodomesticine (17). Reproduced with permission from Conceição et al.[122] 119

Figure 6.1: Metabolites in the (+)ESI-HRMS spectrum of Robusta Tropical at 100% maturity. The standard caffeine-D9 (*m/z* 204.14471) was used to compare the relative content of metabolites between green coffee bean species and across stages of maturity. Reproduced with permission from Lemos et al.[229] 128

Figure 6.2: The chemical structure of metabolites in green coffee beans. A. Small metabolites. B. Phenolic acids. C. Chlorogenic acids. 129

Figure 6.3: Phenolic and Chlorogenic Acids in the (-)ESI-HRMS spectrum of Robusta Tropical at 100% Maturity. The standard Salicylic acid (*m/z* 137.02411) was used to compare the relative content of phenolic and chlorogenic acids between green coffee bean species and across stages of maturity. Reproduced with permission from Lemos et al. [229] 130

Figure 6.4: Caffeine content in green coffee bean species across stages of maturity. Pink and blue bars represent increases and decreases in caffeine content, respectively. 134

Figure 6.5: Total trigonelline content (the sum of the protonated ion and potassium adduct) in green coffee bean species across stages of maturity. Pink and blue bars represent increases and decreases in trigonelline content, respectively. 135

Figure 6.6: Total sugar content in green coffee bean species across stages of maturity. Pink and blue bars represent increases and decreases in sugar content, respectively. 136

Figure 6.7: Caffeoylquinic acid (CQA) content in green coffee bean species across stages of maturity. Pink and blue bars represent increases and decreases in sugar content, respectively. 139

Figure 6.8: Total chlorogenic acid content in green coffee bean species across stages of maturity. Pink and blue bars represent increases and decreases in CGA content, respectively. 140

Figure 6.9: The heat map with the dendrogram scaled to represent the distance between each branch by Pearson's correlation. The vertical axis represents 14 bioactive metabolites and the horizontal axis the green coffee bean species. The red clustered data denotes 100% maturity, blue and green represents 80% and 60% maturity, respectively. 143

List of Abbreviations

2D	Two dimension
3D	Three dimension
Ace	Acetone
AChE	Acetylcholinesterase
ACN	Acetonitrile
AFADESI	Air flow assisted desorption electrospray ionization
AMS	Ambient mass spectrometry
Ben	Benzene
BnOH	Benzyl alcohol
APCI	Atmospheric pressure chemical ionization
CI	Confidence interval
CID	Collision induced dissociation
CMC	Carboxymethylcellulose
CNS	Central nervous system
c-SPESI	Contact mode scanning probe electrospray ionization
Da	Dalton
DAPCI	Desorption atmospheric pressure chemical ionization
DAPPI	Desorption atmospheric pressure photoionization
DDA	Data dependant acquisition
DESI	Desorption electrospray ionization
DESI-MS	Desorption electrospray ionization mass spectrometry
DESI-MSI	Desorption electrospray ionization mass spectrometry imaging
EASI	Easy ambient sonic spray ionization
ESI-MS	Electrospray ionization mass spectrometry
EtOAC	Ethyl acetate
EtOH	Ethanol
FAAH	Fatty acid amide hydrolase
FDA US	Food and drug administration of the United States of America
g	Grams
GC-MS	Gas chromatography-mass spectrometry
HCD	Higher energy collision dissociation
Hex	Hexane
Hr(s)	Hour/hours
HPLC-MS	High performance liquid chromatography-mass spectrometry
HPTLC	High performance thin layer chromatography
HPTLC-DESI-MS	High performance thin layer chromatography desorption electrospray ionization mass spectrometry
RPTLC-DESI-MS	Reverse phase thin layer chromatography desorption electrospray ionization mass spectrometry
I_D/I_{IS}	Ion intensity of the drug divided by the ion intensity of the internal standard

IS	Internal standard
LA-LSCA	Laser ablation liquid surface capture analysis
LADI	Laser ablation direct analysis in real time imaging
LAESI	Laser ablation electrospray ionization
LEMS	Laser electrospray mass spectrometry
LESA	Liquid extraction surface analysis
LMJ-SSP	Liquid microjunction-surface sampling probe
LOD	Limit of detection
LOQ	Limit of quantitation
MALDI-MSI	Matrix assisted laser desorption ionization-mass spectrometry imaging
MeOH	Methanol
MS	Mass spectrometry
MSI	Mass spectrometry imaging
MS^n	Multistage mass spectrometry (n = 2, 3, 4, etc.,)
MS/MS	Mass Spectrometry/Mass Spectrometry
nanoESI-MS	nano electrospray ionization mass spectrometry
NMR	Nuclear magnetic resonance
PIR-LAESI	Picosecond infrared laser ablation electrospray ionization
PPCPs	Pharmaceuticals and personal care products
QC	Quality control
RE	Relative error
RF	Radiofrequency
R_f	Retention factor
RSD	Relative standard deviation
S/N	Signal to noise ratio
SD	Standard deviation
SIM	Selected ion monitoring
SP	Single probe
TLC	Thin layer chromatography
t-SPESI	trapping mode-scanning probe electrospray ionization
v/v	volume by volume

List of Publications

Chapter 1

1. **Perez, C.J.**, Bagga, A.K., Prova, S.S., Yousefi-Taemeh, M., Ifa, D.R. Review and perspectives on the applications of mass spectrometry imaging under ambient conditions. *Rapid Commun Mass Spectrom*. 2019; 33 (S3): 27–53.

Chapter 2

2. **Perez, C.J.**, Ifa, D.R. Internal standard application strategies in mass spectrometry imaging by DESI. *Rapid Commun. in Mass Spectrom.* 2020. **Submitted.**

Chapter 3

3. **Perez, C.J.** Souza, R.C., Ifa, D.R. Chemical profiling of bioactive secondary metabolites from Maca (*Lepidium peruvianum*) by normal and reverse phase TLC coupled to DESI-MS**.** *J Mass Spectrom.* 2020. **Submitted.**

Chapter 4 – My contribution to this project was in the involvement of the mass spectrometry experimental design, performing all the experiments, and the data interpretation.

4. Sousa, R.C., **Perez, C.J**., Branco, A. Botura, M.B., Ifa, D.R. Identification of *Sassafras albidum* alkaloids by high-performance thin-layer chromatography tandem mass spectrometry and mapping by desorption electrospray ionization mass spectrometry imaging. *J. Mass Spectrom*. 2020. **In print.**

Chapter 5 - My contribution to this work was only in the mass spectrometry experiments, such as the experimental design, performing all the mass spectrometry experiments and the data interpretation. However, I was not involved in the biological activity assays or the molecular docking experiments.

5. Sousa, R.C., Reis, I.M.A. Cerqueira, A.P.M. **Perez, C.J.**, Junior, M.C.S., Branco, A. Ifa, D.R., Botura, M.A. Rapid Structural Characterization of Benzylisoquinone and Aporphine Type Alkaloids from *Octea Spixiana* Acaricide Extract by HPTLC-DESI-MS^n. *Phytochemical Analysis.* 2020. 1-11.

Chapter 6 - My contribution to this project was centered on the development of the mass spectrometry experiments, such as the experimental design, performing all the experiments and the data interpretation. However, I was not involved in the sensory analysis of the roasted coffee beans, nor in the statistical analysis by principal component analysis (PCA).

6. Lemos, M.F., **Perez, C.,** Pereira da Cunha, P.H., Filgueiras, P.R., Pereira, L.L., Almeida da Fonseca, A.F., Ifa, D.R., Scherer, R. Chemical and sensory profile of new genotypes of Brazilian *Coffea canephora*. *Food Chemistry.* 2020. 310: 125850.

7. Sales, C.C**.**, **Perez, C.J.,** Lopes, P.S., Leite-Silva, V.R., Ifa, D.R., Andre-Filho, N. A simple and rapid identification method for citronella oil – Nanostructured Lipid Carrier using Electrospray Ionization Mass Spectrometry. *Journal of Pharmaceutical Analysis*. 2020. **Submitted.**

8. Danuello, A., Castro, R., Pilon, A.C., Pires Bueno, P.C., Pivatto, M., Junior, G.M.V., Carvalho, F.A., Oda, F.B., **Perez, C.J.,** Lopes, N.P. Dos Santos, A.G., Ifa, D.R., Cavalheiro, A.J. Fragmentation study of clerodane diterpenes from Casearia species by tandem mass spectrometry (QToF and Ion Trap). *Rapid Commun Mass Spectrom.* 2020.

9. Woolman, M., Tata, A., Dara, D., Meens, J., D'Arcangelo, E., **Perez, C.J.,** Prova, S.S., Bluemke, E., Ginsberg, H.J., Ifa, D.R., McGuigan, A., Ailles, L., Zarrine-Afsar, A. Rapid determination of the tumour stroma ratio in squamous cell carcinomas with desorption electrospray ionization mass spectrometry (DESI-MS): a proof-of-concept demonstration. *Analyst***.** 2017.142; 3250-3260.

Chapter One: General Introduction

Chapter 1 includes sections of the published review:

Perez, C.J., Bagga, A.K., Prova, S.S., Yousefi-Taemeh, M., Ifa, D.R. Review and perspectives on the applications of mass spectrometry imaging under ambient conditions. *Rapid Commun Mass Spectrom.* **2019**. 33 (S3): 27–53.

1.1. The Foundation of Mass Spectrometry

Mass spectrometry (MS) is a powerful analytical tool designed for the analysis of ions based on their mass to charge ratios to discovery the identity of molecules. In 1897, J.J. Thomson observed the deflection of cathode rays in an electric field determining the mass to charge ratio of the electron for the first time.[1,2] A year later, W. Wien discovered and measured the mass of the proton. The birth of mass spectrometry was in 1907 with J.J. Thomson's hypothesis that channel rays were beams of charged particles with the lighter particles deflecting more than heavier ones, giving rise to the basic principle of ion separation based on mass.[2] The first mass spectrograph was invented by Francis W. Aston in 1919 and this instrument was capable of measuring the relative masses of atoms and molecules. A few years later, Aston won the 1922 Nobel Prize in Chemistry for his discovery of isotopes in non-radioactive elements using this instrument.[2] These pioneering contributions from W. Wien, J.J. Thompson and F.W. Aston launched the novel field of mass spectrometry.

1.2. Atmospheric Pressure Ionization Mass Spectrometry

In atmospheric pressure mass spectrometry, the ionization of neutral molecules to positively or negatively charged ions, as well as pre-charged ions and adduct formation is carried out under conditions of atmospheric pressure and temperature where the ions are transferred into the mass spectrometer under vacuum. The most common ionization techniques are atmospheric pressure chemical ionization (APCI) and electrospray ionization (ESI). The invention of ESI by John Fenn in 1989 revolutionized the analysis of polar biological molecules in MS.[3]

1.2.1. Electrospray Ionization Mass Spectrometry (ESI-MS)

Electrospray ionization (ESI) is a soft ionization technique operated at atmospheric pressure for the analysis of polar small molecules and large biological macromolecules.[3] The charged solution at the capillary tip is ejected as a Taylor cone that emits a mist of charged droplets. The droplets undergo solvent evaporation as the charge density builds up on the

shrinking droplets. At the Rayleigh limit, Coulombic repulsion of the surface charge equals the surface tension of the solution and Coulombic explosion leads to splitting of the droplets into smaller highly charged nanodroplets to form gas-phase ions (Figure 1.1.A).[4] The ion evaporation model (IEM) and charge residue model (CRM) explain the ionization mechanisms in ESI.[5] Low molecular weight ions ionize by IEM and large globular biomolecules, such as natively folded proteins by CRM.[5] In CRM, the analyte in charged nanodroplets retains some of its droplet's charge as the solvent shell evaporates. In IEM, small solvated ions are ejected from droplet surfaces when Coulombic repulsion overcomes the liquid's surface tension and solvation forces.[4,5] The chain ejection model (CEM) has been proposed for disordered polymers with nonpolar side chains. The macromolecule is expelled from the droplet surface producing structures where one end of the polymer chain remains within the droplet by charge solvation and the complete ejection of the macromolecule produces the gas phase ion.[4,6]

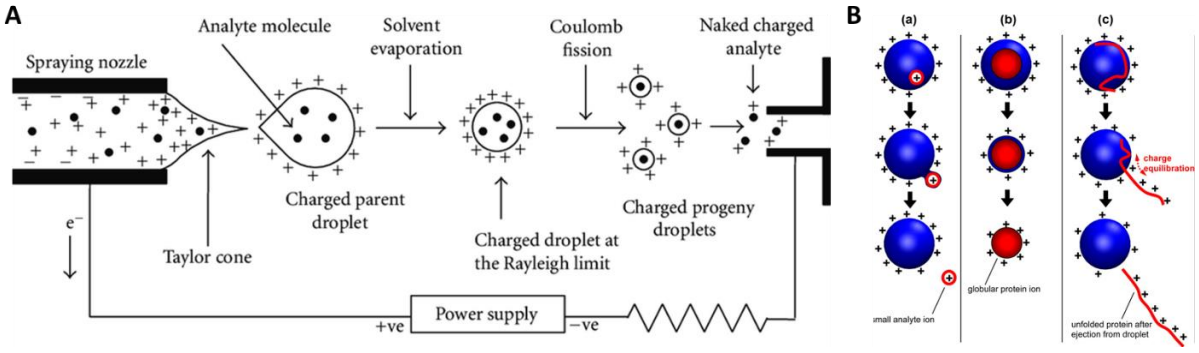

Figure 1.1: A. Electrospray ionization (ESI). Adapted from Banjeree et al.[7] the summary of ESI mechanisms: IEM, CRM and CEM. Reproduced with permission from Konermann et al.[5]

1.3. Ambient Ionization Mass Spectrometry

Ambient mass spectrometry (AMS) is a well-established analytical and bioanalytical tool that enables sampling of chemical and biological samples providing MS information with respect to the identity of molecules on the surface (Figure 1.2).[8]

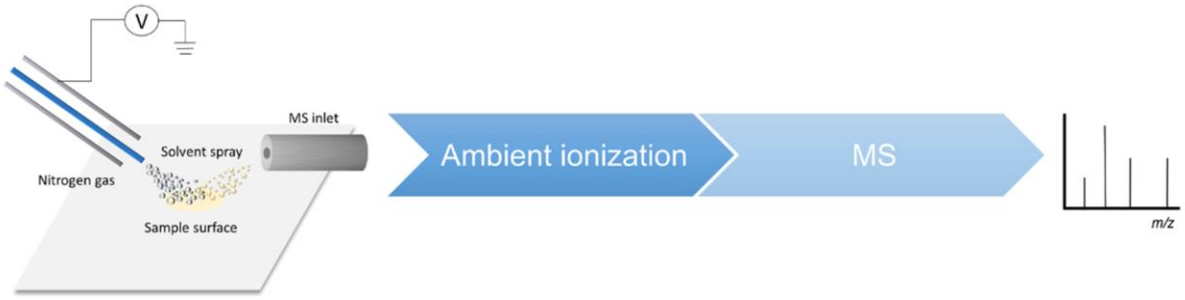

Figure 1.2: Schematic of the general methodology in ambient mass spectrometry. Reproduced with permission from Li et al.[9]

MS analysis in the ambient environment facilitates soft desorption and ionization of analytes. Samples can be analyzed in their native state with little or no sample preparation prior to the analysis.[10] The major benefits associated with AMS methods are the rapid analysis of native samples with reductions in analyses times due to fast processes of desorption/ionization and high throughput capabilities from the substantial chemical information of many compounds in a single analysis compared to histology, autoradiography of radiolabeled compounds, fluorescence microscopy and other imaging techniques. Untreated, native biological tissues are chemically complex, therefore high selectivity and specificity are important aspects considered during the development of AMS imaging methodologies.[8,10]

In AMS methods, desorption and ionization occurs in the open environment externally from the mass spectrometer. A plethora of AMS methods surfaced shortly after the introduction of two pioneer techniques, desorption electrospray ionization (DESI) in 2004 by Cooks et al.[11] and direct analysis in real time (DART) in 2005 by Cody et al.[12] Ambient MS methods can be classified according to the nature of the agents promoting the desorption/ionization of the analytes and the number of steps involved in the process. For instance, in the spray-based methods, a simple solid-liquid phase extraction allows soluble analytes from a solid sample matrix to be extracted into the liquid solvent. The types of analytes extracted depends on the miscibility of the analytes in the solvent, the geometric parameters of the ion source, and the complexity of the biological tissue matrix. Desorption and ionization can occur either as a one-step mechanistic process, desorption/ionization in sequence whereby these processes occur simultaneously and one

cannot be separated from the other, or as a two-step process where either ionization or desorption occurs prior to the other, and so these events are separated in time and space.[13]

DESI, is an example of a one-step process, a charged spray promotes both desorption and ionization of the analytes from the surface.[11] In two-step processes, a neutral solvent desorbs the analytes from the surface and the second step ionizes the analytes to produce gas phase ions. For instance, the two-step method, desorption atmospheric pressure photoionization (DAPPI),[14] a neutral heated jet of vaporized solvent desorbs analytes from the surface and photoionization is carried out by emitted photons from a UV lamp to induce ionization and produce gas phase ions.

To date, there are more than 80 AMS ionization sources published in the literature, yet here we only focus on selected AMS methods that have shown imaging capabilities (Table 1.1).[4,15-19] AMS imaging allows for direct chemical sampling of the surface to map the spatial distribution of molecules from complex matrices in the open environment.[8] Table 1.1 briefly describes the desorption/ionization processes for selected imaging AMS methods such as DESI, air flow assisted desorption electrospray ionization (AFADESI), nano-desorption electrospray ionization mass spectrometry (nano-DESI), ambient sonic-spray ionization (EASI), and the two-step ambient laser ablation methods such as laser ablation electrospray ionization (LAESI) and laser ablation-liquid capture surface analysis (LA-LCSA). So far, the contributions in the literature for ambient MS imaging with spray-based methods are much greater than those for laser and plasma ionization methods.[8] Imaging applications with AMS methods have been demonstrated in many fields such as drug discovery and development[20-24], forensic analysis[25-27], metabolomic profiling of bacterial[28,29] and fungal cultures and cocultures[30-32], plant and natural products[29,33-38], environmental applications and toxicology[39-41], and cancer grading and biomarker discovery.[42-50]

Table 1.1: Summary of selected ambient ionization imaging techniques showing the type of ionization, a schematic of the ion source, common imaging resolutions and references of the first report of the ambient ionization imaging techniques. Reproduced with permission from Perez et al.[8]

Ambient Ionization Technique [Refs]	Type of Ionization	Ion Source Schematic	Imaging Resolutions
Desorption Electrospray Ionization (DESI) [11]	Liquid extraction	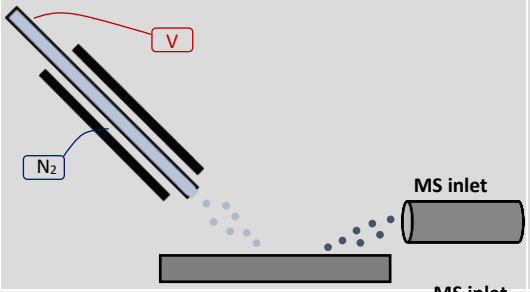	100-200 µm (35 µm)[a]
Air Flow Assisted Desorption Electrospray Ionization (AFADESI) [51]	Liquid extraction	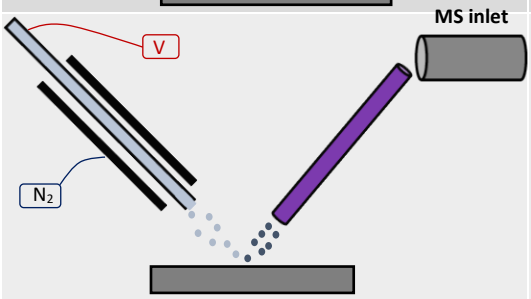	200-300 µm (200 µm)[a]
Easy Ambient Sonic-Spray Ionization (EASI) [52]	Spray based	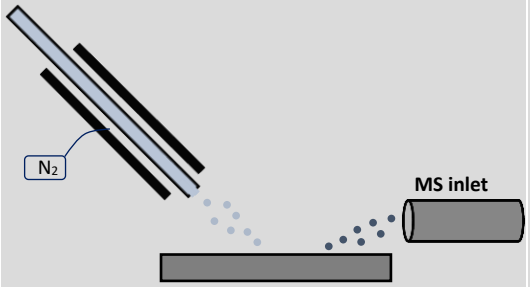	100-200 µm (50 µm)[a]
Nano Electrospray Desorption Ionization (nano-DESI)[53]	Liquid Extraction	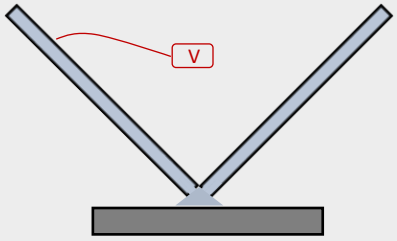	50-100 µm (12.5 µm)[a]

Laser Ablation Electrospray Ionization (LAESI)[54]/ Laser Electrospray Mass Spectrometry (LEMS)[55]	Two steps (Laser ablation and Electrospray ionization)	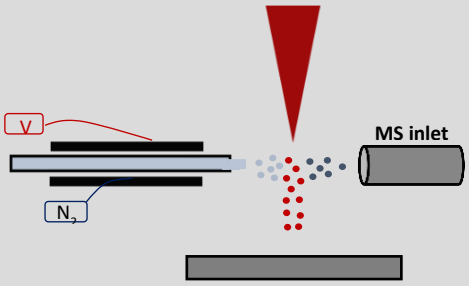	200-300 µm (30 µm)[a]/ 60 µm [a]
Single Probe (SP)[56]	Liquid Extraction	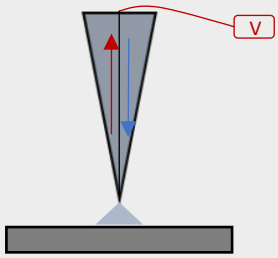	10-20 µm (8.5 µm)[a]
Liquid Microjunction-Surface Sampling Probe (LMJ-SSP)[57]	Liquid Extraction	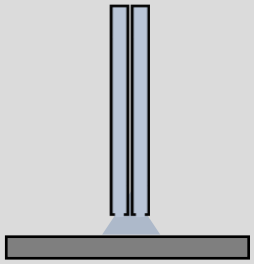	0.5-1 mm (0.5 mm)[a]
Laser Ablation-Liquid Capture Surface Analysis (LA-LCSA)[58]	Liquid Extraction	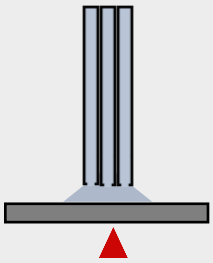	(50 µm)[a]
Contact mode-Scanning Probe Electrospray Ionization/ Tapping mode- Scanning Probe Electrospray Ionization (c-SPESI/t-SPESI) [59,60]	Liquid extraction	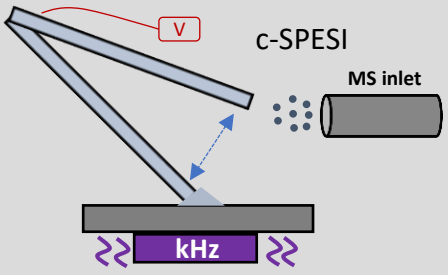	100 µm[a]

Desorption Atmospheric Pressure Chemical Ionization (DAPCI)[61]	Plasma	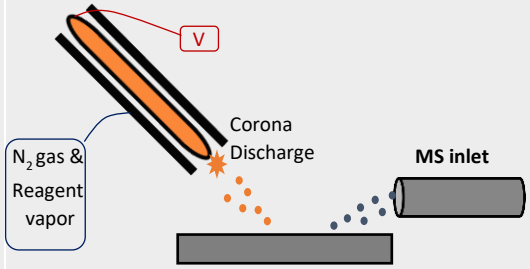	200-500 µm (58 µm)[a]
Desorption Atmospheric Pressure Photoionization (DAPPI)[62]	Photo-ionization	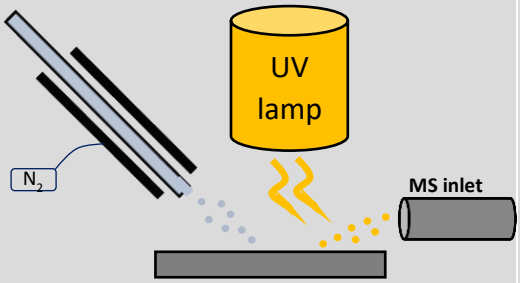	1000 µm (700 µm)[a]
Laser Ablation Direct Analysis in Real Time Imaging (LADI)[63]	Two step- (Laser Ablation and Plasma Ionization)	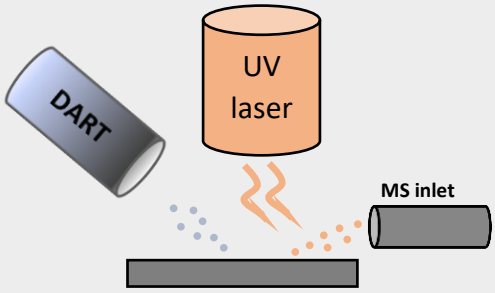	50 µm[a]
Picosecond Infrared-Laser Ablation Electrospray Ionization (PIR-LAESI)[64]	Two step- (Laser Ablation and electrospray ionization)	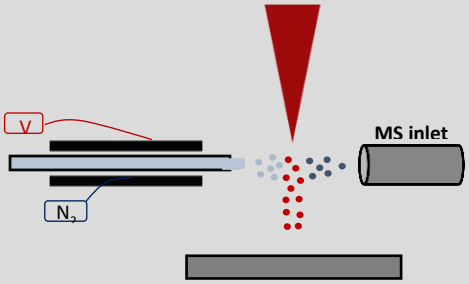	100 µm[a]
Liquid Extraction Surface Analysis (LESA)[65]	Liquid Extraction	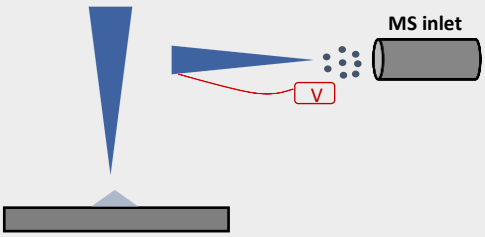	1 mm (350 µm)[a]

[a] The highest lateral resolution reported for the ambient mass spectrometry imaging technique.

1.3.1. Desorption Electrospray Ionization-Mass Spectrometry

DESI is part of the one-step spray-based methods in ambient ionization mass spectrometry. The ionization mechanism is known as the "droplet pickup mechanism".[11] A charged spray of primary droplets of solvent impacts the surface, the analytes in tissues or substrates are desorbed and ionized creating secondary droplets of analyte ions (Figure 1.3.A).[11,66,67] Droplet dynamics in DESI show droplets traveling at average velocities of 120 µm/s with average diameters of 2-4 µm. Under typical DESI conditions, droplets have been shown to roll along the surface increasing contact time and the amount of material collected in the droplets.[66]

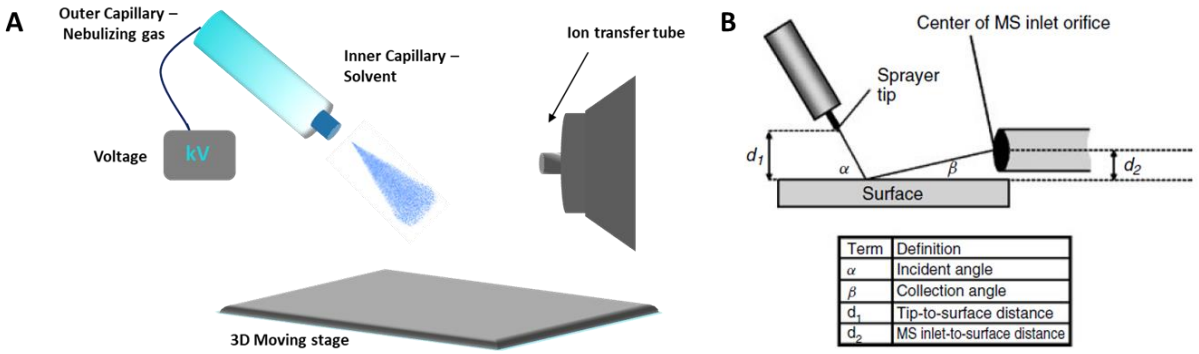

Figure 1.3: A. Schematic of the Desorption Electrospray Ionization Source. B. DESI geometric parameters. Reproduced with permission from Takats et al.[67]

In the DESI experiment, optimizing geometric parameters such as the spray tip-to-surface distance (d_1), MS inlet-to-surface distance (d_2), the incident (α) and collection angle (β) of the sprayer allows for DESI conditions specific to the targeted analytes for maximum desorption and ionization to increase the sensitivity and selectively of the analysis (Figure 1.3.B).[67]

1.3.2. Principles of Ambient Mass Spectrometry Imaging

AMS methods have an interesting feature allowing for *in situ* imaging analyses of the surface such as thin biological tissues to create interactive 2D or 3D chemical images. The ion

source is coupled to an automated x, y, z moving stage which rapidly scans a selected surface area to achieve reproducibility and reliability in the rastering speed for MS imaging (Figure 1.4). Conventional sampling of biological tissue normally proceeds by (i) flash freezing biological tissue (mammalian/human or other specimens) after dissecting (ii) cryosectioning tissue sections into thin slices generally between 10-50 µm (ii) thaw mounting the tissue sections onto substrates for tissue imprints (iii) drying the tissue sections immediately prior to analysis in a vacuum desiccator.[16,68-70]

The acquisition of MS data relies on the ion source (DESI, nano-DESI, LAESI, etc.) to generate ions by desorbing analytes from the surface, and subsequently direct them into the mass spectrometer inlet for MS analysis. Data acquisition involves sampling the surface area (xy) with a prior width (x) and length (y) selection to generate 2D chemical images by collecting mass spectral data on a line-by-line or pixel-by-pixel basis.[68] The lateral resolution is dependent on the sampling spot size, in AMS imaging, typical lateral resolutions range between 8.5-200 µm. In spray-based methods, the surface is scanned as an array of pixels acquired continuously as the solvent spray is delivered onto the sampling surface. The data obtained from an individual pixel is represented by a corresponding single mass spectrum. Spatial resolutions depend on the sampling spot size and operating ion source parameters including the solvent system and flow rate, geometric ion source parameters, moving stage raster speed, and scan speed of the mass spectrometer.[71] A slow raster speed allows for enhanced extraction of analytes from tissues and minimizes carryover but total acquisition time per line increases drastically, while faster raster speeds allow for less imaging time, yet the desorption and ionization efficiency of the analytes can be affected demonstrated by lower signal intensities.

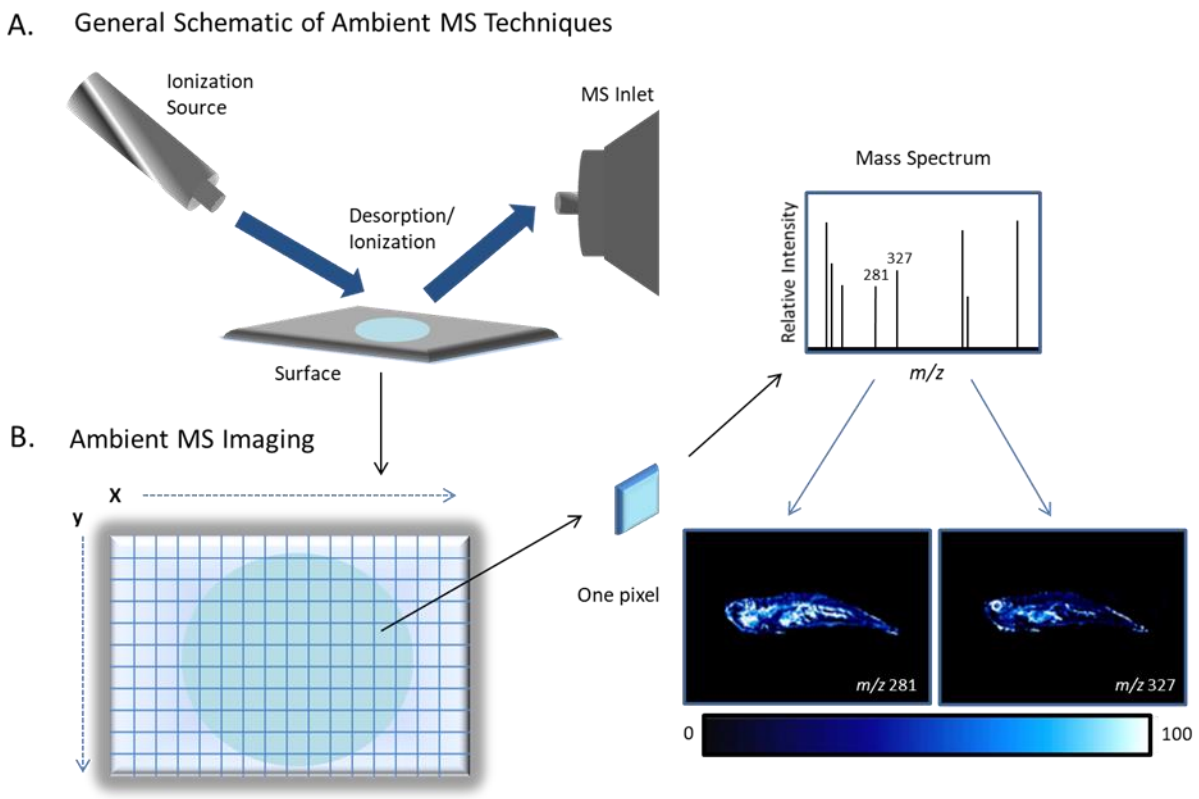

Figure 1.4: (A) General schematic of ambient MS techniques. Ambient ionization can take place as a single step where ionization and desorption occur simultaneously, or as a two-step process in which desorption and ionization are separate processes. (B) Ambient MS imaging. In MS imaging, the total area for imaging is chosen, along with the lateral imaging resolution. xy coordinates are selected and the image is subdivided into individual pixels. For each pixel a single mass spectrum or the average of several mass spectra is collected and stored with its corresponding spatial coordinates. Once the entire surface has been scanned, an average mass spectrum for each acquired line/pixel can be created. The distribution of specific ions can be visualized by the creation of 2D ion images for a specific mass-to-charge (*m/z*) ratio where the colour scale represents the normalized intensity of ions. Each pixel from the image is associated with the original mass spectrum/mass spectra acquired at a specific point (x,y). MSI can map the localization of ions across a selected surface. [Zebrafish ion images in (B) reproduced from Lostun et al.[72]]. Reproduced with permission from Perez et al.[8]

In imaging applications, developments on fine-tuning operating ion source parameters, solvent systems, solvent flow rates, lateral resolution, mass spectrometric scan rate, and inner diameters of the silica capillary have accomplished remarkable enhances in spatial resolution. The best spatial resolution in DESI has been reported by Campbell and coworkers as low as 35 µm from rat cerebellum tissue images.[73] In DESI, the morphologically friendly solvent system

DMF:EtOH (1:2) was superior in resolving features below 100 µm; in comparison to DMF:EtOH (2:1) and MeOH:H_20 (1:1) in rat cerebellum tissues for two lipids, the sterol lipid $[ST(24:1)-H]^-$ and the phosphatidylserine $[PS(18:0/22:6)-H]^-$ of *m/z* 888 and *m/z* 834, respectively.[73] Enhanced performance is attributed to the intrinsic capability of the solvent to minimize redistribution and splashing of the analytes on the surface. The effect of solvent flow rate on the spatial resolution has been examined whereby increases in flow rates allow for more analytes to be desorbed from the surface increasing ion intensities however, increasing the flow rate any further tends to increase the sampling spot size and splashing without substantial increases in ion intensities.[73]

1.3.3. Tandem Mass Spectrometry and Multistage Mass Spectrometry

Tandem mass spectrometry (MS/MS), is a two-step fragmentation technique performed in space (e.g. triple quadrupoles - QQQ) or in time (e.g. linear ion traps - LIT). In the first stage of MS/MS, the precursor ion is isolated from the rest of the ions from the full scan MS and typically fragmented by Collision Induced Dissociation (CID). In the second stage, the product ions are scanned and collected to produce the MS/MS spectrum.[74,75]

Multistage mass spectrometry (MS^n), is a sequential fragmentation technique that can only be performed on ion trap and Fourier transform-ion cyclotron (FT-ICR) type instruments. In the first stage of MS^n, the MS/MS spectrum is obtained from the isolation and fragmentation of the selected precursor ion by CID, in the same way as in MS/MS. From the series of product ions in the MS/MS spectrum, among them a product ion is selected as a precursor ion allowing for another isolation and fragmentation cycle to be performed resulting in the MS^3 spectrum. This fragmentation process can be repeated in a series of MS^n spectra, where n represents the number of times the cycle of precursor isolation-fragmentation-product ion was carried out.[75]

1.4. Mass Spectrometers

A general overview of the mass spectrometers will be discussed in the next sections including the Thermo Finnigan™ LTQ™, Thermo Scientific™ Orbitrap Elite™ Ion trap-Orbitrap and

the QExactive™ Quadrupole-Orbitrap hybrid mass spectrometers. Hybrid mass spectrometers combine powerful features between two or more mass analyzers such as increased scan speed, mass accuracy, multistage fragmentation (MS^n), high mass resolving power, and high sensitivity, among other features.

1.4.1. Thermo Finnigan™ LTQ™ Mass Spectrometer

The linear quadruple ion trap (LTQ) is an analytical instrument that uses radiofrequency (RF) in electric fields to trap charged particles (Figure 1.5). As ions enter the mass spectrometer, the ion sweep cone and the ion transfer tube/capillary aid in the desolvation of ions. The ion guides, such as the tube lens, skimmer, Q00, Q0, and Q focus and transmit the ion beam while lens L0, L1 and the gate lens control the injection and ejection of ions. For example, for positive ions, the gate lens opens at a negative potential (-90V) and closes at a positive potential (50V) to guide the ion beam into the trap.

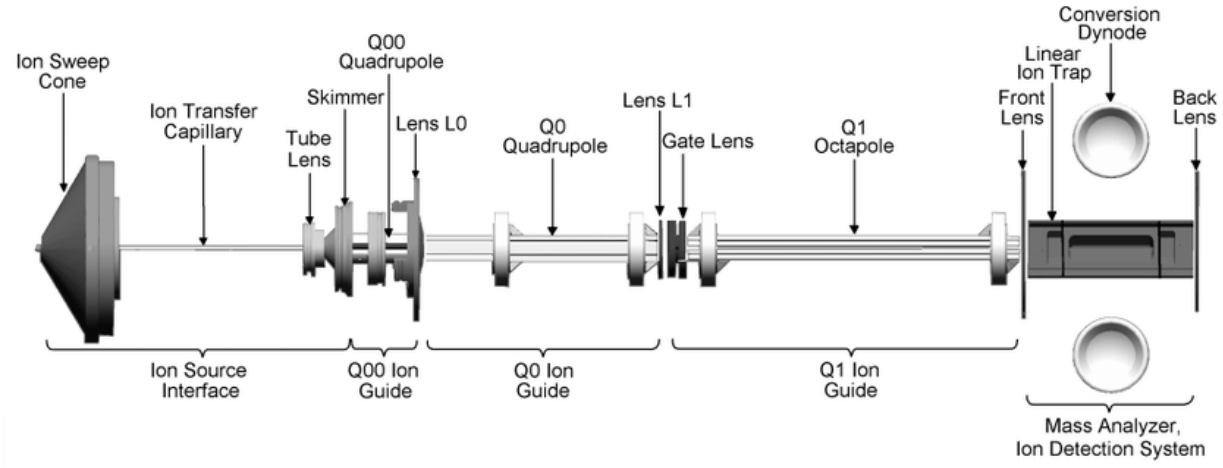

Figure 1.5: Schematic of the Thermo Finnigan™ LTQ™ Mass Spectrometer. Reproduced with permission from[76].

The single 2D linear ion trap is a set of quadrupole rods that collect and trap ions using radio frequencies (RF) to confine ions radially (Figure 1.6).[77] The ions are scanned out to the ion detection system, two electron multipliers with conversion dynodes that consist of a series of

cathodes and anodes. Briefly, an ion strikes the metal surface of the dynode and the signal is amplified by producing secondary electron emissions creating a cascade of electrons.[77]

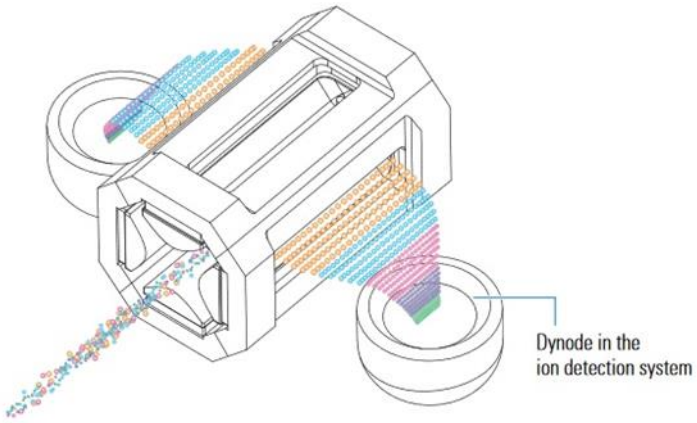

Figure 1.6: The linear ion trap ejecting ions into the dynode detection system - two adjacent electron multipliers in the Thermo Finnigan™ LTQ™. Reproduced with permission from [77].

1.4.2. Thermo Scientific™ LTQ-Orbitrap Elite™ Hybrid Mass Spectrometer

The LTQ-Orbitrap Elite™ combines the tandem MS^n, fast scanning speeds capabilities of the ion trap and the high mass accuracy, sensitivity and high resolution of the Orbitrap.[78] The S-lens focuses and transmits the ions and optimizes the removal of any remaining neutral molecules. The ion beam enters the dual cell 2D linear ion trap that holds the high-pressure and a low-pressure cell. The trapping, isolation, and dissociation of the ions occurs in the high-pressure trap whereas, the ion scan out takes place in the low-pressure cell with the two adjacent electron multipliers.

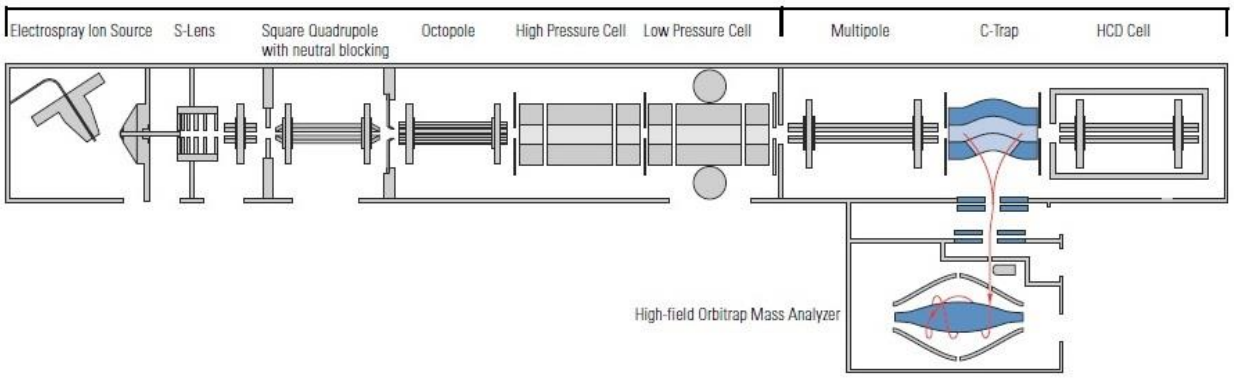

Figure 1.7: Schematic of Thermo Scientific™ LTQ-Orbitrap Elite™. Reproduced with permission from Hecht et al.[74]

Once the ions enter the C-Trap, RF waveforms trap the ions by colliding with Nitrogen gas cooling the ions and oscillating along the length of the trap (Figure 1.9). The ions are injected into the inner electrode of the Orbitrap as discrete packets of ions by ramping down the RF, no longer trapping the ions and then applying a DC voltage to the rods to eject the ions out of the C-trap. The Orbitrap contains an outer electrode and a spindle shaped central electrode. The radial electric field between the outer and central electrode and the centrifugal force drives the ions into harmonic axial oscillations. Outer electrodes serve as receiver plates and detect the frequency of axial oscillations in the form of current detection.

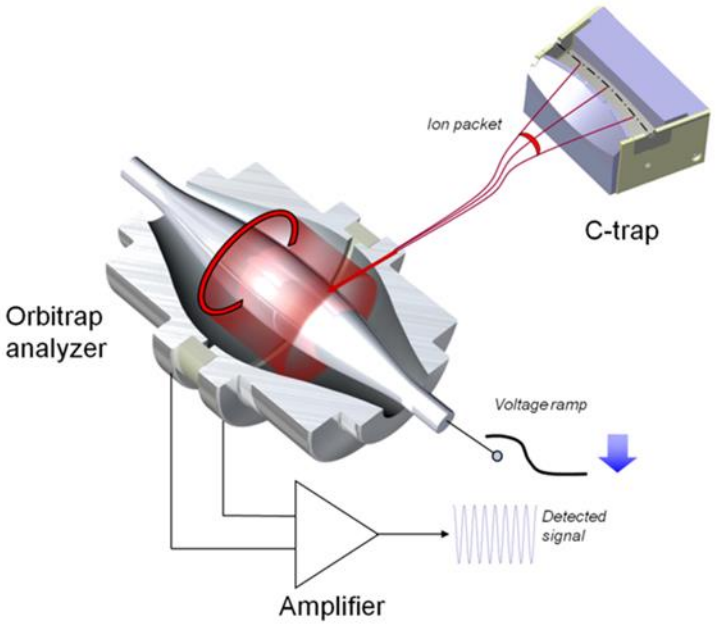

Figure 1.8: Schematic of the C-trap and Orbitrap. Reproduced with permission from Hecht et al.[74]

1.4.3. Thermo Scientific™ QExactive ™ Hybrid Mass Spectrometer

The QExactive is a quadrupole-Orbitrap hybrid instrument that features the power of the quadrupole acting as a mass filter for the isolation of precursors and the high mass accuracy, sensitivity and high mass resolving power of the Orbitrap for MS full scans, high resolution MS/MS spectra and the high-energy collisional dissociation (HCD) cell for precursor ion fragmentation.[79,80]

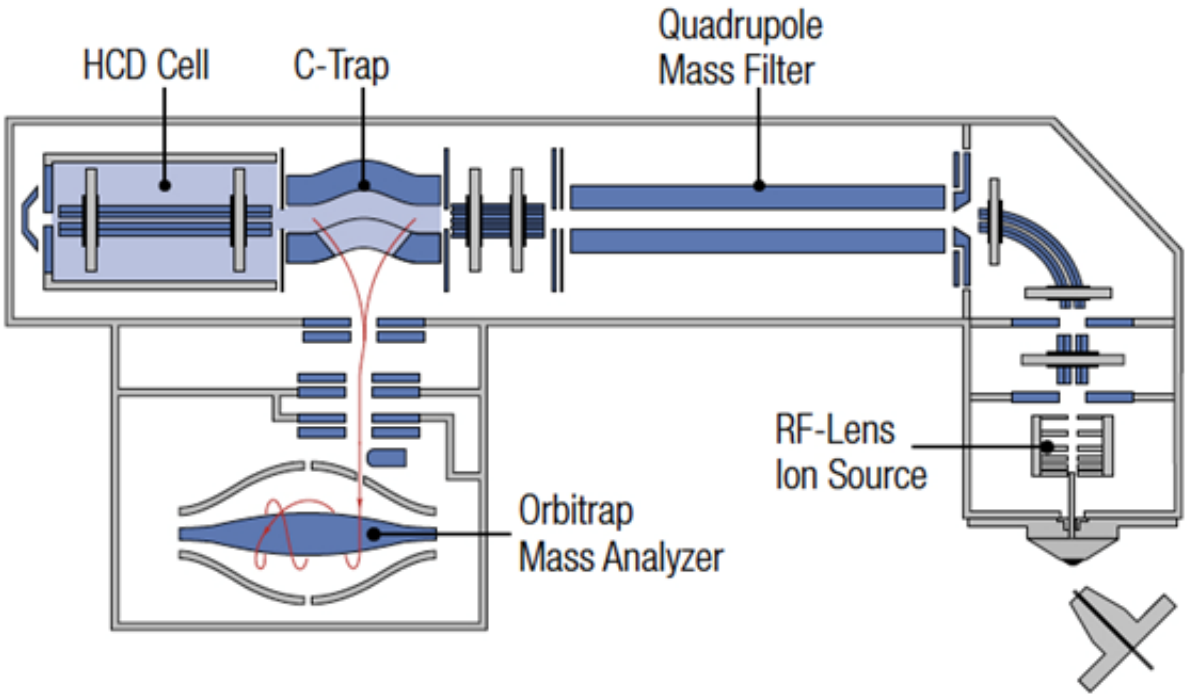

Figure 1.9: Schematic of the Thermo Scientific™ QExactive™. Reproduced with permission from Michalski et al.[79]

1.5. Principles of Thin layer Chromatography

Thin layer chromatography (TLC) is a qualitative and quantitative analytical tool widely used due to its simplicity, low cost, high sensitivity, and high throughput capabilities.[81,82] The principle of the separation is driven by adsorption properties. The strength of the interactions between the analyte, mobile phase and the stationary phase drives the migration of compounds on the TLC plate. The types of interactions are non-covalent such as electrostatic interactions, hydrogen bonding, dispersive forces (Van der Waals), dipole-dipole, and ion-dipole. The migration of compounds is measured by the retention factor (R_f), defined as the distance traveled by the analyte divided by the total length of the separation. The distance travelled is measured from the centre of the deposited spot up to the distance travelled by the solvent front.

High performance thin layer chromatography (HPTLC) is an enhanced version of TLC for better resolution, lower limits of detection and more commonly used for quantitative analysis. HPTLC plates are of higher quality than conventional TLC, the stationary phase has narrower

mean particle size distributions, roughly 5-6 µm (particle ranges: 4-8µm) instead of 10-12 µm (particle ranges: 5-20µm). The volume of the analyte is reduced from 1-5 µL to 0.1-0.5 µL and the thickness of the silica gel layer is thinner at 100-200 µm instead of 200-250 µm in TLC. The surface of the spherical silica gel particle holds microscopic pores (60 Å) where analytes are retained therefore, smaller particle sizes create compact bands with less analyte dispersion.[81] In HPTLC, the separation efficiency improves due to better resolution from narrower peak widths, reproducibility, reduced diffusion and decreased analysis times.

1.5.1. Normal and Reverse Phase TLC

Normal and reverse phase are the two types of polarity modes for the separation of compounds by TLC.[82] In normal phase, the stationary phase is polar with adsorbents such as silica or alumina, while the mobile phase consists of non-polar or non-polar/polar mixtures such as ethyl acetate and hexane (EtOac/Hex). Polar compounds interact strongly with the silanol groups in silica on the TLC surface through non-covalent interactions such as hydrogen bonding, dipole-dipole, ion-dipole, etc. and interact less so with the non-polar mobile phase therefore, polar compounds do not migrate significantly up the TLC plate (low R_f). Non-polar compounds interact with the non-polar mobile phase through non-covalent interactions such as the hydrophobic effect and π-stacking of double bonds/aromatic conjugated systems and migrate farther up the TLC plate than polar compounds (high R_f). In reverse phase TLC (RPTLC), the stationary phase is non-polar, the most common adsorbents are octadecylsilane (C_{18}) and octylsilane (C_8) and polar mobile phases are composed of acetonitrile/water (ACN/H_2O) or methanol/water ($MeOH/H_2O$).[82] Non-polar compounds interact strongly with C_{18} allowing the retention of non-polar compounds on the surface (low R_f). Polar compounds interact more strongly with the polar mobile phase and are not as easily retained on the C_{18} adsorbent, therefore they tend to migrate farther up the TLC plate (high R_f). Table 1.2 summarizes the general principles of normal and reverse phase TLC.

Table 1.2: Summary of the Principles of Normal and Reverse Phase TLC

Parameter	Normal Phase	Reverse Phase
Stationary Phase	Silica	C_{18}
Mobile Phase	Non-polar or non-polar/polar	Polar
Common mobile phases	EtOAC/Hex	ACN/H_2O
Polar compounds	Low R_f	High R_f
Non-polar compounds	High R_f	Low R_f
Increasing solvent polarity	Increases R_f	Decreases R_f

1.5.2. HPTLC Coupled to DESI-MS

Coupling TLC/HPTLC to DESI-MS creates a very powerful, rapid and simple analytical tool to identify, separate, and quantify compounds in a single HPTLC-DESI-MS analysis.[83,84] The high throughput capability of the technique leads to the detection of several compounds in a single run with high sensitivity.[83-86] The analytes from a complex mixture are deposited onto the HPTLC plate into a closed TLC chamber to allow the separation of molecules by the mobile phase system. The TLC plate is secured onto the 3D moving stage for offline DESI-MS analysis and the moving stage is programmed to raster horizontally in the x-direction across the TLC surface with speeds of ~100 µm/s starting from the initial analyte spot up to the solvent front. In conventional TLC, the analyte spots are stained and visualized by UV light allowing the distance travelled by the analyte and the R_f to be measured directly from the TLC plate. In HPTLC-DESI-MS, the compound's R_f is calculated based on the retention time collected from the apex of the chromatographic peak divided by the total analysis time from the chronogram as shown below.

$$R_f = \frac{Retention\ time\ (min.)}{Total\ Analysis\ Time\ (min.)}$$

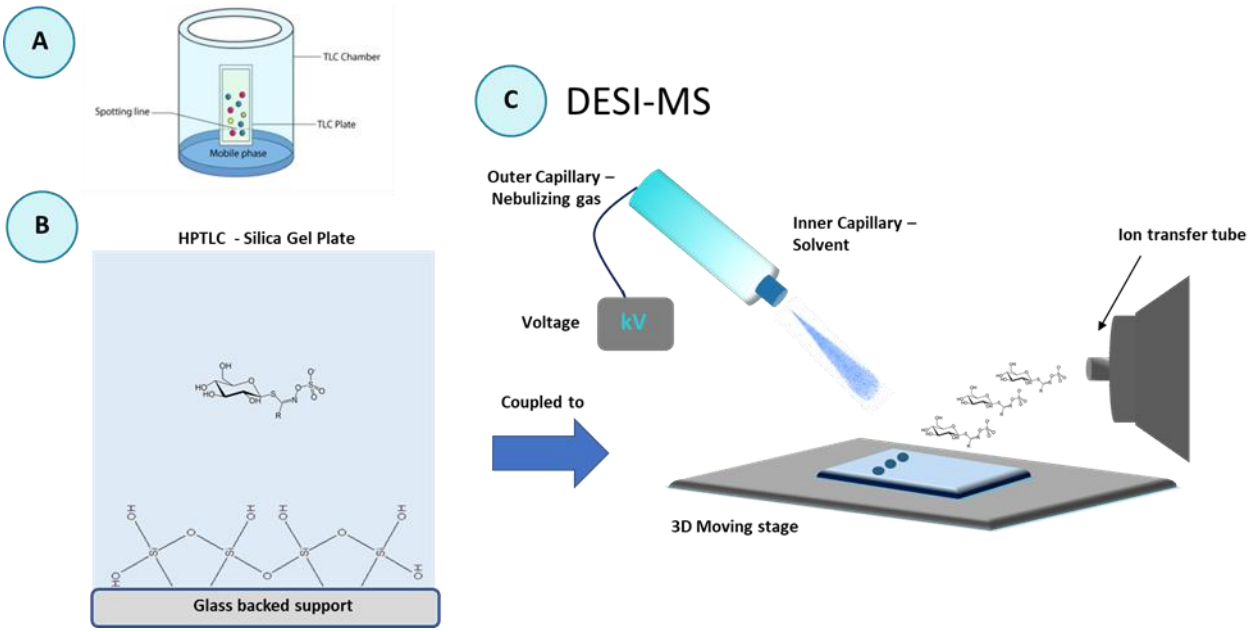

Figure 1.10: Schematic of HPTLC coupled to DESI-MS. A. The separation is performed in a TLC glass chamber. B. The interactions between the analyte, mobile and stationary phase drives the migration of the compounds. C. Offline HPTLC-DESI-MS analysis.

1.6. Dissertation Research Objectives

In this dissertation, the general objective was centered on the development and implementation of rapid and novel mass spectrometry-based methods by atmospheric pressure (ESI-MS) and ambient ionization mass spectrometry techniques (DESI-MS) to chemically profile, separate and/or quantify targeted analytes such as drugs and metabolites from complex matrices. The qualitative and quantitative analytical methods developed by MS techniques were focused in two major fields of study, drug development and plant metabolomics. Specific project objectives are outlined in each corresponding introduction throughout Chapters 2-6.

Chapter Two: Internal Standard Application Strategies in Mass Spectrometry Imaging by Desorption Electrospray Ionization

Chapter 2 is a submitted version of the manuscript:

Perez, C.J., Ifa, D.R. Internal Standard Application Strategies in Mass Spectrometry Imaging by Desorption Electrospray Ionization*. Rapid Commun. Mass Spectrom.* **2020**. **Submitted.**

2.1. Summary

In this chapter, we explored the potential of quantitative mass spectrometry imaging (MSI) by desorption electrospray ionization-mass spectrometry (DESI-MS). We compared three strategies to add an isotopically labelled internal standard (IS) into the DESI-MSI analysis to determine a routine quantitative DESI-MSI method based on its analytical figures of merit (precision, accuracy, linearity, and so forth). A model case study of the psycholeptic, phenobarbital (PB) and the deuterated IS, phenobarbital-D5 (PB-D5) were imaged from thin tissue sections of the invasive golden apple snail (*p.diffusa)* to identify, quantify and map the spatial distribution of the drug from *in vitro* dosed tissue sections by DESI-MSI. In this study, the deposition of the IS as droplets on top of tissues (method I) and applying an IS thin film (method II) were not statistically significantly different, and both, can be used interchangeably in future quantitative DESI-MSI studies.

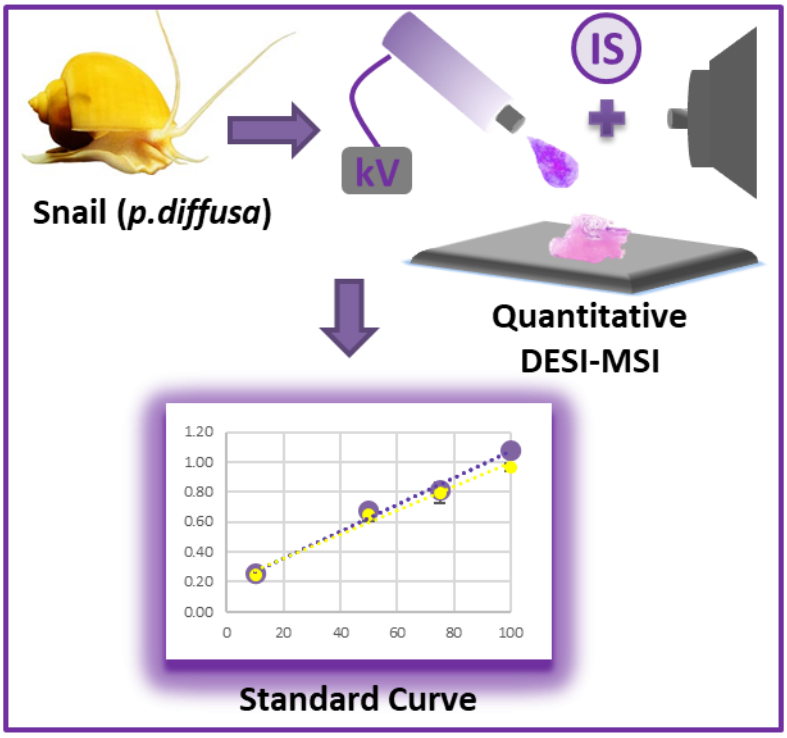

Figure 2.1: Schematic representation of quantitative DESI-MSI.

2.2. Introduction

DESI-MSI is a dynamic and versatile qualitative analytical tool for many applications however, current outlooks on quantitative capabilities in MSI have been limited and for the most part underexplored. There is a significant need to develop quantitative imaging methodologies to map the spatial distribution of chemical compounds and their respective concentrations from biological tissues. To date, a few studies in the literature have investigated its quantitative potential.[23,87] The first report in DESI-MSI revealed the quantification of clozapine from 6 µm rat brain tissue sections from rats dosed *in vivo* after 45 minutes post-dose. External calibration curves were prepared by micropipetting clozapine standards and the internal standard (IS) on top of the tissues, and average response factors were calculated in which clozapine and IS were detected *in vitro* dosed rat brain tissues.[87] DESI-MSI revealed 0.2-1.2 ng of clozapine in brain tissue sections, and results were validated by extracting clozapine from brain tissues and quantifying the drug by liquid chromatography-tandem mass spectrometry (LC-MS/MS).[87]

One of the most challenging aspects in quantitative MSI is the incorporation of the internal standard to report accurate and precise analyte concentrations from biological tissue sections. The IS plays an important role in MSI, where the standard should be similar in structural and chemical properties of the analyte to mimic the ionization and desorption process and accurately calibrate the analytical response.[88] Standards consisting of structural analogs and isotopically labelled versions of the analyte have been previously used in MSI studies to correct for ionization efficiencies, extraction of the analyte from tissues and matrix ion suppression effects.[23,87,89]

A MALDI-MSI study investigated the spatial distribution of imipramine from dosed rat lung tissue by different normalization approaches such as without normalization, total ion count (TIC), root mean squared and normalization to the internal standard.[90] Only by normalizing to the IS signal it was possible to account for the absence of imipramine in a region where tissue was absent. Internal standard normalization provided the most accurate image of analyte spatial distribution compared to other normalizations approaches (TIC, root mean squared, etc.,) that

did not account for an accurate representation of the localization of the drug.[90] In a more recent MALDI-MSI study, the antibiotic rifampicin (RIF), commonly used to treat tuberculosis, was quantified from local microenvironments in liver tissue dosed *in vivo* by the use of the isotopically labelled standard, ^{13}C-RIF from liver tissues dosed *in vitro*.[91] The application of the ^{13}C-RIF standard on top of the tissue followed by matrix deposition was the best performing quantitative method that was not statistically significantly different from HPLC-MS/MS data as shown by ANOVA posthoc Tukey's test. The amounts of RIF from microspots in the MALDI-MS images of liver tissue sections were averaged and cross-validated to liver tissues analyzed by HPLC-MS/MS with a 90.4% similarity between these two analytical techniques.[91]

In this work, we compared three IS application strategies for quantitative DESI-MSI using the psycholeptic, PB and the isotopically labelled IS, PB-D5, from *in vitro* dosed tissues of the freshwater golden apple snail (*p. diffusa*) as an invertebrate model. Molluscs are natural freshwater filter feeders that tend to accumulate pharmaceuticals and personal care products (PPCPs) from aquatic environments and water bodies. The approach herein is a methodology to survey invertebrate models and evaluate the current chemical state of freshwater aquatic ecosystems. We compared the analytical performance of DESI-MSI in the absence of the IS and three different IS application strategies based on its analytical figures of merit such as, precision, accuracy, linearity and overall advantageous and limitations.

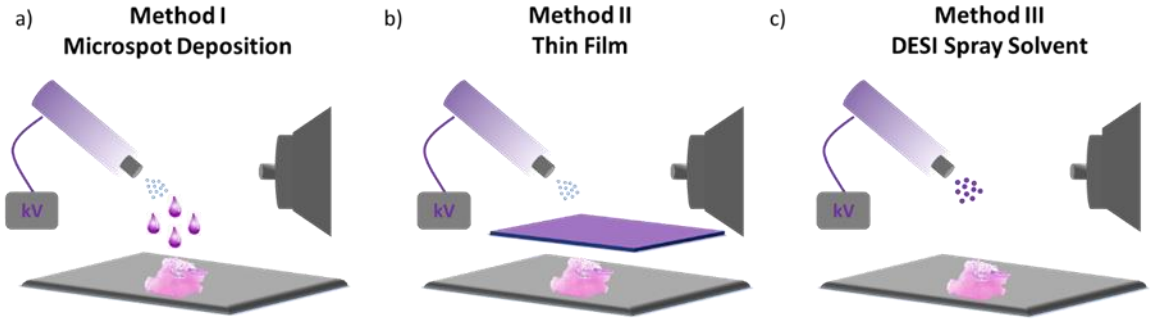

Figure 2.2: IS application strategies in MSI by DESI. a) Method I - IS microspots on top of the tissue. b) Method II – IS thin film using the DESI sprayer. c) Method III - adding the IS in the DESI solvent spray.

2.3. Experimental

2.3.1. Biological Tissue Sample Preparation

Golden apple snails (*p. diffusa*) were purchased from a local PetSmart (North York, ON, CA) and euthanized with 300 mg/mL of MS-222 (tricaine methanesulfonate). Snails were thoroughly washed with HPLC-grade water, snail shells and operculum were removed from the body and placed in flexible peel-away moulds. Whole-body golden apple snails, snail heads and bodies were submerged with 5% CMC and 10% gelatin solution and kept in a -80^{o}C freezer. Bulk tissues were sectioned between 10-30 µm thin sections with a cryomicrotome (Thermo Scientific, Toronto, ON, CA) and mounted onto microscope glass slides (Appendix A). Snail thin tissue sections were kept in the -80°C freezer and later in the -18˚C freezer for immediate use. Tissue sections were air dried for 30 minutes prior to DESI-MSI analysis.

2.3.2. Sample Preparation and ESI-MS Analysis of Golden Apple Snail (*p. diffusa*) Tissue Extracts

Snail tissue extracts were prepared by euthanizing two snails in 300 mg/mL solution of MS-222 (tricaine methanesulfonate). Snail shells and operculum were removed and rinsed with distilled water. Snail tissue was homogenized using chloroform/methanol ($CHCl_3$/MeOH) 1:1 v/v mixture and the homogenate was placed in Eppendorf tubes centrifuged at 12000 rpm for 15 minutes. The supernatant was collected from the homogenates of snail 1 and 2 and the procedure was repeated once more. The MeOH fraction of snail 1 and 2 was combined and placed in a separate tube, while the $CHCl_3$ fraction of snail 1 and 2 was collected in another. The $CHCl_3$ and MeOH fractions were dried down in a vacuum desiccator for 2 hours. The $CHCl_3$ extract was resuspended in $CHCl_3$/MeOH (1:1 v/v) and the other fraction in MeOH immediately before ESI-MS analysis. ESI-MS analysis of snail tissue extracts was performed on a Thermo LTQ (Thermo Scientific, San Jose, USA) linear ion trap mass spectrometer equipped with an ESI source. ESI-MS was operated in positive ion mode using an applied voltage of 3 kV, a flow rate of 3 µL/min and a nebulizing nitrogen gas pressure of 100 psi, an injection time of 20 ms and 3 microscans. For

the ESI-MS analysis in negative ion mode, an injection time of 50 ms and 3 microscans was applied.

2.3.3. DESI-MSI of the Golden Apple Snail (*p. diffusa*) Tissue Sections

DESI-MS imaging was performed on a Thermo LTQ (Thermo Scientific, San Jose, USA) linear ion trap mass spectrometer equipped with a custom-built DESI source and a 2D moving stage for MS imaging. DESI source parameters such as the incident angle, the capillary tip to surface distance, the mass spectrometer inlet to capillary tip distance were optimized. DESI-MS imaging was performed in negative ion mode using an applied voltage of 5 kV, a flow rate of 5 µL/min and a nebulizing nitrogen gas pressure of 120 psi, an injection time of 200 ms and 3 microscans. Golden apple snail metabolites (fatty acids, DAGs, TAGS, saccharides, phospholipids) were identified by DESI-MS/MS in combination with ESI-MS/MS spectra, LIPID MAPS, Human Metabolome and METLIN databases.

2.3.4. The Targeted Method Development for Quantitative DESI-MSI

An Xcalibur™ method was created in SIM mode with a mass isolation window of 12 Da in a mass range between *m/z* 227.5-239.5 to monitor phenobarbital *(m/z* 231) and the isotopically labelled internal standard, phenobarbital-D5 (*m/z* 236). DESI-MS imaging was performed in negative ion mode using an applied voltage of 5 kV, a flow rate of 5 µL/min using MeOH with 0.1% NH_4OH (ammonium hydroxide) and a nebulizing nitrogen gas pressure of 120 psi, an injection time of 150 ms and 3 microscans. Tissue imaging dimensions of x=11,000 µm and y=10,000 µm with a resolution of 150 µm was applied. A total of 67 mass spectral files were collected with a moving stage speed of 349 µm/s for an image acquisition time of 1 hour. The described DESI-MS imaging parameters were used for all internal standard application strategies for comparisons.

2.3.5. DESI-MSI Data Processing and Collection

Mass spectra were processed by QualBrowser Xcalibur. The ImageCreator ver. 3.0 software was used to convert the Xcalibur 2.0 mass spectra files (.raw) into a format compatible

with BioMap (freeware, http://www.maldi-msi.org/) to process the mass spectral data and generate 2D DESI-MS ion images. To generate linear standard curves, ion intensity ratios of the drug and the isotopically labelled IS (I_D/I_{IS}) were extracted and collected from selected pixels from regions of interest (ROIs) in the ion images.

2.3.6. DESI-MSI in the Absence of the Internal Standard

PB was serially diluted between 0.1-100 ng/µL to final volumes of 1 mL in 1.5 mL Eppendorf tubes. For the LOD/LOQ studies and to evaluate PB in the absence of the IS, 1 µL of the drug with or without the IS, respectively were deposited on 10 µm snail tissue sections between 0.1-100 ng/µL. DESI-MSI analyses in negative ion mode were performed under imaging parameters described in section 2.3.4.

2.3.7. Internal Standard Application Strategies

In method I, PB and the IS were deposited in concentrations of 10, 50, 75 and 100 ng/µL spiked with 100 ng/µL PB-D5. The standard/IS mixtures (1 µL) were deposited directly on 10 µm snail tissue sections and dried for 30 minutes before the analysis. In method II, the application of the IS thin film with the DESI sprayer was first optimized. Preliminary experiments were carried out by optimizing the nitrogen gas pressure (40-80 psi) and solvent flow rates (1.5-5 µL/min) on snail tissue sections. The IS thin film was applied in an area of 11,000 x 10,000 µm with a step size of 200 µm by applying either 1 ng/µL (0.34 ng/mm^2), , 10 ng/µL (3.36 ng/mm^2) and 100 ng/µL (33.6 ng/mm^2) of PB-D5 in the DESI spray solvent on 10 µm snail tissue sections. The IS film was air dried for 1 hr, and PB (1 µL) was deposited between 10-100 ng/µL on snail tissue sections. In method III, PB (1 µL) was deposited on snail tissues between 10-100 ng/µL and PB-D5 was applied as the DESI spray solvent in concentrations of 0.1 ng/µL (0.5 µM), 0.2 ng/µL (1 µM), 1.2 ng/µL (5 µM) and 2.4 ng/µL (10 µM) in MeOH with 0.1% NH_4OH (data not shown). The intraday and interday assay consisting of 3 runs on day 1 and day 2 were carried out for method I and II. MEDCALC® software was used to generate the Bland-Altman plot for statistical analysis.

2.3.8. Evaluation of Accuracy

A quality control (QC) solution of PB (75 ng/µL) and PB-D5 (100 ng/µL) was prepared for method I. In method II, the IS thin film of 10 ng/µL (3.36 ng/mm²) was sprayed onto the 10 µm thick snail tissue section. Three QC microspots of PB (1 µL) were deposited onto tissue sections for method I and II and analyzed by DESI-MSI. The I_D/I_{IS} ratios were collected from DESI-MS images and the average PB concentration was back calculated using the I_D/I_{IS} ratios into the linear regression equation from the interday assay and the accuracy (%RE) and the 95% CI were calculated (n=3).

2.4. Results and Discussion

2.4.1. Metabolomic Profiling of the Golden Apple Snail (*p.diffusa*)

The invasive freshwater golden apple snail (*p. diffusa*), formerly known as *p.bridgesii*, is an aquatic gastropod mollusk in the family Ampullariidae. The snail is an invasive species that has spread throughout Asia, India and North America originating in the Amazon Basin. Golden apple snails are amphibious with a ctenidium (gills) and the pulmonary sac (lung) enabling snails to survive long periods in both, air and water. The nervous system consists of interconnected ganglia throughout the body with the absence of a centralized brain, as typically found in mammals. They exhibit an operculum mainly composed of chitin to protect soft tissues when withdrawn in the shell. The digestive system, the stomach and the digestive gland, and the reproductive system (ovotestis) are enclosed in the mantle cavity within the shell.

The metabolome of the freshwater golden apple snail (*p. diffusa*) was investigated as the invertebrate model in this work. A comprehensive table outlined in Appendix A can be found for the identification of snail metabolites. ESI-MS and ESI-MS/MS profiles in negative and positive ion polarities revealed the presence of a wide range of metabolites in tissue extracts (Figure 2.3). Fatty acids, diacylglycerides (DAGs), triacylglycerides (TAGs), and phospholipids were observed in the chloroform fraction of the extract. Fatty acids were found between the mass range of 200-400 Da with the most abundant fatty acid corresponding to linoleic acid [FA (18:2)-H]$^-$ of *m/z*

279. Other fatty acids such as decadienoic acid [FA(10:2)-H]$^-$ of *m/z* 167, myristic acid [FA(14:0)-H]$^-$ of *m/z* 227, palmitoleic acid [FA (16:1)-H]$^-$of *m/z* 253, palmitic acid [FA (16:0)-H]$^-$ of *m/z* 255, α/ɣ-linolenic acid [FA (18:3)-H]$^-$ of *m/z* 277, oleic acid [FA (18:1)-H]$^-$ of *m/z* 281, stearic acid [FA(18:0)-H]$^-$ of *m/z* 283, eicosapentaenoic acid [FA(20:5)-H]$^-$ of *m/z* 301, arachidonic acid [FA(20:4)-H]$^-$ of *m/z* 303, arachidic acid [FA(20:0)]$^-$ of *m/z* 311, unidentified ions of *m/z* 309, *m/z* 317 and *m/z* 319, and docosahexaenoic acid (DHA) [FA (22:6)-H]$^-$ of *m/z* 327 were observed. The most abundant phospholipids found were the glycerophospholipid [GP(16:0/16:0)]$^-$ of *m/z* 721, phosphatidylserine [PS(17:1/20:1)-H]$^-$ of *m/z* 800, and phosphatidylinositol [PI(18:0/20:4)-H]$^-$ of *m/z* 885.

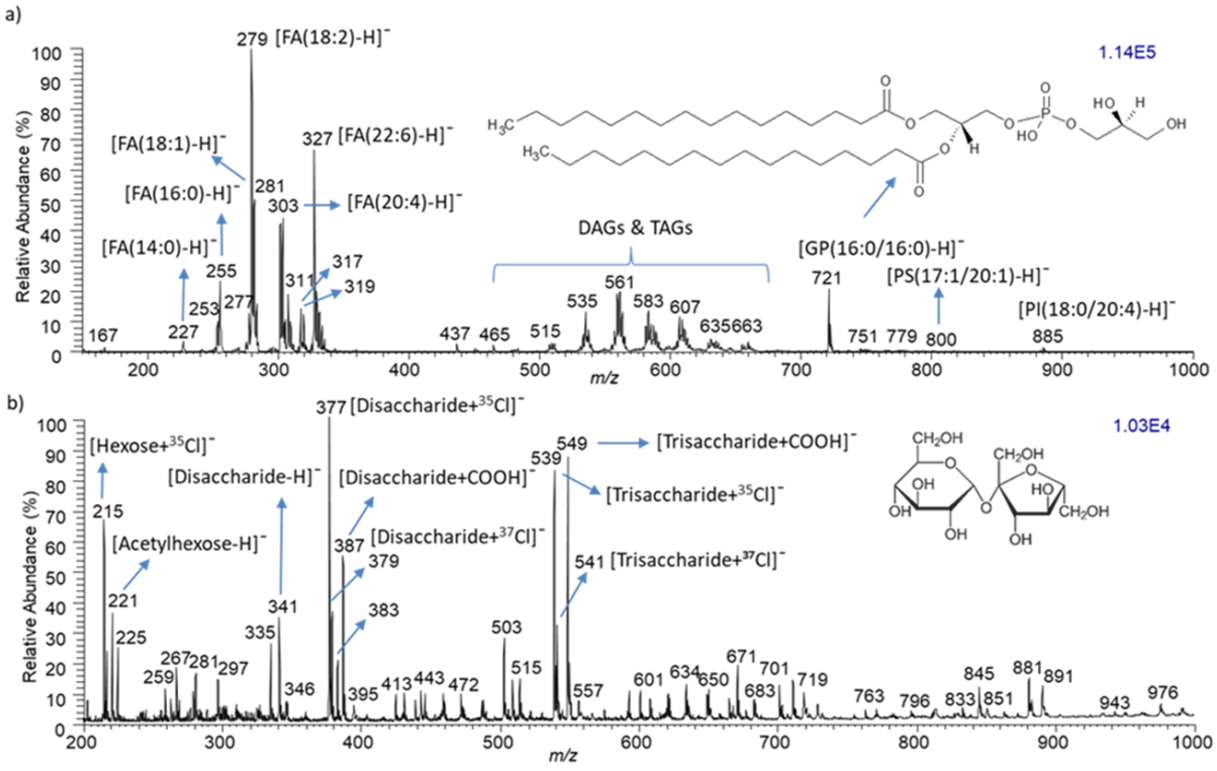

Figure 2.3: ESI-MS full scan spectra of the tissue extracts of the invasive freshwater golden apple snail (*p. diffusa*) from a) the $CHCl_3$ fraction. b) the MeOH fraction. The inset chemical structure on the top spectrum is glycerophosphoglycerol, PG(16:0/16:0), and the disaccharide, sucrose, in the bottom figure.

In the MeOH extract, mainly carbohydrates such as monosaccharides [Glu/Gal+^{35}Cl]$^-$ of *m/z* 215, [Glu/Gal+^{37}Cl]$^-$ of *m/z* 217, and [Acetylhexose-H]$^-$ of *m/z* 221 were identified (Figure 2.3). Deprotonated, chlorine and formate adducts of disaccharides such as [Disaccharide+^{35}Cl]$^-$ of *m/z* 377, [Disaccharide+^{37}Cl]$^-$ of *m/z* 379, [Acetyldisaccharide-H]$^-$ of *m/z* 383, [Disaccharide+COOH]$^-$ of *m/z* 387, and trisaccharides, [trisaccharide-H]$^-$ of *m/z* 503, [trisaccharides+^{35}Cl]$^-$ of *m/z* 539, and [trisaccharides+^{37}Cl]$^-$ of *m/z* 541 and [trisaccharide+COOH]$^-$ *m/z* 549 were present. The metabolome of the golden apple snail (*p.diffusa*) in (+)ESI-MS showed the amino acid, [Arginine+H]$^+$, of *m/z* 175 as the most abundant metabolite. Sodium and potassium adducts of carbohydrates including monosaccharides [Glu/Gal+Na]$^+$ of *m/z* 203, [Glu/Gal+K]$^+$ of *m/z* 219, [Disaccharide+Na]$^+$ of *m/z* 365, [Disaccharide+K]$^+$ of *m/z* 381 and [Trisaccharide+Na]$^+$ of *m/z* 527 and [Trisaccharide+K]$^+$ of *m/z* 543 were observed among others (Figure 2.3.b). Selected ESI-MS/MS spectra of these metabolites can be found in Appendix A.

2.4.2. The Spatial Distribution of Metabolites in the Golden Apple Snail (*p.diffusa*)

The metabolites in coronal head tissues of snail (*p.diffusa*) were mapped by DESI-MSI using MeOH 0.1% NH_4OH (Figure 2.4). The snail head contains two discrete anatomical regions, the general head mass and the cephalic ganglia. Small metabolites of *m/z* 117, *m/z* 125, *m/z* 134, and *m/z* 170 were distributed with high intensities in the inner regions of the cephalic ganglia. The fatty acids, linoleic acid [FA(18:0)-H]$^-$ of *m/z* 279 and arachidonic acid, [FA20:4)-H]$^-$ were evenly distributed in the head but with higher intensities in the top outer region, surrounding the cephalic, ganglia. Unknown ions of *m/z* 307, *m/z* 309 and *m/z* 331 were distributed similar to linoleic and arachidonic acid suggesting that these ions may be FAs with uneven alkyl chains. The phospholipids, phosphatidylcholine [PC (34:1)+Cl^{35}]$^-$of *m/z* 794, phosphatidylserine [PS(17:1/20:1)-H]$^-$ of *m/z* 800 and phosphatidylinositol [PI(18:0/20:4)-H]$^-$ of *m/z* 885 were localized evenly in the general head mass with increased intensities in the cephalic ganglia, while [PS (38:4)-H]$^-$of *m/z* 810 was only localized in the cephalic ganglia. Lastly, the monosaccharides [Glu/Gal-H]$^-$ of *m/z* 179, [Glu/Gal+Cl^{35}]$^-$ of *m/z* 215 and the lactate adduct of the monosaccharide (glucose/galactose), [Glu/Gal+lactate]$^-$ of *m/z* 269, were distributed in the outer region of the

cephalic ganglia. The general head mass showed homogenous distributions of metabolites such as monosaccharides, fatty acids and phospholipids.

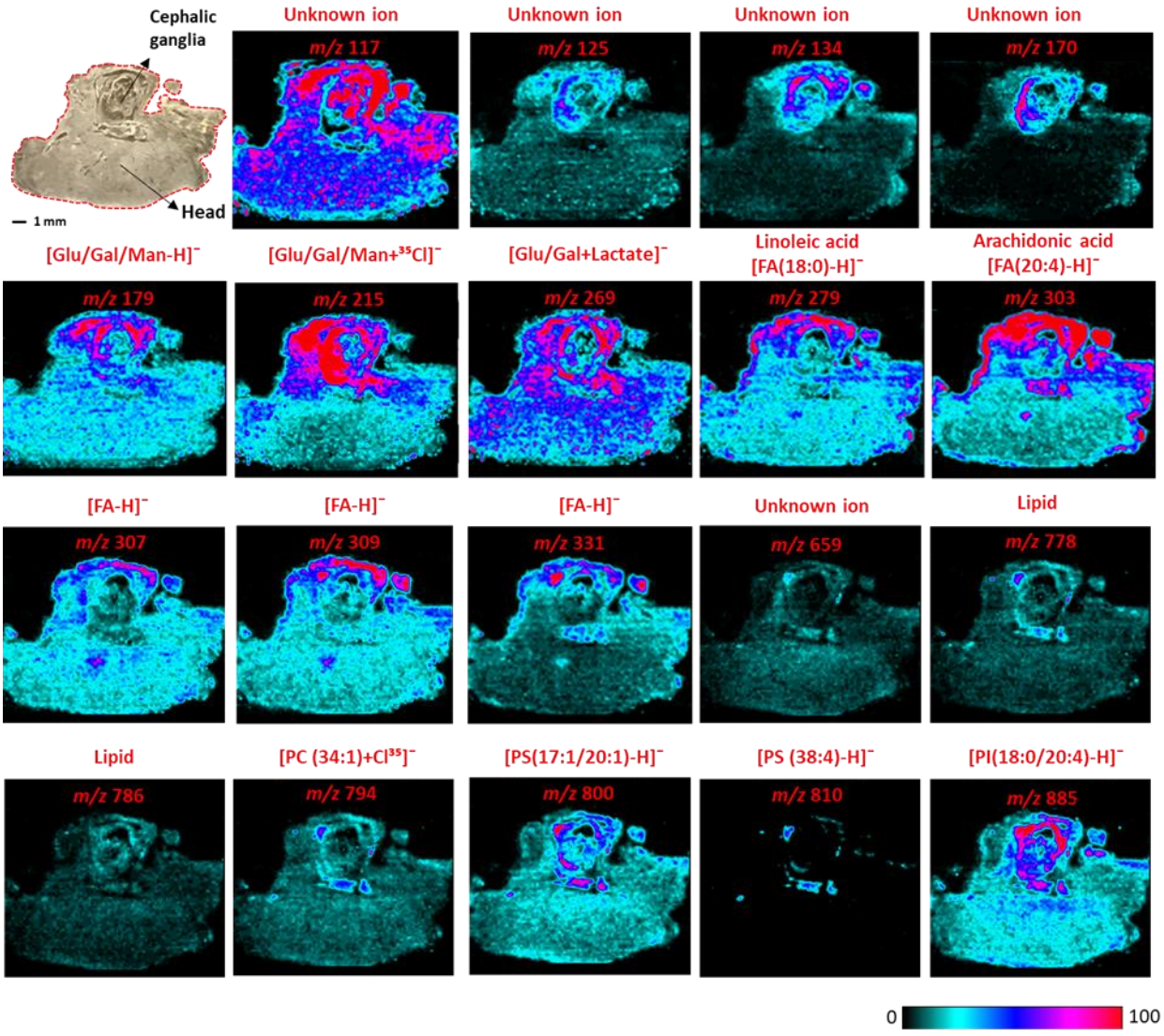

Figure 2.4: (-)DESI-MSI of golden apple snail (*p. diffusa*) tissues with MeOH 0.1% NH_4OH. Imaging dimensions of the snail head tissue section were 16000 µm x 10000 µm set to 150 µm for the lateral resolution.

The metabolites in snail organs inside the mantle cavity protected by the gastropod's shell such as the digestive system (stomach and digestive gland) and reproductive system (ovo-testis) were mapped by DESI-MSI (Figure 2.5). DESI-MS images revealed the detection of 10 and 20 metabolites with MeOH and ACN, respectively. In the mantle cavity of *p.diffusa*, the chlorine adduct of the disaccharide, $[M+^{35}Cl]^-$ of *m/z* 377 has been identified as sucrose (Glu/Fru) and/or trehalose (Glu/Glu) and localized homogenously in the digestive gland and gonads. Sucrose and trehalose are the most abundant carbohydrates in the snail digestive-gonad-gland complex (DGG). Invertebrate animals, such as molluscs and insects, use trehalose, as a major source of energy storage and as a physiological response to cold acclimation.[92] High levels of trehalose and proline act as cryoprotectants and are correlated with cold tolerance in molluscs and insects.[92,93] Interestingly, without this adaptation to colder temperatures it would have been difficult for snails to survive and become invasive in North America.

Deprotonated fatty acids, linoleic $[FA(18:2)-H]^-$, arachidonic acid $[FA(20:4)-H]^-$, and the glycerophospholipid $[PG(16:0/16:0-H]^-$ were mainly localized in the digestive gland. In the gonads, the most prominent ion was the fatty acid, DHA, $[FA(22:6)-H]^-$ of *m/z* 327, and the unidentified ions of *m/z* 349, *m/z* 373, *m/z* 850. Snail metabolites visualized in DESI-MS images using ACN as the solvent show similar spatial distribution patterns to MeOH, however the use of ACN increased the number of detected unsaturated fatty acids (Figure 2.6), such as palmitoleic acid $[FA(16:1)-H]^-$, oleic acid $[FA(18:1)-H]^-$, eicosapentaenoic acid $[FA(20:5)-H]^-$, DAGs and the detection of two unknown lipids, *m/z* 826 and 840, localized only in the gonads.

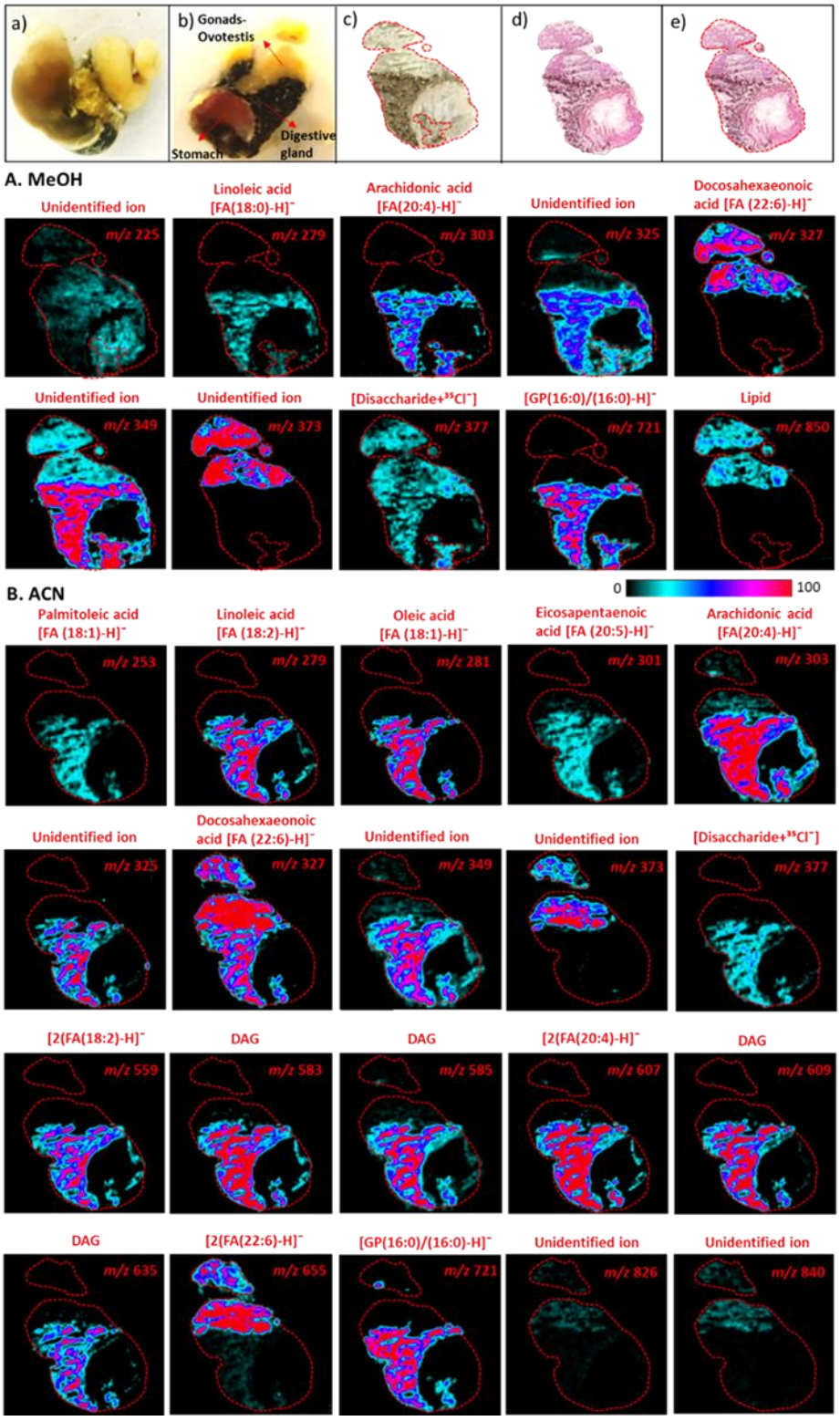

Figure 2.5: (-)DESI-MSI of freshwater golden apple snail (*p. diffusa*) tissues inside the shell using imaging dimensions of 11000 µm x 14000 µm set to 200 µm for the lateral resolution using the solvent A. MeOH and B. ACN. a) Snail body inside the shell fixed in 5% CMC. b) CMC block during

cryosectioning. c) Optical image of 20 µm tissue section. d) H&E stained tissue after MSI analysis. e) H&E stained tissue outlined in red. Panel A. MSI of the snail tissue section with MeOH 0.1% NH_4OH. Panel B. MSI of snail tissue section with ACN 0.1% NH_4OH.

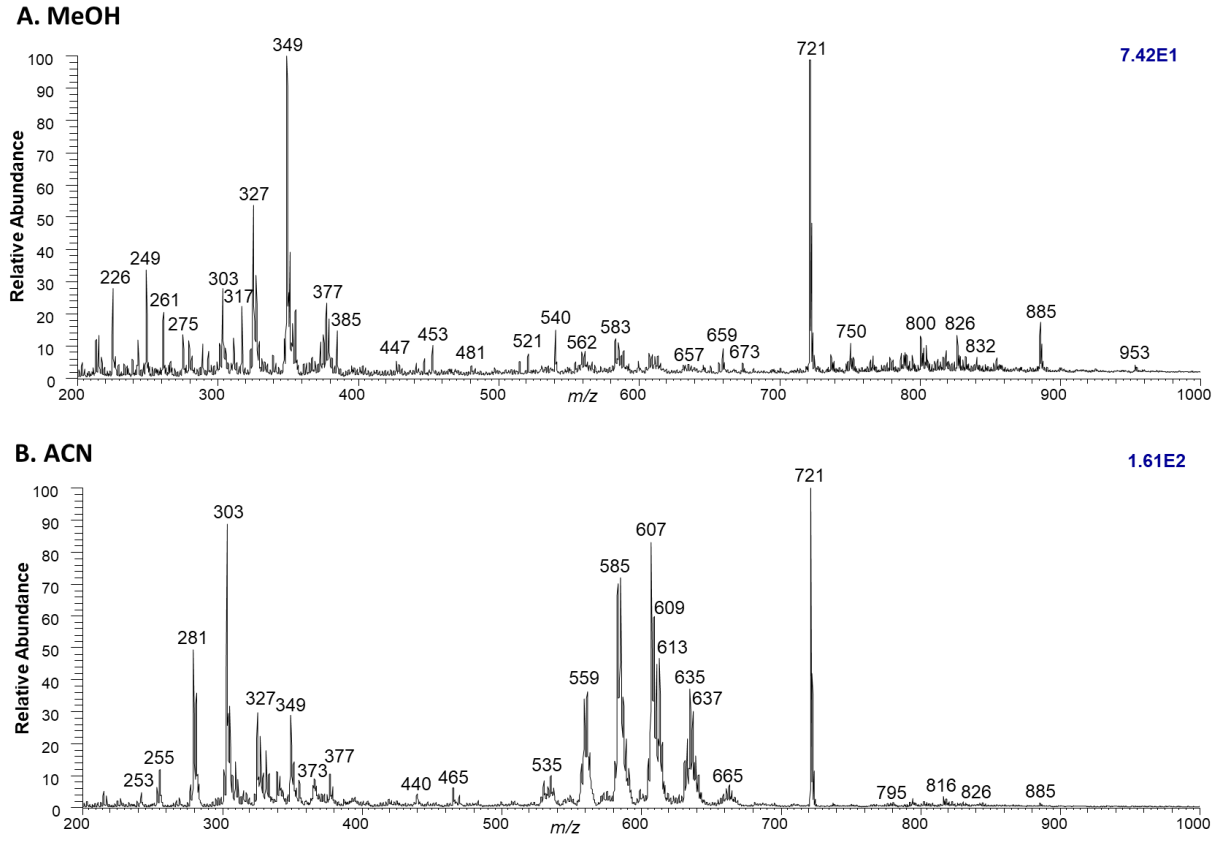

Figure 2.6: (-)DESI-MS profiles of the invasive freshwater golden apple snail (*p.diffusa*) tissues. A. MEOH and B. ACN.

2.4.3. The Development of the Targeted Quantitative DESI-MSI Method

Initially, we compared the tissue section thickness to evaluate the sampling depth of the DESI sprayer. A range of pharmaceutical compounds including carbamazepine, fentanyl, verapamil and phenobarbital were directly deposited in concentrations of 100 µM on snail tissues in thicknesses of 10, 12, 15, 20, 25, 30 µm for DESI-MS analyses in positive and negative ion mode (Figure 2.7). The intensities of the pharmaceutical compounds decreased as the tissue thickness increased from 10 to 30 µm suggesting that these compounds infiltrated much farther into the

tissue and beyond the sampling limit of the DESI sprayer. In general, the optimal tissue thickness was found to be ≤10 µm for the analyzed pharmaceutical compounds. In Table 2.1, the decrease of drug intensities from 10 to 30 µm represents the loss of the drug from infiltrating into deeper parts of the tissue. The overall percent loss of carbamazepine, fentanyl, verapamil, and phenobarbital from 10-30 µm was observed as 33%, 87%, 79%, and 86%, respectively. Carbamazepine showed the least dependence on tissue thicknesses, however this can suggest that the drug remains on top of the tissue surface, and therefore is not a good representation of *in vivo* tissue experiments, in which the drug is embedded within the tissue matrix. In contrast, fentanyl, verapamil, and phenobarbital displayed very similar final losses of the drug from 10-30 µm. Phenobarbital was selected for the quantitative DESI-MSI study based on its signal stability in negative ion mode as shown by low RSDs (3-17%) compared to carbamazepine (2-35%), fentanyl (5-19%) and verapamil (8%-29%) across different tissue thicknesses (10-30 µm) as shown in Table 2.1.

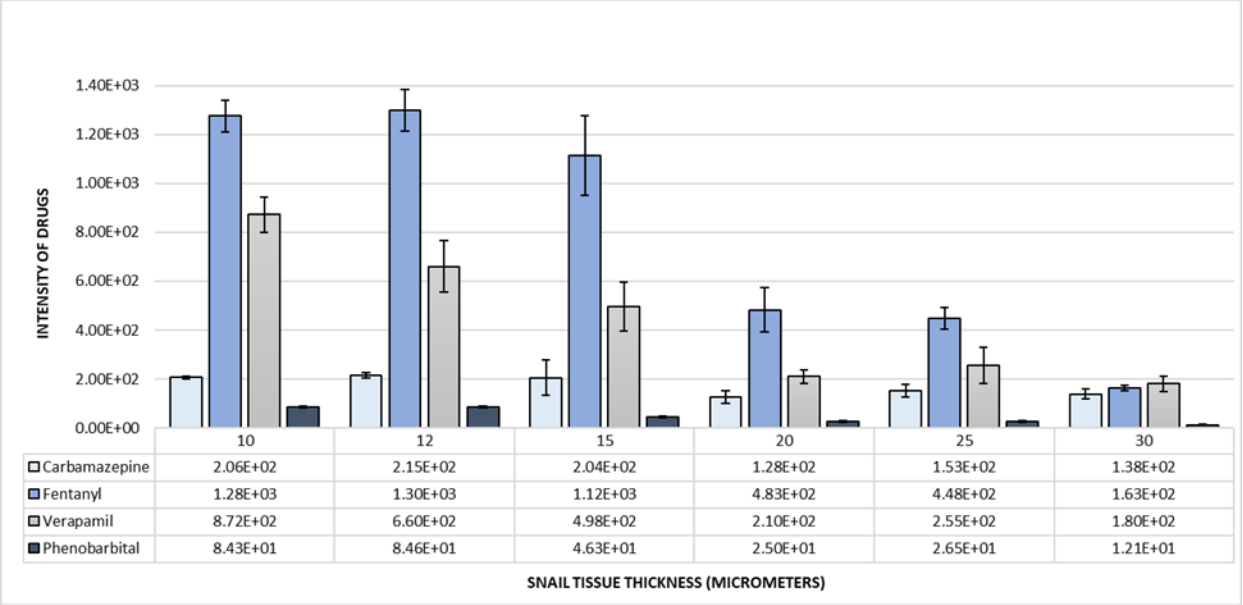

	10	12	15	20	25	30
Carbamazepine	2.06E+02	2.15E+02	2.04E+02	1.28E+02	1.53E+02	1.38E+02
Fentanyl	1.28E+03	1.30E+03	1.12E+03	4.83E+02	4.48E+02	1.63E+02
Verapamil	8.72E+02	6.60E+02	4.98E+02	2.10E+02	2.55E+02	1.80E+02
Phenobarbital	8.43E+01	8.46E+01	4.63E+01	2.50E+01	2.65E+01	1.21E+01

Figure 2.7: Evaluation of tissue sampling depth by the DESI sprayer. 100 µM of carbamazepine, fentanyl, verapamil and phenobarbital were deposited in 1 µL spots on snail tissues ranging from 10, 12, 15, 20, 25, and 30 µm in thickness. The figure displays the average intensity of the pharmaceuticals (n=2). Carbamazepine, fentanyl and verapamil are positively charged ions $[M+H]^+$ in the (+)DESI-MS analysis and phenobarbital is a negatively charged ion $[M-H]^-$ in the (-)DESI-MS analysis.

Table 2.1: Probing the Sampling Depth of the DESI Sprayer from Drugs Deposited at Concentrations of 100 µM on Snail Tissues (*p.diffusa*) from Thicknesses of 10-30 µm.

Carbamazepine							
Tissue Thickness (µm)	Average Spot 1	Average Spot 2	Average Intensity (n=2)	Standard deviation (SD)	Relative Standard Deviation (RSD)	Drug remaining on tissues (%)	Drug losses across tissues (%)
10	2.09E+02	2.03E+02	2.06E+02	4.2	2%	100%	0%
12	2.07E+02	2.22E+02	2.15E+02	10.6	5%	104%	-4%
15	1.53E+02	2.55E+02	2.04E+02	72.1	35%	99%	1%
20	1.09E+02	1.46E+02	1.28E+02	26.2	21%	62%	38%
25	1.35E+02	1.70E+02	1.53E+02	24.7	16%	74%	26%
30	1.53E+02	1.23E+02	1.38E+02	21.2	15%	67%	33%
Fentanyl							
Tissue Thickness (µm)	Average Spot 1	Average Spot 2	Average Intensity (n=2)	Standard deviation (SD)	Relative Standard Deviation (RSD)	Drug remaining on tissues (%)	Drug losses across tissues (%)
10	1.23E+03	1.32E+03	1.28E+03	63.6	5%	100%	0%
12	1.20E+03	1.32E+03	1.26E+03	84.9	7%	99%	1%
15	1.23E+03	1.00E+03	1.12E+03	162.6	15%	87%	13%
20	4.19E+02	5.46E+02	4.83E+02	89.8	19%	38%	62%
25	4.17E+02	4.78E+02	4.48E+02	43.1	10%	35%	65%
30	1.70E+02	1.55E+02	1.63E+02	10.6	7%	13%	87%
Verapamil							
Tissue Thickness (µm)	Average Spot 1	Average Spot 2	Average Intensity (n=2)	Standard deviation (SD)	Relative Standard Deviation (RSD)	Drug remaining on tissues (%)	Drug losses across tissues (%)
10	9.22E+02	8.22E+02	8.72E+02	70.7	8%	100%	0%
12	5.85E+02	7.35E+02	6.60E+02	106.1	16%	76%	24%
15	5.68E+02	4.27E+02	4.98E+02	99.7	20%	57%	43%
20	1.91E+02	2.28E+02	2.10E+02	26.2	12%	24%	76%
25	2.03E+02	3.07E+02	2.55E+02	73.5	29%	29%	71%
30	2.03E+02	1.57E+02	1.80E+02	32.5	18%	21%	79%
Phenobarbital							
Tissue Thickness (µm)	Average Spot 1	Average Spot 2	Average Intensity (n=2)	Standard deviation (SD)	Relative Standard Deviation (RSD)	Drug remaining on tissues (%)	Drug losses across tissues (%)
10	8.73E+01	8.12E+01	8.43E+01	4.3	5%	100%	0%
12	8.65E+01	8.27E+01	8.46E+01	2.7	3%	100%	0%
15	4.89E+01	4.36E+01	4.63E+01	3.7	8%	55%	45%
20	2.20E+01	2.79E+01	2.50E+01	4.2	17%	30%	70%
25	2.36E+01	2.93E+01	2.65E+01	4.0	15%	31%	69%
30	1.09E+01	1.33E+01	1.21E+01	1.7	14%	14%	86%

2.4.4. Phenobarbital

The psycholeptic, PB belongs to the drug class, barbiturates and the main mode of action involves increasing the activity of the inhibitory neurotransmitter γ-aminobutyric acid (GABA) in the central nervous system (CNS) acting as non-selective CNS depressant with sedative, and hypnotic actions.[94] The use of barbiturates in humans has dramatically declined since new and safer alternatives have emerged for anaesthetic sedation and anti-epileptic treatment without genotoxic and hepatoxic effects.[95] Benzodiazepines have largely replaced barbiturates in routine medical practice because barbiturates have a narrow therapeutic range, high potential for abuse and toxicity. However, PB is still commonly used in veterinary medicine for surgical sedation, anti-epileptic treatment, and euthanasia.[96]

2.4.5. Selectivity

The selectivity of the MSI analysis depends on the ability to detect the analyte from a complex biological matrix without the interference of other analytes. MSI analysis allows PB and PB-D5 to be detected as deprotonated ions $[M-H]^-$ of *m/z* 231 and *m/z* 236, respectively. To eliminate the possibility of interference from other analytes, such as endogenous metabolites from the snail tissue matrix, we examined the MS/MS profiles of the pure standards, PB and PB-D5, from PTFE substrates (Appendix A) and snail tissue sections. (-)DESI-MS/MS profiles of deprotonated PB (*m/z* 231) and PB-D5 (*m/z* 236) are shown in Figure 2.8.a. The MS/MS data revealed the ion of *m/z* 188 $[M-CONH]^-$ as the primary fragment from the neutral loss of 43 Da (-CONH). Minor fragment ions of *m/z* 85 and *m/z* 144 identified as $[C_2H_2N_2O_2]^-$ and $[C_{10}H_{10}N]^-$ were observed from the losses of 146 Da and 87 Da, respectively (Figure 2.8.c). The isotopically labelled IS, PB-D5 (*m/z* 236) showed a similar MS/MS fragmentation pattern. The MS/MS data showed that interferences from endogenous metabolites from the snail tissue matrix were not present in the analysis.

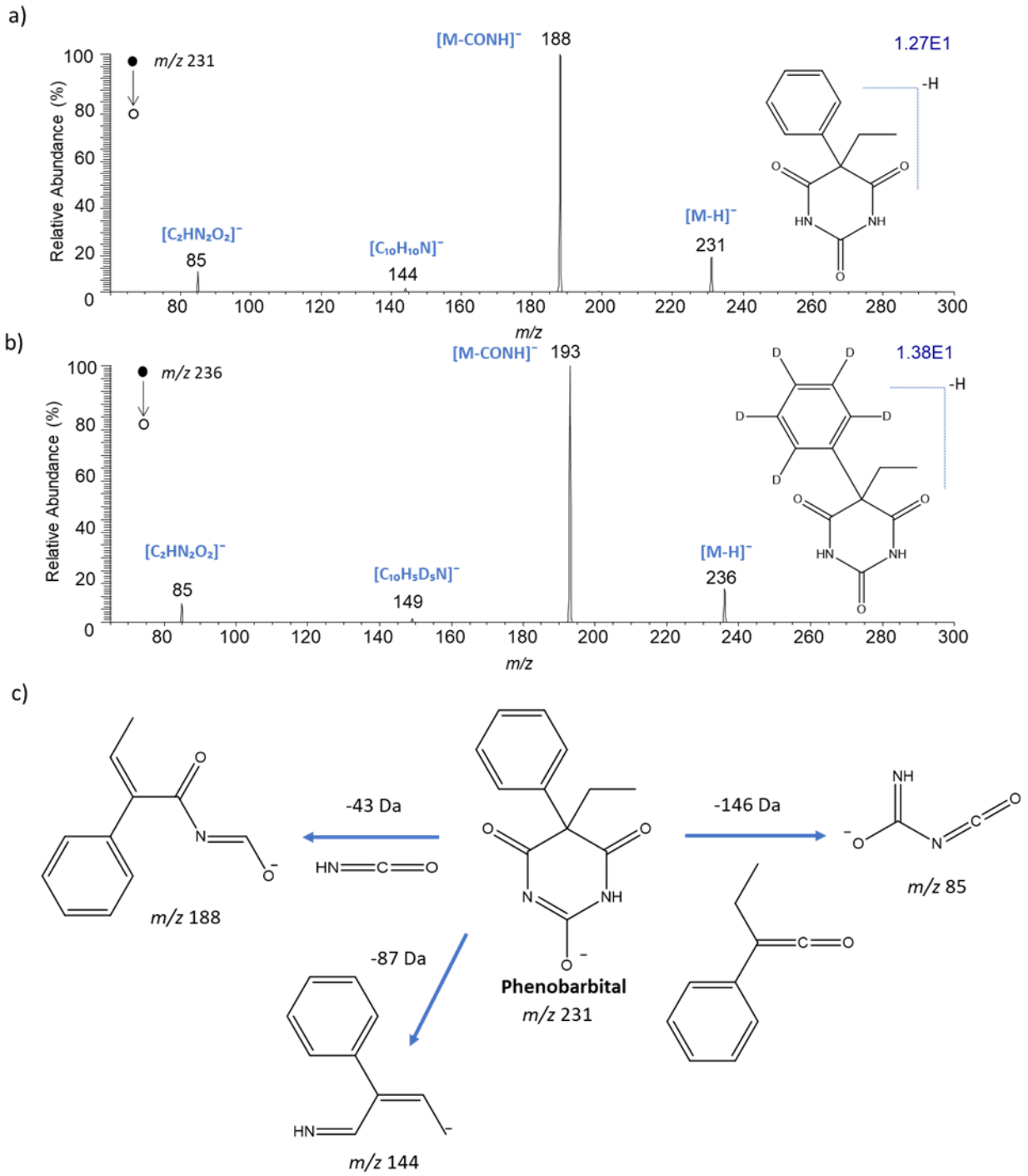

Figure 2.8: Average (-)DESI-MS/MS spectra of a) PB (*m/z* 231). b) The isotopically labelled IS, PB-D5 (*m/z* 236) on 10 µm snail tissue sections. c) MS/MS fragmentation pathway of Phenobarbital. The MS/MS profiles were collected via CID from 1 µL spots of 100 ng/µL of each standard and fragmented with collision energies of 20 (manufacturer's unit).

2.4.5. Specificity

The targeted DESI-MSI approach was developed by monitoring PB (*m/z* 231) and PB-D5 (*m/z* 236) in SIM mode within a mass window of 12 Da (*m/z* 227.5-239.5). The full scan MS and SIM mode spectra are shown in Figure 2.9 below for comparison. In full scan MS between *m/z* 200-300, the average intensity of PB and PB-D5 was 1.63E1 (100%) and 1.62 E1 (99.5%), respectively, while in SIM mode, the average intensity of PB and PB-D5 was 1.97 E2 (97.5%) and 2.02 E2 (100.0%). The quantitative DESI-MSI study was performed in SIM mode since the relative intensity of PB and PB-D5 increased significantly.

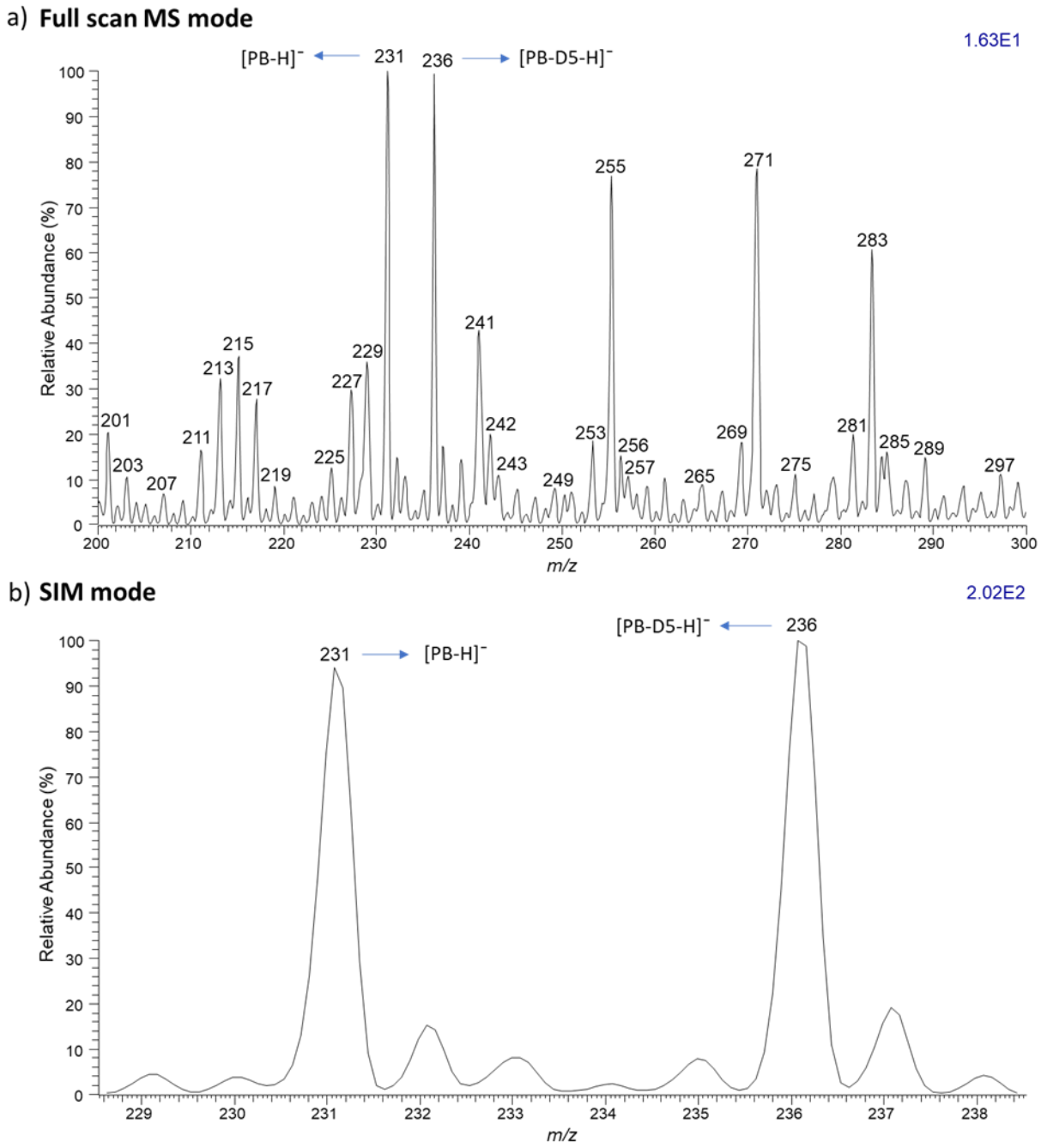

Figure 2.9: (-)DESI-MS profiles of PB (*m/z* 231) and the isotopically labelled IS PB-D5 (m/z 236) deposited (100 ng/µL) directly on 10 µm snail (*p. diffusa*) tissue sections collected for 30 secs in a) Full scan MS mode (*m/z* 200-300) displaying the average intensity PB as 1.63E1 (100%) and PB-D5 as 1.62 E1 (99.5%). b) SIM mode (*m/z* 228.5-238.5) depicting the average intensity of PB and PB-D5 as 1.97 E2 (97.5%) and 2.02 E2 (100.0%).

2.4.6. Sensitivity

The limit of detection (LOD) and quantification (LOQ) of phenobarbital was investigated based on the signal to noise (S/N) ratio from DESI-MS images (n=3). The LOD and LOQ are standard limits set by the FDA by comparing measured signals from samples with known low concentrations of analyte to establish the minimum concentration at which the analyte can be reliably detected. A S/N ratio between 3 or 2:1 is generally considered acceptable for estimating the detection limit and S/N of 10 as the quantification limit.[97] In Figure 2.10.b, PB microspots of 0.1, 1, 10, 100 ng/µL (43-4200 nM) were deposited on the 10 µm snail tissue section. The S/N=2 and S/N=9 was found for 1 ng/µL (43 nM) and 10 ng/µL (430 nM), which was near the LOD and LOQ, respectively.

2.4.7. Dynamic range

We investigated a lower linear dynamic range from 10-100 ng/µL and a higher linear dynamic range from 100-1000 ng/µL. We explored whether the drug was completely extracted from the snail tissue section in a single MSI analysis. A consecutive image of the tissue section was performed after the first analysis revealed that PB was completely extracted from the tissue section (data not shown). A higher dynamic range (250-1000 ng/µL) was compared to the lower range (10-100 ng/µL). The ion images of the drug revealed incomplete extraction from the tissue at concentrations ≥250 ng/µL after a second, consecutive MS image of the same tissue section (data not shown). We found that PB in the higher dynamic range led to non-linear standard curves due to the saturation of the analytical response therefore, the lower dynamic range was selected for MSI quantification experiments.

2.4.8. DESI-MSI of Phenobarbital in the Absence of the Internal Standard

In the absence of the IS, the standard curve was plotted by depositing PB directly on the snail tissue section in concentrations of 10, 50, 75, and 100 ng/µL (430-4300 nM) (Figure 2.10). The precision showed high SDs and RSDs ranging from 10-27% in the linear range of 10-100 ng/µL, respectively (n=3) (Figure 2.10.e). Higher RSDs were observed at lower concentrations due to

greater variations near the LOQ. Moreover, the correlation coefficient r^2, from the standard curve was found to be r^2=0.9554. The U.S. Food and Drug Administration (FDA) suggests that the precision (RSD) should be <20% at the LLOQ and <15% at all other concentrations and the linearity should not fall below r^2=0.99.[98] The SD, RSD and linearity of the DESI-MSI analysis in the absence of the IS would not meet the guidelines set by the FDA.

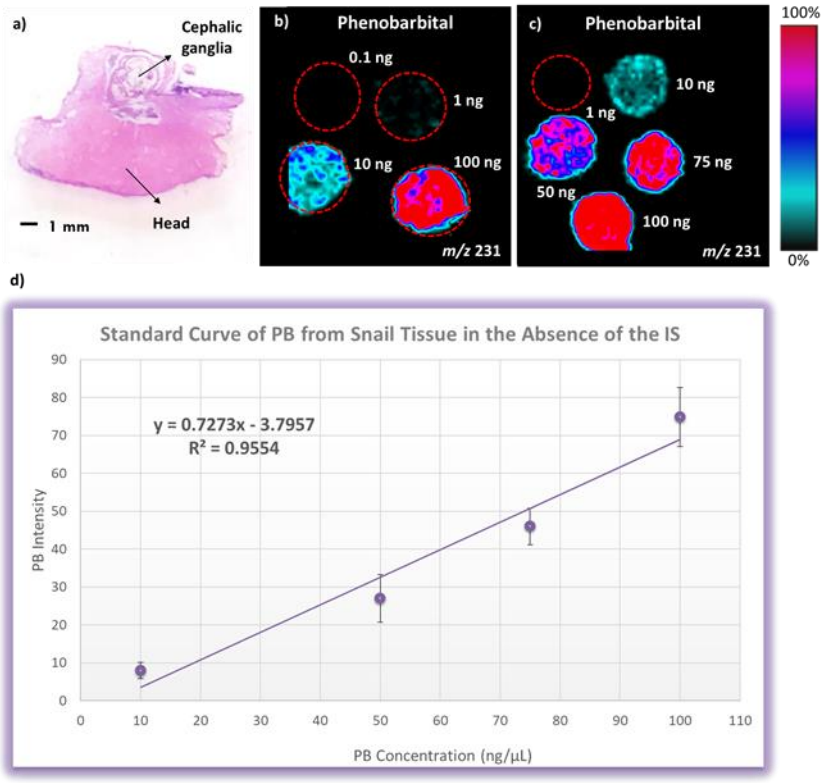

e)

The Standard Curve Data of PB from Snail Tissues in the Absence of the IS

PB (ng/uL)	Run 1	Run 2	Run 3	Analytical Performance		
	Intensity of PB			Average	SD	RSD (%)
1	nd	nd	nd	nd	nd	nd
10	7.8	10.1	5.8	8	2	27%
50	33.8	21.4	25.8	27	6	23%
75	47.0	40.7	50.2	46	5	11%
100	78.0	66.0	80.7	75	8	10%

Figure 2.10: (-)DESI-MSI analytical performance in the absence of the IS on 10 µm snail (*p. diffusa*) tissues. a) H&E stained 10 µm tissue section after MSI analysis. b) LOD study of PB (*m/z* 231). c) PB microspots of 1-100 ng/µL on the snail tissue section. d) Standard curve of PB from snail tissues in the absence of the IS from three separate (-)DESI-MS imaging analyses (n=3). e) Table of the overall analytical performance.

2.4.9. Tissue Homogeneity

The homogeneity of the biological tissue is an important aspect of the MSI study. The composition of the tissue matrix must remain constant to compare between different IS application strategies. The snail head was selected as the model tissue because of its overall homogenous composition containing two distinct anatomical regions, the bulk snail head and the cephalic ganglia (Figure 2.10.a). DESI-MSI of the snail head tissue revealed that metabolites, such as fatty acids, monosaccharides and phospholipids were spatially localized evenly in this region. Moreover, the uniform spatial distributions of PB in Figure 2.10.c also suggests that the snail head tissues are in fact homogenous.

2.4.10. Method III - The Internal Standard in the DESI Spray Solvent

In method III, the IS was spiked in the DESI solvent spray and PB was deposited on snail tissue sections (10-100 ng/µL), however, this method did not display a good representation of the extraction and ionization efficiency of the drug from tissues and it was challenging to produce a linear response. In DESI, the desorption and ionization of analytes from tissues is driven by a solid-liquid extraction. The IS added into the DESI solvent becomes charged in solution before the "droplet pickup mechanism" takes place, on the other hand, the analyte ionizes via the "droplet pickup mechanism", in which compounds on the surface are extracted into the thin liquid film by means of primary solvent droplets and analytes are desorbed/ionized as secondary droplets. Therefore, this method does not mimic well the ionization/desorption process that the analyte undergoes by typical DESI mechanisms. Quantitative MSI by adding the IS in the DESI solvent spray may be quite challenging from an analytical standpoint. Method I and II showed much better overall analytical performance, and therefore method III was not investigated further.

2.4.11. Method II – Optimization of the IS Thin Film

The IS thin film applied on top of tissue sections was optimized to prevent the disruption and delocalization of endogenous metabolites from the snail tissue matrix. The spatial

distribution of fatty acids and phospholipids in rat brain tissue sections by DESI-MSI are well described in the literature.[99-102] Rat brain tissue sections were used as controls to evaluate changes in the spatial distribution of endogenous metabolites as a result of applying the thin film under different conditions of Nitrogen gas pressure (40-80 psi) and solvent flow rates (1.5-5 µL/min). In rat brain tissues, three phosphatidylcholine adduct ions, $[PC(16:0/18:1+Na]^+$ of *m/z* 782, $[PC(16:0/18:1+K]^+$ of *m/z* 798 were localized across the brain except in the corpus callosum, and $[PC(36:1)+Na]^+$ of *m/z* 810 was localized in the corpus callosum, thalamus and hypothalamus (Figure 2.11.A). The spatial distribution of the phospholipids was conserved as compared to controls under conditions of 40 psi and 1.5 µL/min used to apply the IS thin film (Figure 2.11.B). These results indicated that the tissue remains intact after the film's application since metabolite delocalization and splashing effects were not observed.

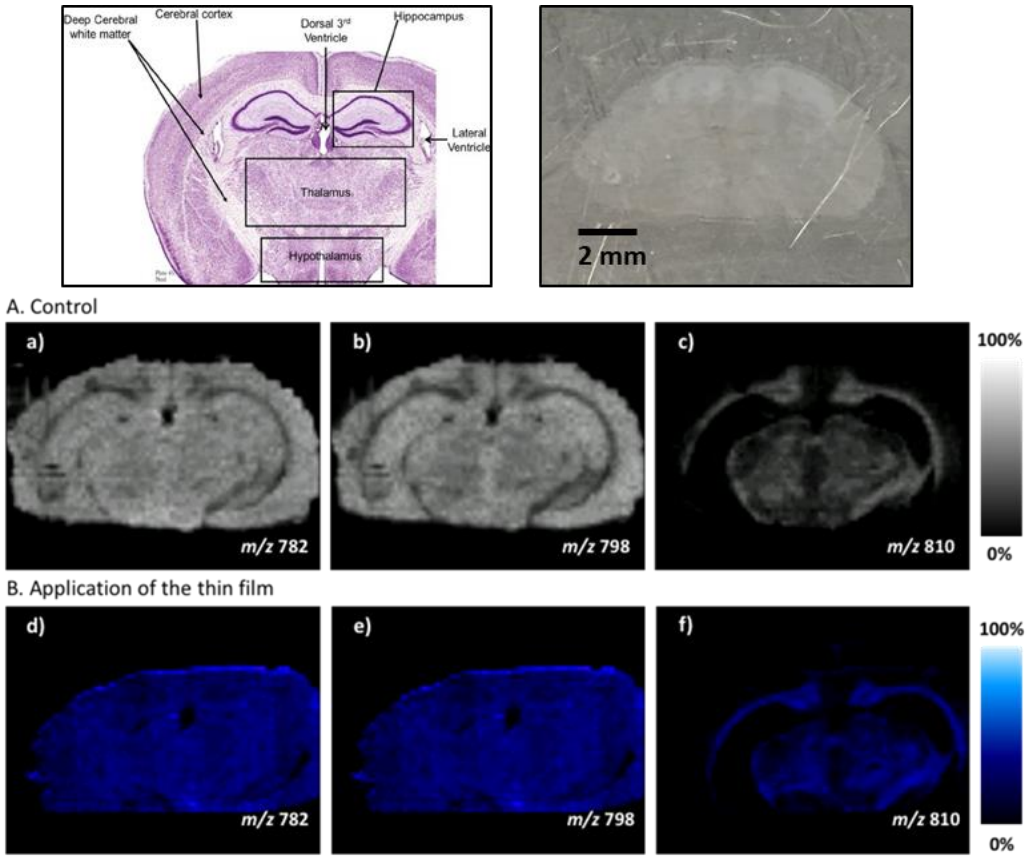

Figure 2.11: (+)DESI-MSI analysis of phospholipids in 10 µm rat brain tissue sections using MeOH. Panel A. Control rat brain tissue. Panel B. After the addition of the IS thin film using a Nitrogen gas pressure of 40 psi and a solvent flow rate of 1.5 µL/min. DESI-MS image dimensions of 16000 x

10000 µm set to a lateral resolution of 200 µm. The top image illustrates the brain substructures of a coronal rat brain tissue section adapted from Woods et al.[103]

In parallel, we investigated the concentration of IS thin film by applying 1, 10 and 100 ng/µL within an area of 110 mm² on snail tissues corresponding to 0.3, 3.4 and 33.4 ng/mm², respectively (Figure 2.12). The optimal thin film was 10 ng/µL (3.4 ng/mm²) that showed good I_D/I_{IS} ratios and the correlation coefficient of r^2= 0.9866 compared to r^2=0.9506 using 1 ng/µL (0.3 ng/mm²).

Table 2.2: The application of the IS thin film on top of snail (*p.diffusa*) tissue sections.

Method II: Application of thin film with 1 ng/µL							
[PB] ng/µL	ROI intensity ratio	ROI intensity PB	ROI intensity PB-D5	Thin film Volume	Image Area	Film Mass (ng)	Thin Film Conc.
10	0.95	4.3	4.5	37 µL	11 mm x 10 mm = 110 mm²	37 ng	0.34 ng/mm²
50	2.00	7.8	3.9				
75	2.10	9.6	4.6				
100	2.71	18.9	7.0				

Method II: Application of thin film with 10 ng/µL							
[PB] ng/µL	ROI intensity ratio	ROI intensity PB	ROI intensity PB-D5	Thin film Volume	Image Area	Film Mass (ng)	Thin Film Conc.
10	0.17	48.8	293.1	37 µL	11 mm x 10 mm = 110 mm²	370 ng	3.36 ng/mm²
50	0.62	182.3	293.6				
75	0.88	247.4	281.1				
100	1.32	336.1	253.7				

Method II: Application of thin film with 100 ng/µL							
[PB] ng/µL	ROI intensity ratio	ROI intensity PB	ROI intensity PB-D5	Thin film Volume	Image Area	Film Mass (ng)	Thin Film Conc.
10	0.02	2.2	112.8	37 µL	11 mm x 10 mm = 110 mm²	3700 ng	33.6 ng/mm²
50	0.03	3.5	105.4				
75	0.03	2.9	102.7				
100	0.03	3.1	96.7				

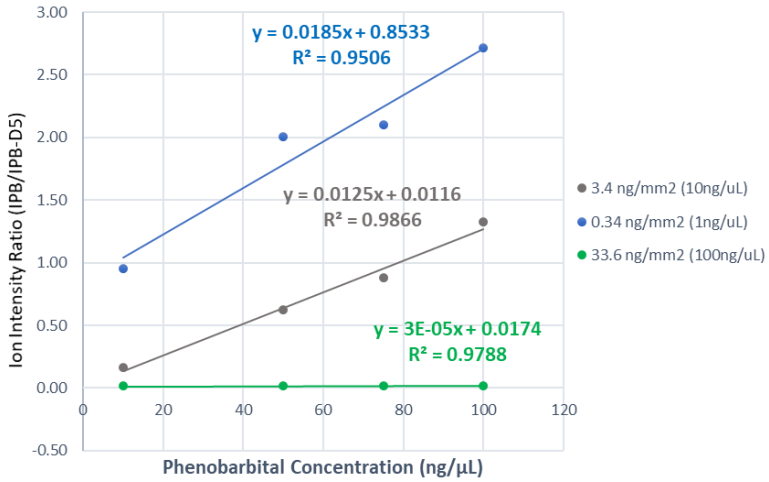

Figure 2.12: Method II – The optimization of PB-D5 thin film on snail tissues by DESI-MSI. a) IS film of 1 ng/µL. b) IS film of 10 ng/µL. c) IS film of 100 ng/µL. d) Standard curves of the IS thin film of 1 ng/µL (0.34 ng/mm²) blue line, 10 ng/µL (3.4 ng/mm²) grey line, and 100 ng/µL (33.6 ng/mm²) green line.

2.4.12. Comparison of the Internal Standard Application Strategies

In this study, the freshwater golden apple snail (*p.diffusa*) was used as the invertebrate model to compare between three IS application strategies. The isotopically labelled IS, PB-D5 and the psycholeptic drug, PB were used to evaluate the accuracy and precision of the three IS strategies from *in vitro* dosed snail tissue sections. In method I, the drug and the IS were deposited as microspots on top of snail tissue between 10-100 ng/µL spiked with 100 ng/µL of the IS. In method II, thin films of the IS were applied on top of the snail tissues followed by the deposition of PB microspots (10-100 ng/µL).

Intra- and interday DESI-MSI experiments were performed to assess the precision (repeatability), and linearity of method I and II. In the (-)DESI-MSI study, PB (*m/z* 231) and PB-D5 (*m/z* 236) precursor ions were monitored in 12 Da mass window in SIM mode. Imaging analyses for method I and II were completed on two separate days (day 1 and day 2) with 3 imaging runs per day (Figure 2.13). The intra- and interday standard curves were generated by extracting the ion intensity ratios of PB to PB-D5 (I_D/I_{IS}) from ROIs in the DESI-MS images and plotting PB

concentration vs the average ion intensity ratios (I_D/I_{IS}) (Figure 2.14). In method I and II, PB microspots displayed a gradual increase in relative intensities from 10-100 ng/µL. In method I, the IS showed similar intensities between microspots with uniform spatial distributions. In method II, the IS thin film also revealed uniform distributions with the exception of a few pixels located at the centre of the snail tissue (Figure 2.13.B). However, these pixels did not coincide with PB microspots, and were not included in the linear regression analysis (Figure 2.13.B.f,l,n).

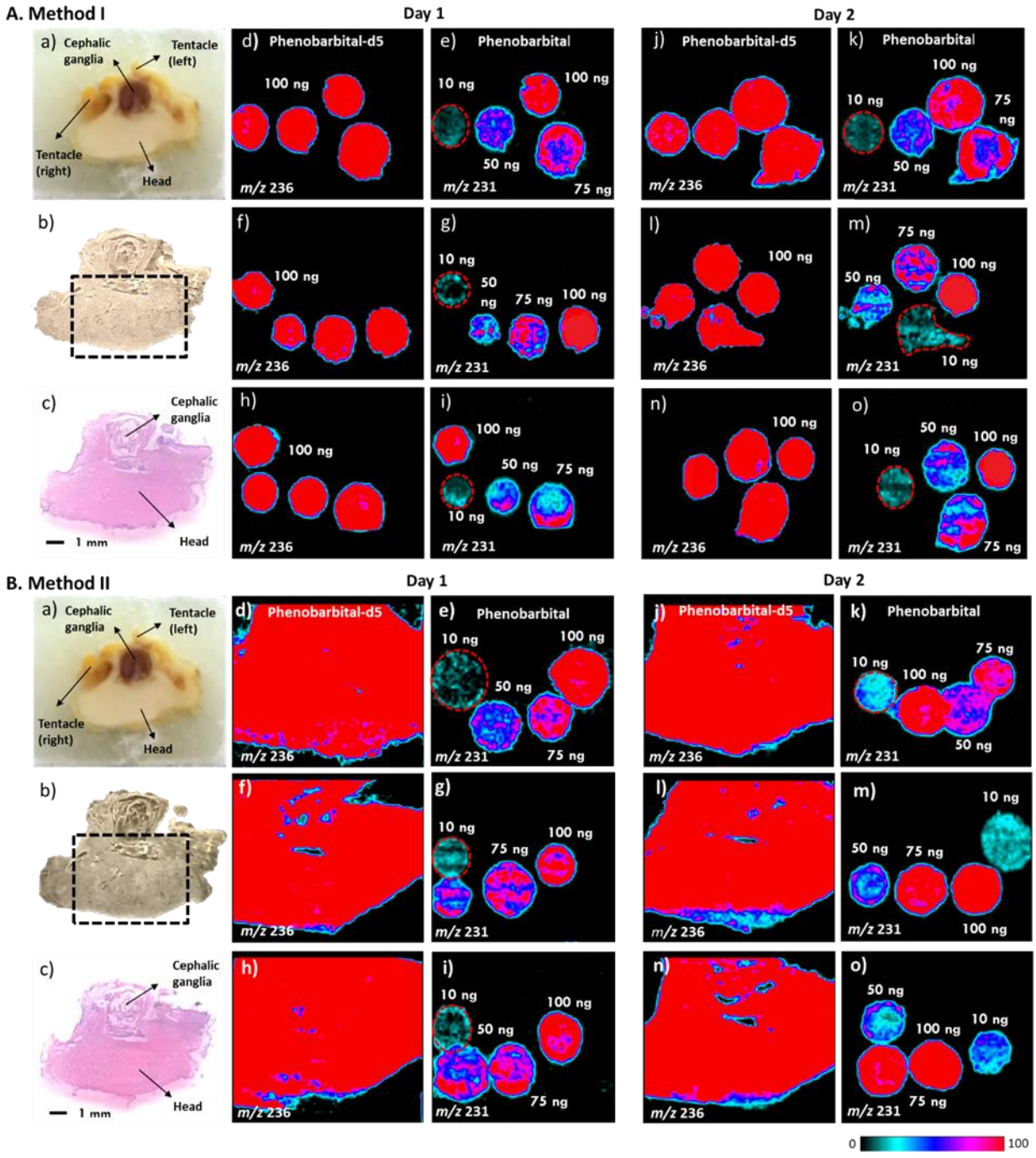

Figure 2.13: Intra- and Interday (-)DESI-MSI study of PB and PB-D5 on snail (*p. diffusa*) tissues between 10-100 ng/µL. Panel A. Method I – Microspots on top of the tissue. a) Snail head tissue block during cryosectioning. b) Optical image. c) H&E stained tissue section after MSI analysis. d) f) & h) Day 1 –100 ng/µL of PB-D5 (*m/z* 236). e), g) & i) Day 1– PB (*m/z* 231). j), l) and n) Day 2 - 100 ng/µL of PB-D5 (*m/z* 236). k), m), o) Day 2– PB (*m/z* 231). Panel B. Method II – Application of the IS thin film with the DESI sprayer. a) Snail head tissue block during cryosectioning. b) Optical image. c) H&E stained tissue section after (-)DESI-MSI analysis. d), f), h) Day 1 – 10 ng/µL of PB-D5

(m/z 236) corresponding to (3.4 ng/mm²). e), g) & i) Day 1– PB (*m/z* 231). j), l) and n) Day 2 - PB-D5 (*m/z* 236). k), m), o) Day 2– PB (*m/z* 231).

The linear regression analysis for method I and II are summarized in Table 2.3. We found RSDs of 2.3-7.6% (day 1) and 2.8-8.1% (day 2) and interday RSDs of 6.5-7.4% for method I. Meanwhile, for method II RSDs ranged from 13.8-18.9% (day 1) and 9.9-19.6% (day 2) and interday RSDs of 10.7-17.6% in the same dynamic range. In comparison, method I exhibited better precision than method II, in both, the intra- and interday DESI-MSI analysis.

The linearity for the interday DESI-MSI analysis was to some extent improved from the intraday results due to the increasing number of replicates corresponding to correlation coefficients of r^2=9894 and r^2= 0.9945 for method I and II, respectively (Figure 2.14). In summary, the intra- and interday precision experiments meet the FDA criteria for precision (repeatability) in which RSDs encompass >20% at the LOQ and <15% at all other concentrations. The dynamic range spanned two orders of magnitude. The lowest and highest PB concentration had RSDs between 7.4-17.6% at 10 ng/µL and 6.5-10.7% at 100 ng/µL for method I and II, respectively.

A. Intraday Analyses

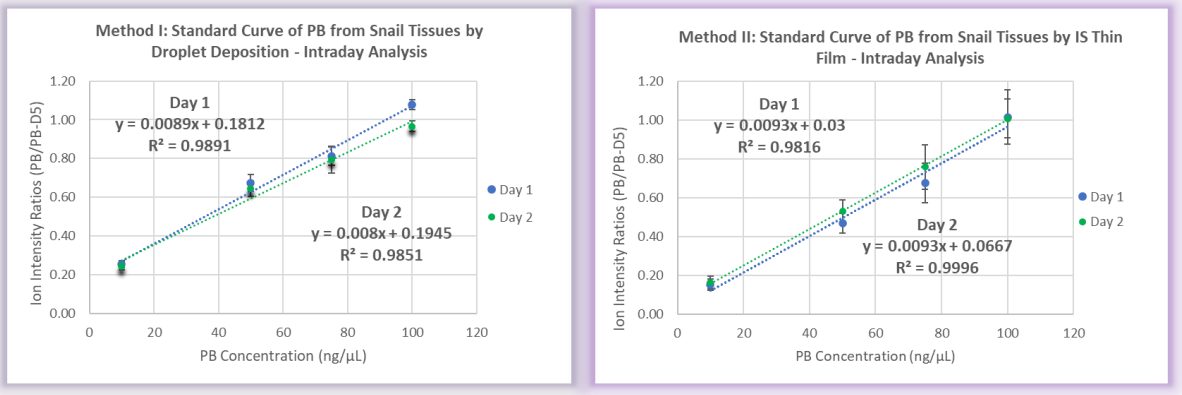

B. Interday Analyses

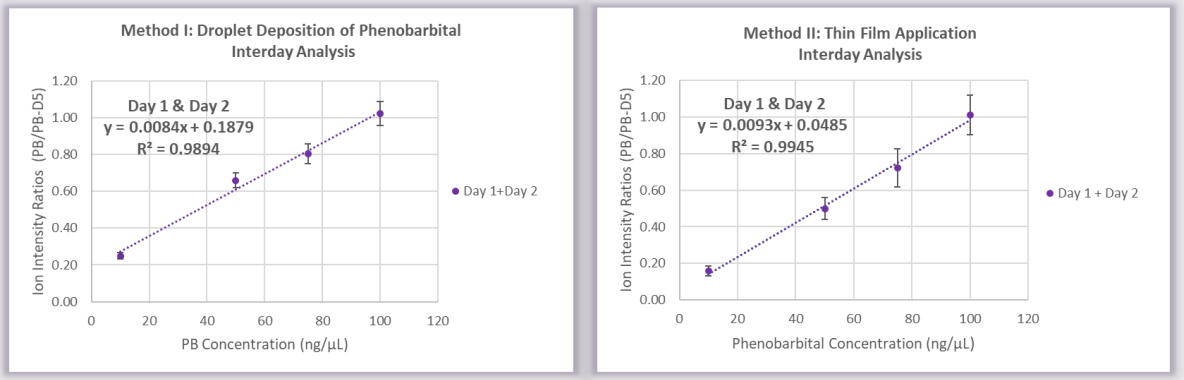

Figure 2.14: Intra- and interday standard curves plotting PB (ng/µL) vs the ion intensity ratios of PB/PB-D5 for method I and II. Panel A. Method I and II intraday analyses. Panel B. Method I and II interday analyses.

Table 2.3: Intra- and interday MSI linear regression analyses for method I and II.

Method I and Method II						
[Pb] ng/µL	10	50	75	100		
nM	433	2164	3245	4327		
Method I - Deposition of PB/PB-D5 microspots on top of the tissue						
Day 1					**Linear equation y= mx + b**	
n	3	3	3	3	n	12
Average (I_D/I_{IS})	0.25	0.67	0.81	1.08	m	0.0089
SD	0.02	0.04	0.05	0.02	b	0.1812
RSD	7.6%	6.4%	5.9%	2.3%	r^2	0.9891
Day 2						
n	3	3	3	3	n	12
Average (I_D/I_{IS})	0.24	0.64	0.79	0.97	m	0.0080
SD	0.02	0.04	0.07	0.03	b	0.1945
RSD	8.1%	6.2%	8.8%	2.8%	r^2	0.9851
Interday						
n	6	6	6	6	n	24
Average	0.25	0.66	0.80	1.02	m	0.0084177
SD	0.02	0.04	0.05	0.07	b	0.1896
RSD	7.4%	6.2%	6.8%	6.5%	r^2	0.9894
Method II - IS thin film on top of the tissue						
Day 1					**Linear equation y= mx + b**	
n	3	3	3	3	n	12
Average (I_D/I_{IS})	0.15	0.47	0.68	1.01	m	0.0093
SD	0.03	0.05	0.09	0.14	b	0.03
RSD	18.9%	10.7%	12.8%	13.8%	r^2	0.9816
Day 2						
n	3	3	3	3	n	12
Average (I_D/I_{IS})	0.16	0.53	0.76	1.01	m	0.0093
SD	0.03	0.06	0.11	0.10	b	0.06
RSD	19.6%	11.4%	15.2%	9.9%	r^2	0.9996
Interday						
n	6	6	6	6	n	24
Average (I_D/I_{IS})	0.16	0.50	0.72	1.01	m	0.009332
SD	0.03	0.06	0.10	0.11	b	0.04924
RSD	17.6%	12.0%	14.5%	10.7%	r^2	0.9945

2.4.13. Statistical Analysis

Statistical analysis was performed by the Bland-Altman plot as the graphical representation of the agreement between the IS application strategies (Figure 2.15). The Bland-Altman plot was created with a total of 24 data points including the ion intensity ratios (I_D/I_{IS}) versus PB concentrations (10-100 ng/µL) for method I and II from Table 2.3. The horizontal blue line drawn at the mean (0.09) shows the scattering of the data points around this central mean. The data points are well contained within the low and high limits of agreement as the mean difference ± 1.96 SD and found within the lower and upper 95% confidence interval (CI) limits represented by green error bars. The Bland-Altman plot results showed that method I and II are not statistically significantly different and both can be used interchangeably for quantitative DESI-MSI.

a)

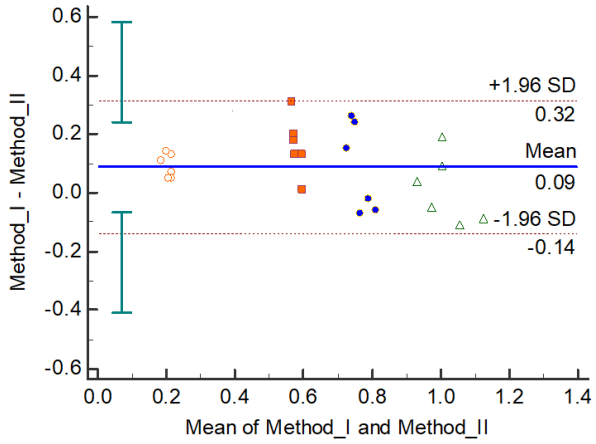

b)

Bland-Altman plot with multiple measurements per subject	
Method A	Method_I
Method B	Method_II
Differences	
Sample size	24
Arithmetic mean	0.08667
Lower limit	-0.1424
95% CI	-0.4095 to -0.06788
Upper limit	0.3157

Figure 2.15: a) A Bland-Altman plot with multiple measurements per subject (concentration) by plotting the differences between the methods against the averages of the methods as a comparison between IS application strategies. The horizontal line represents the mean difference (blue line) and the lower and upper limits of the SD (±1.96) of the mean (red dotted lines) and the upper and lower limits of the 95% CI (green error bars). The red hollow circles (10 ng/µL), red squares (50 ng/µL), blue circles (75 ng/µL) and the green triangles (100 ng/µL). b) The Bland-Altman input and output data.

2.4.14. Method Validation by Accuracy Assessment

The accuracy of the IS strategies was compared by evaluating the percent relative error (%RE) of PB from *in vitro* dosed snail tissue sections. Quality control (QC) PB microspots of 75 ng/µL were deposited and the IS was applied by method I and II (Figure 2.16). From the 2D DESI images, the average I_D/I_{IS} ratios were found to be 0.79 ± 0.01 and 0.82 ± 0.06 and the average QC concentrations were 71 ± 4 ng/µL and 83 ± 9 ng/µL for method I and II, respectively (n=3).

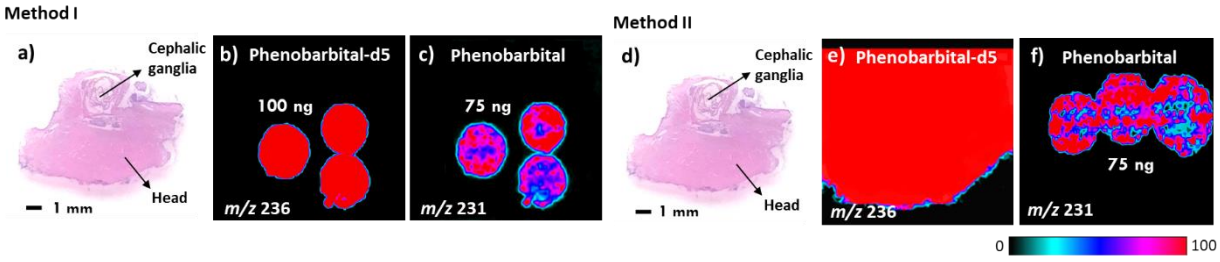

Figure 2.16: Method validation by assessing the accuracy of method I and II from PB QCs (75 ng/µL) on 10 µm snail tissue sections. a) PB-D5 (*m/z* 236) QC microspots of 100 ng/µL (n=3). b) PB (*m/z* 231) QC microspots of 75 ng/µL (n=3). c) PB-D5 thin film (10 ng/µL) in the DESI solvent spray corresponding to 3.4 ng/mm² on tissues (*m/z* 236). d) PB (*m/z* 231) QC microspots of 75 ng/µL (n=3).

In method II, a slight overestimate of PB (83 ± 9 ng/µL) was found from QCs of 75 ng/µL from applying the film first, followed by depositing the PB microspots on top of the IS film. The order in which the drug and IS were deposited lead to higher PB intensities and I_D/I_{IS} ratios somewhat higher than expected. In comparison, method I showed lower SDs, RSDs and narrower 95% CI (67-76 ng/µL) than method II (73-93 ng/µL). However, both methods contained the target QC (75 ng/µL) in the 95% CI. The accuracy represented as the average %RE was -5.3% and 10.6% for method I and II suggested only minor differences in accuracy between these methods (n=3). The accuracy evaluated here falls within the FDA accuracy requirements of <15% of the nominal value of the expected content.[98] In summary, the DESI-MSI data showed two major sources of variation that impact the accuracy and precision, when all other aspects of the DESI experiment (source parameters, solvent, solvent flow rate, nebulizing gas pressure, tissue matrix, etc.,) are kept constant, such as:

(i) The uniformity of the IS on tissues, and

(ii) The sequence in which the drug and IS was applied

The uniformity of the IS is important so that I_D/I_{IS} ratios do not vary significantly from pixel to pixel and encompass smaller deviations that represent the concentration of the drug more accurately in ROIs. Another important consideration is the sequence the drug and IS are applied onto *in vitro* dosed tissues that may result in an under or overestimation of the concentration as shown for method II. The investigation of IS strategies in MSI and validating new quantitative methods can lead to understanding of the factors involved for the best performing strategy to quantify and map the spatial distribution of targeted analytes on a pixel by pixel basis from biological tissues.

2.5. Conclusions

Quantitative MSI continues to be a challenging area of research with ambient ionization techniques to identify, quantify and map the spatial distribution of analytes from complex biological matrices. In the present work, the invasive freshwater golden apple snail (*p. diffusa*) was used as the invertebrate model to evaluate different internal standard application strategies for quantitative DESI-MSI. We presented a comprehensive qualitative and quantitative evaluation of three methods to add the IS with the aim of establishing an approach for routine targeted quantitative DESI-MSI analysis for exogenous compounds. In the intra- and interday MSI studies, the deposition of the drug and the IS as droplets on top of the tissue (method I) showed the best overall analytical performance in terms of precision and accuracy compared to method II. In this study, the two major sources of variation that impact the accuracy and precision in the DESI-MSI analysis, were found to be as a result of (i) the uniformity of the IS on tissues, and (ii) the sequence the drug and IS were applied. The analytical figures of merit for method I and II fall within all the acceptable guidelines set by the FDA. Finally, statistical analysis by the Bland-Altman plot revealed that method I and II are not statistically significantly different and may be used interchangeably for quantitative DESI-MSI. In future MSI studies, it would be interesting to

quantify drugs classified as PPCPs from aquatic invertebrates dosed *in vivo* and animals that have been exposed to PPCPs from Canadian environments such as rivers, lakes and watersheds.

Chapter Three: Chemical Profiling of Bioactive Secondary Metabolites from Maca (*Lepidium peruvianum)* by Normal and Reverse Phase TLC Coupled to DESI-MS

Chapter 3 is a submitted version of the manuscript:

Perez, C.J. Souza, R.C., Ifa, D.R. Chemical profiling of bioactive secondary metabolites from Maca (*Lepidium peruvianum*) by normal and reverse phase TLC coupled to DESI-MS**.** *J Mass Spectrom.* **2020. Submitted.**

3.1. Summary

Maca (*Lepidium peruvianum*) is a Peruvian tuberous root of the Brassicaceae family with important biological activities and medicinal properties. We report a rapid HPTLC-(-)DESI-MS method to profile and separate intact glucosinolates from the hydromethanolic extracts of red and black Maca (*L.peruvianum*) seeds. In the first stage of the plant's lifecycle, aromatic glucosinolates were the main chemical constituents. In the seeds, Glucolepigramin/Glucosinalbin were the most predominant precursors, rather than Glucotropaeolin, as previously reported in hypocotyls and roots. These findings lead us to suggest that Glucolepigramin/Glucosinalbin play important roles as active precursors in the biosynthetic pathways of other secondary metabolites in the early stages of plant development. Between red and black Maca seeds, minor differences in the relative abundances of glucosinolates were observed rather than different plant metabolites. For the first time, we report six potential plant antibiotics, phytoanticipins: glycosylated ascorbigens and dihydroascorbigens from Maca seeds. Moreover, we developed a targeted reverse phase C_{18} functionalized TLC-DESI-MS method with high sensitivity and specificity for Brassicaceae fatty acids in Maca seeds and health supplements. The investigation of secondary metabolites by normal and reverse phase TLC-DESI-MS can aid in the identification of these compounds as they begin to emerge in later stages of development in plant tissues such as leaves, hypocotyls, and roots.

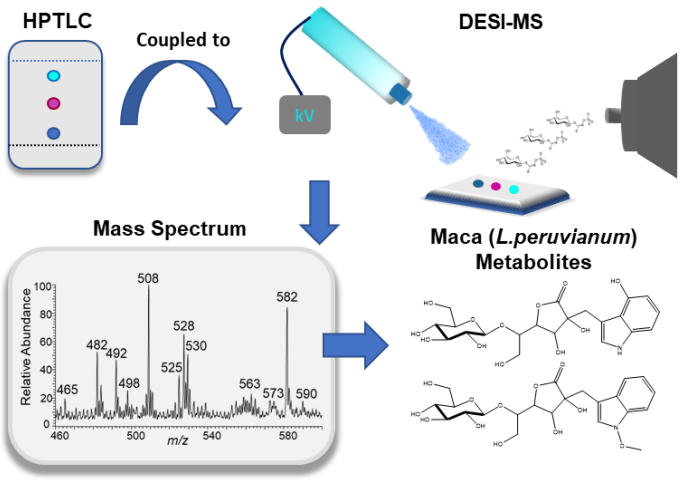

Figure 3.1: Schematic representation of HPTLC coupled to DESI-MS for phytometabolomics.

3.2. Introduction

Maca (*Lepidium peruvianum)* is a tuberous root native to South America in the Andes mountains of Peru. Maca is an biennial herbaceous plant, in the Brassicaceae family, grown in the Andes mountains at high altitudes of 3800 to 4500 m.[104] Maca is a medicinal plant with important biological activities[105] such as antioxidant and anti-inflammatory activities[106], neuroprotective[107] and hepatoprotective effects, anti-depressant[108,109], fertility enhancing properties[106,110,111], energizing, and anti-proliferative activities. Three major phenotypes, yellow, red, and black exist distinguishable from colours of the hypocotyl and tuberous root of the plant.[112] Interestingly, Maca phenotypes have shown different biological activities, however, the correlations between phenotypes and the biosynthetic mechanisms driving these differences in biological activities are not yet understood.

Chemical profiling of Maca has led to the discovery of many bioactive secondary metabolites such as glucosinolates, alkamides (macamides and macaenes), imidazole and pyrrole alkaloids, thiohydantoins, fatty acids, flavonoids, flavonolignans and phenolic compounds.[113,114] Glucosinolates, are anionic precursors to many secondary metabolites, they are sulfur rich compounds, typically found in Brassicaceae plants.[104,115] Structurally, these precursors are β-thioglucoside N-hydroxysulfates, also known as (Z)-N-hydroximinosulfate esters, with aromatic, aliphatic and indoyl (R) groups with a β-D-thioglucose moiety.[113] In the last decade, they have been of interest due to their chemoprotective and anti-proliferative activities against HeLa cancer cell lines.[113,116] The glucosinolate-myrosinase system (“mustard oil bomb”), is a chemical defense mechanism in plants activated during pathogenic infection or tissue disruption from herbivores feeding on the plant. By myrosinases (thioglucosidases), glucosinolates are converted into isothiocyanates, nitriles and thiocyanates, epithionitriles, and oxazolidine-2-thiones to defend the plant under attack.[113,117] Aromatic isothiocyanates are known to be highly toxic to herbivore insects. Current MS analyses involve the enzymatic conversion by thiosulfates into desulfo-glucosinolates and myrosinase into isothiocyanates. However, the desulfation rate of glucosinolates can be affected by feedback inhibition of the enzyme causing the incomplete

removal of the sulfate group.[118] Therefore, these methods most likely yield an underestimation of the final glucosinolate contents from plant tissues.

Desorption electrospray ionization (DESI) is an ambient MS analytical tool for the direct analysis of analytes deposited on surfaces and from biological tissue sections with minimal to no sample pretreatment.[8,11] DESI is a spray based ambient technique that operates in the open environment. A charged spray of solvent droplets directed towards the surface desorbs and ionizes analytes which are directed to the MS inlet under vacuum conditions.[11,13,66] The investigation of phytochemicals from TLC imprints or directly from intact plant tissues such as flowers, leaves, roots, and twigs are well described in the literature.[29,30,33,34,119-123] In this study, we report the main chemical constituents in red and black Maca (*L. peruvianum*) seeds to investigate plant precursors in the first stage of development in the plant's lifecycle. We developed HPTLC and RPTLC-DESI-MS methods for the analysis of bioactive classes of secondary metabolites such as intact glucosinolates, glycosylated ascorbigens and dihydroascorbigens, free fatty acids and imidazole alkaloids from Maca seeds and health supplements such as lyophilized root powder and tinctures.

3.3. Experimental

3.3.1. Materials and Reagents

HPLC-grade methanol (MeOH), water (H_2O), acetonitrile (ACN), acetone (Ace), ethanol (EtOH), chloroform ($CHCl_3$), benzyl alcohol (BnOH), benzene (Ben) and C_{18} silica gel RPTLC plates F_{254} were purchased from Sigma-Aldrich (Oakville, ON, CA). HPTLC plates (glass backed, 250 µm stationary phase) were purchased from SiliCycle (Quebec City, QC, CA). Red and Black Maca (*L.peruvianum)* seeds were purchased from Strictly Medicinal LLC. (Williams, OR, USA) lot# 9776 and lot# 10644, respectively. Black Maca (*L.meyenii*) root lyophilized powder and St.Francis Herb Farm Maca (*L.meyenii*) root tincture were purchased from a local health food store (Toronto, ON, CA).

3.3.2. The Extraction of Secondary Metabolites from Maca Seeds and Supplements

Red and black Maca (*L. peruvianum*) seeds were extracted for glucosinolates by the protocol described from Doheny-Adams et al. with some modifications.[124] Briefly, red (54.4 mg ± 0.01 mg) and black (54.1 mg ± 0.01 mg) seeds were weighed and extracted with 1 mL of cold 80% MeOH (-20°C). The seeds were manually macerated to thoroughly grind the sample with a glass pestle maintaining the temperature at 4°C. The crude extract was ultrasonicated for 30 min at 8 ± 2°C and centrifuged for 15 min. at 5000 rpm. The supernatant was collected and kept frozen in a -20°C freezer. For the fatty acid extraction, red Maca seeds (55.5 mg) were manually macerated with $CHCl_3$/MeOH (1 mL/0.5 mL v/v) and vortexed for 15 min. The crude extract was left to stand for 1 hr, ultrasonicated for 1 hr and centrifuged for 15 min at 5000 rpm. The $CHCl_3$/MeOH fractions were separated and the $CHCl_3$ fraction was placed in another tube and evaporated to dryness. The $CHCl_3$ extract was stored at -20°C prior to DESI-MS analysis and resuspended on day of analysis. Black Maca (*L.meyenii*) root powder was weighed (1.0097 g) and extracted with 10 mL of H_2O/$CHCl_3$ (1:1 v/v). The $CHCl_3$ layer was collected, air dried for 3 days, and resuspended in 1 mL $CHCl_3$.

3.3.3. ESI-HRMS Analysis of Red and Black Maca (*L. peruvianum*) Seeds

The red and black hydromethanolic seed extracts were serially diluted and analyzed by (-)nanoESI-HRMS using the Thermo Fischer QExactive hybrid Quadrupole-Orbitrap mass spectrometer coupled to the dual ESI/MALDI-MS injector (Spectroglyph LLC., Kennewick, WA, USA) described elsewere.[125] The ESI-HRMS analysis was performed with the following parameters: capillary spray voltage 4 kV, capillary temperature 250°C, an injection time of 50 ms and 3 microscans. The mass resolving power was set to 140,000 at *m/z* 200 and mass accuracies of ≤ 7 ppm were observed for all glucosinolate ions.

3.3.4. The HPTLC/RPTLC-(-)DESI-MS Analysis of Secondary Metabolites

Maca (*L.peruvianum*) seed extracts (0.1 µL) were deposited 0.5 cm from the bottom of the HPTLC/RPTLC plates and developed in a glass TLC chamber. For glucosinolates and glycosylated ascorbigens and dihydroascrobigens, the HPTLC plate was developed along 4.2 cm with BnOH:EtOH (7:3) v/v. A wide range of solvent combinations for the mobile phase were tested and BnOH:EtOH (7:3) v/v was selected as the best system to separate glucosinolates. DESI-MS analysis was performed on a Thermo Scientific LTQ linear ion trap mass spectrometer (San Jose, CA, USA) equipped with the custom built, automated DESI ion source coupled to a 2D moving stage described in detail elsewhere.[99] Mass spectral data was collected by continuously scanning with a speed of 100 µm/s in a total time of 4.8 mins. DESI ion source parameters were optimized as follows: a capillary tip to surface distance of 4 mm, an incident angle to the surface of 52° and a 4-6 mm distance from the mass inlet to the solvent capillary using ACN as the DESI solvent. The injection time was set to 200 ms and 3 microscans. The nitrogen gas pressure and the flow rate applied was 100 psi and 5 µL/min, respectively. For Brassicaceae fatty acids, a reverse phase RPTLC-(-)DESI-MS method was applied using ACN:H_2O (8:2) v/v as the DESI solvent.

3.3.5. The HPTLC-(+)DESI-MS Analysis of Imidazole Alkaloids

The HPTLC developing solvent Ace:Ben:H_2O (7:2:1) v/v was most efficient system for the separation of imidazole alkaloids from the $CHCl_3$ extract of black Maca (*L.meyenii*) root powder and directly from Maca tinctures. The HPTLC plate was developed along 3.5 cm and DESI-MS analysis was performed in positive ion mode with parameters as described above in a total analysis time of 5.8 min.

3.4. Results and Discussion

3.4.1. Glucosinolates

In the Brassicaceae family, different species have aromatic, indoyl and aliphatic type glucosinolates, but each plant typically contains six high-content glucosinolates and several others in minor and trace amounts.[113] In the first stage of plant development, red and black Maca (*L. peruvianum*) seeds presented MS profiles containing a total of 10 glucosinolates. 6 aromatic, 3 indoyl and 1 aliphatic glucosinolate were found by HPTLC-DESI-MS in negative ion mode as shown in Figure 3.2 and Table 3.1. The identification of these metabolites was supported by (-)ESI-HRMS analyses of the hydromethanolic seed extracts set to the mass resolving power of 140,000 at *m/z* 200 (Appendix B). A total of 6 aromatic and one aliphatic glucosinolate were identified in the HRMS analysis with mass accuracies of ≤7 ppm for all ions.

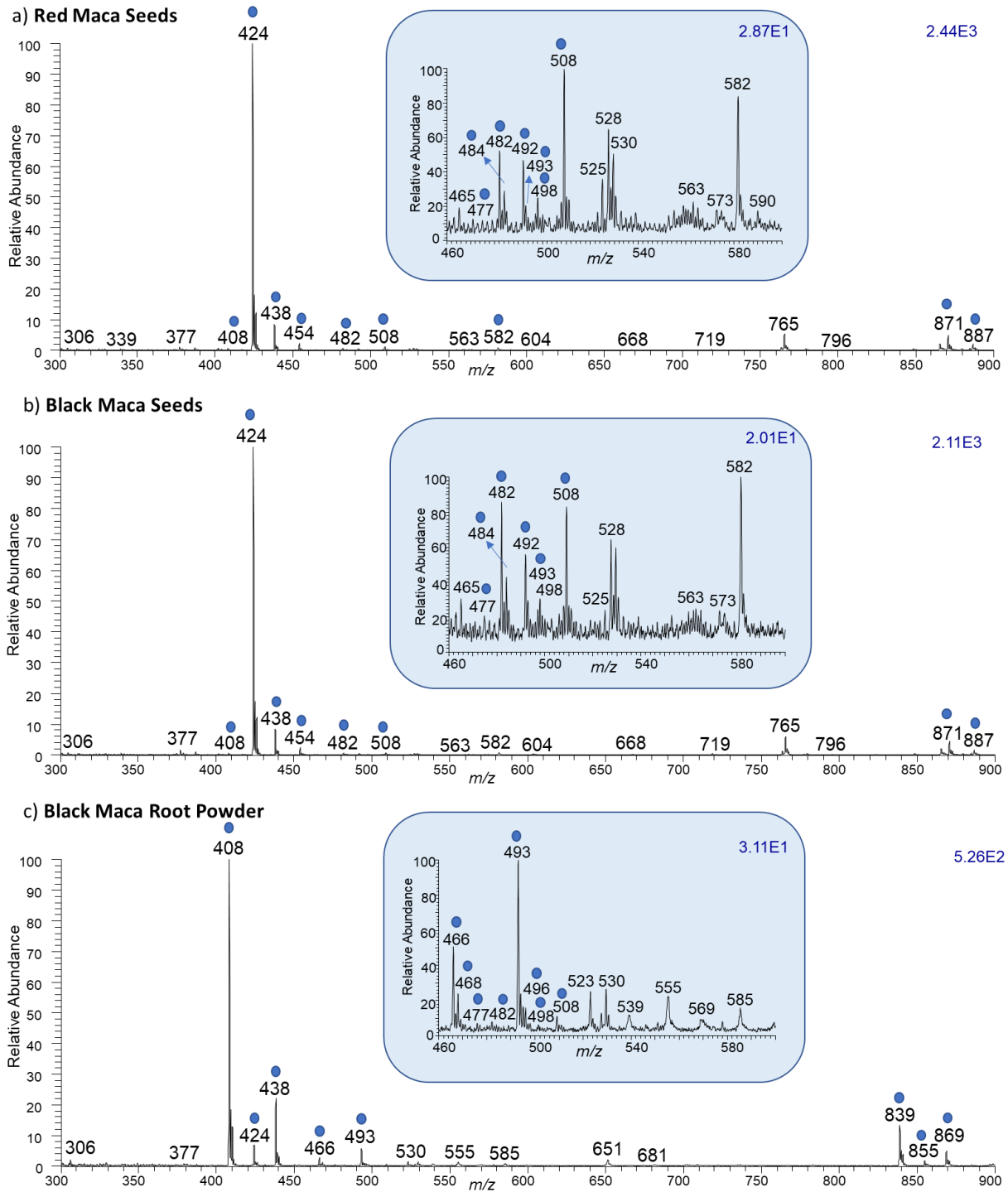

Figure 3.2: HPTLC-(-)DESI-MS profiles of glucosinolates from the hydromethanolic extracts of Maca (*L. peruvianum*) using ACN. a) Red Maca seeds. b) Black Maca seeds. c) Black Maca root lyophilized powder. The inset MS spectra illustrates glycosylated ascorbigens and dihydroascorbigens in the mass range of *m/z* 460-600.

Table 3.1: Bioactive Secondary Metabolites in Red and Black Maca (*L. peruvianum*) Seeds and Black Maca Root Powder analyzed by HPTLC and RPTLC-DESI-MS in Negative Ion Mode.

N°	Tentative Metabolite	Chemical Formula	Monoisotopic mass	Type of Ion	Ion (*m/z*)	CID (%)	MS/MS Fragment Ions
G1	n-hexyl glucosinolate	$C_{13}H_{24}NO_9S_2$	402.08925	$[M-H]^-$	402[a,b]	20	nd
G2	Glucotropaeolin	$C_{14}H_{18}NO_9S_2$	408.04230	$[M-H]^-$	408[d]	20	**259** (100), 275, 230, 291, 166, 195
G3	Glucolepigramin	$C_{14}H_{18}O_{10}NS_2$	424.03722	$[M-H]^-$	424[d]	20	**259** (100), 275, 228, 291, 344, 406, 182, 246, 148
G4	Glucosinalbin						
G5	Glucolimnanthin	$C_{15}H_{20}NO_{10}S_2$	438.05287	$[M-H]^-$	438[d]	20	**259** (100), 275, 291, 242, 358, 195
G6	Glucoaubrietin						
G7	Unknown	$C_{13}H_{25}NO_{10}S_3$	450.05624	$[M-H]^-$	450[a,b]	20	nd
G8	3-hydroxy-4-methoxy benzyl glucosinolate	$C_{15}H_{20}NO_{11}S_2$	454.04778	$[M-H]^-$	454[a,b]	20	**259** (100), 275, 375, 291, 212, 242, 195
G9	4-hydroxy Glucobrassicin	$C_{16}H_{19}N_2O_{10}S_2$	463.04812	$[M-H]^-$	463[d]	20	nd
G10	Unknown glucosinolate	-	-	$[M-H]^-$	466[c]	20	**408** (100), 268, 259, 212
G11	Unknown glucosinolate	-	-	$[M-H]^-$	468[c]	20	**408** (100)
G12	3,4-dimethoxybenzyl glucosinolate	$C_{16}H_{25}NO_{11}S_2$	470.07908	$[M-H]^-$	470[c]	20	**408** (100)
G13	4-methoxy-Glucobrassicin/ Neoglucobrassicin	$C_{17}H_{22}N_2O_{10}S_2$	477.06377	$[M-H]^-$	477[d]	20	nd
G14	Hydroxy-methoxy glucobrassicin	$C_{17}H_{21}N_2O_{11}S_2$	493.05868	$[M-H]^-$	493[d]	20	nd

G15	Indoyl-3-hexyl-4-methyl-cyclohexane glucosinolate	$C_{22}H_{38}N_2O_8S_2$	521.19913	$[M-H]^-$	521[c]	20	nd
G16	Unknown	-	-	-	540[a,b]	20	**482** (100), 424, 342, 326
G17	Unknown	-	-	-	582[a,b]	20	386
G18	Glucotropaeolin dimer	$C_{28}H_{37}N_2O_{18}S_4Na$	839.07438	$[2M-2H+Na]^-$	839[c]	20	**408** (100)
G19	Glucotropaeolin-Glucolepigramin/ Glucosinalbin dimer	$C_{28}H_{37}N_2O_{19}S_4Na$	855.06929	$[2M-2H+Na]^-$	855[c]	20	**408** (100), 424
G20	Glucotropaeolin-Glucolimnanthin/ Glucoaubrietin dimer	$C_{29}H_{39}N_2O_{19}S_4Na$	869.08494	$[2M-2H+Na]^-$	869[c]	20	**408** (100), 438
G21	Glucolepigramin/ Glucosinalbin dimer	$C_{28}H_{37}N_2O_{20}S_4Na$	871.06421	$[2M-2H+Na]^-$	871[a,b]	20	**424** (100), 408
G22	Glucotropaeolin-Glucolepigramin/ Glucosinalbin dimer	$C_{28}H_{37}N_2O_{19}S_4K$	871.04323	$[2M-2H+K]^-$	871[a,b]	20	**424** (100), 408
G23	Glucolepigramin/ Glucosinalbin- 3-hydroxy-4-methoxy glucosinolate dimer	$C_{29}H_{40}N_2O_{21}S_4$	879.09282	$[2M-H]^-$	879[a,b]	20	**424** (100)
G24	Glucolepigramin/ Glucosinalbin dimer	$C_{28}H_{37}N_2O_{20}S_4K$	887.03814	$[2M-2H+K]^-$	887[a,b]	20	**424** (100)
			Glycosylated ABGs and dABGs				
A1	β-D-glucose-ABG & Glucolepigramin/ Glucosinalbin adduct	$C_{21}H_{25}NO_{12}$	482.12985	$[M-H]^-$/ $[M-2H+2H_2O+Na]^-$	482[d]	20	**446** (100), 424, 326, 284, 250, 164
A2	β-D-glucose-4-hydroxy-dABG &	$C_{21}H_{27}NO_{12}$	484.14550	$[M-H]^-$	484[d]	20	**446** (100), 284, 424, 250

	Glucolepigramin/ Glucosinalbin adduct						
A3	Unknown	-	-	-	492[a,b]	20	**446** (100), 284, 250
A4	β-D-glucose-methyl-ABG	$C_{22}H_{27}NO_{12}$	496.14550	$[M-H]^-$	496[c]	20	**438** (100), 446, 268
A5	β-D-glucose-dneoABG/ β-D-glucose-4-methoxy-dABG	$C_{22}H_{29}NO_{12}$	498.09781	$[M-H]^-$	498	20	**462** (100), 424, 438, 446
A6	Unknown	-	-	-	508[a,b]	20	**424** (100), 446, 284, 250, 164
			Brassicaceae Fatty Acids				
FA1	Palmitic acid	$C_{16}H_{32}O_2$	255.23241	$[FA(16:0)-H]^-$	255[d]	30	**211** (100), 237
FA2	α/γ-Linolenic acid	$C_{18}H_{32}O_2$	277.21676	$[FA(18:3)-H]^-$	277[d]	30	**233** (100), 259
FA3	Linoleic acid	$C_{18}H_{30}O_2$	279.23240	$[FA(18:2)-H]^-$	279[d]	30	**235** (100), 261
FA4	Oleic acid	$C_{18}H_{34}O_2$	281.24806	$[FA(18:1)-H]^-$	281[d]	30	**237** (100), 263
FA5	Stearic acid	$C_{18}H_{36}O_2$	283.26371	$[FA(18:0)-H]^-$	283[d]	30	**239** (100), 265
FA6	Hydroxy Linolenic acid	$C_{18}H_{30}O_3$	293.21167	$[FA(18:2)OH-H]^-$	293[d]	30	**235** (100), 275, 249
FA7	Hydroxy α/γ-Linoleic acid	$C_{18}H_{32}O_3$	295.22732	$[FA(18:3)OH-H]^-$	295[d]	30	**237** (100), 251
FA8	Dihydroxy Linolenic acid	$C_{18}H_{30}O_4$	309.20659	$[FA(18:3)(OH)_2-H]^-$	309[d]	-	nd
FA9	Dihydroxy Linoleic acid	$C_{18}H_{32}O_4$	311.22223	$[FA(18:2)(OH)_2-H]^-$	311[d]	35	**223** (100), 275, 183, 235, 253, 293

Glucosinolates found in red[a], black[b] Maca (*L.meyenii*) seeds, Maca root powder[c] and all natural products[d].
Bold illustrates the primary fragment ion at 100% relative intensity in brackets.
nd = not detected.

Aromatic glucosinolates were the most abundant precursors in red and black Maca (*L. peruvianum)* seeds. Glucolepigramin/Glucosinalbin (3- and 4-hydroxy benzyl glucosinolate), of *m/z* 424, Glucolimnanthin/Glucoaubrietin (3/4-methoxy benzyl glucosinolate) of *m/z* 438, Glucotropaeolin (benzyl glucosinolate) of *m/z* 408, and 3-hydroxy-4-methoxy benzyl glucosinolate (*m/z* 454) were found (Figure 3.3). Three tentatively identified indoyl glucosinolates such as 4-methoxy-Glucobrassicin/Neoglucobrassicin (*m/z* 477), 4-hydroxy-Glucobrassicin (*m/z* 463) and hydroxy-methoxy Glucobrassicin (*m/z* 493) were also found in red and black Maca seeds.

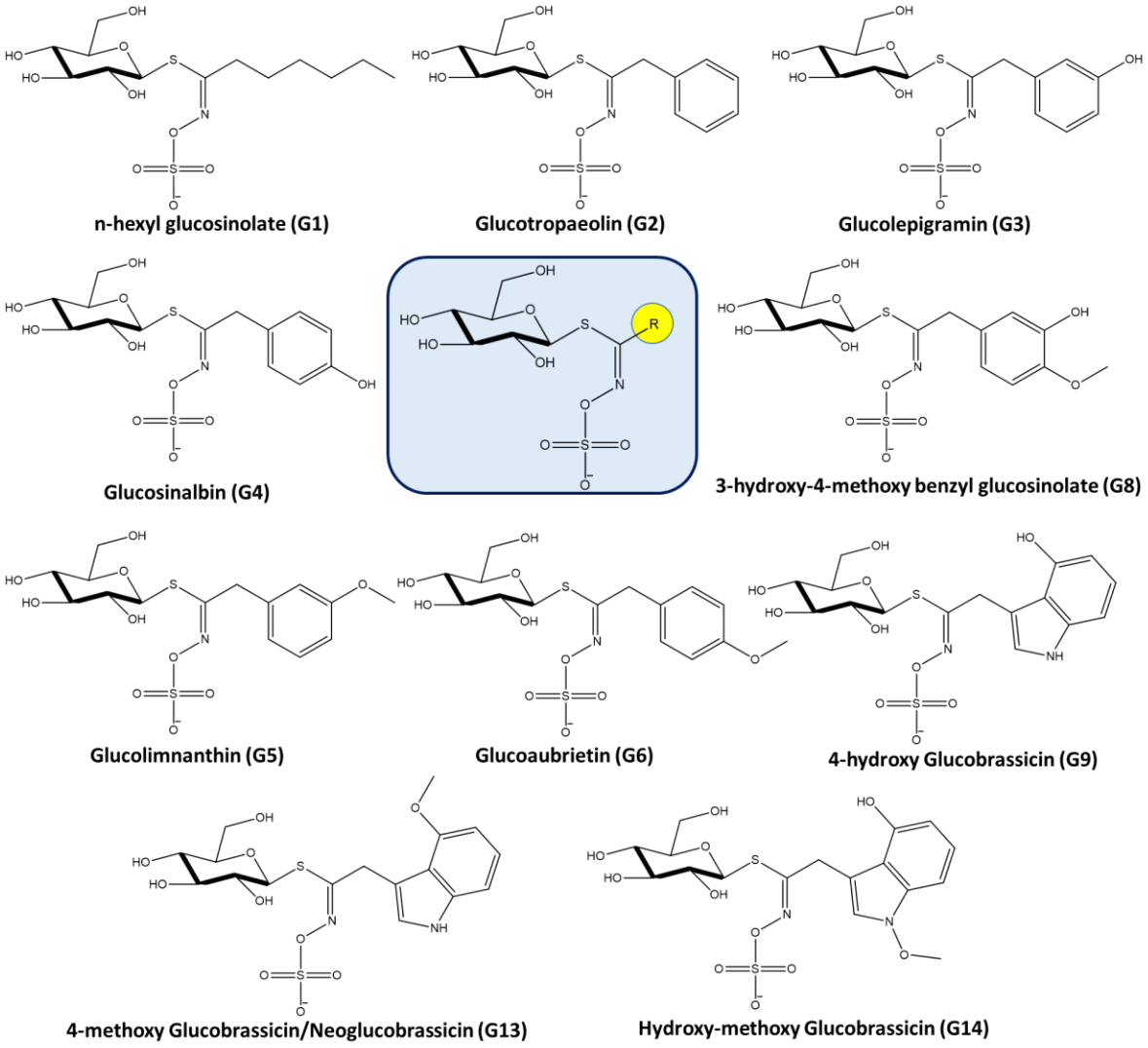

Figure 3.3: Aromatic, indoyl, and aliphatic glucosinolates in red and black Maca (*L. peruvianum*) seeds.

In Maca (*L. meyenii*) root powder, Glucotropaeolin (*m/z* 408) was the most abundant ion followed by Glucolimnanthin/Glucoaubrietin (*m/z* 438), and hydroxy-methoxy Glucobrassicin (*m/z* 493), and Glucolepigramin/Glucosinalbin (*m/z* 424). Two unknown glucosinolates of *m/z* 466 and *m/z* 468 were identified in Maca root powder but not in seeds, whereas 3-hydroxy-4-methoxy benzyl glucosinolate (*m/z* 454) and 4-hydroxy-Glucobrassicin (*m/z* 463) were observed in seeds but not in root powder. The separation of glucosinolates was performed by HPTLC developed with BnOH:EtOH (7:3 v/v) coupled to (-)DESI-MS analysis (Figure 3.4 and Table 3.2). In seeds, aromatic, indoyl and aliphatic glucosinolates showed good separations, for example, the retention factors (R_f) of Glucotropaeolin (t_r= 2.41), 4-hydroxy-Glucobrassicin (t_r= 1.47) and n-hexyl glucosinolate (t_r= 3.15 min) were 0.53, 0.32, and 0.68, respectively.

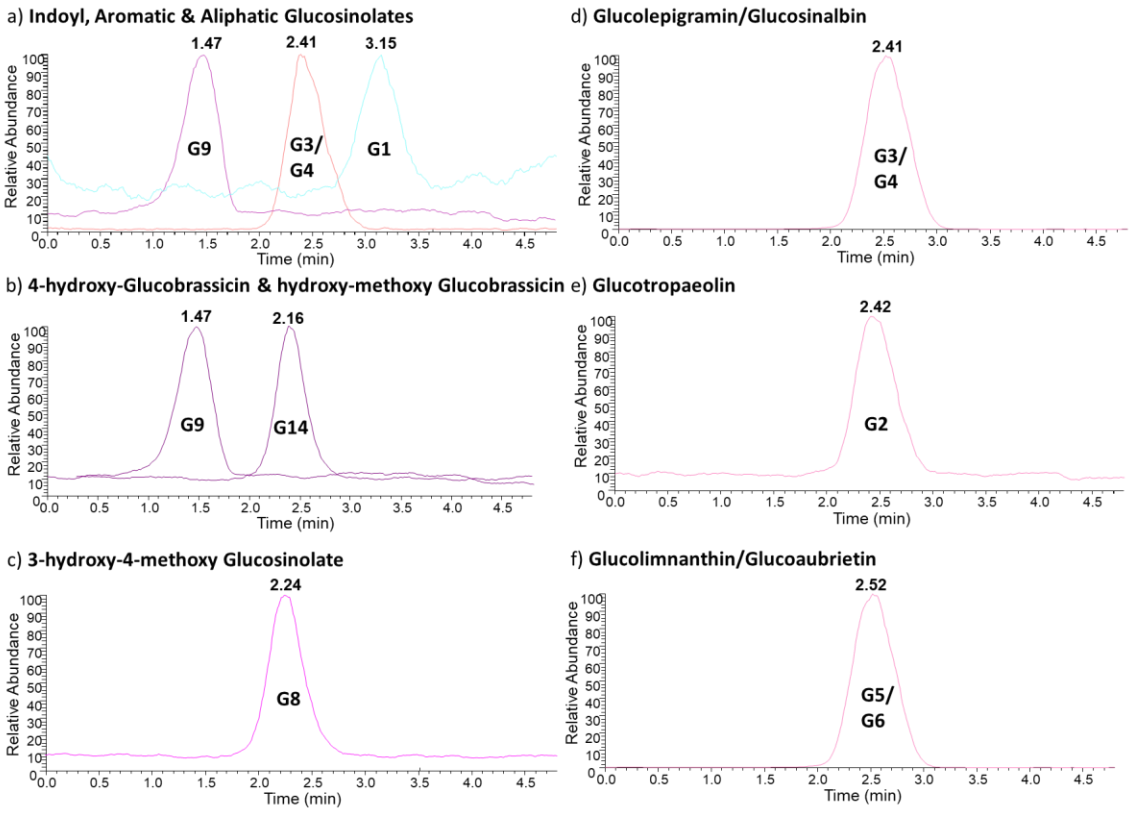

Figure 3.4: The separation of intact glucosinolates from the hydromethanolic extract of red Maca (*L. peruvianum*) seeds with BnOH:EtOH (7:3) v/v and ACN as the DESI solvent. a) The superimposed extracted ion chromatograms of indoyl (4-hydroxy-Glucobrassicin), aromatic (Glucolepigramin/Glucosinalbin) and aliphatic (n-hexyl glucosinolate) glucosinolates. b) 4-hydroxy-Glucobrassicin (*m/z* 463) and hydroxy-methoxy Glucobrassicin (*m/z* 493). c) 3-hydroxy-4-methoxy

glucosinolate (*m/z* 454). d) Glucolepigramin/Glucosinalbin (*m/z* 424). e) Glucotropaeolin (*m/z* 408). f) Glucolimnanthin/Glucoaubrietin (*m/z* 438).

Table 3.2: The Separation of Glucosinolates in Red Maca (*L. peruvianum*) Seeds Analyzed by HPTLC-DESI-MS in Negative Ion Mode.

Metabolite	**Chemical Formula**	**Ion (*m/z*)**	**Type of Ion**	**t_r (min)**	**R_f**
n-hexyl Glucosinolate	$C_{13}H_{24}NO_9S_2$	402	$[M-H]^-$	3.15	0.68
Glucotropaeolin	$C_{14}H_{18}NO_9S_2$	408	$[M-H]^-$	2.42	0.53
Glucolepigramin / Glucosinalbin	$C_{14}H_{18}O_{10}NS_2$	424	$[M-H]^-$	2.41	0.52
Glucolimnanthin / Glucoaubrietin	$C_{15}H_{20}NO_{10}S_2$	438	$[M-H]^-$	2.52	0.55
3-hydroxy-4-methoxy benzyl glucosinolate	$C_{14}H_{18}NO_{11}S_2$	454	$[M-H]^-$	2.24	0.48
4-hydroxy Glucobrassicin	$C_{16}H_{19}N_2O_{10}S_2$	463	$[M-H]^-$	1.47	0.32
Hydroxy-methoxy Glucobrassicin	$C_{17}H_{21}NO_{11}S_2$	493	$[M-H]^-$	2.16	0.46

Many studies report aromatic glucosinolates as the main compounds in fresh and dried Maca (*L. meyenii*) hypocotyls and roots, in which Glucotropaeolin, exhibits the highest concentration among all other glucosinolates.[107,126-128] In the seeds, Glucolepigramin/Glucosinalbin (*m/z* 424) rather than Glucotropaeolin (*m/z* 408) were the most predominant precursors. These findings may suggest that Gluclopigramin/Glucosinlabin at some point in the plant's lifecycle becomes depleted due to its consumption as a precursor in the production of other secondary metabolites and so, low contents are observed later on in mature hypocotyls and roots. For this reason, Glucolepigramin/Glucosinalbin may play a major role as precursors in biosynthetic pathways of other secondary metabolites, since these compounds are the most abundant in Maca seeds.

3.4.2. MS^2 Fragmentation Pattern of Aromatic Glucosinolates

The MS^2 fragmentation pathway of aromatic glucosinolates were investigated by HPTLC-(-)DESI-MS/MS as shown in Figure 3.5 and Figure 3.6.A. As an example, the fragmentation of Glucolimnanthin/Gucosinalbin (*m/z* 424) $[C_{14}H_{19}O_{10}NS_2\text{-}H]^-$ formed a total of 10 characteristic fragments (a-j) in the MS^2 spectrum. Fragment ions a, b and e were formed through intramolecular rearrangements. The a and b-type ion of *m/z* 259 $[C_6H_{12}O_9S\text{-}H]^-$ and *m/z* 275 $[C_6H_{12}O_8S_2\text{-}H]^-$ were generated by the cleavage, and then the transfer of the sulfate $[SO_4]^-$ and sulfite $[SO_3]^{2-}$ group to the β-D-glucose and β-D-thioglucose moiety, respectively. The e-type ion of *m/z* 291, $[C_6H_{12}O_9S_2\text{-}H]^-$, is the cleavage and transfer of the sulfate $[SO_4]^-$ group to β-D-thioglucose group. The subsequent loss of H_2O (-18 Da) from ion a, generated the h ion of *m/z* 241 $[C_6H_{10}O_8S\text{-}H]^-$. The f-type ion of *m/z* 212 $[C_8H_7O_4NS\text{-}H]^-$ was formed by the neutral loss of the β-D-thioglucose moiety, $C_6H_{12}O_5S$ (-196 Da), while the g-type ion (*m/z* 195) was assigned as the negatively charged β-D-thioglucose ion. c and d-type fragments of *m/z* 328 $[C_{14}H_{19}O_6NS\text{-}H]^-$ and *m/z* 166 $[C_8H_9ONS\text{-}H]^-$ were assigned as the loss of SO_3 (-80 Da) and the subsequent loss of the β-D-glucose moiety, $C_6H_{10}O_5$ (-162 Da) as shown in Figure 3.6.A. d-type ions in the MS^2 can elucidate the substitutions, such as hydroxy (-OH) and methoxy ($-OCH_3$), attached to the benzyl ring, therefore, R groups can be elucidated based on these diagnostic ions in unknown glucosinolates. Lastly, the i-type ion was assigned as the loss of $C_6H_{10}O_6$ (-178 Da) and the h-type ion as the loss of H_2O (-18 Da) from the β-D-thioglucose group to form the dehydrated glucosinolate molecule.

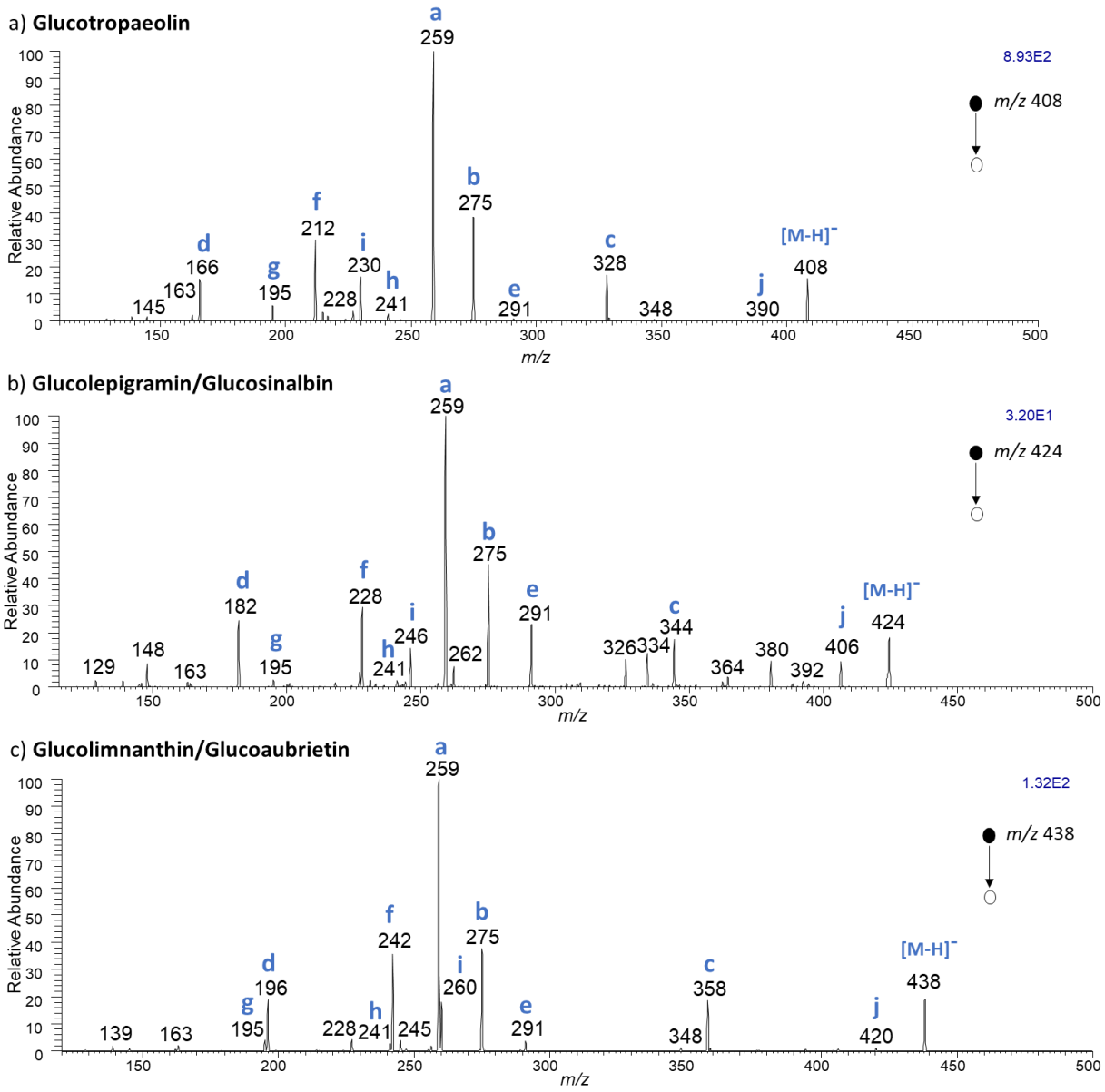

Figure 3.5: HPTLC-(-)DESI-MS^2 profiles of intact glucosinolates from the hydromethanolic extract of red Maca (*L. peruvianum*) seeds via CID. a) Glucotropaeolin (*m/z* 408) using 30 as the collision energy. b) Glucolepigramin/Glucosinalbin (*m/z* 424) using 30 as the collision energy. c) Glucolimnanthin/Glucoaubrietin (*m/z* 438) using 30 as the collision energy.

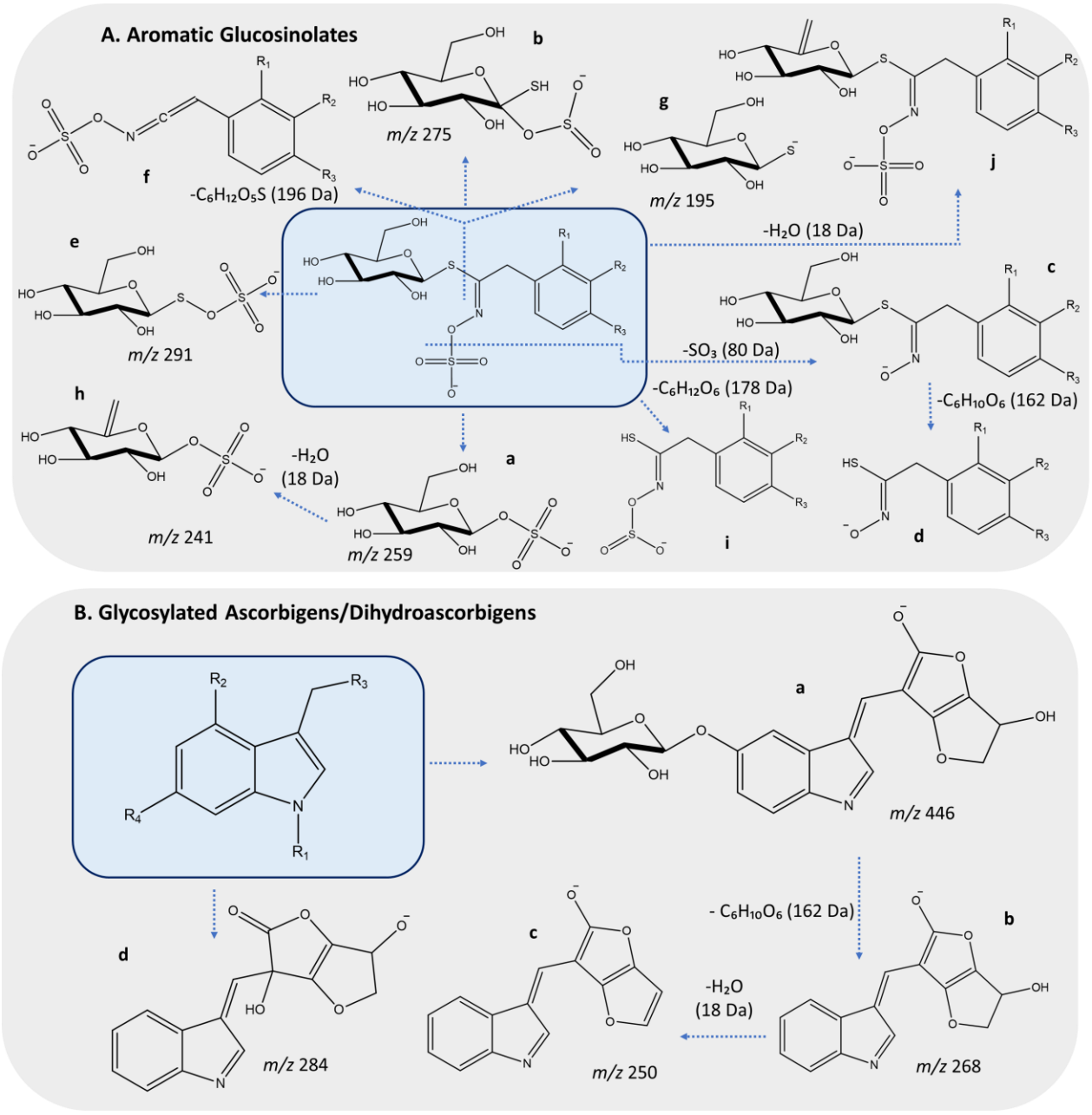

Figure 3.6: The DESI-MS^2 fragmentation pathway of bioactive secondary metabolites in Maca (L.peruvianum). A. Aromatic Glucosinolates. B. Glycosylated Ascorbigens/Dihydroascorbigens.

3.4.3. Comparison of Glucosinolates in Red and Black Maca (*L.peruvianum*) Seeds

In red and black Maca seeds, only minor differences in the relative abundances of glucosinolates were found rather than different metabolites. The relative abundances for major constituents such as Glucolepigramin/Glucosinalbin (*m/z* 424), Glucolimnanthin/Glucoaubrietin (*m/z* 438), Glucotropaeolin (*m/z* 408), and 3-hydroxy-4-methoxy benzyl glucosinolate (*m/z* 454) were similar in both phenotypes (Figure 3.2). A study by Meissner and coworkers reported similar findings, glucosinolate contents in fresh red and black Maca hypocotyls were not significantly different, but glucosinolate contents were nearly ten times higher in red and black compared to yellow.[126] In fresh and dried hypocotyls, the authors also found that, Glucotropaeolin, showed the highest concentration. Interestingly, in dried hypocotyls, significantly higher glucosinolate contents were detected in red Maca compared to black and yellow phenotypes.[126]

Yellow, red and black Maca phenotypes show clear differences in biological activities which has been suggested as a result of the proportion of secondary metabolites.[105,129,130] For example, red Maca (*L. meyenii*), but not black and yellow varieties, prevented testosterone enanthate induced prostatic hyperplasia in normal and treated rats.[131] Black maca (*L. meyenii*) extracts enhanced cognitive function by improving memory and learning, in ovariectomized mice and in scopolamine-induced memory impaired mice, compared to red and yellow types.[108,132,133] Black, and in minor proportion yellow Maca, are responsible in increasing spermatogenesis such as sperm count and motility in rats, whereas red Maca had no effect.[134] In this study, the chemical constituents in red and black seeds did not show major differences. These findings support the hypothesis that different ratios of bioactive secondary metabolites may lead to different biological activities as part of a more complex synergistic mode of action as secondary metabolites begin to diverge in later stages of development. As opposed to the presence of diverse metabolites in Maca phenotypes responsible for the differences in biological activities.

3.4.4. Glycosylated Ascorbigens and Dihydroascorbigens

Glycosylation of ascorbigens, other than indole ABGs, are widespread in cruciferous vegetables in *Brassica* species including ascorbigen, 4-hydroxyascorbigen, 4-methoxyascorbigen, and (the N-methoxy derivative) neoascorbigen.[135] However, only a few studies report the presence of glycosylated indole ABG in plants.[136] In Maca (*L.peruvianum*) seeds, we report for the first time six tentatively identified, glycosylated ascorbigens (ABGs) and dihydroascorbigens (dABGs) as potential plant antibiotics, phytoanticipins, typically biosynthesized in plants before pathogenic infection (Figure 3.6. B. and Figure 3.7).[136,137] β-D-glucose-ABG (*m/z* 482), β-D-glucose-4-hydroxy-dABG (*m/z* 484), β-D-glucose-N-methyl ABG (*m/z* 496), β-D-glucose-neodABG/β-D-glucose-4-methoxy-dABG (*m/z* 498) and two unknown compounds of *m/z* 492 and *m/z* 508 were identified based on their MS^2 fragmentation pattern (Figure 3.8).

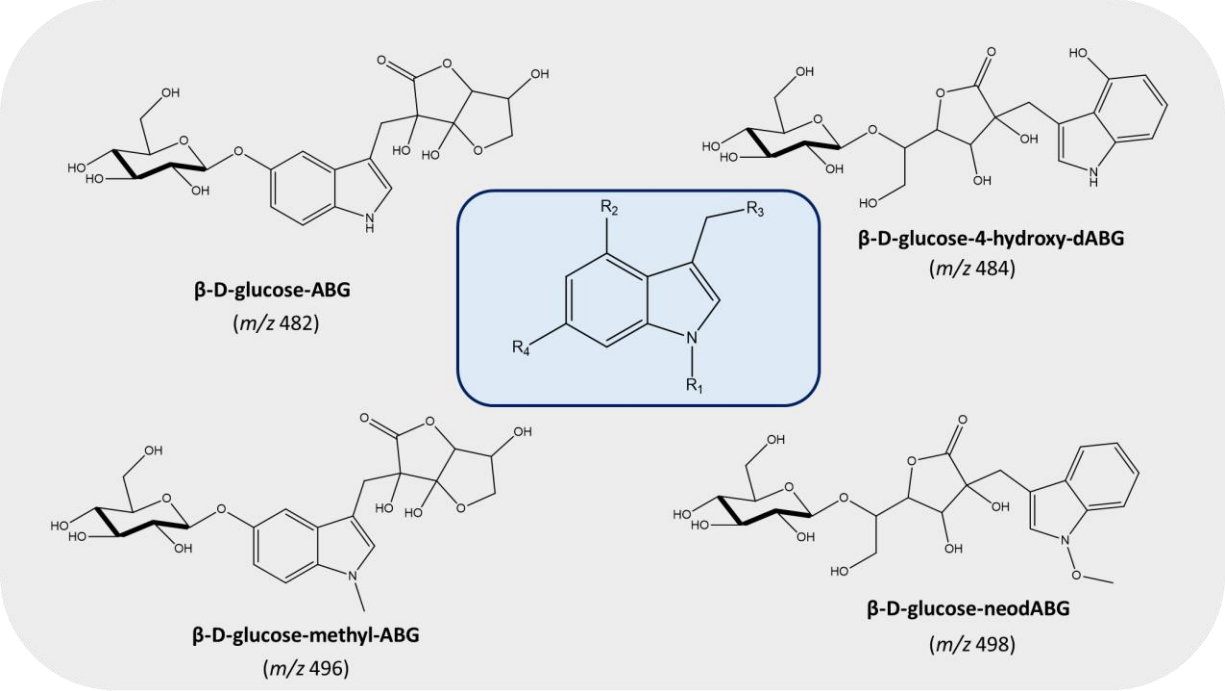

Figure 3.7: Glycosylated ABGs/dABGs in red and black Maca (*L. peruvianum*) seeds.

Glycosylated ABGs and dABGs revealed four major fragment ions (a-d). The a-type fragment was identified as the glycosylated ABG ion with the loss of the R_1 and R_2 substituents and cleavage of one hydroxyl group (-OH) from the ABG ion (*m/z* 446). Interestingly, dABGs and ABGs resulted in the same fragmentation pattern suggesting that dABGs undergo cyclization resulting in the ring closure of dABG to ABG to form the a-type ion. The b-type fragment is the deglycosylated ABG ion from the loss of the β-D-glucose moiety (-162 Da) and the further loss of water (-H_2O) in the c-type ion. The d-type ion (*m/z* 284) was formed from the loss of β-D-glucose (-162 Da) and losses of the R_1 and R_2 substituents. In this study, the position of the β-D-glucose moiety in dABGs and ABGs is unknown, however, previous nuclear magnetic resonance (NMR) studies report the β-D-glucose moiety bonded to the 5-O position in dABGs (e.g. 5-O-β-D-glucose-dihydroneoABG) and bonded to the 6-C of the indole substituent in ABGs (e.g. 6-β-D-glucose-ABG).[136]

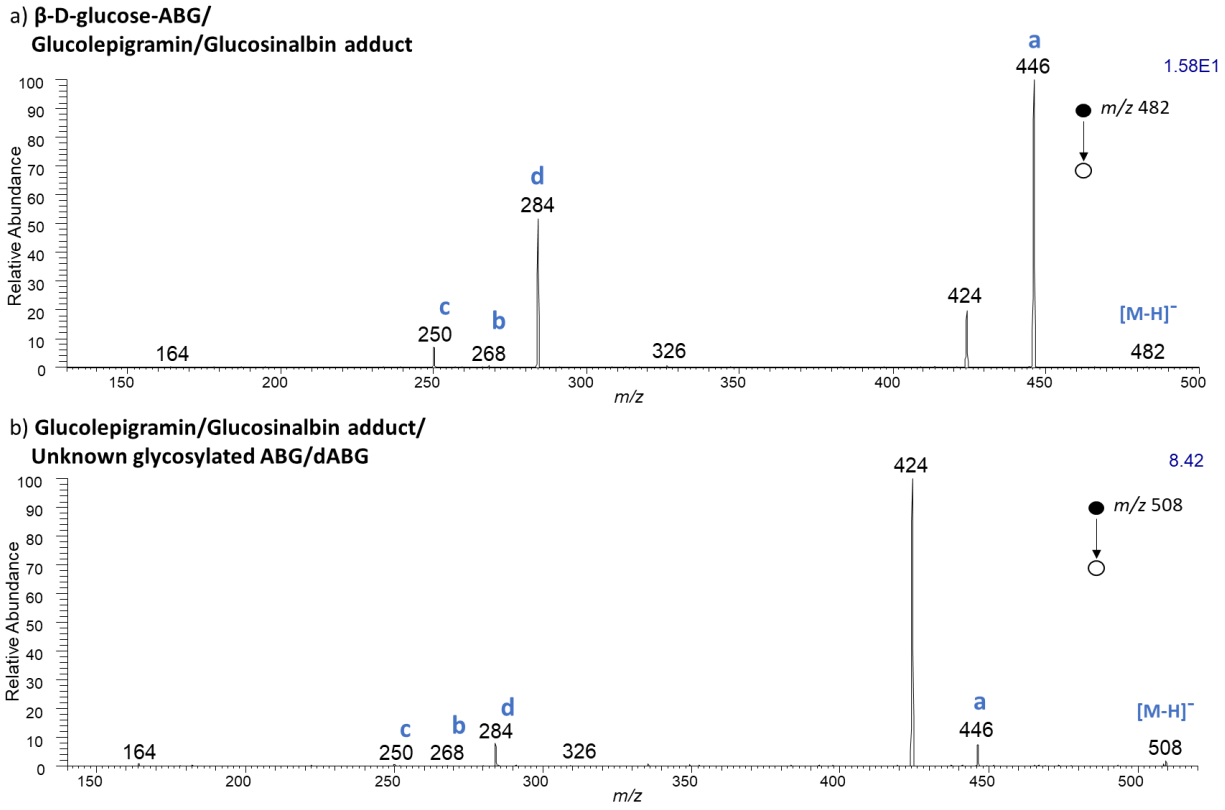

Figure 3.8: Glycosylated ABGs/dABGs fragmented by HPTLC-(-)DESI-MS/MS via CID from the hydromethanolic extracts of red Maca (*L. peruvianum*) seeds. a) β-D-glucose-ABG and Glucolepigramin/Glucosinalbin adduct (*m/z* 482) using 20 as the collision energy. b)

Glucolepigramin/Glucosinalbin adduct and an unknown glycosylated ABG/dABG (*m/z* 508) using 20 as the collision energy.

3.4.5. Brassicaceae Fatty Acids

FAs are important precursors in the biosynthesis of alkamides (macamides and macaenes). Alkamides are Maca biomarkers as these bioactive secondary metabolites have not been found in any other plant. Benzyl amine and fatty acid buildup during traditional open-field or industrial postharvest drying promotes the amide condensation between benzyl amine and saturated/unsaturated FAs to biosynthesize macamides and macaenes, respectively, and do not occur in intact fresh plant tissues.[138] A series of benzylalkamides exhibit moderate FAAH inhibitory activity with potential neuroprotective, analgesic and anti-inflammatory properties by modulating the release of neurotransmitters.[113,139]

For the first time, we implemented a novel RPTLC-(-)DESI-MS method using ACN:H_2O (8:2) v/v as the DESI solvent for free fatty acids isolated from the $CHCl_3$ extract of Maca (*L. meyenii*) seeds and root powder (Figure 3.9). The C_{18} functionalized RPTLC surface allows the desorption and ionization of amphiphilic and hydrophobic molecules with higher sensitivity and specificity than silica TLC. Mixtures of polar aprotic solvents with small fractions of polar protic solvents (e.g. ACN:H_2O 8:2 (v/v) targets the desorption and ionization of amphiphilic fatty acids without the interference of easily ionized and highly polar constituents. In silica TLC, it can be challenging to detect hydrophobic molecules due to low solubilities in polar/aqueous DESI solvents (MeOH, ACN, MeOH/H_2O), lower ionization efficiencies and ion suppression as a result of competing with more easily ionized polar molecules. One of the advantages of RPTLC is that it avoids non-aqueous/non-polar solvents (e.g. toluene, tetrahydrofuran, $CHCl_3$, etc.,) typically added into the DESI analysis to solubilize and desorb hydrophobic compounds from paper and Teflon surfaces.[140] Moreover, the separation of hydrophobic analytes prior to DESI-MS analyses by RPTLC, rather than HPTLC, offers a targeted and reproducible approach. In RPTLC, the hydrophobic interactions between hydrophobic analytes and the C_{18} functionalized surface, facilitates their separation by partitioning with common polar (aprotic/protic) mobile phases (e.g.

ACN/MeOH). In contrast, it is much more challenging to separate hydrophobic analytes by normal phase silica TLC, where the fractions of non-polar/polar binary mobile phase systems (e.g. EtOAc/Hex), and in certain circumstances, more complex ternary systems need to be probed to find the appropriate solvent polarity to drive the separation between hydrophobic compounds.

In Maca seeds, a total of 9 unsaturated/saturated FAs such as palmitic acid $[FA(16:0)-H]^-$ (*m/z* 255), linoleic acid $[FA\ (18:3)-H]^-$ (*m/z* 277), α/γ-linolenic acid $[FA\ (18:2)-H]^-$ (*m/z* 279), oleic acid $[FA(18:1)-H]^-$ (*m/z* 281) and stearic acid $[FA(18:0)-H]^-$ (*m/z* 283) were identified by MS/MS (Table 3.1). In seeds, α/γ-linolenic acid was the most abundant FA, similar to other studies, the highest free FA content was indeed, linoleic and linolenic acid, in Maca (*L. meyenii)* found in hypocotyl and root.[138,141] Four hydroxylated FAs were tentatively identified as hydroxy-linolenic acid $[FA(18:3)OH-H]^-$ (*m/z* 293), hydroxy-linoleic acid $[FA(18:2)OH-H]^-$ (*m/z* 295), dihydroxy-linolenic acid $[FA(18:3)(OH)_2-H]^-$ (*m/z* 309), and dihydroxy-linoleic acid $[FA(18:2)(OH)_2-H]$ (*m/z* 311). Interestingly, these hydroxylated FAs have also been reported in the turnip *Brassica campestris* L. var *oleifera* of the Brassicaceae family.[142]

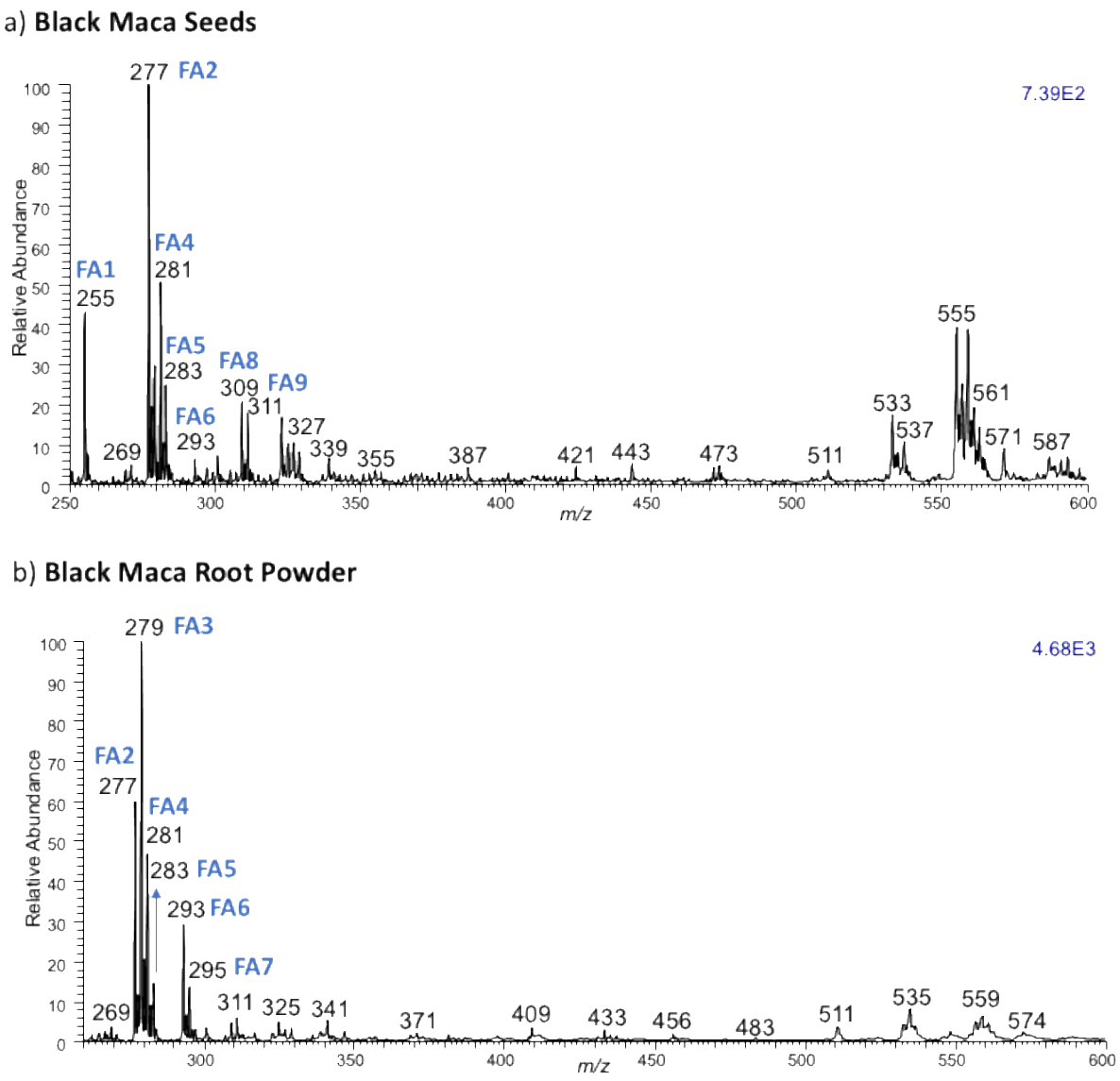

Figure 3.9: C_{18} functionalized RPTLC coupled to (-)DESI-MS for the analysis of Brassicaceae fatty acids from the $CHCl_3$ extract of Maca (*L. meyenii*) using ACN:H_2O (8:2) v/v as the DESI solvent from a) Black Maca seeds. b) Black Maca root lyophilized powder.

3.4.6. Imidazole Alkaloids

Imizadole alkaloids are phytochemicals with anti-microbial, anti-cancer activity and protection against cytotoxicity.[143-145] Lepidiline A and B[143], and Lepidiline C and D[146], were first isolated from dried and fresh Maca (*L. meyenii*) roots. As expected, we did not detect imidazole alkaloids in extracts of red and black Maca seeds, as these secondary metabolites are most likely biosynthesized in later stages of development. Imidazole alkaloids were detected from the $CHCl_3$ extract of Maca (*L.meyenii*) root powder and directly from Maca tinctures (Figure 3.10). Imidazole alkaloids were characterized and separated by HPTLC-(+)DESI-MS with Ace:Ben:H_2O (7:2:1) v/v (Figure 3.11 and Table 3.3). Lepidiline A $[M]^+$, B $[M]^+$, C $[M]^+$, and D $[M]^+$ of *m/z* 277, *m/z* 291, *m/z* 307 and *m/z* 321 and the proposed MS^2 fragmentation pathway can be found in Figure 3.12.B. The presence of three other minor imidazole alkaloids was observed such as 1,3-dibenzyl-2-butyl-4,5-dimethylimidazolium $[M]^+$, 1,3-dibenzyl-2-pentyl-4,5-dimethylimidazolium $[M]^+$, and 1,3-dibenzyl-2-phenyl-4,5-dimethylimidazolium $[M]^+$ of *m/z* 333, *m/z* 347 and *m/z* 353, respectively.

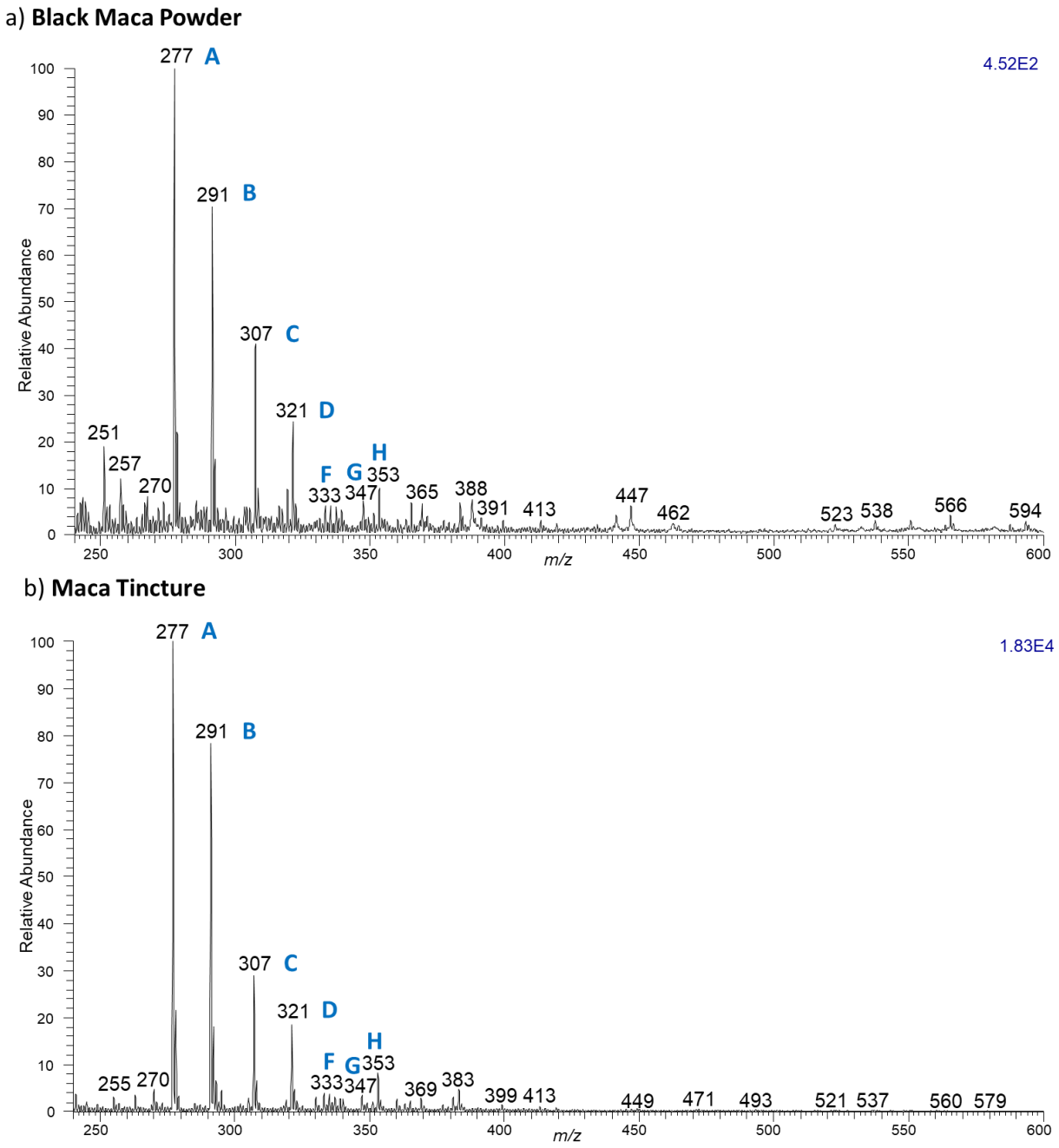

Figure 3.10: The HPTLC-(+)DESI-MS spectra of imidazole alkaloids using ACN as the solvent in the mass range of *m/z* 240-600 extracted from a) The $CHCl_3$ extract of black Maca (*L. meyenii*) root lyophilized powder and b) Directly from Maca root tinctures.

Table 3.3: Imidazole Alkaloids in Black Maca (*L. meyenii*) Root Powder and Tinctures Analyzed by HPTLC-DESI-MS in Positive Ion Mode.

N°	Tentative Metabolite	Ion Chemical Formula	Exact mass	Type of Ion	Observed Ion (*m/z*)	CID (%)	MS/MS Fragment Ions	R group
				Imidazole Alkaloids				
A	Lepidiline A	$C_{19}H_{21}N_2$	277.17047	$[M]^+$	277	30	**185** (100), 91, 109, 181, 199	R_1= H, R_2= H
B	Lepidiline B	$C_{20}H_{23}N_2$	291.18612	$[M]^+$	291	30	**199** (100), 91, 200, 158, 250, 205, 213, 109	R_1= CH_3, R_2= H
C	Lepidiline C	$C_{20}H_{23}N_2O$	307.18104	$[M]^+$	307	25	**121** (100), 185, 215, 109, 229, 275, 109, 105	R_1= H, R_2= OCH_3
D	Lepidiline D	$C_{21}H_{25}N_2O$	321.19669	$[M]^+$	321	25	**121** (100), 199, 229, 230, 91, 289, 243, 109	R_1= CH_3,R_2=OCH_3
E	1, 3-dibenzyl-2-butyl-4,5-dimethylimidazilium	$C_{23}H_{29}N_2$	333.23307	$[M]^+$	333	25	**242** (100), 185, 109	R_1= $(CH_2)_3CH_3$, R_2= H
F	1, 3-dibenzyl-2-pentyl-4, 5-dimethylimidazilium	$C_{24}H_{31}N_2$	347.24872	$[M]^+$	347	25	**256** (100), 185	R_1= $(CH_2)_4CH_3$, R_2= H
G	1, 3-dibenzyl-2-phenyl-4, 5-dimethylimidazilium	$C_{25}H_{25}N_2$	353.20177	$[M]^+$	353	25	**262** (100), 185	R_1= C_6H_6, R_2= H

Bold illustrates the primary fragment ion at 100% relative intensity in brackets.

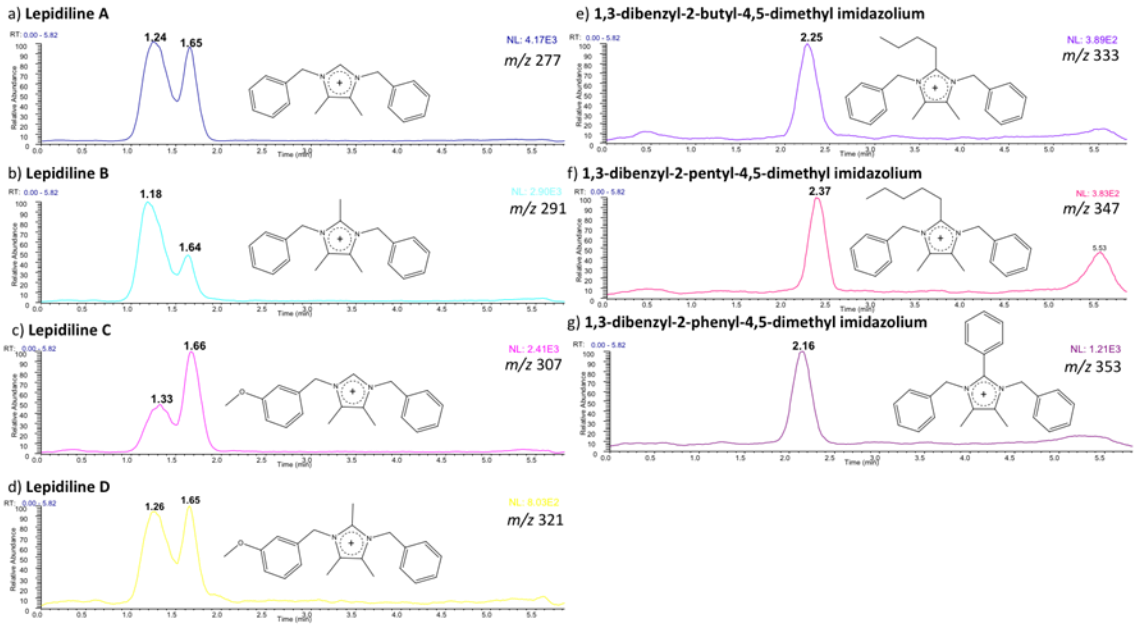

Figure 3.11: The separation of Lepidiline A-D and three minor imidazole alkaloids from the $CHCl_3$ extract of black Maca (*L. meyenii*) lyophilized root powder with Ace:Ben:H_2O (7:2:1) v/v.

3.4.7. MS^2 Fragmentation Pathway of Imidazole Alkaloids

The fragmentation of imidazole alkaloids generated a total of 9 characteristic fragment ions (a-i) (Figure 3.12.B). The most predominant MS^2 fragmentation pathway for Lepidiline A-D were the a/b and c/d types, however, the a/b fragmentation pattern dominated over c/d. The general alkaloid structure presents a positively charged imidazole center with the R_1 substituent (-H, $-CH_3$) and two N-ethylbenzene rings A and B, with the R_2 substituent (-H, $-OCH_3$) *meta*-bonded to ring B. In Lepidiline A and B (R_2= H), ring A and B are identical and therefore, a/b, c/d and h/i, are essentially the same fragments cleaved from either side of the imidazole ring. The a-type fragment corresponds to the cleavage of the ethylbenzene ring A (-92 Da) in Lepidiline A (*m/z* 185) and B (*m/z* 199), and the methoxy (R_2=OCH_3) substituted ethylbenzene ring A (-122 Da) in Lepidiline C (*m/z* 215) and D (*m/z* 229). The c-type ion arises from the loss of the ethylbenzene ring B (-92 Da). The b-type fragment was identified as the positively charged, hydrogen (R_1=H) substituted in Lepidine A, B of *m/z* 91 or methoxy (R_1=OCH_3) substituted ethylbenzene ring A in Lepidine C, D of *m/z* 121. The positively charged ethylbenzene ring B (*m/z* 91) was assigned as

the d-type ion cleaved from all four alkaloids. Only Lepidiline C and D presented e-type ions as the loss of the R_2 methoxy (-OCH_3) substituent from ring A (-32 Da). In Lepidiline A and B, the g-type ion (*m/z* 109) was identified as the positively charged imidazole center from the simultaneous cleavage of rings A and B. In Lepidiline C and D, the ion of *m/z* 109, can arise from both f and g-type ions, whereby the f-type ion was linked to the loss of the methoxy (-OCH_3) substituted ethylbenzene ring A. The h and i-type fragments arise from the neutral loss of benzene (-78 Da) from ring A or B in Lepidine A and B, respectively, whereas only h-type ions are cleaved from ring B in Lepidiline C and D.

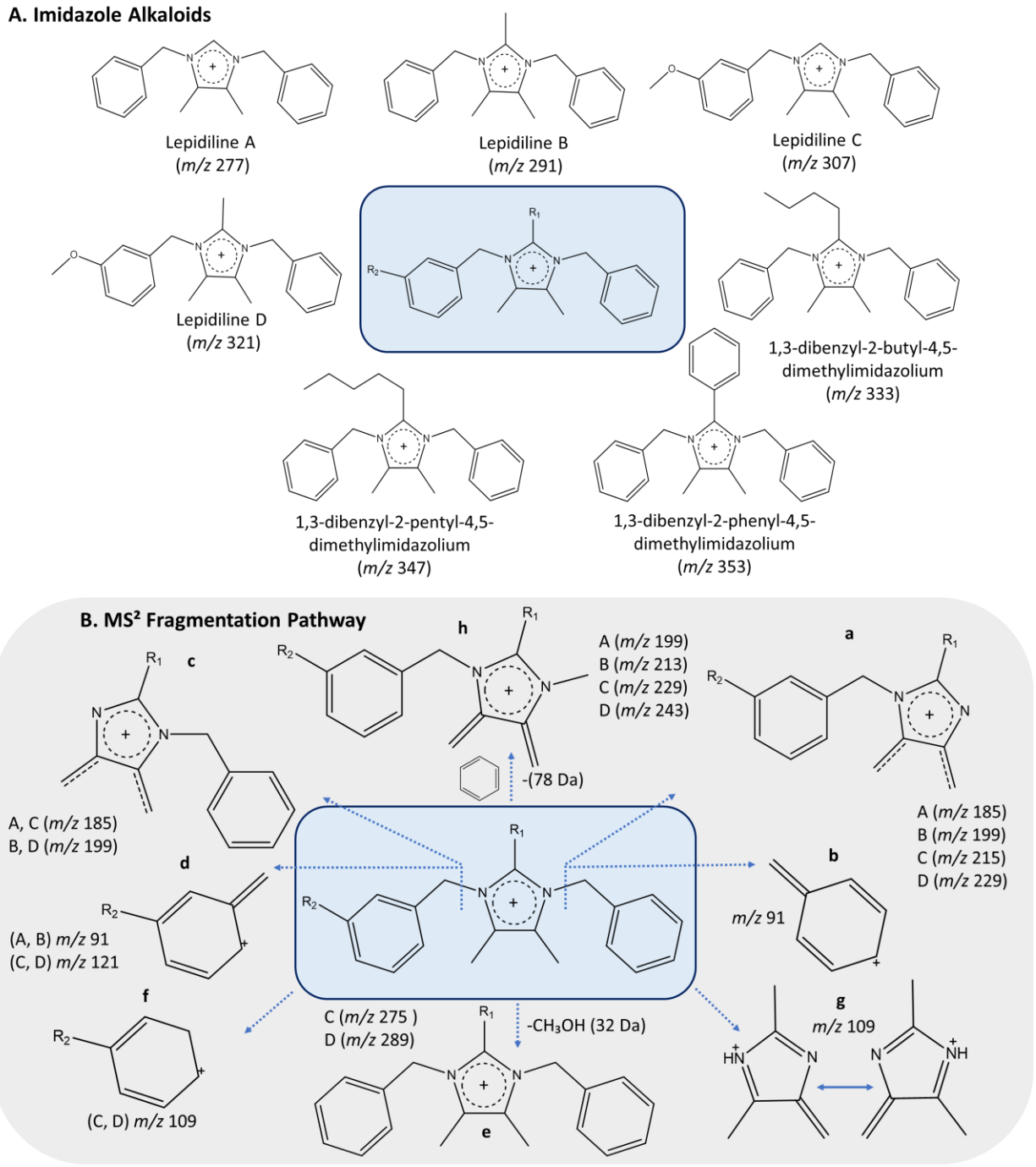

Figure 3.12: Imidazole alkaloids in Maca (*L. meyenii*) health supplements such as black Maca root lyophilized powder and Maca root tincture. B. MS^2 fragmentation pathway.

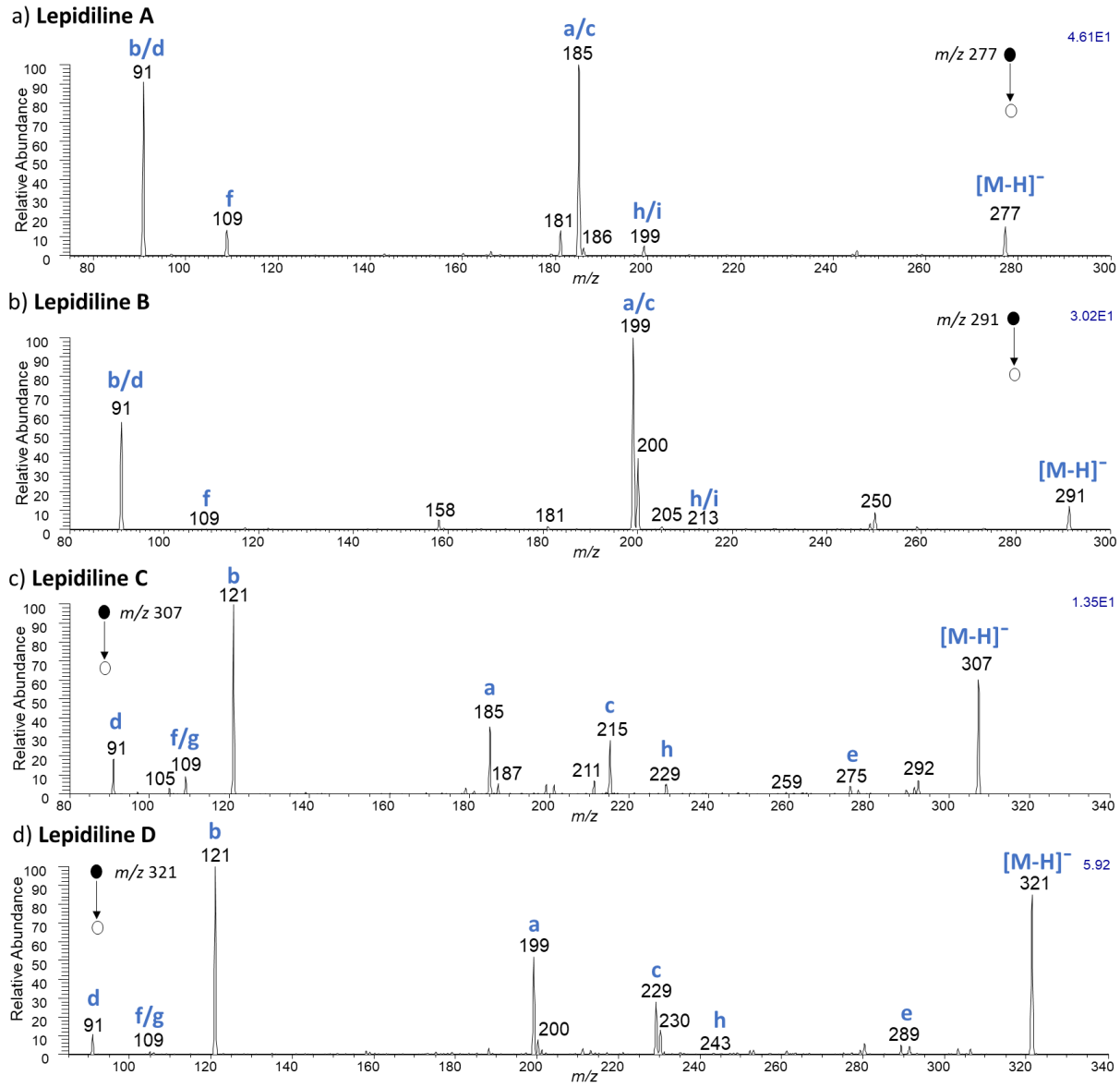

Figure 3.13: Imidazole alkaloids, Lepidiline A, B, C and D fragmented by HPTLC-(+)DESI-MS/MS via CID from $CHCl_3$ extracts of black Maca (*L. meyenii*) lyophilized root powder. a) Lepidiline A (*m/z* 277) using 30 as the collision energy. b) Lepidiline B (*m/z* 291) using 30 as the collision energy. c) Lepidiline C (*m/z* 307) using 25 as the collision energy. d) Lepidiline D (*m/z* 321) using 25 as the collision energy.

3.5. Conclusion

The main chemical constituents in red and black Maca (*L. peruvianum*) seeds were investigated in the first stage of development of the plant's lifecycle. We presented a rapid HPTLC-(-)DESI-MS method for the identification and separation of intact aromatic, indoyl and aliphatic type glucosinolates. Aromatic glucosinolates were the major secondary metabolites in red and black Maca (*L. peruvianum)* seeds, while indoyl and aliphatic glucosinolates were rather minor constituents. For the first time, we presented six tentatively identified ABGs and dABGs as potential phytoanticipins and developed a novel RPTLC-DESI-MS method for the identification of free FAs from Maca seeds and health supplements. By modifying the surface chemistry, such as using hydrophobic C_{18} functionalized TLC surfaces can expand the boundaries of polarity for the detection of hydrophobic compounds, not easily detected by DESI-MS. The reverse phase method completely avoids the need to supplement with non-aqueous/non-polar solvents (e.g. toluene, tetrohydrofuran, $CHCl_3$, etc.) to solubilize and desorb hydrophobic molecules as in silica TLC-DESI-MS. We foresee the application of RPTLC-DESI-MS based methods for hydrophobic plant metabolites such as terpenes, terpenoids, phytosterols, neutral lipids and waxes.

In future studies, we aim on elucidating the chemical constituents at different stages of development in Maca (*L. peruvianum*) phenotypes, as well as, quantify glucosinolates from plant tissues by HPTLC-DESI-MS with the high sensitivity and high accuracy approach such as, isotope dilution mass spectrometry (IDMS), as isotopically labelled reference standards become available. The IDMS method can make use of the four stable sulfur isotopes, ^{32}S (95.02%), ^{33}S (0.75%), ^{34}S (4.21%), and ^{36}S (0.02%) naturally present in glucosinolates. Mapping the spatial distribution of secondary metabolites (glucosinolates, alkaloids, thiohydantoins, fatty acids, flavonoids, phenolics, etc.,) in Maca roots, hypocotyls, and leaves by DESI-MS imaging revealing the metabolites produced through stages of plant development. These studies may indicate specific time points in the plant's lifecycle where the ratios of metabolites may begin to diverge in tissues to correlate between the metabolome of phenotypes to the diverse biological activities and medicinal properties.

Chapter Four: The Characterization and Spatial Distribution of Isoquinoline and Aporphine Alkaloids from *Sassafras Albidum* by HPTLC-DESI-MS^n and DESI-MS Imaging

Chapter 4 is a version of the published manuscript:

Sousa, R.C., **Perez, C.J**., Branco, A. Botura, M.B., Ifa, D.R. Identification of *Sassafras albidum* alkaloids by high-performance thin-layer chromatography tandem mass spectrometry and mapping by desorption electrospray ionization mass spectrometry imaging. *J. Mass Spectrom*. **2020. In print.**

4.1. Summary

Sassafras albidum is a tree species with distinctive aromatic characteristics that grows in North America. Mass spectrometry imaging has become an important tool in analysis of plants metabolites, uncovering important contributions with the functional role, biosynthetic pathways, and accumulation of compounds in plants. This work aimed to identify alkaloids present in *S. albidum* roots, twigs and leaves by HPTLC coupled to DESI-MS^n and to map the spatial distribution of these compounds by DESI-MSI. A total of twelve benzylisoquinoline and aporphine alkaloids in which six novel alkaloids were detected for the first time. In *S. albidum*, the alkaloids were characterized by investigating their fragmentation pattern by multistage mass spectrometry DESI-MS^n fragmented to MS^3-MS^7. A high number of alkaloids was found in *S. albidum* roots however, alkaloids were not detected in leaves. The spatial distribution of these phytochemicals was mapped by solvent and heat assisted TLC imprints of cross sections of roots and twigs and analyzed by DESI-MSI. The profile of alkaloid spatial distribution in DESI-MS images showed different accumulation patterns across and within different plant parts. Most alkaloids displayed higher intensities in the the outer-most layer of the roots and twigs. The spatial localization pattern of these alkaloids analyzed by DESI-MS imaging in diferent plant tissues could contribute to a better undestanding of the profile of localization, acummulation and biosynthesis of benzylisoquinoline and aporphine type alkaloids.

4.2. Introduction

Sassafras albidum is a medium-sized aromatic deciduous tree with distinctive leaf shapes that occurs in the Eastern regions of the United States and Southern Ontario.[147] The species is well known for the previous use of the root in the folk medicine and as food additive in soft drinks, such as root beer, but the use was banned in 1960 due to studies that indicated the carcinogenic potential of safrole, the main component of the root oil.[148] In recent years, the FDA has allowed the use of safrole-free extracts as food flavoring additive.[149] Other studies of the root

of *S. albidum* reported the presence of different metabolites, such as lignans, terpenoids and six isoquinoline alkaloids in root bark extracts.[150-152] The Lauraceae family is characterized by the presence of alkaloids as the main class of compounds with more than 300 isoquinoline alkaloids.[153] The chemical characterization of these alkaloids has great importance since many biological activities have been described as anti-nociceptive, anti-cholinesterase and anti-cancer.[154-156] *Sassafras albidum* is a tree species with distinctive aromatic characteristics and leaf shapes widely distributed in Eastern regions of the United States and Southern Ontario.[147,157] Previous studies of the root oil of *Sassafras albidum* reported metabolites such as a high content of safrole (85%), and the presence of lignans, terpenoids and isoquinoline alkaloids in root extracts.[150,158,159]

Ambient mass spectrometry has become significantly more widespread over the past few years due to many advantages of the technique such as minimal or no sample preparation prior to MS analysis.[8,11] DESI is one of the most prominent AMS techniques belonging to the spray based type of ambient ionization techniques. The process of ionization of the molecules present on the sample surface occurs upon the impact of electrosprayed charged droplets, these gaseous ions are transferred into the vacuum system and a mass spectrum similar to ESI is recorded.[11,160] Coupling HPTLC with DESI makes this an interesting alternative in the analyses of natural compounds of plant extracts, with a robust separation technique allied with high sensitivity, minimal sample treatment, high throughput and little molecular ion fragmentation in the analysis.[85,161] Several studies have applied HPTLC-DESI-MS to identify secondary metabolites to evaluate the quality and authenticity of natural products.[86,122,162]

Mass spectrometry imaging (MSI) is an analytical tool to visualize the spatial distribution of metabolites using common techniques, such as MALDI-MS and DESI-MS. The use of MSI allows the investigation of compounds to map their spatial distribution from the sample surface indirectly from TLC imprints or directly from plant tissues. In plant metabolomics, it helps to understand the spatial context of metabolite biosynthesis, accumulation and spatial localization.[119,163] DESI-MS-imaging has been used to describe the distribution of alkaloids, glycoalkaloids, glucosides and flavonoids in different plant tissues such as leaves, fruits, flower

and root.[33,37,164] Here, we report a HPLTC-DESI-MS method to separate and identify benzylisoquinoline and aporphine type alkaloids establishing an alternative approach to the conventional methods in separation and identification of bioactive secondary metabolites. In the face of the importance of isoquinoline alkaloids, the characterization of novel alkaloids in *Sassafras albidum* and their respective spatial distributions has significant impact in understanding the metabolic processes that regulate the accumulation, distribution, and biosynthesis of these compounds in the Lauraceae family.

4.3. Experimental

4.3.1. *Sassafras albidum* Extract Preparation

Roots, twigs and leaves of *Sassafras albidum* were collected at High Park, Toronto, Canada in August 2019. The roots (10 g), twigs (10 g) and leaves (10 g) were ground to a fine powder and extracted with a mixture of EtOH/H_2O (100 mL, 80:20 v/v) for 72 hrs at room temperature. The crude extracts were obtained after filtration and further removal of the solvent by air drying.

4.3.2. ESI-MS and ESI-MS^n of the *Sassafras albidum* Extracts

Solutions of the root, twig and leaf extract (50 µg/mL) were prepared in MeOH for ESI-MS analysis using a Thermo Scientific LTQ linear ion trap mass spectrometer (San Jose, CA, USA). The spray voltage was set to 4 kV and the capillary temperature to 219°C. The extracts were analyzed by direct infusion (+)ESI-MS at a flow rate of 5 µL/min, using a Nitrogen gas pressure of 100 psi. Full scan ESI-MS spectra of the extracts were obtained in positive mode with a mass range of *m/z* 100-600.

4.3.3. The Separation of Alkaloids from *Sassafras albidum* by HPTLC

HPTLC plates (glass backed scored, 250 µm stationary phase; Silicycle Inc., (Quebec, QC, Canada) with dimensions of 5x5 cm were used for the extract separation prior to DESI-MS.

Aliquots containing 50 µg of the root extract were applied on HPTLC plates for each analysis. A solvent system containing $CHCl_3$, MeOH, and acetic acid (75:20:5 v/v/v) was used to develop the HPTLC plate. After the development, the HPTLC plates were dried at room temperature and then analyzed by DESI-MS.

4.3.4. DESI-MS^n of Alkaloids in *Sassafras albidum*

DESI-MS^n analysis of the developed HPTLC was carried out in positive mode using a Thermo Scientific LTQ linear ion trap mass spectrometer (San Jose, CA, USA) equipped with a custom built, automated DESI ion source. The 2D moving stage was used to collect mass spectral data by continuously scanning in horizontal rows in the x direction. The total time of each analysis was 7 min using a velocity of 95 µm/s to scan 4 cm of the HPLTC plate. DESI ion source parameters were optimized for the HPTLC analysis as follow: a capillary tip to surface distance of 4 mm, an incident angle to the surface of 52° and a 4-6 mm distance from the mass inlet to the capillary tip. The optimal desorption of the alkaloids was obtained using nitrogen gas pressures of 100 psi and solvent flow rates of 5 µL/min with pure MeOH. Full scan MS and multistage mass spectrometry (MS^n) analyses were performed to allow the screening and identification of compounds. In the DESI-MS^n analysis, each characteristic alkaloid ion was fragmented from MS^3 up to MS^7 depending on the type of alkaloid and on the ion intensity.

4.3.5. DESI-MSI of TLC Imprints of *Sassafras albidum* Roots and Twigs

The HPTLC plates were wetted with 0.3 mL of MeOH prior to the blotting process. The root and twig were cross-sectioned and manually blotted on TLC plates by pressing the sectioned material directly onto the TLC plate for 30s against a hot plate at 80 °C. The HPTLC imprints were scanned in horizontal rows with a lateral resolution of 200 µm. The imaging area 13000 µm x 13000 µm of the root imprint for a total analysis time of 1.3 hours with a velocity of 350 µm/s. The analyses were performed in positive mode with pure MeOH, the injection time was set to 200 ms and 3 microscans within the mass range of *m/z* 200- 400. The software Qual Browser Xcalibur 2.0 was used to process the mass spectra data (.raw) and Image Creator 3.0 converted the (.raw) files into a format compatible with BioMap (freeware, http:// www.maldi-msi.org/).

BioMap was used to process the mass spectral data and generate 2D ion images of the HPTLC surface.

4.4. Results and Discussion

4.4.1. The Presence of Alkaloids in Extracts of Roots and Twigs by (+)ESI-MS

The direct infusion (+)ESI- MS spectra of root and stem of *S. albidum* showed the presence of many even pseudo-molecular ions indicative of alkaloid compounds (Figure 4.1). The root extract showed a larger number of alkaloid ions including *m/z* 330, *m/z* 314, *m/z* 328, *m/z* 300, *m/z* 298, *m/z* 286, *m/z* 284, and *m/z* 342, while the extract of the twig showed only three ions of *m/z* 330), *m/z* 328 and *m/z* 298. The (+)ESI-MS spectrum of the extract of *S. albidum* leaves did not show any characteristic alkaloid ions, probably due the absence of these compounds in the extract or very low intensities in the extract.

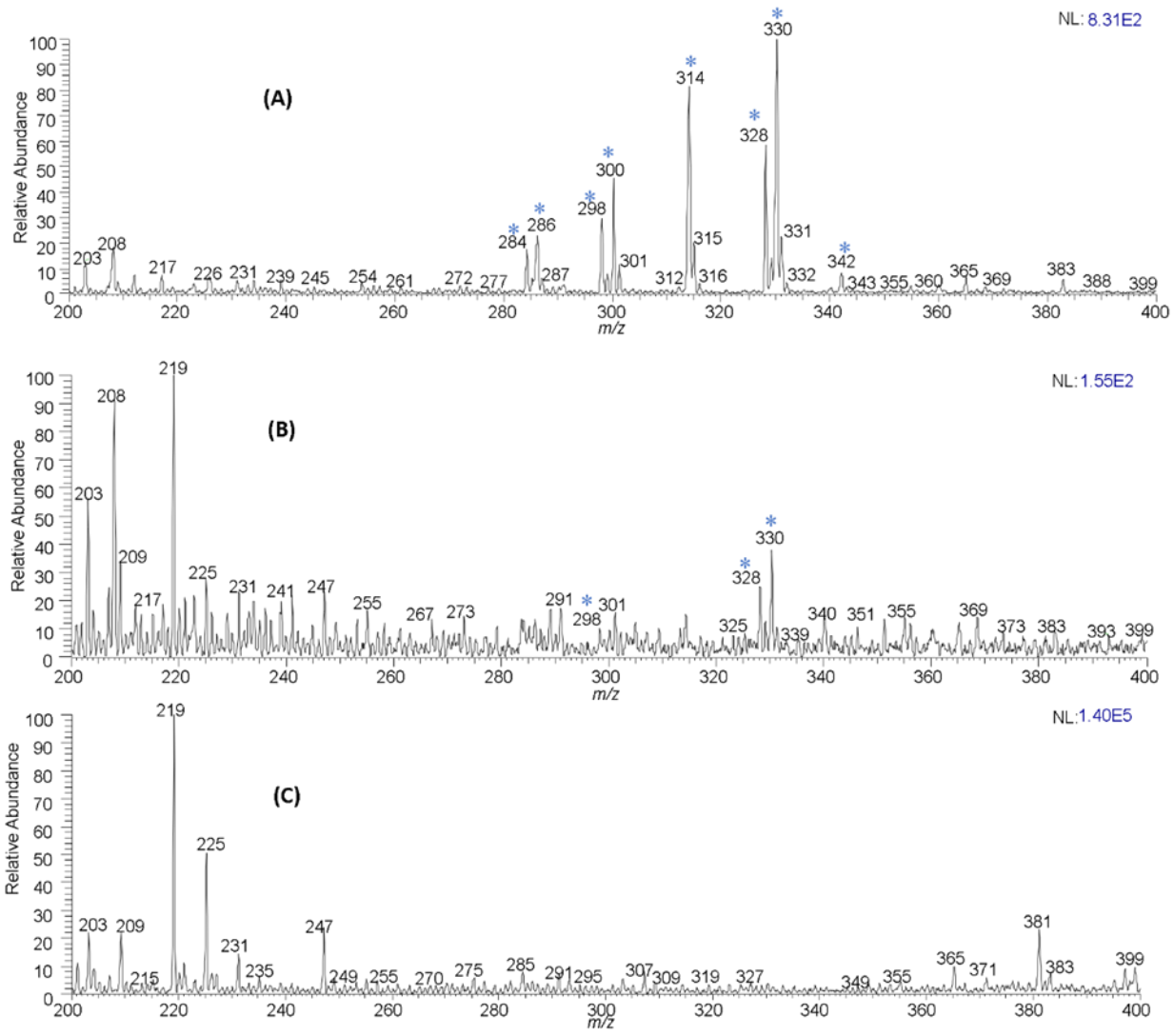

Figure 4.1: Full scan (+)ESI-MS spectra of *Sassafras albidum* extracts from A. Roots, B. Twigs, and C. Leaves. Reproduced with permission from Conceição et al.[165]

4.4.2. HPTLC-DESI-MS^n of *Sassafras albidum* Roots and Twigs

The HPTLC-DESI-MS analysis of *S. albidum* root extract allowed the identification and separation of a series of isobaric compounds, 2 compounds of *m/z* 300 (3-4), 3 compounds of *m/z* 314 (6-8) and 2 compounds of *m/z* 328 (10-11) (Figure 4.2). DESI-MS^n analysis was performed for all alkaloids separated offline by HPTLC and the structural characterization was investigated

based on the fragmentation pattern of these compounds and comparisons with literature data. Both isoquinoline and aporphine alkaloids have known fragment pathways that help characterize the main substituents and structure.[166-168] A total of 12 alkaloids were identified, 5 aporphine and 7 benzylisoquinoline alkaloids. The extract of the twig did not show any isobaric alkaloids, however, three compounds were identified that were also found in the roots, cinnamolaurine (3) (*m/z* 298), boldine (9) (*m/z* 328) and reticuline (11) (*m/z* 330). Figure 4.3 shows all the benzylisoquinoline and aporphine alkaloids identified in *S. albidum* extracts.

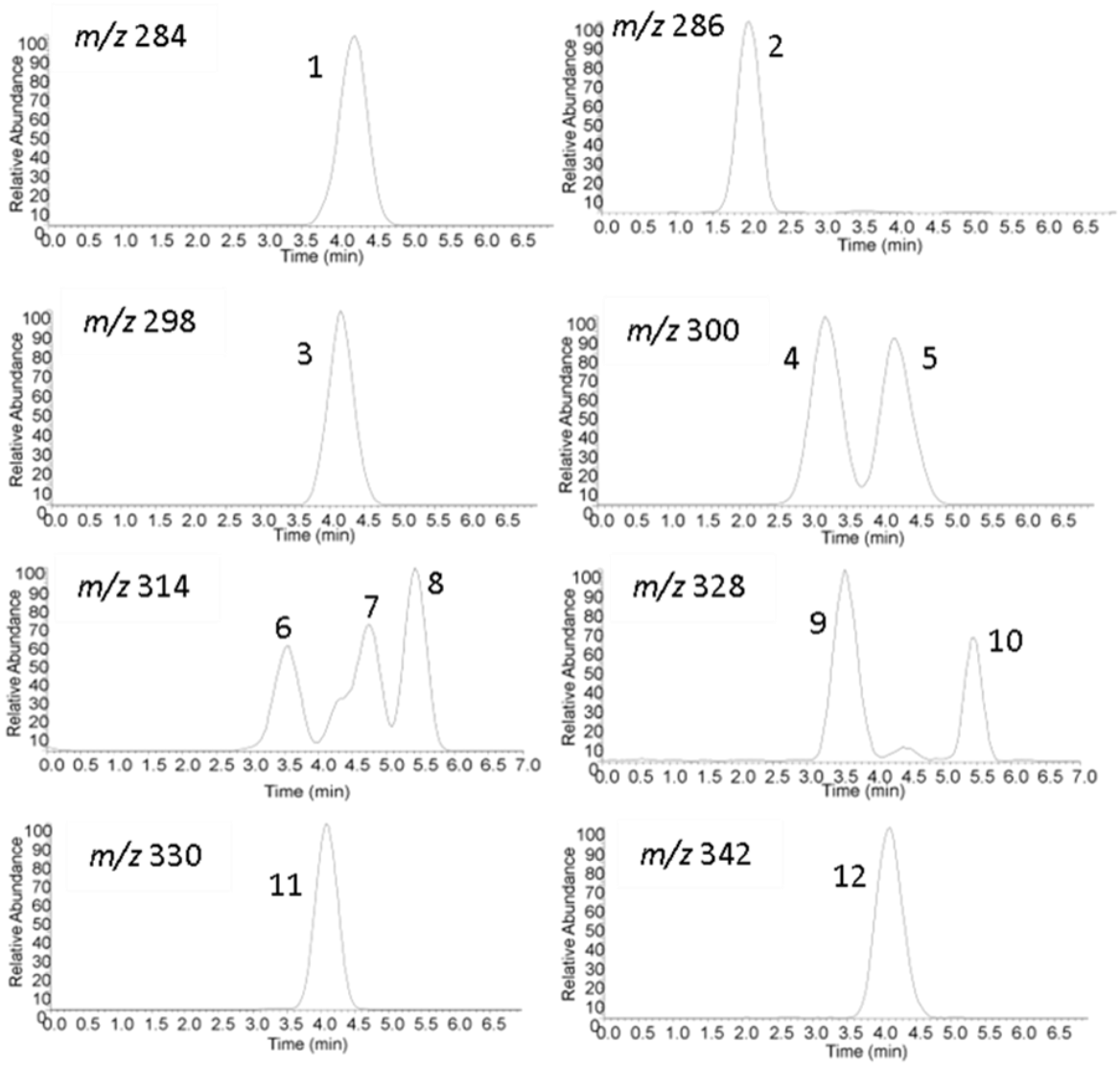

Figure 4.2: SIM mode extracted ion chromatograms of *Sassafras albidum* root extract by HPTLC-DESI-MS separated with Ben:EtOH (7:3 v/v). Reproduced with permission from Conceição et al.[165]

A)

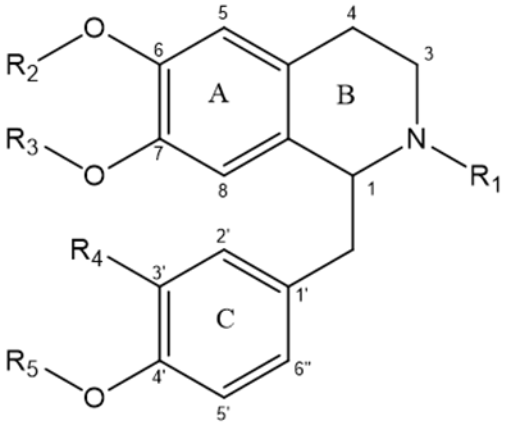

Compound	R_1	R_2	R_3	R_4	R_5
1	H	-CH_2-		H	H
2	H	CH_3	H	H	H
3	CH_3	-CH_2-		H	H
4	CH_3	CH_3	H	H	H
5	CH_3	H	CH_3	H	H
8	CH_3	CH_3	CH_3	H	H
11	CH_3	CH_3	H	OH	CH_3

B)

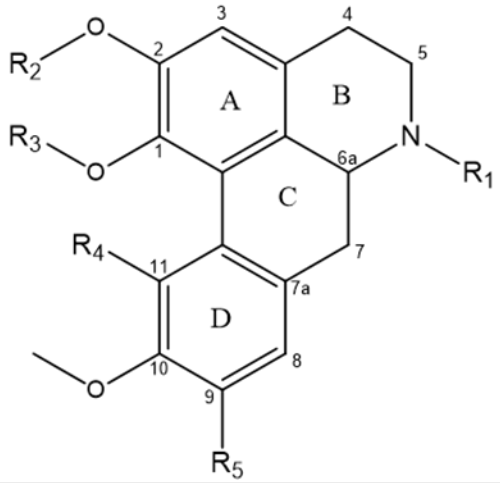

Compound	R_1	R_2	R_3	R_4	R_5
6	H	H	CH_3	H	OH
7	H	CH_3	H	OH	H
9	CH_3	H	CH_3	H	OH
10	H	CH_3	CH_3	OH	H
12	CH_3	CH_3	CH_3	H	OH

Figure 4.3: Alkaloids from *Sassafras albidum*. A) Isoquinoline and B) Aporphine. Reproduced with permission from Conceição et al.[165]

4.4.3. Benzylisoquinoline Alkaloids

Seven benzylisoquinoline alkaloids were observed in the root extract. The MS^n fragmentation pattern displayed key fragment ions (a-e) generated in the MS^2 and MS^3 (Table 4.1 and Figure 4.4). These ions (a-e), previously described in literature, help to identify the substitutions in two essential parts of benzylisoquinoline alkaloid structure, the benzyl and isoquinoline moiety.[167,168] Similar to aporphine alkaloids, secondary and tertiary benzylisoquinolines display the loss of 17 Da and 31 Da representing the cleavage of the amino group as $[M+H-NH_3]^+$ and $[M+H-NH_2CH_3]^+$, respectively, generating ion a.[168] Compounds 1 (norcinnamolaurine), 2 (coclaurine) and 3 (cinnamolaurine) were characterized as secondary alkaloids, compounds 4 (*N*-methyl coclaurine), 5 (*N*-methyl isococlaurine), and 11 (reticuline) were characterized as tertiary compounds.

Table 4.1: Key fragment ions of isoquinoline alkaloids of *Sassafras albidum* from HPTLC-DESI-MS^n analyses. Reproduced with permission from Conceição et al.[165]

#	Alkaloid	*m/z*	Type of Ion	**a**	**b**	**c**	**d**	**e**
1	Norcinnamolaurine	284	$[M+H]^+$	267	176	173	143	107
2	Coclaurine	286	$[M+H]^+$	269	178	175	143	107
3	Cinnamolaurine	298	$[M+H]^+$	267	190	173	143	107
4	N-methyl coclaurine	300	$[M+H]^+$	269	192	175	143	107
5	N-methyl isoclaurine	300	$[M+H]^+$	269	192	175	143	107
8	Armepavine	314	$[M+H]^+$	283	206	189	145	107
11	Reticuline	330	$[M+H]^+$	299	192	175	143	137

The b ion represents the isoquinoline moiety and occurs in the MS^2, directly from the $[M+H]^+$ ion. It is formed after an "even electron" type of rearrangement with a reversed charge distribution. Ion b is the main ion in the MS^2 of reticuline (11), however it showed low intensity

in all other alkaloids identified. The e-type ion occurs secondary to ion b and represents the benzyl component, this ion can also occurs as a MS^3 fragment from ion a. Reticuline (11) displayed ion e of *m/z* 137 indicating the presence of a methoxy and hydroxy groups present in the benzyl part of the alkaloid, all other compounds possess only the hydroxy group in this part of the moiety represented by an e ion of *m/z* 107. Ion c occurs after rearrangement of ion a, forming a naphthalene-derived ion. The *m/z* of ion c hints towards the substitution in ring A, most alkaloids in this work displayed a c-type ion of *m/z* 175 indicating the presence of vicinal methoxy and hydroxy groups in ring A. The two alkaloids with a methylenedioxy group identified were norcinnamolaurine (1) and cinnamolaurine (3), displaying an c ion of *m/z* 173. The unspecific ion d of *m/z* 143 was formed in the MS^3 as a rearrangement of ion a. Norcinnamolaurine, cinnamolaurine and reticuline were previously described in *Sassafras albidum.*[159] Coclaurine, *N*-methyl coclaurine, and armepavine showed similar fragmentation pattern described in previous works[122,167,168] and are described here for the first time in the genus *Sassafras*. Coclaurine and *N*-methyl coclaurine are important intermediates in the biosynthesis pathway of reticuline.[169,170] Reticuline has been identified as an important branch-point intermediate in the biosynthesis of more complex isoquinoline alkaloids such as, protoberberine, benzophenanthridines and aporphines.[171]

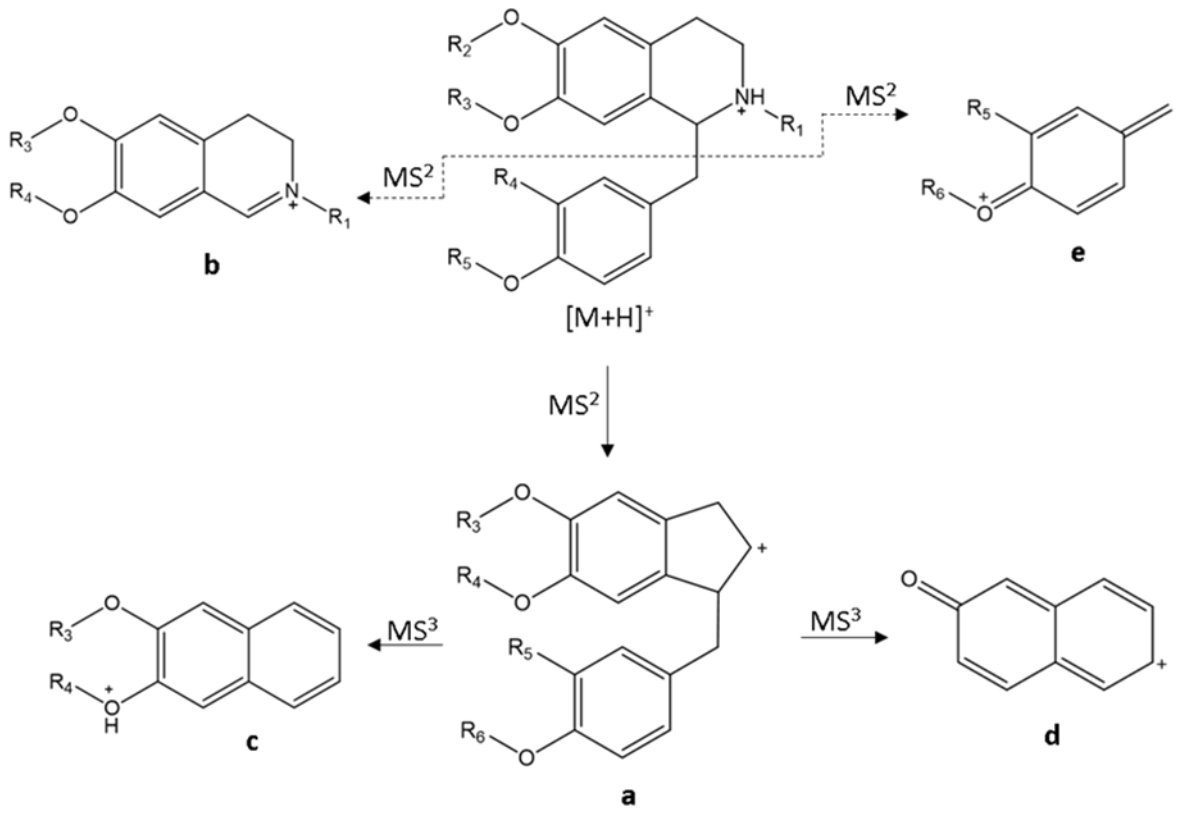

	Compound	*m/z*	a	b	c	d	e
1	norcinamolaurine	284 $[M+H]^+$	267	176	173	143	107
2	Coclaurine	286 $[M+H]^+$	269	178	175	143	107
3	cinamolaurine	298 $[M+H]^+$	267	190	173	143	107
4	N-methylcoclaurine	300 $[M+H]^+$	269	192	175	143	107
5	N-methyl isoclaurine	300 $[M+H]^+$	269	192	175	143	107
8	armepavine	314 $[M+H]^+$	283	206	189	145	107
11	Reticuline	330 $[M+H]^+$	299	192	175	143	137

Figure 4.4: MS^n fragmentation pattern of the Benzylisoquinoline alkaloids and their characteristic fragment ions. Reproduced with permission from Conceição et al.[165]

4.4.4. Aporphine Alkaloids

DESI-MS^n data of all the aporphine alkaloids detected are described in Table 4.2 all identified compounds were fragmentated up to MS^6 or MS^7. Aporphine alkaloids have known fragmentation patterns,[122,166] and these patterns differ according to the ring substituent that occurs in positions 1 and 2 of ring A and 9, 10 and 11 of ring D.[166,172] The aporphine alkaloids identified were (6) norboldine (*m/z* 314), (7) muricine (*m/z* 314), (9) boldine (*m/z* 328), (10) norisocorydine (*m/z* 328) and (12) *N*-methyl laurotetanine (*m/z* 342). The initial loss was represented by the cleavage of the amino group as $[M+H-NH_3]^+$ in the secondary compounds 6, 7 and 10 and as $[M+H-NH_2CH_3]^+$ in the tertiary compounds 9 and 12. After the cleavage of the amino group, norboldine (6) and boldine (9) displayed sequential losses of CH_3OH (32 Da) and CO (28 Da) that indicates the presence of vicinal methoxy and hydroxy groups in both rings A and D.[166,173] The final fragment of *m/z* 177 in the MS^6 represents the loss of all peripheral groups. Boldine and norboldine were identified based on the fragmentation pattern, comparison with literature data and the authentic boldine standard.[166] N-methyl laurotetanine (12) after the loss of amino group $[M+H-NH_2CH_3]^+$ displayed further losses of $CH_3\bullet$ (15 Da) and $CH_3O\bullet$ (31 Da) in competition, followed by a loss of CO (28 Da), a known pattern of compounds with two vicinal methoxy groups.[166] However, further losses in competition of $CH_3\bullet$ and CO represent a different pattern for two vicinal methoxy and hydroxy groups present in ring D, already described for this compound in the literature.[174]

Table 4.2: Aporphine alkaloids of *Sassafras albidum* analyzed by DESI-MS^n. Reproduced with permission from Conceição et al.[165]

#	Alkaloids	Type of Ion	MS	MS^2	MS^3	MS^4	MS^5	MS^6	MS^7
6	Norboldine	$[M+H]^+$	314	**314 (3)**, 297 (100)	**297 (0),** 265 (100)	**265 (30)**, 237 (100), 233 (20)	**237 (40),** 205 (100), 222(20), 177 (10)	**205 (30),** 177 (100)	-
7	Muricine	$[M+H]^+$	314	**314 (3)** 297 (100)	**297 (5)** 265 (100) 282 (25)	**265 (40),** 237(100), 219 (40), 209(28)	**237 (70),** 209 (100), 219 (65), 222 (36)	**209 (100),** 191(40), 181(20), 194(15)	-
9	Boldine	$[M+H]^+$	328	**328 (0),** 297 (100), 265 (40)	**297 (10),** 265 (100)	**265 (30),** 237 (100), 233 (25), 205 (10)	**237 (40),** 205 (100), 222 (30), 177 (10)	**205 (20),** 177 (100)	-
10	Norisocorydine	$[M+H]^+$	328	**328 (5),** 311 (100), 279(35)	**311(0),** 279 (100), 296 (20)	**279 (30),** 264 (100), 248 (25)	**264 (90),** 236 (100), 233 (20)	**236 (100),** 206 (50), 178 (45)	-
12	N-Methyl Laurotetanine	$[M+H]^+$	342	**342 (2),** 311 (100)	**311 (10),** 280 (100), 296 (80)	**280 (3),** 265 (100)	**265 (20),** 237 (100)	**237 (60),** 222 (100), 206 (30), 209 (25)	**222 (10),** 194 (100), 204 (70)

The fragment ion subjected to MS^n analysis is shown bolded and the relative intensity in brackets.

Muricine (7) and norisocorydine (10) have substitutions at positions 10 and 11 of ring D which leads to characteristic fragmentation pathways. Both are secondary alkaloids and lose NH_3 (17 Da) in the MS^2. Muricine (7) showed losses in the MS^3 and MS^4 that follow the general rules of compound with vicinal methoxy and hydroxy groups, but further losses of CO (28 Da) and H_2O (18 Da) were different from the previous pattern described for boldine in reference to other vicinal methoxy and hydroxy groups, but in agreement with alkaloids of these types of substitutions.[122] After the cleavage of the amino group, norisocorydine (10) displayed a loss of CH_3OH (32 Da), CH_3• (15 Da) and CO (28 Da). This fragmentation behavior was previously explained by the formation of a furan type intermediate between positions 1 and 11 that seems to be more stable.[166] Boldine and norboldine were previously described in the root of *S. albidum*.[159] Norisocorydine, muricine and N-methyl laurotetanine have been described in other genera of the Lauraceae family as well.[153,175,176]

4.4.5. The Spatial Distribution of Alkaloids in *S. albidum* by DESI-MSI

The DESI-MS imaging profile of *S.albidum* root and twig cross-sections presented distinct patterns of distribution from TLC imprints. In the root, most ions showed a higher intensity in the exoderms and epidermis, N-methyl coclaurine and N-methyl isococlaurine (*m/z* 300), norboldine and muricine (*m/z* 314) and reticuline (*m/z* 330) showed high intensities in most parts of the root (Figure 4.5). Reticuline (*m/z* 330), is the benzylisoquinoline precursor of most isoquinoline alkaloids, and was observed as the most intense ion among all other plant ions suggesting its important role in the formation of these alkaloids. It was not possible to map the coclaurine ion (*m/z* 286) due to very low intensities and interferences with other ions from the plant matrix. Cinnamolaurine (*m/z* 284) and N-methyl laurotetatine (*m/z* 342) were visualized as low intensity ions spatially distributed only in the exodermis and epidermis of the root.

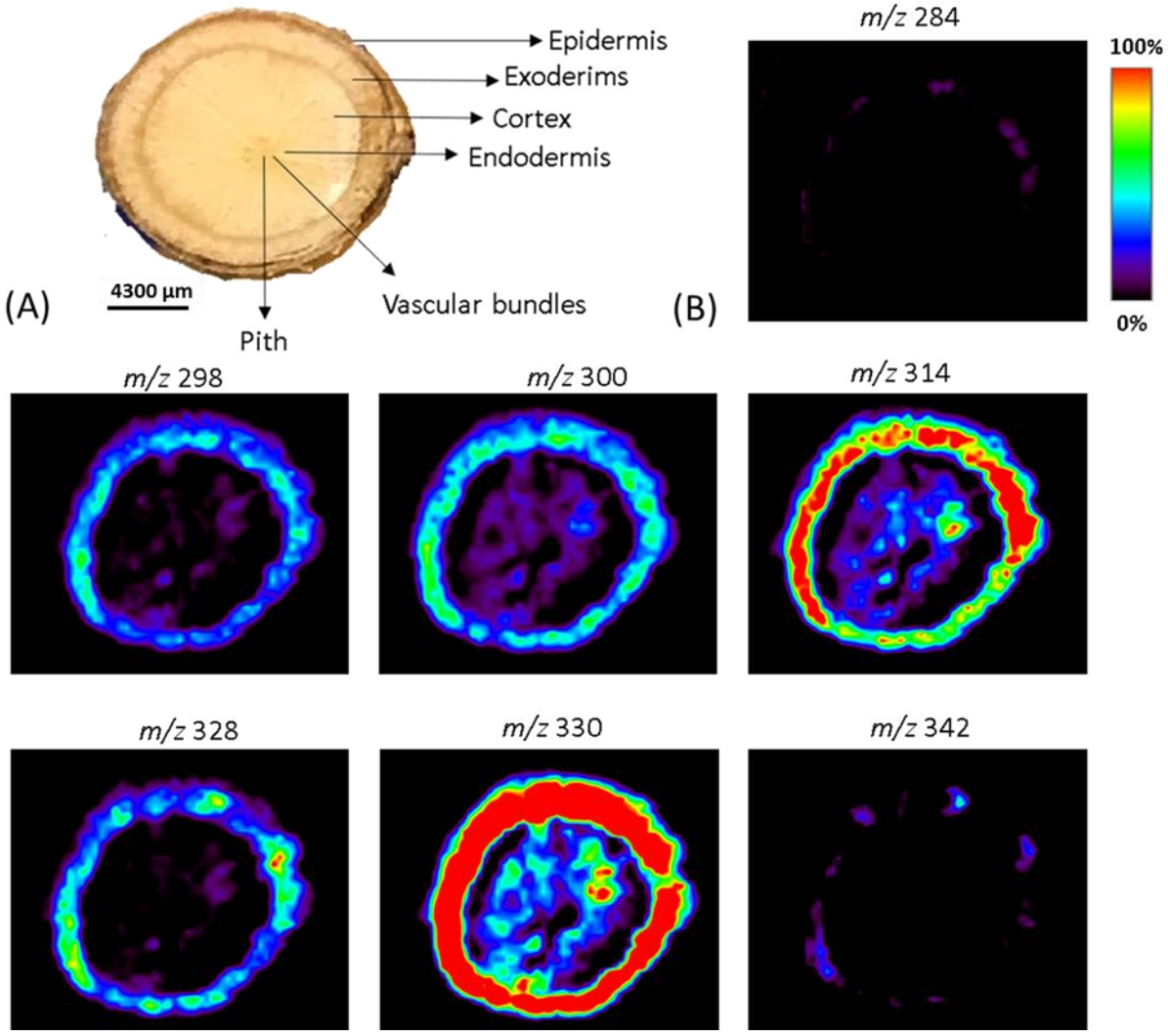

Figure 4.5: 2D-DESI-MS image of *Sassafras albidum* root with imaging dimensions of 13000 µm x 13000 µm and a spatial resolution of 200 µm showing the spatial distribution of benzylisoquinoline and aporphine alkaloids. Reproduced with permission from Conceição et al.[165]

All alkaloids seem to accumulate more in the outer layers of *S. albidum* roots, this pattern of localization could be influenced by the functional role of these compounds in the plants. It is well known that secondary metabolites play an important function in plant defence against herbivores, fungi, bacteria and physical damage. Aporphine alkaloids such as boldine and glaucine are toxic to insects, reticuline and coclaurine have anti-bacterial and anti-viral activity, respectively.[177,178] The alkaloid, berberine has strong antimicrobial activity[179] and accumulates in the endodermal cells of *Thalictrum flavum* roots prior to secondary growth.[180] As secondary

growth progresses, the endoderm is pushed by the growing stele and berberine accumulates in the outer-most layer of the mature root. This process provides an outer barrier with cells containing potent anti-microbial activity.[180] The abundant accumulation of berberine in *T. flavum* roots and rhizomes, surrounded by several soil-borne pathogens, is consistent with the putative role of berberine in plant defence.[180,181]

In twigs of *S. albidum*, three ions presented low intensities, similar to the ESI analysis, showing minor accumulations in this part of the plant. Even though, these less intense ions are minor constituents in the plant matrix, it was possible to visualize their accumulation patterns in the twigs (Figure 4.6). Reticuline (*m/z* 330) seems to be distributed more across different parts of the twig as shown in the roots. The superimposed image of cinnamolaurine (*m/z* 298) and boldine (*m/z* 328) can be found in Figure 4.6, cinnamolaurine (*m/z* 298) was localized in internal regions such as the vascular bundle and the cortex, while boldine/norisocorydine (*m/z* 328) was localized around the epidermis. In contrast to the twigs, cinnamolaurine (*m/z* 298) in the root showed higher intensity in outer regions.

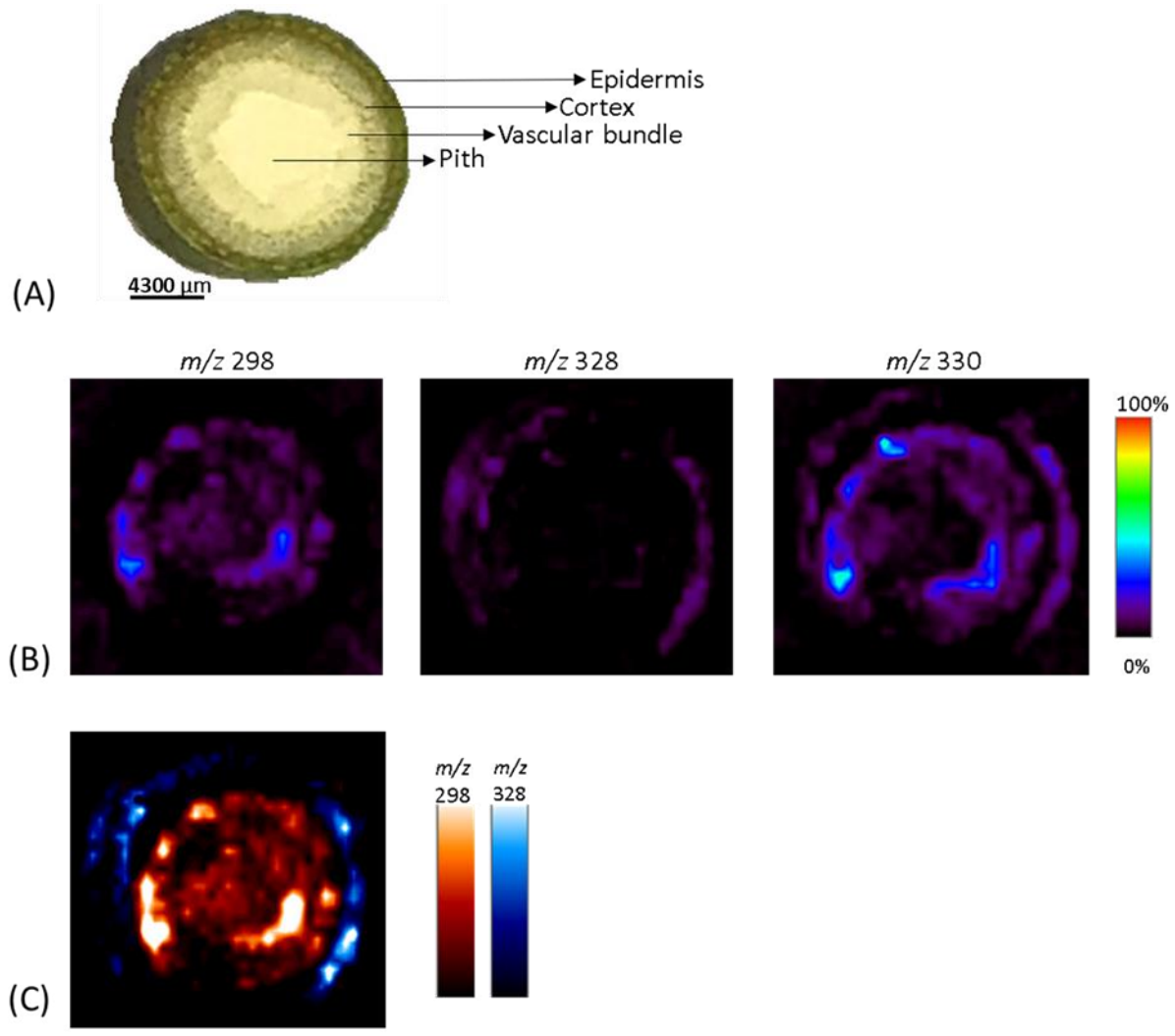

Figure 4.6: 2D-DESI-MS image of *S. albidum* twig with imaging dimensions of 13000 µm x 13000 µm and a spatial resolution of 200 µm showing the spatial distribution of benzylisoquinoline and aporphine alkaloids. B) Superimposed image of the distribution of cinammoralurine (*m/z* 298) and boldine (*m/z* 328). Reproduced with permission from Conceição et al.[165]

Recent studies have shown that the spatial localization pattern of secondary metabolites can be diverse in different parts within the same tissue and across many parts of the plant.[182,183] In a recent work, the localization pattern of monoterpenoid indole alkaloids in the root, stem leaf and fruits of *Rauvolfia tetraphylla* L. was described with distinct pattern across plant tissues and the highest number of alkaloids was found in the roots.[182] Secondary metabolites can accumulate in the same tissues where they were initially biosynthesized, but intermediates and end-products

can also be transported to other parts of the plant for further accumulation or biosynthesis as precursors in other metabolic processes.[184] Nicotine, is an example of such an alkaloid, it is typically produced near the root apex and accumulates in the leaves of Nicotiana species.[184,185] The systemic transport of pathway intermediates or end-products might also occur with isoquinoline alkaloids[180,184], and could explain the pattern and the large number of alkaloids found in the root of *Sassafras albidum*. The imaging results from this work could be valuable in uncovering the biosynthetic pathways of these alkaloids based on their accumulation within and across different parts of the plant.

4.5. Conclusion

The study of plant secondary metabolites by ambient ionization methods by HPTLC coupled to DESI-MS^n to separate and identify alkaloids in *Sassafras albidum* extracts provides an alternative method of analysis to conventional plant metabolomic methods. The separation and identification of secondary metabolites in *Sassafras albidum* are important to discovery the pathways involved in plant defence mechanisms. The characterization of benzylisoquinoline and aporphine type alkaloids and their spatial distribution within and across different plant tissues of *Sassafras albidum*, such as roots and twigs by DESI-MS imaging provided insights into the unknown processes of biosynthesis and accumulation of benzylisoquinoline and aporphine type alkaloids.

Chapter Five: The Fragmentation and Separation of Benzylisoquinoline and Aporphine Alkaloids from the Acaracide Extract of *Ocotea Spixiana* by HPTLC-DESI-MS^n

Chapter 5 is a version of the published manuscript:

Sousa, R.C., Reis, I.M.A. Cerqueira, A.P.M. **Perez, C.J.**, Junior, M.C.S., Branco, A. Ifa, D.R., Botura, M.A. Rapid Structural Characterization of Benzylisoquinone and Aporphine Type Alkaloids from *Octea Spixiana* Acaricide Extract by HPTLC-DESI-MS^n. *Phytochemical Analysis.* **2020**. 1-11.

5.1. Summary

Ocotea is a genus of the Lauraceae family, mainly occurring in tropical and subtropical regions. The importance of discovering alkaloids with acaricidal activity from medicinal plants allows for new parasite control strategies to protect animals against tick infestations, to reduce parasite resistance and the incidence of parasite transmitted diseases. In this study, we identified and separated a total of 13 aporphine and 4 benzylisoquinoline type alkaloids, and two unknown alkaloids, reported for the first time from the twigs of the tropical tree species, *Octea spixiana* by HPTLC-DESI-MS^n. Ethyl acetate extracts of *Octea spixiana* and the alkaloid boldine have shown significant *in vitro* acaricide activity against larvae of the tick, *R. microplus*. In this chapter, we present an in-depth identification by elucidating their fragmentation pathway, up to MS^3 for isoquinoline and MS^7 for aporphine alkaloids. This work demonstrates HPTLC-DESI-MS^n as a powerful technique to rapidly screen and identify novel phytochemicals from natural products.

5.2. Introduction

Ocotea is a genus of the Lauraceae family, mainly occurring in tropical and subtropical regions.[186] Species of the genus are known for producing a variety of important secondary metabolites, such as neolignans, aporphine and benzylisoquinoline-type alkaloids as the most representative classes.[153,187] A wide range of biological activities from *Ocotea* species have been described in the literature, including acaricidal[188,189], anti-proliferative[190], anti-inflammatory[191] and the inhibition of acetylcholinesterase (AChE).[192] Interestingly, the *in vitro* evaluation of the ethyl acetate extract, and the alkaloid boldine have shown significant *in vitro* acaricide activity of *O. spixiana* through interactions with AChE from the larvae of the tick, *R. microplus*.[122,188]

Natural products play an important role in the discovery of bioactive metabolites since plants are the main source of novel compounds.[193,194] Moreover, the analysis of secondary metabolites in complex biological matrices has been quite the challenge. Usually, the identification is laborious, extensive sample preparation is needed and isolation techniques prior to analyses are required to obtain accurate identifications. LC-MS is the gold standard for

analyses of plant extracts, although due to the need of sample preparation and long analysis times, there is a high demand in the study of plant metabolomics for the discovery and application of rapid and high-throughput methods.[195,196]

Desorption electrospray ionization (DESI) is an ambient ionization technique that is carried out directly by electrically charged droplets composed of solvent ions directed towards the surface.[197] The impact of these charged droplets on the surface with the aid of the nebulizing gas produces gaseous ions of compounds present on the sampled surface; these gaseous ions are transferred into the mass spectrometer under vacuum and mass spectra similar to ESI-MS can be recorded.[11,160] DESI has many characteristics that improves the analyses of compounds in complex mixtures, such as high sensitivity, specificity and the occurrence of little to no fragmentation.[160,195] Accurate compound characterization is enhanced using MS/MS fragmentation techniques such that fragment ions pertaining to the precursor ion can be easily elucidated.[195,198] Thin layer chromatography (TLC) is a fast, robust, and powerful technique that can be used to separate and analyze complex mixtures without extensive sample preparation.[196,198] It is widely used to separate plants components, in extracts, oils, tinctures, and other natural products.[196,199] Coupling TLC with DESI-MS creates a fast and powerful technique, that combines the robust separation of TLC and DESI-MS with good selectivity and sensitivity to identify compounds.[85,161] In this report, we present the fragmentation and separation of benzylisoquinoline and aporphine type alkaloids from the ethyl acetate extract with *in vitro* acaricide activity of *Ocotea spixiana* twigs using HPTLC-DESI-MS^n as a rapid and robust ambient MS technique.

5.3. Experimental

5.3.1. Plant Material and Preparation of the Extract

Twigs of *Ocotea spixiana* were collected in August 2012 in Rio de Contas (Latitude 13°22’26.9’’S; Longitude 41°53’27.5’’W) Bahia, Brazil. The identification of the species was

performed by a botanist. A voucher specimen (HUEFS 205865) was deposited at the herbarium of the State University of Feira de Santana, Brazil. Powdered twigs of *Ocotea spixiana* were subjected to extraction with ethanol/water (4000 mL, 80:20 v/v,) for 5 days at room temperature. The crude extract was obtained after the removal of the solvent. This crude extract was resuspended in H_2O/EtOH (3:1) and subsequently partitioned in hexane, ethyl acetate and n-butanol, thereafter the extracts were subsequently concentrated under vacuum conditions.

5.3.2. ESI-MS and Tandem MS of *O. spixiana* Extracts

ESI-MS experiments were carried out using a Thermo Scientific LTQ linear ion trap mass spectrometer (San Jose, CA, USA). The extract solution was analyzed by direct infusion ESI-MS at a flow rate of 5 µL/min, using a gas pressure of 100 psi. The spray voltage was set to 4 kV and the capillary temperature to 219 °C. Full scan ESI-MS spectra of the extracts were obtained in positive mode.

5.3.3. The Separation of Alkaloids by HPTLC

The separation by HPTLC was performed on 5x5 cm HPTLC plates (glass backed scored, 250 µm stationary phase from SiliCycle Inc., (Quebec, QC, Canada). Before the TLC development, a solution of propanol, H_2O and NH_4OH (9:1:0.5 v/v/v) was applied to improve the separation of the alkaloids. Aliquots containing 50 µg of ethyl acetate extract were applied on HPTLC plates for each analysis. The TLC plates were developed with a mobile phase containing Ben/MeOH (8:2 v/v). After the development, the TLC plates were dried at room temperature and then analyzed by DESI-MS.

5.3.4. DESI-MS^n Analysis of Alkaloids in *O. spixiana*

DESI-MS^n was performed in positive mode using a Thermo Scientific LTQ linear ion trap mass spectrometer (San Jose, CA, USA) equipped with the custom built, automated DESI ion source. DESI ion source parameters were optimized for HPTLC analysis. A capillary tip to surface distance of 4 mm, a 4-6 mm distance from the mass inlet to the solvent capillary and an incident

angle to the surface of 52° were used. A nitrogen gas pressure of 100 psi and a flow rate of 5 µL/min of pure MeOH was chosen based on the highest intensities of the alkaloid ions present in the extract for optimal desorption and ionization. HPTLC-MS experiments were performed with a two-dimensional moving stage collecting mass spectral data by continuously scanning in horizontal rows in the *x* direction with a velocity of 95 µm/s in a total length of 4 cm of the HPTLC for a total time of 7 min/analysis. To screen compounds, the previously developed TLC was analysed in full scan mode. Multistage mass spectrometry was performed to allow the identification of compounds. Collision induced dissociation (CID) was used for the fragmentation of alkaloid precursor ions. Each precursor ion was selected and fragmented by MS/MS, then the primary fragment was selected for each consecutive MS^n, performed from MS^3 up to MS^7 depending on the alkaloid precursor.

5.4. Results and Discussion

5.4.1. Alkaloids in Twigs of *O. spixiana*

The extract was first analyzed by direct infusion ESI-MS in positive ion mode as shown in Figure 5.1. The MS analysis displayed 10 pseudo molecular ions with even nominal mass characteristic of protonated alkaloids. Isoquinoline are the most common type of alkaloids present in *Ocotea* species, mainly aporphines with similar structures and the presence of isobaric compounds. To evaluate the presence of alkaloids with the same mass in the extract, a separation with HPTLC was performed prior to DESI-MS analyses. Different HPTLC mobile phase systems were investigated to improve the separation of the alkaloids. The chosen system allowed the separation of many alkaloid ions in less than 5 min of analysis. HPTLC coupled to DESI-MS led to the detection of the isobaric ions of *m/z* 314 (2 and 3), *m/z* 328 (5 and 6), *m/z* 356 (7–10), *m/z* 342 (11–13) and *m/z* 340 (15 and 16) for a total of 19 compounds. The extracted ion chromatograms of these peaks separated as a function of time are shown in Figure 5.2. The HPTLC-DESI analyses improved the identification of peaks with low abundance as shown for compounds 7, 9, 11, 13 and 15.

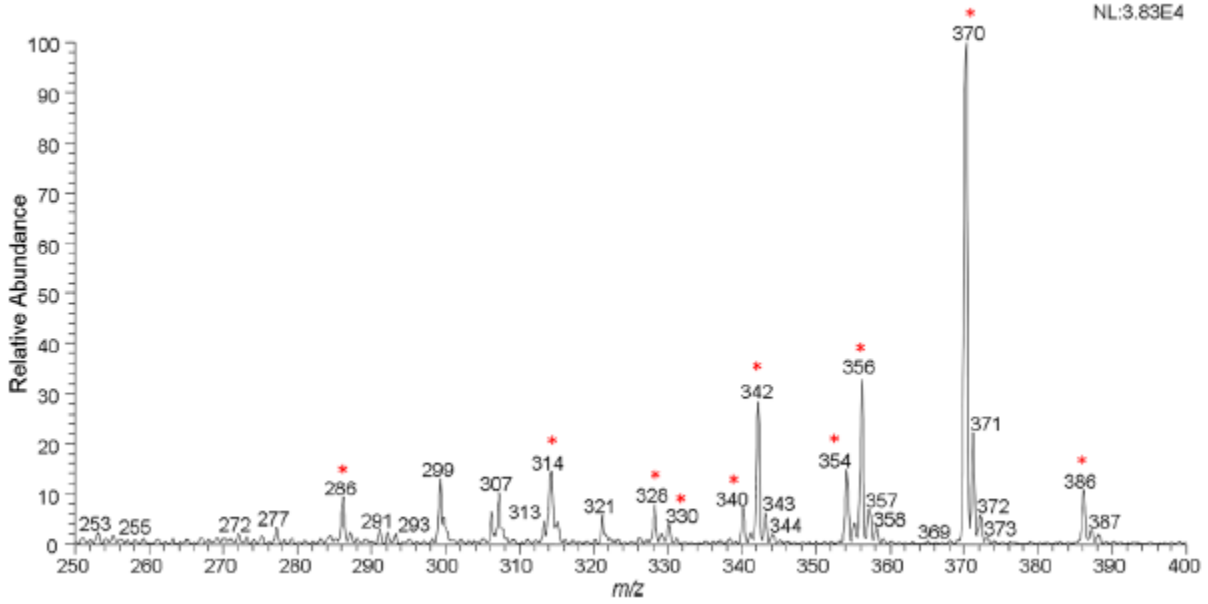

Figure 5.1: Full scan (+)ESI-MS spectrum of the ethyl acetate extract from *Ocotea spixiana* twigs. Reproduced with permission from Conceição et al.[122]

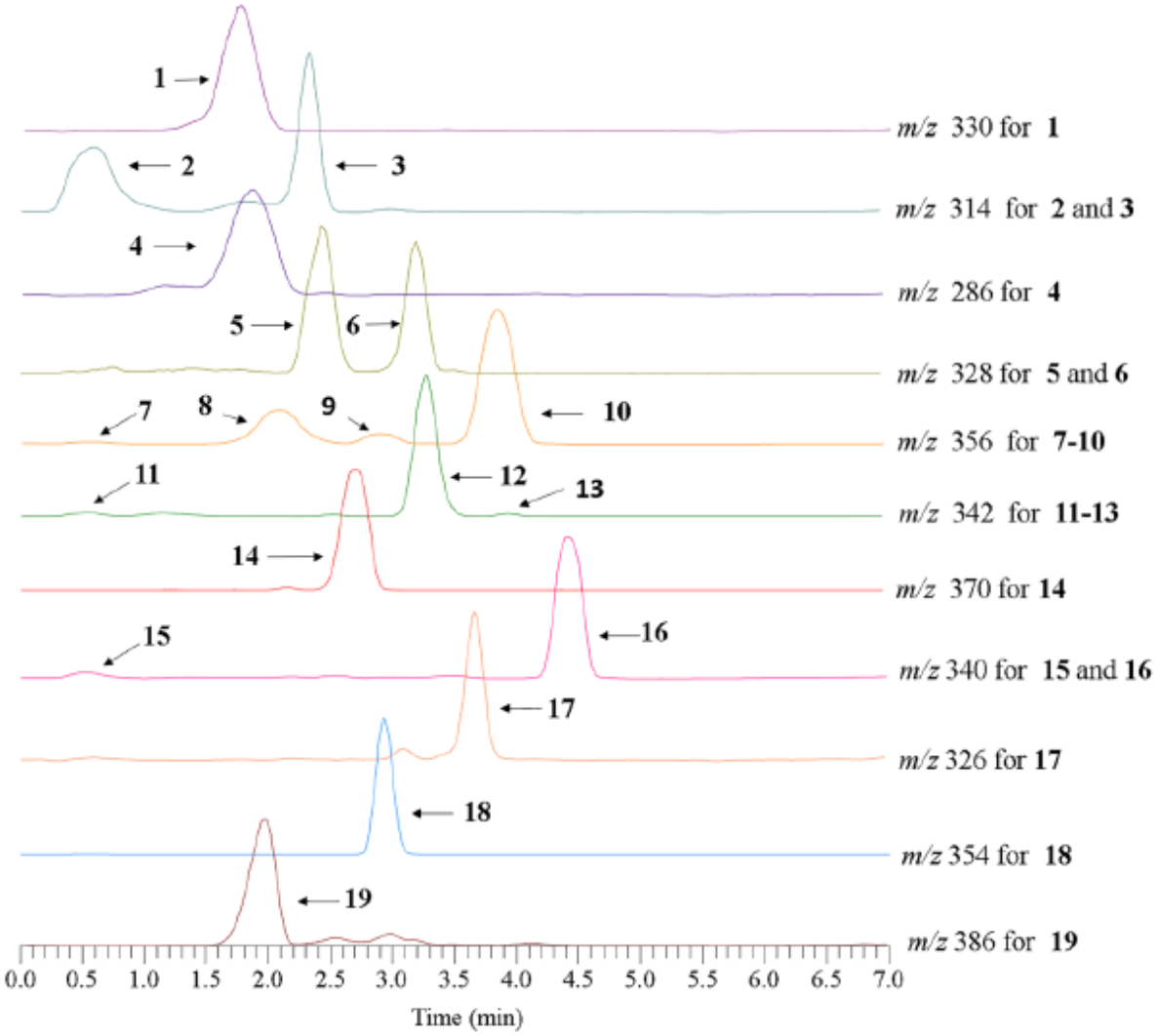

Figure 5.2: HPTLC-DESI-MS SIM extracted ion chromatograms of the ethyl acetate extract with acaricide activity of *O. spixiana* twigs. Reproduced with permission from Conceição et al.[122]

DESI-MS^n analysis was performed of all precursor alkaloid ions detected. In general, tertiary and secondary alkaloids produced $[M+H]^+$ protonated ions and quaternary alkaloids generated $[M]^+$ ions. $[M+H]^+$ or $[M]^+$ ions were selected as precursor ions for CID experiments in positive ion mode. Extensive fragmentation up to MS^6 and MS^7 was possible on most compounds. The MS^n of benzylisoquinoline and aporphine alkaloids possess a set of key fragmentation patterns that help characterize these compounds.[166,167,172,173] A total of 13 aporphine and 4 benzylisoquinoline alkaloids were identified based on the fragmentation pathway and comparison with literature data (Figure 5.3).

(A)

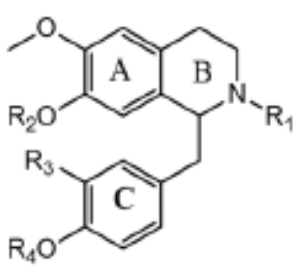

Compound	R_1	R_2	R_3	R_4
1	CH_3	H	OH	CH_3
2	$(CH_3)_2$	H	H	H
3	CH_3	CH_3	H	H
4	H	H	H	H

(B)

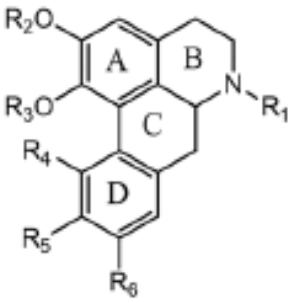

Compound	R_1	R_2	R_3	R_4	R_5	R_6
5	CH_3	H	CH_3	H	OCH_3	OH
6	CH_3	CH_3	H	OH	OCH_3	H
7	$(CH_3)_2$	H	CH_3	H	OCH_3	OCH_3
8	$(CH_3)_2$	CH_3	CH_3	H	OCH_3	OH
10	CH_3	CH_3	CH_3	H	OCH_3	OCH_3
11	$(CH_3)_2$	H	CH_3	H	OCH_3	OH
12	CH_3	H	CH_3	H	OCH_3	OCH_3
13	CH_3	CH_3	CH_3	OH	OCH_3	H
14	$(CH_3)_2$	CH_3	CH_3	H	OCH_3	OCH_3
15	$(CH_3)_2$	H	CH_3	H	$-OCH_2O-$	
16	CH_3	CH_3	CH_3	H	$-OCH_2O-$	
17	CH_3	H	CH_3	H	$-OCH_2O-$	
18	$(CH_3)_2$	CH_3	CH_3	H	$-OCH_2O-$	

Figure 5.3: Alkaloids in ethyl acetate extract of twigs of *O. spixiana*. A) Benzylisoquinoline alkaloids. B) Aporphine alkaloids. Reproduced with permission from Conceição et al.[122]

5.4.2. Benzylisoquinoline Alkaloids

The MS^n spectra of alkaloids 1–4 presented strong evidence of the benzylisoquinoline skeleton with the presence of key ions (a-e), a pattern of fragmentation described in the literature (Table 5.1).

Table 5.1: Key fragment ions in the MS/MS spectra of Benzylisoquinoline type alkaloids. Reproduced with permission from Conceição et al.[122]

#	Alkaloid	*m/z*	Type of Ion	a	b	c	d	e
1	Reticuline	330	$[M+H]^+$	299	192	175	143	137
2	Magnocurarine	314	$[M]^+$	269	206	175	143	107
3	Armepavine	314	$[M+H]^+$	283	206	189	145	107
4	Coclaurine	286	$[M+H]^+$	269	178	175	143	107

The first fragmentation is the loss of the nitrogen group as ammonia (NH_3) (4), as methylamine (CH_3NH_2) (1 and 3) or as dimethylamine ($(CH_3)_2NH$) (2) generating ion a. This fragmentation pattern is exemplified in compound 1 in Figure 5.4. The b-type ion is formed in the MS^2 after a β-cleavage and rearrangement involving the nitrogen proton and the aromatic ring of the benzyl substituent.[167] The e-type ion represents the benzyl group and is generated in the MS^2 secondary to the formation of ion b, and as a MS^3 fragmentation of ion a. The different masses of ions from a-e observed among these compounds are due to the type of substituent. Compounds 2, 3 and 4 showed an e-type ion of *m/z* 107 indicating the presence of one hydroxy group in ring C, while the e-type ion from compound 1 (*m/z* 137) indicates the presence of one additional methoxy ($-OCH_3$) group.

The MS^3 fragmentation of ion a generates the d-type ion after rearrangement. The c-type ion is the key ion of the MS^3 fragmentation of ion a, occurring as a rearrangement after the loss of the benzyl groups. Alkaloids 1, 2 and 4 showed the c-type ion of *m/z* 175 suggesting the presence of vicinal $-OCH_3$ and -OH groups in ring A.[168] Compound 1 (*m/z* 330) and 3 (*m/z* 314) were identified as tertiary amine with the loss of 31 Da, $[M+H-CH_3NH_2]^+$ in the MS^2 spectrum, showing a-type ions of *m/z* 299 and *m/z* 283, respectively. Compound 1 showed ion b of *m/z* 192 and characteristic of $-OCH_3$ and -OH groups present in ring C identified as the well-known alkaloid reticuline.[166,173,200] Compound 3 showed ion b of *m/z* 206 indicating one more $-CH_3$ group in ring A than compound 1. The c ion of this compound of *m/z* 189 supported this data.

The MS^4 spectrum of *m/z* 189 showed losses of $CH_3O•$ (31 Da) and $CH_3•$ (15 Da), similar to previously reported MS^2 profiles of losses of alkaloids with two vicinal -OCH_3 groups.[166] The pattern observed by compound 3 is consistent with the previously described alkaloid armepavine.[201] Compounds 4 (*m/z* 286) and 2 (*m/z* 314) were identified as secondary and quaternary amines with the same a-type ion of *m/z* 269, indicating losses of 17 Da $[M+H-NH_3]^+$ and 45 Da $[M+H-(CH_3)_2NH)]^+$, respectively. They both showed the same *m/z* of ions e, c and d, demonstrating that the only difference between them were the nitrogen group substituents. Ion e of *m/z* 107 indicates the presence of one -OH group on the benzyl moiety and ion b of *m/z* 175 indicative of vicinal -OCH_3 and -OH groups in ring A. Compound 4 was postulated as coclaurine in comparison with literature data.[166] The fragmentation pathway of compound 2, allowed its identification as the quaternary nitrogen alkaloid, magnocurarine.[200]

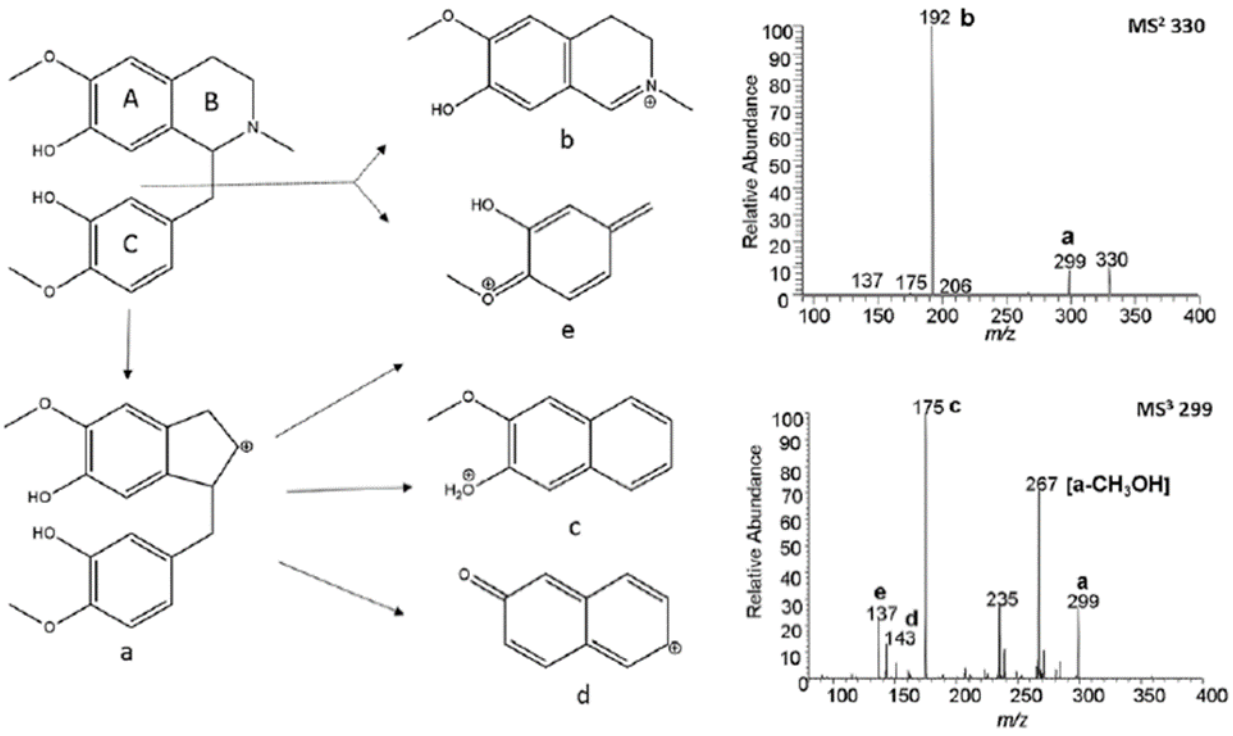

Figure 5.4: Proposed fragmentation pathway and MS^n spectra of Reticuline (1). Reproduced with permission from Conceição et al.[122]

5.4.3. Aporphine Alkaloids

Table 5.2 presents the DESI-MS^n data of all aporphine alkaloids detected. The DESI-MS^n analysis showed seven protonated alkaloids as $[M+H]^+$, and six alkaloids as $[M]^+$ as the molecular ions. The key MS^2 fragment from the protonated $[M+H]^+$ precursor ions was $[M+H-31]^+$ and from quaternary $[M]^+$ precursor ions $[M-45]^+$, characteristic losses of tertiary and quaternary aporphine alkaloids, respectively. These fragments were attributed to the loss of CH_3NH_2 (31 Da) and $(CH_3)_2NH$ (45 Da). Further fragmentation after the cleavage of the amino group displayed patterns with losses of different substituents from the aromatic rings. Aporphine alkaloids have known fragmentation patterns that help characterize the substitution that mainly occurs in rings A and D.[166,173] Mass fragmentation analysis was performed based on the following fragment patterns as described in the literature: the sequential loss of CH_3OH (32 Da) and CO (28 Da) as the preferred fragment pathway of compounds with hydroxy and methoxy groups in vicinal positions (Figure 5.5.A).[166,173,174]

The fragmentation pattern of compounds with two vicinal methoxy groups lead to losses in competition of CH_3• (15 Da) and CH_3O• (31 Da), followed by the loss of CO (Figure 5.5.B).[166,173,174] The loss of CH_2O (30 Da) followed by a loss of CO (28 Da) typically occurs in aporphine alkaloids with a methylenedioxy group as the ring substituent (Figure 5.5.C).[166] Boldine (5) of *m/z* 328 $[M+H]^+$ and N-methyl boldine (11) of *m/z* 342 $[M]^+$ after the respective losses of 31 Da $[M+H-CH_3NH_2]^+$ and 45 Da $[M+H-(CH_3)_2NH)]^+$, showed only sequential losses of CH_3OH (32 Da) and CO (28 Da), in the major pathway. They followed the general rules of fragmentation of compounds with hydroxy and methoxy groups in vicinal positions, leading to the ion of *m/z* 177 from losses of all the peripheral substituents on rings A and D (Figure 5.5.A). These results were also confirmed by the MS^2 analysis of the authentic boldine standard.

Table 5.2: Major fragment ions observed by DESI-MS^n analysis of aporphine alkaloids of *Ocotea spixiana*. Reproduced with permission from Conceição et al.[122]

#	Compounds	MS	Type of Ion	MS^2	MS^3	MS^4	MS^5	MS^6	MS^7
5	Boldine	328	$[M+H]^+$	**328 (3)** 297 (100) 265 (30)	**297 (10)** 265 (100)	**265 (30)** 237 (100) 233 (20)	**237 (35)** 205 (100) 177 (20)	**205 (35)** 177 (100)	
6	Corytuberine	328	$[M+H]^+$	**328(2)** 297 (100) 265 (40)	**297(5)** 265 (100) 282 (25) 233 (20)	**265 (50)** 237 (100) 209 (30) 219 (20)	**237(35)** 209 (100) 219 (80) 205 (20)	**209 (100)** 191 (50) 194 (30) 181 (20)	
7	*N*-methyl predicentrine	356	$[M]^+$	**356 (40)** 311 (100) 279 (80)	**311(10)** 279 (100) 296 (20)	**279(5)** 251 (100) 264 (20)	**251(30)** 220 (40) 236 (10)		
8	Xanthoplanine	356	$[M]^+$	**356 (15)** 311 (100) 280 (8) 296 (5)	**311 (10)** 280 (100) 296 (80)	**280 (3)** 265 (100)	**265 (20)** 237 (100)	**237 (60)** 222 (100) 206 (40) 209 (30)	**222 (10)** 194(100) 204(80)
9	Unknown	356	$[M]^+$	**356 (15)** 311 (100) 296 (8)	**311(10)** 283 (100) 296 (20)	**283 (3)** 255 (100)	**255 (60)** 240 (100) 223 (50)	**240 (70)** 212 (100) 210 (90)	
10	Glaucine	356	$[M+H]^+$	**356 (30)** 325 (100) 294 (5) 310 (4)	**325 (20)** 294 (100) 310 (60)	**294(20)** 279 (100) 251 (10)	**279 (5)** 251(100) 236 (15)	**251(15)** 236 (100) 220 (25) 233(20)	
11	*N*-methyl boldine	342	$[M]^+$	**342 (20)** 297 (100) 265 (50)	**297 (50)** 265 (100)	**265 (80)** 237 (100) 233 (12) 205 (10)	**237 (40)** 205 (100) 177 (15) 222(30)	**205 (80)** 177 (100)	
12	Predicentrine	342	$[M+H]^+$	**342 (3)** 311 (100) 279(40)	**311(10)** 279 (100) 296 (10)	**279 (20)** 251(100)	**251(30)** 220(100) 236 (90)	**220 (60)** 205 (100)	**205 (80)** 177(100)
13	Isocoridyne	342	$[M+H]^+$	**342 (5)** 311 (100)	**311(8)** 279 (100)	**279 (2)** 264 (100)	**264 (90)** 236(100)	**236(50)** 206 (100)	

				279(35)	296 (10)	248 (30)		178(30)	
14	*N*-methyl glaucine	370	$[M]^+$	**370 (10)** 325(100) 294 (20) 310 (15)	**325(10)** 294(100) 310 (60)	**294(25)** 279(100) 251 (10)	**279 (15)** 251(100) 236 (12) 223 (10)	**251 (60)** 236(100) 220 (30)	
15	*N*-methyl isodomesticine	340	$[M]^+$	**340 (20)** 295 (100) 263 (70)	**295 (15)** 263(100) 235 (10)	**263 (2)** 235 (100) 233(30)	**235 (20)** 205 (100)	**205 (65)** 177 (100)	
16	Nantenine	340	$[M+H]^+$	**340 (10)** 309 (100)	**309 (10)** 294(100) 278 (80)	**294 (30)** 279 (100)	**279 (40)** 251 (100) 261 (50) 223 (40)	**251(5)** 223 (100)	**223(100)** 193 (60) 165(60)
17	Isodomesticine	326	$[M+H]^+$	**326 (2)** 295(100) 263 (40)	**295 (10)** 263 (100) 235 (15)	**263 (20)** 235 (100) 233(40)	**235 (40)** 205 (100) 177(15)	**205 (40)** 177 (100)	
18	*N*-methyl nantenine	354	$[M]^+$	**354 (10)** 309 (100)	**309 (20)** 294 (100) 278 (80)	**294 (40)** 279 (100)	**279 (40)** 251 (100) 261 (45) 223 (40)	**251 (10)** 223 (100)	**223(100)** 193 (60) 165(40)
19	Unknown	386	$[M]^+$	**386 (20)** 341(100) 325(30)	**341(10)** 310 (100) 326 (30)	**310 (20)** 295 (100) 267(20)	**295 (20)** 267(100)	**267 (20)** 239(100) 249(90) 236 (70) 252(50)	

The precursor ion selected for MS^n has been bolded and the relative intensity shown in brackets.

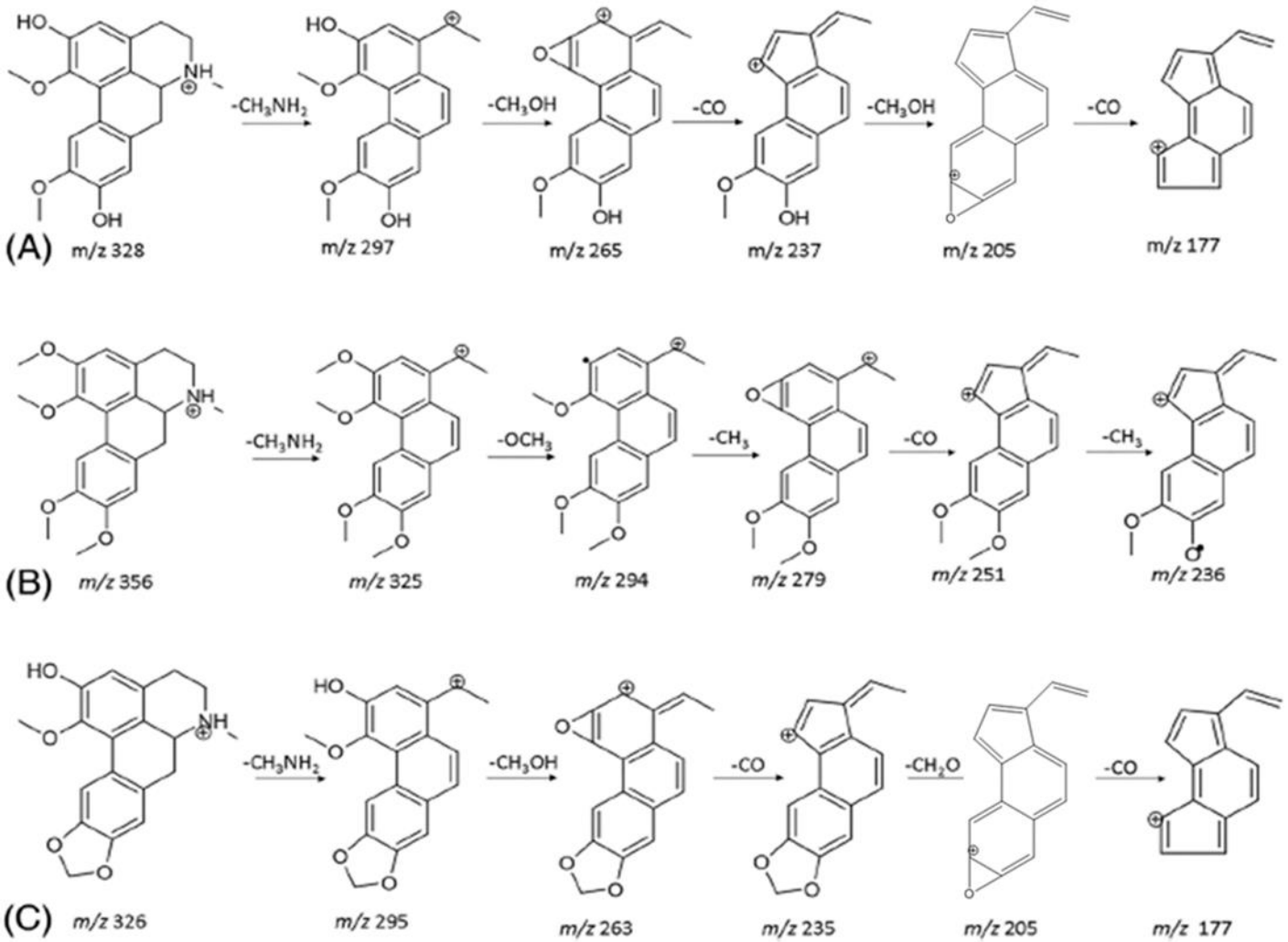

Figure 5.5: Fragmentation pathway of aporphine alkaloids from *Ocotea spixiana*. (A) Compounds with hydroxy and methoxy groups in vicinal positions represented by boldine (5). (B) Compounds with two vicinal methoxy groups represented by glaucine (10). (C) Compounds with a methylenedioxy group represented by isodomesticine (17). Reproduced with permission from Conceição et al.[122]

Compounds 10 (*m/z* 356 $[M+H]^+$) and 14 (*m/z* 370 $[M]^+$) after the cleavage of amino group showed sequential losses of CH_3• (15 Da), CH_3O• (31 Da) and CO (28 Da) indicative of the presence of vicinal -OCH_3 groups, identified as glaucine and *N*-methyl-glaucine based on the fragmentation pattern and comparison with literature data.[166,174] Isodomesticine (17) (*m/z* 326 $[M+H]^+$) and *N*-methylisodomesticine (15) (*m/z* 340 $[M]^+$) showed first characteristic losses of vicinal hydroxy and methoxy groups and following losses of CH_2O (30 Da) and CO (28 Da) indicative of the presence of the methylenedioxy group (Figure 5.5.C). To the best of our knowledge, this is the first report of *N*-methyl-isodomesticine in *Ocotea* species. Nantenine (16) (*m/z* 340 $[M+H]^+$) and *N*-methyl-nantenine (18) (*m/z* 354 $[M]^+$) also showed a fragmentation pattern indicative of the presence of the methylenedioxy group, after the first losses that suggests two -OCH_3 groups in vicinal positions. Predicentrine (12) (*m/z* 342 $[M+H]^+$) and *N*-methyl-predicentrine (7) (*m/z* 356 $[M]^+$) showed losses of CH_3OH (32 Da) and CO (28 Da) which strongly suggests the presence of adjacent methoxy and hydroxy groups. These alkaloids exhibited accompanying losses characteristic of vicinal methoxy groups in the aporphine skeleton.[174] Xantoplanine (8) (*m/z* 356 $[M]^+$) also showed characteristic losses of vicinal methoxy groups, with further losses of CH_3• (15 Da) and CO (28 Da), a different fragmentation pattern, already described in the literature, for the loss of vicinal methoxy and hydroxy.[174]

Compound 6 ($[M+H]^+$ of *m/z* 328) and 13 ($[M+H]^+$ of *m/z* 342) were identified as corytuberine and isocoridyne, respectively in comparison with literature data.[166,200,202] Both compounds have the -OH group in position 11, which seems to change the fragment pathway in comparison with the patterns described earlier. Isocoridyne (13) showed a behaviour that has been described before.[166] The MS^3 of the fragment ion, $[M+H-CH_3NH_2]^+$, showed the loss of CH_3OH (32 Da), however the accompanying loss of CO (28 Da) that usually happens in compounds with -OCH_3 and -OH vicinal groups was not observed. Another fragmentation pathway that takes place, in this case, are the losses of CH_3• (15 Da) and CH_3O• (31 Da), observed after the losses of CH_3OH. Corytuberine (6) showed the loss of CH_3OH (32 Da) and CO (28 Da), with subsequent losses of CO (28 Da) and H_2O (18 Da), displaying a different pattern of compounds with vicinal methoxy and hydroxy groups.

Several alkaloids identified in this work have been found in other *Ocotea* species described in the literature. For example, predicentrine was identified in *O. vellosiana*,[203] *O. Macropoda*,[204] *O. brachybotra*[205] and *O. minarum*.[206] Glaucine has been found in *O. macrophylla*, *O. vellosiana*[203] and *O. duckei.*[207] The compounds boldine,[208] reticuline,[203,209] coclaurine,[210] nantenine,[211,212] isocorydine,[212] and isodomesticine[208] were also identified in *Ocotea* species and xantoplanine and armepavine were detected in the genus *Litsea.*[213]

5.5. Conclusion

In the present study, for the first time 13 benzylisoquinoline, 4 aporphine type alkaloids and two unknown aporphine alkaloids were detected in the ethyl extract with acaricidal activity of the tropical tree species, *Octea spixiana*. The ethyl acetate extract of *O. spixiana* twigs were investigated by coupling HPTLC to DESI-MS^n. This work demonstrated that HPTLC-DESI-MS^n is a rapid and robust analytical tool to identify alkaloids from plant extracts. The MS^n fragmentation pathway of benzylisoquinoline and aporphine alkaloids were elucidated up to MS^3 and MS^7, respectively and compared with the MS^2 fragmentation of the authentic boldine standard. The separation of these alkaloids by HPTLC revealed a series of isobaric ions with distinct fragmentation patterns. In future studies of *O. spixana*, we aim to explore the spatial distribution of these bioactive alkaloids with acaricidal activity involved in important plant defence mechanisms from plant tissues such as roots, twigs and leaves.

Chapter Six: A Quantitative Metabolomic Study of Novel *Coffea Canephora* Genotypes Across Stages of Maturity by High Resolution Mass Spectrometry

Chapter 6 is a version of the published manuscript:

Lemos, M.F., **Perez, C.,** Pereira da Cunha, P.H., Filgueiras, P.R., Pereira, L.L., Almeida da Fonseca, A.F., Ifa, D.R., Scherer, R. Chemical and sensory profile of new genotypes of Brazilian *Coffea canephora. Food Chemistry.* **2020**. 310: 125850.

6.1. Summary

Coffea arabica and *Coffea canephora*, commonly known as Arabica and Robusta are two coffee bean species used for worldwide consumption. More than 700 compounds contribute to the aroma and flavour of coffee beans however, the most important metabolites involved in regulating its sensory properties include caffeine, trigonelline, saccharides, fatty acids, lipids, phenolic and chlorogenic acids in green and roasted coffee beans. In this study, we developed a relative ESI-HRMS quantitation method using caffeine-D9, and the structural analog salicylic acid, to quantify and compare the levels of green coffee bean metabolites such as caffeine, trigonelline, saccharides, phenolic and chlorogenic acids in Arabica, Robusta and three novel *Coffea canephora* species across three stages of bean maturity. The metabolome of the three new species Diamante 101, 105 and 108 were compared against Arabica and Robusta. Diamante 105, and 108 presented higher caffeine, trigonelline, sugars and comparable levels of chlorogenic acids to Arabica and Robusta. Among the three novel *Coffea canephora* species, Diamante 108 showed the most promising coffee bean quality based on its metabolome.

6.2. Introduction

Coffee is one of the most consumed beverages in the world and a major source of economic revenue for many developing countries.[214] There are many species of the genus *Coffea* in the Rubiaceae family; however, only two species are commercially distributed for consumption, *Coffea arabica* and *Coffea canephora*, more commonly known as Arabica and Robusta coffees, respectively. Arabica beans are known to produce high-quality brews with intense aromas and more desirable tastes and overall superior sensory properties than Robusta.[215] On the other hand, Robusta beans, also known as Conilon, have a stronger and bitter taste than Arabica, yet the species has shown to be more resistant against pests, diseases and more tolerant to changes in climate and harvesting conditions.[216-218] Recent studies are focused on improving sensory properties of Robusta species to obtain better quality coffee brews. More than 700 compounds contribute to the aroma and flavour of coffee beans however, the most important metabolites

involved in regulating its sensory properties include caffeine, trigonelline, saccharides, fatty acids, lipids, phenolic and chlorogenic acids in green and roasted coffee beans.[219-221] Metabolomic studies of Arabica (*Coffea arabica*) and Robusta (*Coffea canephora*) green coffee beans have reported that Arabica generally contains more trigonelline and sugars, and less phenolic acids, chlorogenic acids and caffeine compared to Robusta species.[221,222]

The biochemical diversity of the metabolites in green coffee beans not only depends on genetic variability, such as the species, but also from agronomic conditions such as harvesting at different levels of maturation, agricultural practices, climate and soil conditions.[219,223,224] The harvest is an important phase that exerts a strong influence on the composition of the coffee beans and should be performed at its ideal point of maturation, because in these crucial stages, important chemical precursors are accumulated into the coffee resulting in beans of higher quality. However, many production farms collect coffee fruits before all of them are fully ripe; that is, the fruits are picked with different degrees of ripeness (cherry, green or dried in the plant) and this practice can damage the final quality of the coffee.[225] The chemistry of coffee quality is highly complex, with numerous compounds that may change during fruit maturation.

Currently, the relationship between the chemical composition, stages of maturity and coffee bean quality has not been thoroughly explored. In this work, we developed a rapid and simple ESI-HRMS relative quantitation method to investigate the metabolomic profiles of three novel genotypes *Coffea canephora* genotypes of green coffee beans compared to common cultivars of Robusta (Tropical) and three Arabica cultivars (Arabica Catuai 81, Obata and Topazio) harvested across three stages of bean maturity (60%, 80% and 100%). We present for the first time, the metabolome of three novel *Coffea canephora* genotypes, Diamante 101, 105, and 108.

6.3. Experimental

6.3.1. The Origin of Brazilian Green Coffee Beans

Green coffee beans were collected from the experimental farms of INCAPER in Espírito Santo State, Brazil, during 2017. Three cultivars of green Arabica coffee beans (Catuai 81: AC; Obata: AO; Topazio: AT) (Lat: 20°22'38.56"S Long: 41°11'54.24"W), three genotypes of green Conilon coffee beans (genotypes Diamante C101, C105 and C108) and one cultivar of green Robusta coffee beans (RT) (Lat: 20°45'21.30"S Long: 41°17'4.33"W) were collected. All species were harvested at three different levels of maturity, namely, 60%, 80% and 100% of cherry stage fruits, for a total of 21 green coffee bean samples. Approximately 5 kg of each coffee was collected and naturally sun-dried in a greenhouse, processed and cleaned. Only non-defective and 16 sieve-sized beans (Brazil, 2003) were selected. Green coffee beans were stored in the dark at room temperature.

6.3.2. Extract Preparation of Green Coffee Beans

To facilitate grounding from bean to powder, coffee beans were stored for 3 days at –80°C. 21 coffee bean samples (7 green coffee bean cultivars at 3 stages of maturity) were grounded to a fine powder with a bladed coffee grinder (Hamilton Beach) and 1.0000 g of the powder was extracted with 10 mL of MeOH. The samples were placed in an ultrasonic water bath (Branson 2510MT) for 40 min. The samples were centrifuged for 10 min. at 5000 rpm (2800 g) using an Allegra 25R centrifuge (Beckman Coulter) and the supernatant was collected and kept at –80°C until HRMS analysis.

6.3.3. ESI-LTQ-Orbitrap: Sample Preparation

A fast, relative quantitation method by direct infusion ESI-HRMS using Data Dependent Acquisition (DDA) was created to investigate the selected metabolites: caffeine, trigonelline, phenolic acids and sugars. Prior to the ESI-HRMS analysis, 10.0 µL aliquots of each extract were transferred to 1.5 mL Eppendorf tubes, and 988 µL of MeOH was added. The samples were

analysed in positive and negative ion modes. For positive mode, the solutions were acidified with 1.0 µL of concentrated formic acid, and 10.0 µL of deuterated caffeine at a concentration of 1 mg/mL was spiked into the sample for a final standard concentration of 48 µmol/L caffeine in each extract. In negative mode, 1.0 µL of ammonium hydroxide and 2.0 µL of the standard salicylic acid solution at a concentration of 1 mg/mL were added for a final concentration of 14.4 µM salicylic acid in each extract. Before injection in the ESI-LTQ-Orbitrap Elite mass spectrometer, samples were stirred for 10–15 s using a vortex (Bench Mixer™).

6.3.4. ESI-HRMS LTQ-Orbitrap Elite™ Analysis

Coffee bean extracts were injected using a 2 µL loop valve injection into the mass spectrometer (LTQ-Orbitrap™ Elite, Thermo Scientific) equipped with an electrospray ionization (ESI) source, operating in positive and negative ion mode. The optimized parameters in positive ion mode were as follows: flow rate 3 µL/min, spray voltage 3.5 kV, 1 microscan, injection time 10 ms, capillary temperature 275 °C, source heat temperature 75 °C, tube lens 64 V, resolution 240,000 at *m/z* 200 and the mass spectra were acquired over the range of *m/z* 120–500. In (-)ESI-HRMS, the spray voltage was set to 3.0 kV, tube lens to 50 V and the full scan mass spectra were used over the range of *m/z* 120–600. A method was created in Xcalibur™ Software for DDA by which the top 100 ions were selected for MS/MS by High Energy Collision Dissociation (HCD) using a collision energy of 100 arbitrary units. The DDA method was performed once on the same day for 21 green coffee bean samples across three stages of maturity (60%, 80%, 100%).

6.3.4. mMass Data Calibration

The LTQ-Orbitrap™ Elite was calibrated online and offline in positive and negative ion mode, respectively. The mass calibration was performed offline in negative ion mode by mMass. Xcalibur™ mass spectral files were converted from .raw files with Proteowizard to .xmL format and these files were uploaded onto mMass. mMass was used to automatically subtract blanks from samples. A metabolite list was created with exact and accurate masses of all the ions of interest including the internal standard, salicylic acid. The negative ion mode data set of 21 mass

spectra files were successfully calibrated and the mass calibrated data achieved a mass accuracy ≤2 ppm for all ions.

6.4. Results and Discussion

6.4.1. Bioactive Metabolites Across Green Coffee Bean Species

Coffee is a complex natural product that contains over 700 compounds that are responsible for its pleasant aroma and flavour. Coffee undergoes several steps (postharvest processing, roasting, storage, transportation and seed maturation) to reach its human destination, and, genetic factors also have an impact on its chemical composition.[226,227] *Coffea arabica* and *Coffea canephora* are genetically different species based on their chemical composition and quality. Arabica is known to have a better sensory profile than Robusta/Conilon, where Robusta presents stronger tastes with pronounced bitterness.[228] Due to the complex chemical composition of coffee beans, different metabolites (caffeine, trigonelline, carbohydrates, phenolic and chlorogenic acids) were analyzed to contribute to the characterization of new coffee genotypes and then to correlate the metabolites with the quality of the coffee. Green coffee bean extracts from Arabica (Catuai, Obata, and Topazio), three novel genotypes Diamante 101, 105, 108 and Robusta Tropical species at three different stages of maturity, 60%, 80%, and 100% were characterized by (+)ESI-HRMS and (-)ESI-HRMS. The green coffee bean metabolites shown in Figure 6.1 were the most abundant polar constituents from ethanolic extracts.

Caffeine (*m/z* 195.08840), trigonelline (*m/z* 138.05547) and its potassium adduct (*m/z* 176.01166) were identified in (+)ESI-HRMS profiles (Table 6.1 and Figure 6.1). Phenolic and chlorogenic acids such as caffeoylquinic acid (CQA) (*m/z* 355.10459), feruloylquinic acid (FQA) (*m/z* 393.05933), and the sodium and the potassium adduct of sucrose (*m/z* 365.10739) and (*m/z* 381.08034), respectively were also found in green coffee beans. The FAAH inhibitor, N-arachinoyl-5-hydroxytryptamide or 5-HT (*m/z* 471.39783) was present in the extract of all green

coffee bean species. The metabolites were identified by HRMS in which the mass accuracy of the precursor ions ranged between 0.2-3.8 ppm and MS/MS fragment ions produced by HCD were compared to the literature (Table 6.1)

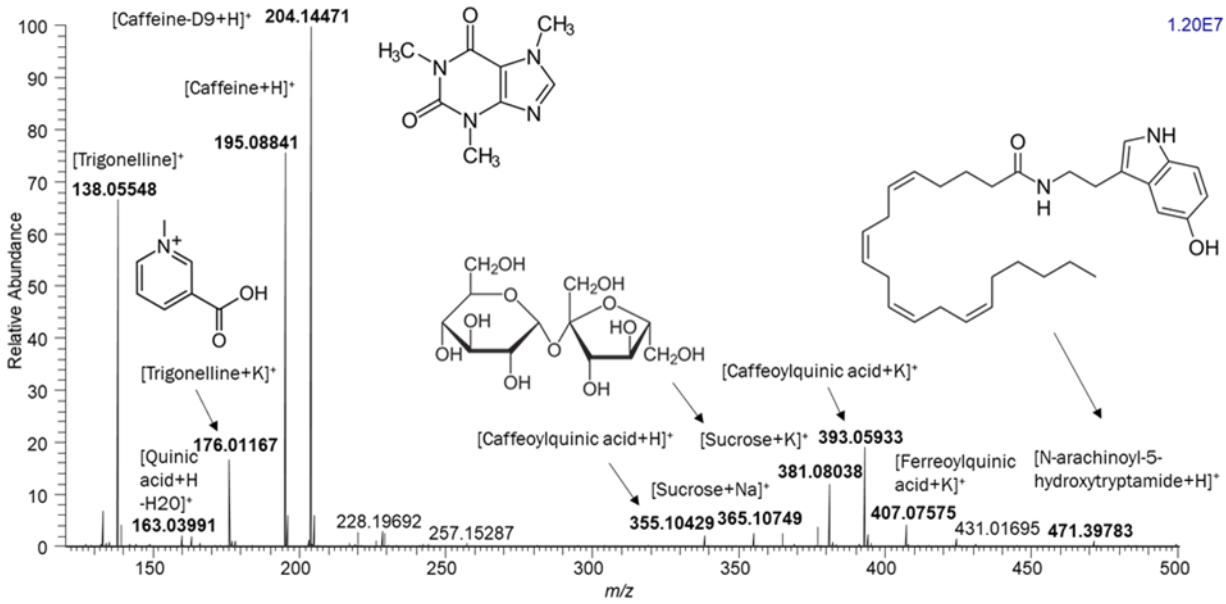

Figure 6.1: Metabolites in the (+)ESI-HRMS spectrum of Robusta Tropical at 100% maturity. The standard caffeine-D9 (*m/z* 204.14471) was used to compare the relative content of metabolites between green coffee bean species and across stages of maturity. Reproduced with permission from Lemos et al.[229]

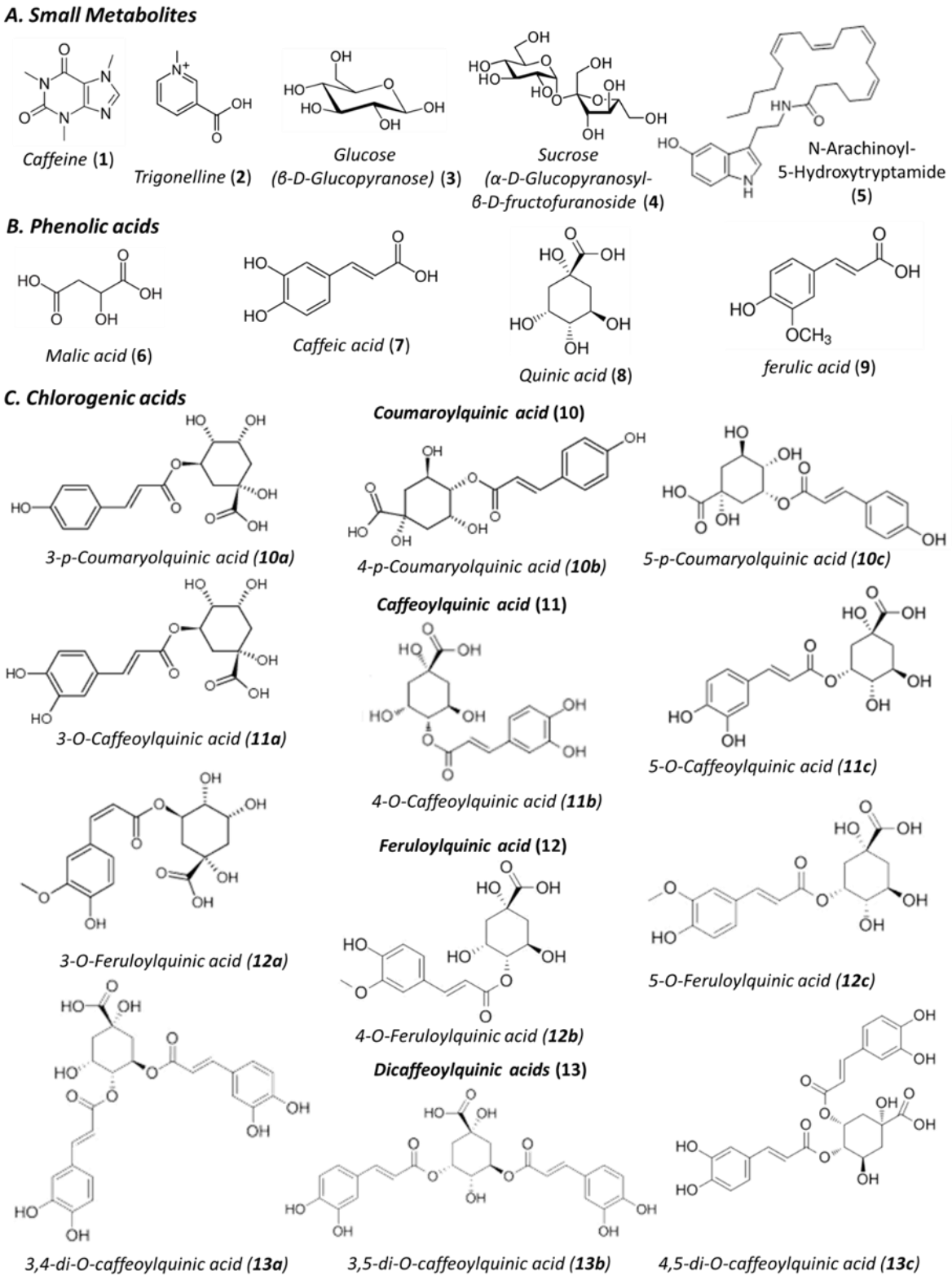

Figure 6.2: The chemical structure of metabolites in green coffee beans. A. Small metabolites. B. Phenolic acids. C. Chlorogenic acids.

The green coffee bean extracts from Arabica Catuai, Obata, and Topazio, novel *coffea canephora* genotypes Diamante 101, 105, 108 and Robusta Tropical at three different stages of maturity, 60%, 80%, 100% were analyzed by (-)ESI-HRMS. The major constituents in the ethanol extract were phenolic acids, such as malic acid (MA) of *m/z* 133.01351, caffeic acid (CA) of *m/z* 179.03455, quinic acid (QA) of *m/z* 191.05577 and ferulic acid (FA) of *m/z* 193.05023. Chlorogenic acids, such as coumaroylquinic acid (pCoQA) with 3 isomers 3-, 4-, and 5-pCoQA of *m/z* 337.09299, caffeoylquinic acid (CQA) with 3 isomers 3-, 4-, and 5-CQA, of *m/z* 353.08701, feruloylquinic acid (FQA) with 3 isomers 3-, 4-, and 5-FQA of *m/z* 367.10241, dicaffeoylquinic acid (diCQA) with three possible isomers 3,4-diCQA; 3,5-diCQA; 4,5-diCQA of *m/z* 515.11906, and lastly, feruroylcaffeoylquinic acid (FCQA) of *m/z* 529.13474 were present as shown in Table 6.1 and Figure 6.3.

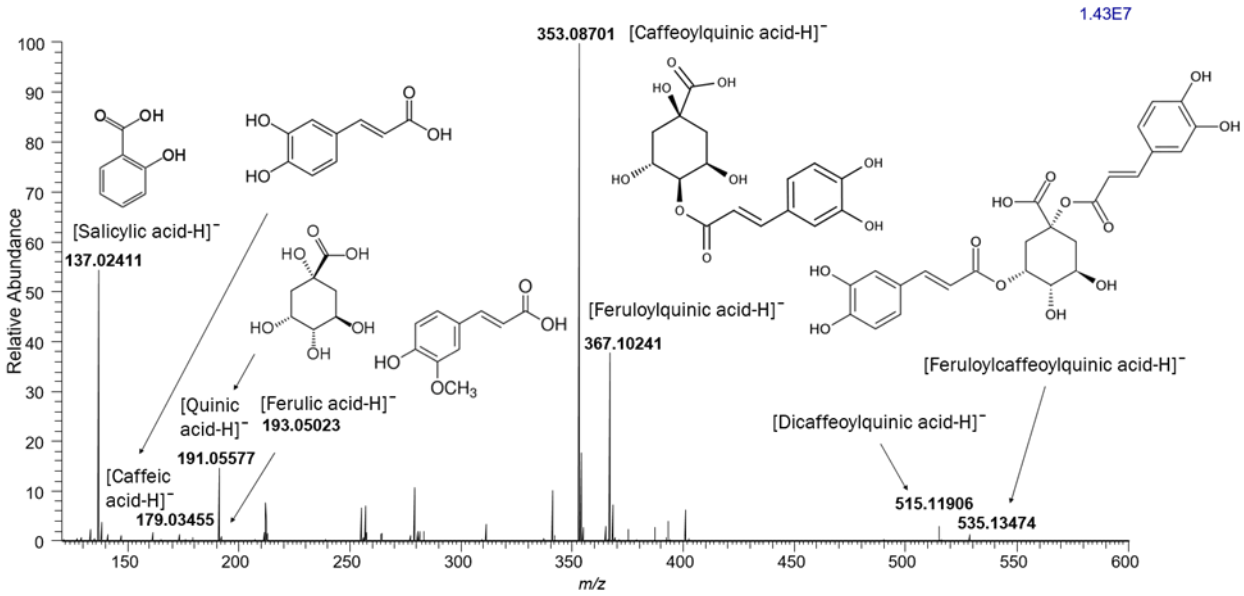

Figure 6.3: Phenolic and Chlorogenic Acids in the (-)ESI-HRMS spectrum of Robusta Tropical at 100% Maturity. The standard Salicylic acid (*m/z* 137.02411) was used to compare the relative content of phenolic and chlorogenic acids between green coffee bean species and across stages of maturity. Reproduced with permission from Lemos et al. [229]

Table 6.1: High-resolution MS/MS characterization of green coffee bean metabolites in Arabica (Catuai 81, Obata, Topazio), novel genotypes Diamante 101, 105 and 108 and Robusta Tropical at three stages of maturity. Reproduced with permission from Lemos et al.[229]

Polarity	Compounds	Type of Ion	Molecular Formula	Exact Mass (*m/z*)	Accurate Mass (*m/z*)	Mass Error (ppm)	MS/MS Fragments (*m/z*)	
POSITIVE							Precursor Ion	Fragment Ions
	Trigonelline	$[M]^+$	$C_7H_8NO_2$	138.05550	138.05547	0.2	138.05547[a]	110.06015,
		$[M+K]^+$	$C_7H_7NO_2K$	176.01139	176.01166	-1.6	176.01166[a]	138.05471
	Caffeine	$[M+H]^+$	$C_8H_{10}N_4O_2$	195.08820	195.08840	-1.0	195.08840[a]	123.04293, 138.06660, 110.07145
	Standard-Caffeine-D9	$[M+H]^+$	$C_8H_1N_4O_2D_9$	204.14469	204.14470	-0.03	204.14470[a]	126.06179, 144.10418, 116.10911 113.06509
	Glucose	$[M+Na]^+$	$C_6H_{12}O_6Na$	203.05316	203.05375	-2.9	203.05375[a]	-
		$[M+K]^+$	$C_6H_{12}O_6K$	219.02710	219.02778	-3.1	219.02778[a]	-
	Sucrose	$[M+Na]^+$	$C_{12}H_{22}O_{11}Na$	365.10599	365.10739	-3.8	365.10739[a]	-
		$[M+K]^+$	$C_{12}H_{22}O_{11}K$	381.07992	381.08034	-1.1	381.08034[a]	-
NEGATIVE								
	Malic acid	$[M-H]^-$	$C_4H_6O_5$	133.013700	133.01351	1.4	133.01332[a]	115.002755
	Caffeic acid	$[M-H]^-$	$C_9H_8O_4$	179.034435	179.03455	-0.6	179.03455[a]	135.05084, 105.49029
	Quinic Acid	$[M-H]^-$	$C_7H_{12}O_6$	191.055565	191.05577	-1.1	191.05577[a]	110.02035, 173.04821, 132.42753, 127.04935
	Ferulic Acid	$[M-H]^-$	$C_{10}H_{10}O_4$	193.050085	193.05023	-0.7	193.05023[b]	134.04546, 161.02859, 136.09716
	Coumaroylquinic acid	$[M-H]^-$	$C_{16}H_{18}O_8$	337.092345	337.09299	-1.9	337.09299[a]	191.05560, 173.04779, 163.04378, 119.06032
	Caffeoylquinic acid	$[M-H]^-$	$C_{16}H_{18}O_9$	353.087260	353.08701	0.7	353.08701[a]	191.05551, 135.05296, 179.03640, 173.04788, 161.02851

	Feruloylquinic acid	$[M-H]^-$	$C_{17}H_{20}O_9$	367.102910	367.10241	1.4	367.10241[a]	191.05552, 173.04771, 134.04515, 193.04960
	Dicaffeoylquinic acid	$[M-H]^-$	$C_{25}H_{24}O_{12}$	515.118955	515.11906	-0.2	515.11906[a]	173.04774, 179.03630, 191.05560, 135.05289, 161.02838, 155.03984
	Feruloylcaffeoylquinic acid	$[M-H]^-$	$C_{26}H_{26}O_{12}$	529.134605	529.13474	-0.2	529.13474[a]	173.04781
	Standard – Salicylic Acid	$[M-H]^-$	$C_7H_6O_3$	137.023870	137.02411	-1.7	137.02411[a]	-

[a]MS/MS data reported from Robusta Tropical at 100% maturity. [b]MS/MS data reported from Arabica Obata at 100% maturity. High-resolution MS/MS by HCD using a set collision energy of 100 arbitrary units.

6.4.2. Caffeine, Trigonelline and Total Sugar Content in Green Coffee Bean Species Across Stages of Maturity

In this study, we centered on investigating the relative concentrations of green coffee bean metabolites with respect to the standards, caffeine-D9 and salicylic acid, to evaluate changes across green coffee bean species and stages of bean ripeness from 60%, 80% to 100% by means of a relative quantitation approach by (+)ESI-HRMS and (-)ESI-HRMS, respectively. The metabolomic profiles of novel genotypes Diamante 101, 105, and 108 were compared to common coffee species, Arabica and Robusta.

Caffeine is an important bioactive metabolite in green and roasted coffee beans acting as a CNS stimulant, with anti-oxidant and anti-bacterial activities.[230] In this study, caffeine was identified as the ion of *m/z* 195.08840 within the concentration range of 7.7 to 48.5 µM across species and stages of maturity. The highest caffeine concentrations were found in genotypes Diamante 105 and 108 at 41.7 – 48.5 µM and 36.6 – 47.2 µM, respectively, quantities that were higher in comparison to Robusta Tropical and Arabica coffees (Catuai, Obata, Topazio). However, genotype Diamante 101 (18.8 – 26.1 µM) resembled caffeine concentrations more closely to Arabica (Table 6.1 and Figure 6.4). Caffeine content in green coffee beans is generally higher in Robusta species than Arabica.[222,231] At 100% maturity, caffeine in Robusta Tropical compared to Arabica (Catuai, Obata, Topazio) was two- or three-fold higher as expected.[222] Throughout stages of maturity (60%-100%), the caffeine content in Arabica species (Catuai, Obata, and Topazio) slightly decreased with concentrations ranging from 23.7-19.1 µM, 23.5-7.7 µM and 20.8-18.5 µM, respectively (Figure 6.4). In contrast, caffeine in Robusta Tropical (26.0-36.3 µM) increased with bean ripeness 60%-100% and this increasing trend was also found for genotypes Diamante 101, 105, and 108.

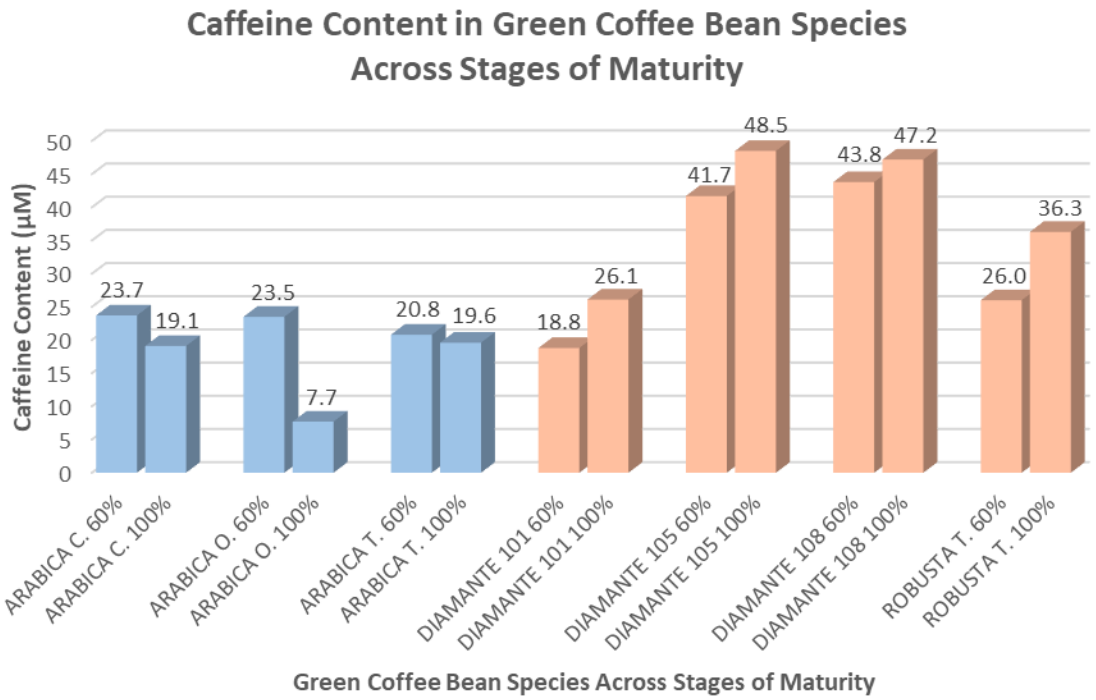

Figure 6.4: Caffeine content in green coffee bean species across stages of maturity. Pink and blue bars represent increases and decreases in caffeine content, respectively.

Trigonelline and carbohydrate influence good coffee quality contributing to its sweetness, colour and aroma formation in the coffee brew.[232] In previous studies, Arabica species have higher trigonelline and sugars than Robusta[233-235] and this trend was also observed in the findings reported in this study. In the HRMS analysis, the sum of the concentration between the positively charged trigonelline ion and the potassium adduct ($[M]^+$ + $[M-H+K]^+$) was defined as the total trigonelline content ranging from 21.9-61.4 µM across all species. Higher trigonelline concentrations were found in Arabica Catuai (59.2-48.9 µM), Topazio (47.5-52.3 µM) and genotypes Diamante 105 (53.1-50.7 µM), Diamante 108 (55.2-60.4 µM) compared to Robusta Tropical (33.1-43.4 µM) and Diamante 101 (29.6-46.3 µM). Diamante 101 presented the lowest trigonelline concentrations comparable to Robusta Tropical. Across stages of maturity, the concentration of trigonelline in Arabica Catuai decreased slightly yet, decreased significantly in

Arabica Obata from 60%-100% maturity. However, trigonelline increased in Arabica Topazio, genotype Diamante 101, Diamante 108 and Robusta Tropical (Table 6.2 and Figure 6.5).

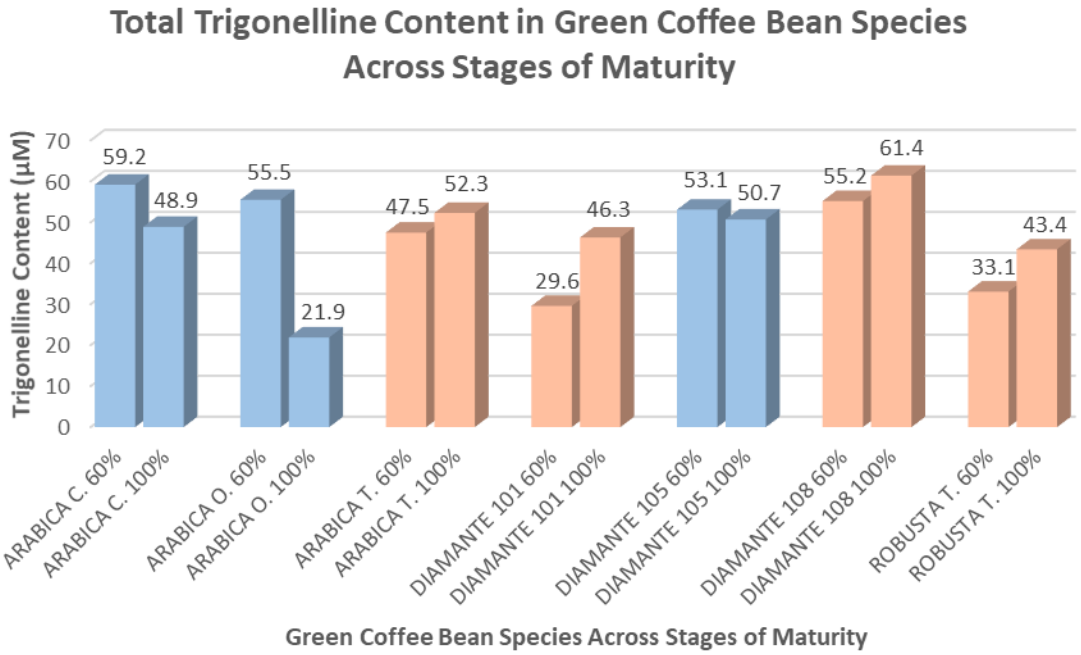

Figure 6.5: Total trigonelline content (the sum of the protonated ion and potassium adduct) in green coffee bean species across stages of maturity. Pink and blue bars represent increases and decreases in trigonelline content, respectively.

The total saccharide content was compared between coffee bean species as the sum of the glucose ($[M+Na]^+$ + $[M+K]^+$) and sucrose ($[M+Na]^+$ + $[M+K]^+$) concentrations (Table 6.2 and Figure 6.6). As expected, Robusta Tropical (6.6-8.1 µM) contained lower total sugar content than Arabica Catuai and Topazio (8.5-13.3 µM and 8.0-12.7 µM), respectively however sugars increased across stages of maturity. Arabica Obata (13.2-4.6 µM) was the only species to significantly decrease in sugar content almost three-fold from 60-100% maturity representing a lower quality coffee in terms of sweetness to Arabica cultivars, Catuai and Topazio. Diamante 108 showed the highest total sugar content which increased across stages of maturity (12.1-16.4 µM). Similarly, Diamante 105 (9.0-9.5 µM) and Diamante 101 (7.3-10.2 µM) showed slightly lower total sugar content than Diamante 108 but also with an increasing trend from 60-100% maturity.

In summary, caffeine, trigonelline and sugars were found with the highest concentrations in genotype Diamante 108, even higher than Arabica cultivars.

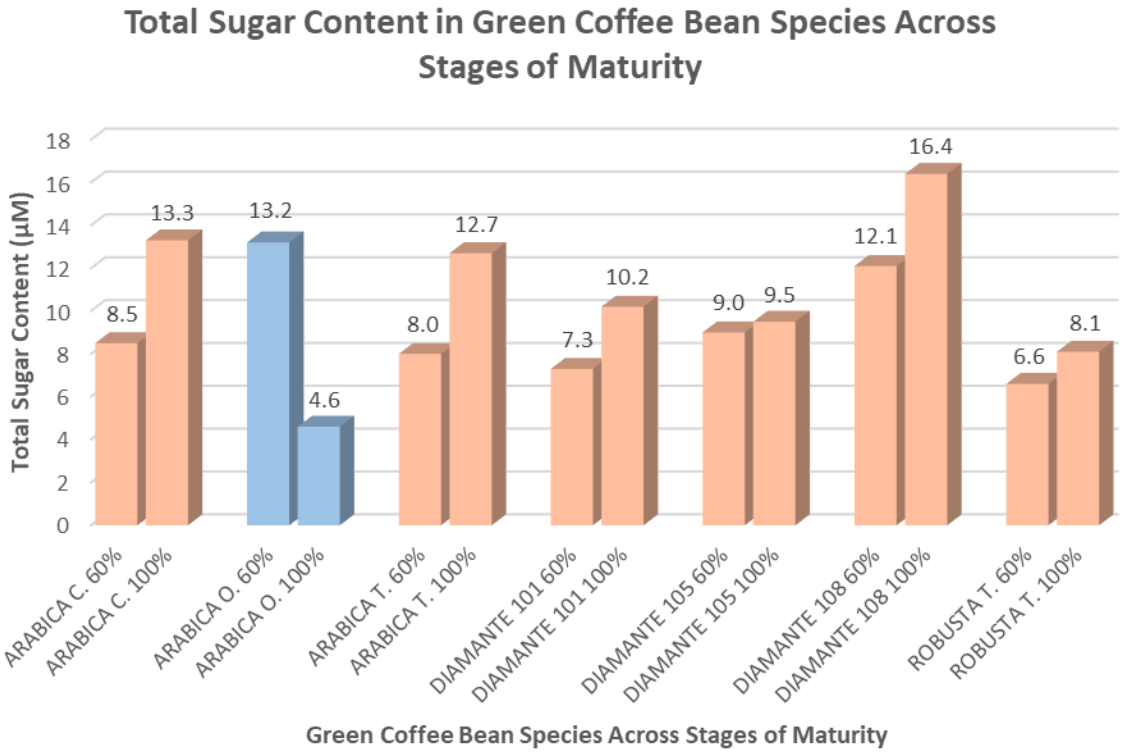

Figure 6.6: Total sugar content in green coffee bean species across stages of maturity. Pink and blue bars represent increases and decreases in sugar content, respectively.

Table 6.2: Caffeine, trigonelline and sugar content (µM) in green coffee species by (+)ESI-HRMS. Reproduced with permission from Lemos et al.[229]

Green Coffee Species	Caffeine-D9 (µM)	Caffeine (µM)	Trigonelline $[M+H]^+ + [M+K]^+$ Sum (µM)	Glucose $[M+Na]^+ + [M+K]^+$ Sum (µM)	Sucrose $[M+Na]^+ + [M+K]^+$ Sum (µM)	Total Sugar[1] (µM)
AC.60	48.7	23.7	59.2	0.1	8.4	8.5
AC.80	48.7	20.6	51.0	1.5	11.6	13.1
AC.100	48.7	19.1	48.9	0.8	12.5	13.3
AO.60	48.7	23.5	55.5	0.5	12.7	13.2
AO.80	48.7	16.3	39.0	1.3	8.1	9.4
AO.100	48.7	7.7	21.9	0.3	4.2	4.6
AT.60	48.7	20.8	47.5	0.2	7.8	8.0
AT.80	48.7	18.5	52.0	1.3	10.4	11.7
AT.100	48.7	19.6	52.3	1.0	11.7	12.7
C101.60	48.7	18.8	29.6	0.3	7.0	7.3
C101.80	48.7	25.4	33.8	3.0	7.2	10.3
C101.100	48.7	26.1	46.3	1.6	8.5	10.2
C105.60	48.7	41.7	53.1	0.2	8.8	9.0
C105.80	48.7	41.8	48.9	0.8	8.4	9.2
C105.100	48.7	48.5	50.7	1.3	8.1	9.5
C108.60	48.7	43.8	55.2	0.4	11.7	12.1
C108.80	48.7	36.6	39.8	1.1	11.0	12.1
C108.100	48.7	47.2	61.4	1.7	14.7	16.4
RT.60	48.7	26.0	33.1	0.2	6.4	6.6
RT.80	48.7	34.7	40.6	0.3	7.5	7.8
RT.100	48.7	36.3	43.4	0.9	7.2	8.1

[1]Sum of the total sugar content (glucose+sucrose).

6.4.3. Phenolic and Chlorogenic Acid Content in Green Coffee Bean Species Across Stages of Maturity

Chlorogenic and phenolic acids are metabolites that influence the quality of coffee. These metabolites are important biomarkers to distinguish between Arabica and Robusta species. Many studies have reported higher concentrations of chlorogenic acids in Robusta than Arabica beans.[221,234,236] Previous studies that have investigated the metabolomic profile of Robusta silverskin presented nearly six times more chlorogenic acids than Arabica.[237] These observations are in agreement with this study, since the highest chlorogenic acid concentrations were found in Robusta Tropical, Diamante 105 and Diamante 108. Compared to Arabia cultivars, Diamante 105 and Robusta Tropical contained nearly two to three times as much caffeoylquinic acid. Among chlorogenic acids, caffeoylquinic acid (CQA) and feruloylquinic acid (FQA) were influenced by the stage of maturity (Table 6.3). The CQA content in Arabica Catuai, Topazio, Obata and Diamante 101 was the lowest among all species across stages of maturity. In Arabica Obata and Topazio, CQA decreased across stages of maturity and slightly increased in Arabica Catuai. The CQA concentration in genotype Diamante 101 (6.1-6.3 µM) and Diamante 108 (9.3-9.0 µM) remained constant throughout the stages of maturity, while in Diamante 105 (11.8-13.0 µM) and Robusta Tropical (8.4-13.6 µM), a slight increase was observed as the bean ripened.

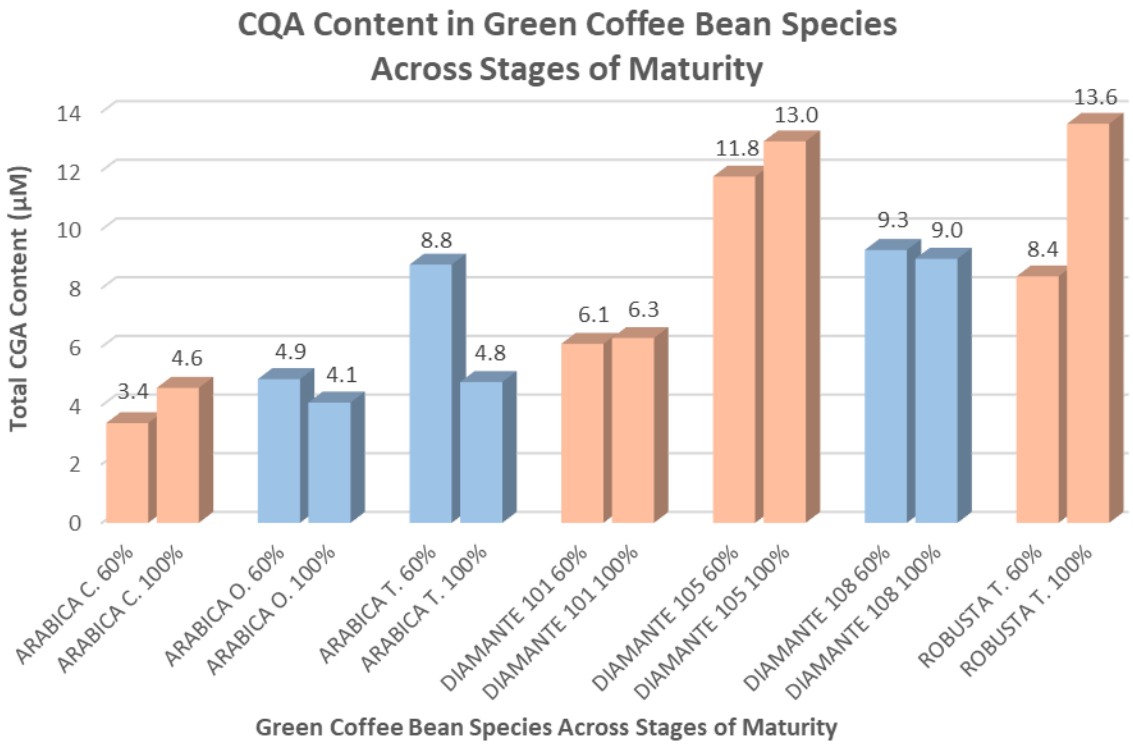

Figure 6.7: Caffeoylquinic acid (CQA) content in green coffee bean species across stages of maturity. Pink and blue bars represent increases and decreases in sugar content, respectively.

Similar to CQA, FQA concentrations were the lowest in all Arabica species, Arabica Catuai (0.5-0.7 µM), Obata (0.7-0.8 µM) and Topazio (1.3-0.7 µM), as shown in Table 6.3. In Arabica Catuai and Topazio, FQA was constant across all stages of maturity and slightly decreased in Arabica Obata. Diamante 101 contained slightly higher FQA content at 1.7-2.1 µM across stages of maturity compared to the Arabica species. On the other hand, higher FQA concentrations of 3.0-4.4 µM were obtained for Robusta Tropical and it was also observed that this metabolite increased as the bean matured. In genotypes Diamante 105 and 108, FQA remained constant across all stages of maturity. Other phenolic and chlorogenic acids, such as caffeic acid, ferulic acid, coumaroylquinic acid, dicaffeoylquinic acids and feruloylcaffeoylquinic acid, were found at low and constant concentrations across green coffee bean species at all stages of maturity. The total chlorogenic acid content as the sum of the concentrations of five chlorogenic acids CoQA, CQA, FQA, DCQA and DFQA can be found below in Figure 6.8.

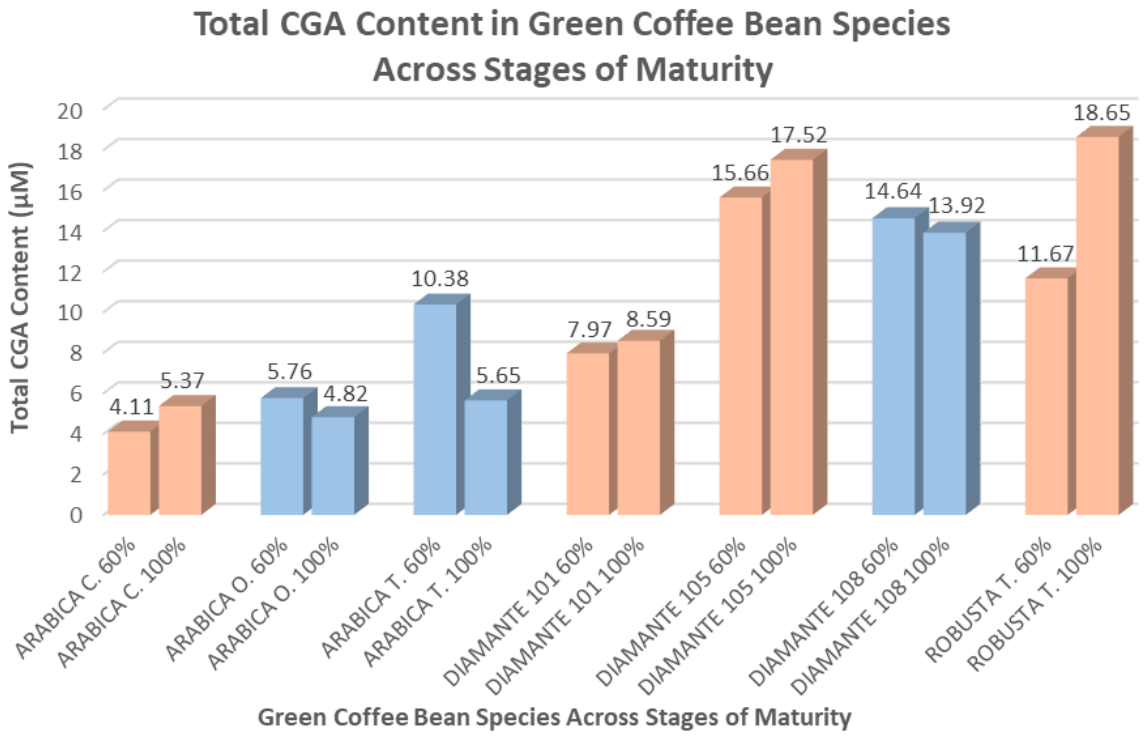

Figure 6.8: Total chlorogenic acid content in green coffee bean species across stages of maturity. Pink and blue bars represent increases and decreases in CGA content, respectively.

Table 6.3: Phenolic and chlorogenic acid content (µM) in different coffee species by (-)ESI-HRMS. Reproduced with permission from Lemos et al.[229]

Green Coffee Species	Salicylic Acid (µM)	Malic Acid (µM)	Caffeic Acid (µM)	Quinic Acid (µM)	Ferulic Acid (µM)	Coumaroyl quinic Acid (µM)	Caffeoyl quinic Acid (µM)	Feruloyl quinic Acid (µM)	Dicaffeoyl quinic Acid (µM)	Feruloyl Caffeoyl quinic Acid (µM)	Total CGA[1] (µM)
AC.60	14.6	0.05	0.01	1.68	0.09	0.01	3.41	0.54	0.15	0.00	4.11
AC.80	14.6	0.23	0.01	1.36	0.01	0.01	3.42	0.52	0.07	0.00	4.02
AC.100	14.6	0.56	0.01	1.60	0.00	0.01	4.60	0.65	0.09	0.00	5.37
AO.60	14.6	0.31	0.01	1.58	0.02	0.01	4.85	0.81	0.09	0.00	5.76
AO.80	14.6	0.56	0.01	1.73	0.05	0.02	4.95	0.85	0.07	0.00	5.89
AO.100	14.6	0.35	0.01	1.32	0.02	0.01	4.09	0.66	0.06	0.00	4.82
AT.60	14.6	1.05	0.04	2.72	0.04	0.12	8.80	1.33	0.13	0.00	10.38
AT.80	14.6	0.65	0.05	2.62	0.06	0.12	8.39	1.21	0.11	0.00	9.84
AT.100	14.6	0.47	0.01	1.43	0.02	0.05	4.85	0.71	0.05	0.00	5.65
C101.60	14.6	0.13	0.02	1.00	0.01	0.02	6.10	1.70	0.12	0.04	7.97
C101.80	14.6	0.14	0.12	0.85	0.02	0.01	4.81	1.37	0.09	0.03	6.32
C101.100	14.6	0.14	0.02	1.12	0.06	0.01	6.29	2.13	0.11	0.05	8.59
C105.60	14.6	0.42	0.28	1.28	0.01	0.05	11.78	3.36	0.37	0.10	15.66
C105.80	14.6	0.35	0.28	1.60	0.02	0.09	13.52	3.87	0.47	0.15	18.11
C105.100	14.6	0.34	0.25	1.42	0.01	0.06	12.97	3.86	0.46	0.16	17.52
C108.60	14.6	0.36	0.04	1.65	0.17	0.01	9.27	4.96	0.21	0.19	14.64
C108.80	14.6	0.23	0.03	1.22	0.01	0.01	7.40	3.52	0.18	0.11	11.21
C108.100	14.6	0.37	0.06	1.62	0.10	0.01	8.96	4.60	0.19	0.16	13.92
RT.60	14.6	0.15	0.20	0.88	0.00	0.02	8.41	2.96	0.21	0.07	11.67
RT.80	14.6	0.11	0.17	1.03	0.00	0.04	10.63	3.47	0.32	0.12	14.58
RT.100	14.6	0.14	0.28	1.44	0.01	0.08	13.59	4.36	0.44	0.18	18.65

CGA: chlorogenic acids. [1]Sum of the chlorogenic acid content (pCoQA + CQA + FQA + DCQA + DFQA)

Acidity is an important characteristic of coffee quality in combination with its sweetness, bitterness and aroma profile.[232] A previous study has shown that coffee fruits contain malic acid, citric acid, quinic acid and tartaric acid and together, these organic acids influence coffee fruit acidity, which favours the quality of the beverage.[238] Here, only malic (MA) and quinic acid (QA) were identified in green coffee beans at different stages of maturity. The MA content changed between species and studied genotypes, with higher concentrations in Arabica species than in Robusta Tropical. Compared with the novel genotypes, Diamante 105 and 108 were similar in MA content to Arabica species, while genotype Diamante 101 was similar to Robusta Tropical. Across stages of maturity, a decrease in the MA content was observed in Arabica Obata and Arabica Topazio, while an increase was observed in Arabica Catuai. In contrast, in genotypes Diamante 101, 105, 108 and Robusta Tropical, MA concentrations remained constant throughout stages of maturity (Table 6.3). QA content did not change between the species and studied genotypes but some variations were observed across stages of maturity. QA slightly increased from 0.9 -1.4 µM in Robusta Tropical and Arabica Obata, whereas QA slightly decreased from 2.7-1.4 µM as the bean matured in Arabica Topazio. Whereas, QA remained constant throughout stages of maturity in Arabica Catuai, Arabica Topazio, and genotypes Diamante 101, 105, and 108 (Table 6.3).

For the metabolomic study, the heat map depicts the overview of the 14 most important bioactive metabolites in green coffee bean species across stages of maturity (Figure 6.9).

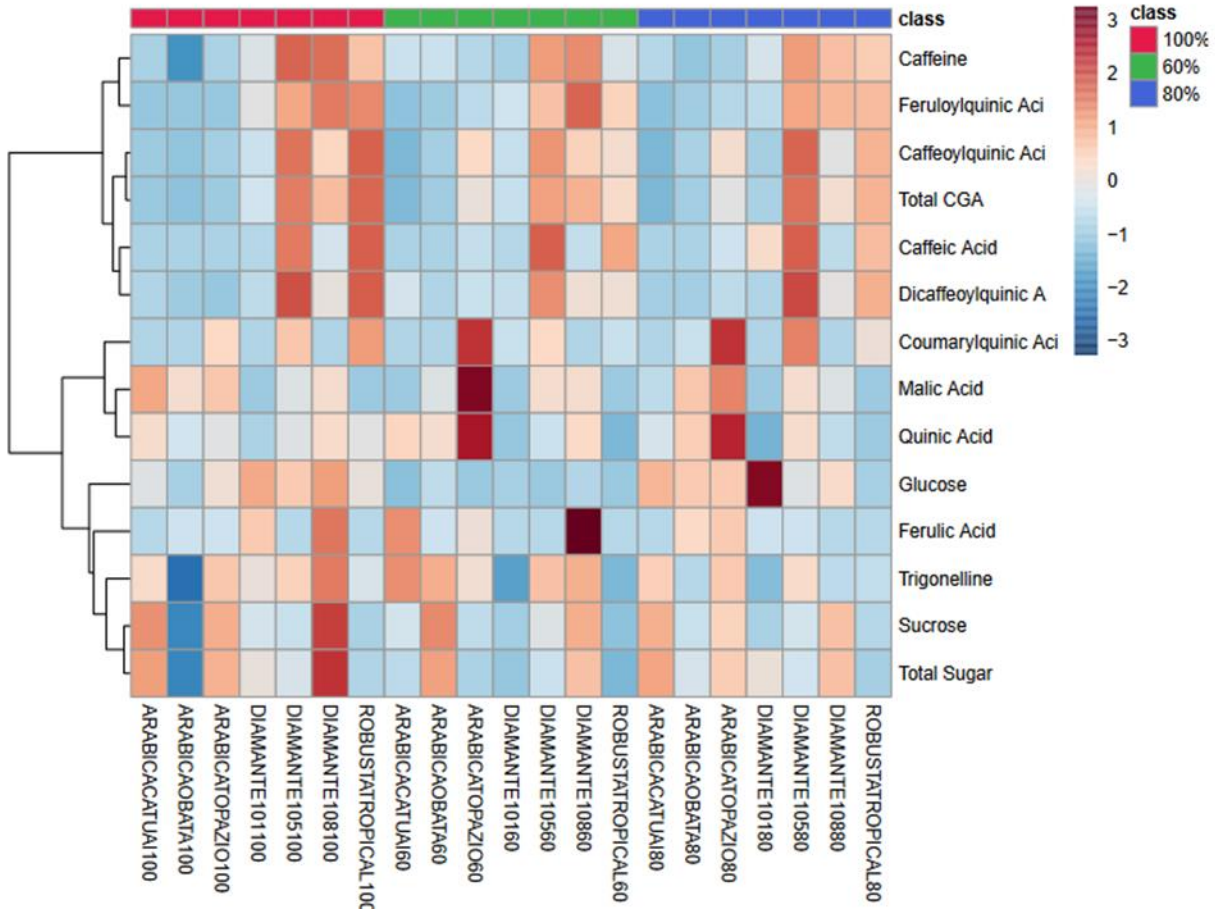

Figure 6.9: The heat map with the dendrogram scaled to represent the distance between each branch by Pearson's correlation. The vertical axis represents 14 bioactive metabolites and the horizontal axis the green coffee bean species. The red clustered data denotes 100% maturity, blue and green represents 80% and 60% maturity, respectively.

Finally, roasted coffee bean species of Arabica Catuai, Obata, Topazio, novel genotypes Diamante 101, 105, 108 and Robusta Tropical at all stages of maturity were subjected to sensory profiling and chemometric analysis by principal component analysis (PCA).[229] The sensory analysis evaluated 11 attributes from roasted coffee beans such as fragrance/aroma, flavour, acidity, sweetness, balance, aftertaste, mouthfeel, body, uniformity, clean cup, defects and

overall quality. Diamante 108 showed the highest quality cup score which was slightly higher or comparable to Arabica species. Diamante 108 (80% and 100%) and Arabica Obata (100%) showed scores of 82, 81 and 81, respectively, and were classified as very good coffees (80-84.99 represent scores of very good quality coffees).[229] The findings from the metabolomic study and the sensory profiling combined with the PCA analysis are in good agreement with respect to the conclusions presented here of the correlations between the metabolome and the quality of novel genotypes Diamante 101, 105, and 108.

6.5. Conclusion

In this study, green coffee bean metabolites such as caffeine, trigonelline, sugars, phenolic and chlorogenic acids were compared between novel genotypes Diamante 101, 105, and 108 across stages of maturity to two common species used for consumption, three cultivars of Arabica (Catuai, Obata, Topazio) and Robusta (Tropical). A relative quantitative ESI-HRMS method was developed to correlate between green coffee bean metabolites and overall bean quality. The novel *Coffea caneffora* species, Diamante 105 and 108 presented higher caffeine, trigonelline, sugars and comparable levels of chlorogenic acids to Arabica and Robusta species. Among the three novel *Coffea canephora* species investigated Diamante 108 presented the most promising coffee bean quality based on its desirable metabolome.

Chapter Seven: Conclusions and Future Work

7.1. Conclusions and Future Work

The work presented in this dissertation was focused on developing rapid, robust, and sensitive atmospheric pressure (ESI-MS) and ambient ionization mass spectrometry techniques (DESI-MS) for the analysis of pharmaceuticals and nutraceuticals. Chapter 2 described the quantitative potential of DESI-MSI by comparing three strategies to add the IS into the analysis to quantify exogenous analytes, such as pharmaceuticals, from *in vitro* dosed snail (*p.diffusa*) tissues. The impact of quantifying exogenous compounds by applying the internal standard as microspots on top of tissues or as a thin film on top of tissues may open new avenues in quantitative DESI-MS imaging. For the most part, since the introduction of DESI-MS in 2004, the technique has been mainly applied for qualitative analysis, for the identification of unknown compounds and mapping the spatial distribution of drugs and metabolites from tissue sections. In this work, we performed a comprehensive method validation to show that the technique can be used for quantitative purposes and that DESI-MS abides to all of the analytical figures of merit of precision, accuracy, and linearity set out by the guidelines of the FDA.

In future DESI-MSI studies, the development of an isotope dilution mass spectrometry method, by first using double isotope dilution to ascertain an accurate concentration of the isotopically labelled standard, and later the quantification of the analyte from the tissue section by isotope dilution, (using the known concentration of the isotopically labelled standard) can provide even better precisions and accuracies for quantitative DESI-MSI. Further investigations could also be centred on the quantification of endogenous metabolites, analytes originally present in the tissue matrix, from *in vitro* dosed tissue sections. The validation of these methods could give better insights towards the precision and accuracy of DESI-MSI to quantify both, exogenous and endogenous types of analytes.

In chapters 3, 4 and 5, coupling HPTLC and RPTLC to DESI-MS or DESI-MS^n for the analysis of bioactive secondary metabolites offered an in-depth characterization that added a supplementary layer of chemical information from the separation of chemically similar analytes, such as structural isomers and isobaric ions. The impact of these DESI-MS methods allowed for

the discovery of new phytochemicals with important biological activities from their functional roles in plant defence mechanisms in the species investigated (*L. peruvianum*, *S. albidum* and *O. spixiana*). Novel secondary metabolites such as glycosylated ascorbigens and dihydroascorbigens, hydroxylated fatty acids, benzylisoquinoline and aporphine alkaloids were discovered for the first time in the plant species under investigation, as a result of the development of sensitive methods for low abundance compounds from complex tissue matrices. In the last decade, the global demand and interest of novel compounds from natural sources with biological activities and medicinal properties has seen a rapid increase. Novel compounds, such as phytoanticipins, could provide a solution to fight against the increasing microbial resistance associated with common broad-spectrum antibiotics used to treat a wide range of infections in the clinic. The secondary metabolites discovered in this work could have potential uses as lead compounds in therapeutics for the treatment of infections for clinical applications. In future studies, the discovery of novel compounds from plant sources by DESI-MS and DESI-MS^n could be improved, for example, by modifying the surface chemistry in TLC in order to separate a wider range of analyte polarities. The simultaneous separation of polar and non-polar analytes in a single analysis could increase even further the speed and high throughput capabilities of DESI-MS. Surface modifications in TLC such as, functionalizing the surface to include both hydrophilic and hydrophobic components by creating a polarity gradient on the surface, or implementing a two-dimensional TLC separation (x and y-dimensional separations) by using different mobile phase systems in each spatial direction could help in separating analytes with very different polarities.

Finally, in chapter 6, the quantification of important sensory metabolites involved in regulating the flavour and aroma of green coffee beans across species and stages of development was analyzed by ESI-MS using a targeted MS/MS mode by data dependant acquisition. This method presented a fast metabolomic screening of new coffee genotypes to correlate their complex metabolome with the quality of the coffee bean. The targeted tandem mass spectrometry method by DDA and spiking isotopically labelled standards and stucutral analogs directly in the green coffee bean cultivars across stages of bean maturity allowed for the rapid identification and quantification with minimal sample preparation required, while

obtaining metabolite concentrations that correlate to those reported by other studies in the literature. Ambient and atmospheric pressure mass spectrometry will continue to be powerful and robust techniques to help solve a range of biologically relevant problems in many fields of applications (metabolomics, lipidomics, clinical, and forensic analysis) and aid in the rapid discovery and emergence of novel compounds without the need of laborious, cumbersome and intensive sample preparations.

REFERENCES

(1) Thomson, J. J. *Philos. Mag.* **1897**, *44*, 293-316.
(2) Münzenberg, G. *Int. J. Mass spectrom.* **2013**, *349-350*, 9-18.
(3) Fenn, J. B.; Mann, M.; Meng, C. K.; Wong, S. F.; Whitehouse, C. M. *Science* **1989**, *246*, 64-71.
(4) Monge, M. E.; Harris, G. A.; Dwivedi, P.; Fernández, F. M. *Chem. Rev.* **2013**, *113*, 2269-2308.
(5) Konermann, L.; Ahadi, E.; Rodriguez, A. D.; Vahidi, S. *Anal. Chem.* **2013**, *85*, 2-9.
(6) Ahadi, E.; Konermann, L. *The Journal of Physical Chemistry B* **2012**, *116*, 104-112.
(7) Banerjee, S.; Mazumdar, S. *Int. J. Anal. Chem.* **2012**, *2012*, 1-40.
(8) Perez, C. J.; Bagga, A. K.; Prova, S. S.; Yousefi-Taemeh, M.; Ifa, D. R. *Rapid Commun. Mass Spectrom.* **2019**, *33*, 27-53.
(9) Li L.H; Hsieh H.Y; C.C, H. *Mass Spectrom (Tokyo)* **2017**, *6*.
(10) Venter, A. R.; Douglass, K. A.; Shelley, J. T.; Hasman, G.; Honarvar, E. *Anal. Chem.* **2014**, *86*, 233-249.
(11) Takats, Z.; Wiseman, J. M.; Gologan, B.; Cooks, R. G. *Science* **2004**, *306*, 471-473.
(12) Cody, R. B.; Laramee, J. A.; Durst, H. D. *Anal. Chem.* **2005**, *77*, 2297-2302.
(13) Venter, A.; Nefliu, M.; Cooks, R. G. *Trends Anal Chem* **2008**, *27*, 284-290.
(14) Haapala, M.; Pól, J.; Saarela, V.; Arvola, V.; Kotiaho, T.; Ketola, R. A.; Franssila, S.; Kauppila, T. J.; Kostiainen, R. *Anal. Chem.* **2007**, *79*, 7867-7872.
(15) Huang, M. Z.; Cheng, S. C.; Cho, Y. T.; Shiea, J. *Analytica Chimica Acta* **2011**, *702*, 1-15.
(16) Smoluch, M.; Mielczarek, P.; Silberring, J. *Mass Spectrom. Rev.* **2016**, *35*, 22-34.
(17) Laskin, J.; Lanekoff, I. *Anal. Chem.* **2016**, *88*, 52-73.
(18) Abraham, K.; Tawiah, B.; Eberlin, L. S.; Zheng, O.; Cooks, R. G. *Annu. Rev. Phys. Chem* **2013**, *64*, 481-505.
(19) Flanigan, P.; Levis, R. *Annu Rev Anal Chem* **2014**, *7*, 229-256.
(20) Kertesz, V.; Van Berkel, G. J.; Vavrek, M.; Koeplinger, K. A.; Schneider, B. B.; Covey, T. R. *Anal. Chem.* **2008**, *80*, 5168-5177.
(21) Wiseman, J. M.; Ifa, D. R.; Zhu, Y.; Kissinger, C. B.; Manicke, N. E.; Kissinger, P. T.; Cooks, R. G. *Proc. Natl. Acad. Sci. USA* **2008**, *105*, 18120-18125.
(22) Vismeh, R.; Waldon, D. J.; Teffera, Y.; Zhao, Z. Y. *Anal. Chem.* **2012**, *84*, 5439-5445.
(23) Muramoto, S.; Forbes, T. P.; van Asten, A. C.; Gillen, G. *Anal. Chem.* **2015**, *87*, 5444-5450.
(24) J. Liu, J. G., K. P. Ganley, R. Vismeh, Y. Teffera; Zhao, a. Z. *Rapid Commun. Mass Spectrom.* **2014**, *28*, 185-190.
(25) Khatami, A.; Prova, S. S.; Ting, M. Y. C.; Brar, G.; Ifa, D. R. *Rapid Commun. Mass Spectrom.* **2017**, *31*, 983-990.
(26) Ifa, D. R.; Gumaelius, L. M.; Eberlin, L. S.; Manicke, N. E.; Cooks, R. G. *Analyst* **2007**, *132*, 461-467.
(27) Mirabelli, M. F.; Chramow, A.; Cabral, E. C.; Ifa, D. R. *J. Mass Spectrom.* **2013**, *48*, 774-778.
(28) Sica, V. P.; Raja, H. A.; El-Elimat, T.; Oberlies, N. H. *RSC Adv* **2014**, *4*, 63221-63227.
(29) Tata, A.; Perez, C. J.; Hamid, T. S.; Bayfield, M. A.; Ifa, D. R. *J. Am. Soc. Mass. Spectrom.* **2015**, *26*, 641-648.
(30) Tata, A.; Perez, C. J.; Ore, M. O.; Lostun, D.; Passas, A.; Morin, S.; Ifa, D. R. *RSC Adv* **2015**, *5*, 75458-75464.

(31) Tata, A.; Perez, C.; Campos, M. L.; Bayfield, M. A.; Eberlin, M. N.; Ifa, D. R. *Anal. Chem.* **2015**, *87*, 12298-12305.
(32) Sica, V. P.; Raja, H. A.; El-Elimat, T.; Oberlies, N. H. *RSC Adv* **2014**, *4*, 63221-63227.
(33) Cabral, E. C.; Mirabelli, M. F.; Perez, C. J.; Ifa, D. R. *J. Am. Soc. Mass. Spectrom.* **2013**, *24*, 956-965.
(34) Muller, T.; Oradu, S.; Ifa, D. R.; Cooks, R. G.; Krautler, B. *Anal. Chem.* **2011**, *83*, 5754–5761.
(35) Garrett, R.; Rezende, C. M.; Ifa, D. R. *LWT-Food SciTechnol* **2016**, *65*, 711-717.
(36) Kumara, P. M.; Srimany, A.; Ravikanth, G.; Shaanker, R. U.; Pradeep, T. *Phytochemistry* **2015**, *116*, 104-110.
(37) Kumara, P. M.; Srimany, A.; Arunan, S.; Ravikanth, G.; Shaanker, R. U.; Pradeep, T. *PLoS One* **2016**, *11*, 1-14.
(38) Freitas, J. R. L.; Vendramini, P. H.; Melo, J. O. F.; Eberlin, M. N.; Augusti, R. *J. Braz. Chem. Soc.* **2018**, *29*, 17-23.
(39) Perez, C. J.; Tata, A.; de Campos, M. L.; Peng, C.; Ifa, D. R. *J. Am. Soc. Mass. Spectrom.* **2017**, *28*, 1136-1148.
(40) Pirro, V.; Guffey, S. C.; Sepulveda, M. S.; Mahapatra, C. T.; Ferreira, C. R.; Jarmusch, A. K.; Cooks, R. G. *Mol. Biosyst.* **2016**, *12*, 2069-2079.
(41) Gerbig, S.; Brunn, H. E.; Spengler, B.; Schulz, S. *Anal. Bioanal. Chem.* **2015**, *407*, 7379-7389.
(42) Alfaro, C. M.; Jarmusch, A. K.; Pirro, V.; Kerian, K. S.; Masterson, T. A.; Cheng, L.; Cooks, R. G. *Anal. Bioanal. Chem.* **2016**, *408*, 5407-5414.
(43) Calligaris, D.; Caragacianu, D.; Liu, X.; Norton, I.; Thompson, C. J.; Richardson, A. L.; Golshan, M.; M.L., E.; Santagata, S.; Dillon, D. A.; Jolesz, F. A.; Agar, N. Y. *Proc Natl Acad Sci* **2014**, *42*.
(44) Woolman, M.; Tata, A.; Bluemke, E.; Dara, D.; Ginsberg, H. J.; Zarrine-Afsar, A. *J. Am. Soc. Mass. Spectrom.* **2017**, *28*, 145-153.
(45) Inglese, P.; McKenzie, J. S.; Mroz, A.; Kinross, J.; Veselkov, K.; Holmes, E.; Takats, Z.; Nicholson, J. K.; Glen, R. C. *Chem. Sci.* **2017**, *8*, 3500-3511.
(46) Zhang, J. L.; Feider, C. L.; Nagi, C.; Yu, W. D.; Carter, S. A.; Suliburk, J.; Cao, H. S. T.; Eberlin, L. S. *J. Am. Soc. Mass. Spectrom.* **2017**, *28*, 1166-1174.
(47) Pirro, V.; Jarmusch, A. K.; Alfaro, C. M.; Hattab, E. M.; Cohen-Gadol, A. A.; Cooks, R. G. *Analyst* **2017**, *142*, 449-454.
(48) Bilkey, J.; Tata, A.; McKee, T. D.; Porcari, A. M.; Bluemke, E.; Woolman, M.; Ventura, M.; Eberlin, M. N.; Zarrine-Afsar, A. *Anal. Chem.* **2016**, *88*, 12099-12107.
(49) Tata, A.; Zheng, J.; Ginsberg, H. J.; Jaffrey, D. A.; Ifa, D. R.; Zarrine-Afsar, A. *Anal. Chem.* **2015**, *87*, 7683-7689.
(50) Gerbig, S.; Golf, O.; Balog, J.; Denes, J.; Baranyai, Z.; Zarand, A.; Raso, E.; Timar, J.; Takats, Z. *Anal. Bioanal. Chem.* **2012**, *403*, 2315-2325.
(51) Luo, Z.; He, J.; Chen, Y.; Gong, T.; Tang, F.; Wang, X.; Zhang, R.; Huang, L.; Zhang, L.; Lv, H.; Ma, S.; Fu, Z.; Chen, X.; Yu, S.; Abliz, Z. *Anal. Chem.* **2013**, *85*, 2977-2982.
(52) Haddad, R.; Milagre, H. M. S.; Catharino, R. R.; Eberlin, M. N. *Anal. Chem.* **2008**, *80*, 2744-2750.
(53) Roach, P. J.; Laskin, J.; Laskin, A. *Analyst* **2010**, *135*, 2161-2452.
(54) Nemes, P.; Vertes, A. *Anal. Chem.* **2007**, *79*, 8098-8106.
(55) Brady, J. J.; Judge, E. J.; Levis, R. J. *Pro Natl Acad Sci USA* **2011**, *108*, 12217-12222.

(56) Pan, N.; Rao, W.; Kothapalli, N. R.; Liu, R.; Burgett, A. W. G.; Yang, Z. *Anal. Chem.* **2014**, *86*, 9376-9380.
(57) Coon, J. J.; McHale, K. J.; Harrison, W. W. *Rapid Commun. Mass Spectrom.* **2002**, *16*, 681-685.
(58) Lorenz, M.; Ovchinnikova, O. S.; Van Berkel, G. J. *Rapid Commun. Mass Spectrom.* **2014**, *28*, 1312-1320.
(59) Lorenz, M.; Ovchinnikova, O. S.; Kertesz, V.; Van Berkel, G. J. *Anal. Chem.* **2014**, *86*, 3146-3152.
(60) Otsuka, Y.; Shide, S.; Naito, J.; Kyogaku, M.; Hashimoto, H.; Arakawa, R. *Rapid Commun. Mass Spectrom.* **2012**, *26*, 2725-2732.
(61) Takats, Z.; Cotte-Rodriguez, I.; Talaty, N.; Chen, H.; Cooks, R. G. *Chem. Commun.* **2005**, 1950-1952.
(62) Haapala, M.; Pól, J.; Saarela, V.; Arvola, V.; Kotiaho, T.; Ketola, R.; Franssila, S.; Kauppila, T.; Kostiainen, R. *Anal. Chem.* **2007**, *79*, 7867-7872.
(63) Fowble, K. L.; Teramoto, K.; Cody, R. B.; Edwards, D.; Guarrera, D.; Musah, R. A. *Anal. Chem.* **2017**, *89*, 3421-3429.
(64) Zou, J.; Talbot, F.; Tata, A.; Ermini, L.; Franjic, K.; Ventura, M.; Zheng, J. Z.; Ginsberg, H.; Post, M.; Ifa, D. R.; Jaffray, D.; Miller, R. J. D.; Zarrine-Afsar, A. *Anal. Chem.* **2015**, *87*, 12071-12079.
(65) Eikel, D.; Vavrek, M.; Smith, S.; Bason, C.; Yeh, S.; Korfmacher, W. A.; Henion, J. D. *Rapid Commun. Mass Spectrom.* **2011**, *25*, 3587-3596.
(66) Venter, A.; Sojka, P. E.; Cooks, R. G. *Anal. Chem.* **2006**, *78*, 8549-8555.
(67) Takats, Z.; Wiseman, J. M.; Cooks, R. G. *J. Mass Spectrom.* **2005**, *40*, 1261-1275.
(68) Wu, C.; Dill, A. L.; Eberlin, L. S.; Cooks, R. G.; Ifa, D. R. *Mass Spectrom. Rev.* **2013**, *32*, 218-243.
(69) Bennett, R. V.; Gamage, C. M.; Fernandez, F. M. *Jove-Journal of Visualized Experiments* **2013**.
(70) Nazari, M.; Bokhart, M. T.; Muddiman, D. C. *Jove-Journal of Visualized Experiments* **2016**.
(71) Bodzon-Kulakowska, A.; Drabik, A.; Ner, J.; Kotlinska, J. H.; Suder, P. *Rapid Commun. Mass Spectrom.* **2014**, *28*, 1-9.
(72) Lostun, D.; Perez, C. J.; Licence, P.; Barrett, D. A.; Ifa, D. R. *Anal. Chem.* **2015**, *87*, 3286-3293.
(73) Campbell, D. I.; Ferreira, C. R.; Eberlin, L. S.; Cooks, R. G. *Anal. Bioanal. Chem.* **2012**, *404*, 389–398.
(74) Hecht, E. S.; Scigelova, M.; Eliuk, S.; Makarov, A. In *Encyclopedia of Analytical Chemistry*, Meyers, R. A., Ed., 2020, pp 1-40.
(75) Raymond, M. E. *Int. J. Mass Spectrom. Ion Processes* **1992**, *118-119*, 71-135.
(76) *LTQ Series Hardware Manual*; Thermo Fisher Scientific, 2009, p 1-165.
(77) *LTQ Series Hardware Manual*; Thermo Fisher Scientific, 2015, p 1-172.
(78) Michalski, A.; Damoc, E.; Lange, O.; Denisov, E.; Nolting, D.; Müller, M.; Viner, R.; Schwartz, J.; Remes, P.; Belford, M.; Dunyach, J.-J.; Cox, J.; Horning, S.; Mann, M.; Makarov, A. *Mol. Cell. Proteomics* **2012**, *11*, O111.013698.
(79) Michalski, A.; Damoc, E.; Hauschild, J.-P.; Lange, O.; Wieghaus, A.; Makarov, A.; Nagaraj, N.; Cox, J.; Mann, M.; Horning, S. *Mol. Cell. Proteomics* **2011**, *10*, M111.011015.
(80) Eliuk, S.; Makarov, A. *Annu. Rev. Anal. Chem. (Palo Alto Calif.)* **2015**, *8*, 61-80.
(81) Gocan, S. *J. Chromatogr. Sci.* **2002**, *40*, 1-12.
(82) *Handbook of Thin Layer Chromatography*; Marcel Dekker: New York, 2003; Vol. 89.
(83) Ford, M. J.; Van Berkel, G. J. *Rapid Commun. Mass Spectrom.* **2004**, *18*, 1303-1309.

(84) Ford, M. J.; Deibel, M. A.; Tomkins, B. A.; Van Berkel, G. J. *Anal. Chem.* **2005**, *77*, 4385-4389.
(85) Van Berkel, G. J.; Ford, M. J.; Deibel, M. A. *Anal. Chem.* **2005**, *77*, 1207-1215.
(86) Van Berkel, G. J.; Tomkins, B. A.; Kertesz, V. *Anal. Chem.* **2007**, *79*, 2778-2789.
(87) Vismeh, R.; Waldon, D. J.; Teffera, Y.; Zhao, Z. *Anal. Chem.* **2012**, *84*, 5439-5445.
(88) Ellis, S. R.; Bruinen, A. L.; Heeran, R. M. A. *Anal. Bioanal. Chem.* **2014**, *406*, 1275-1289.
(89) Ifa, D. R.; Manicke, N. E.; Rusine, A. L.; Cooks, R. G. *Rapid Commun. Mass Spectrom.* **2008**, *22*, 503-510.
(90) Källback, P.; Shariatgorji, M.; Nilsson, A.; Andrén, P. E. *J. Proteomics* **2012**, *75*, 4941-4951.
(91) Chumbley, C. W.; Reyzer, M. L.; Allen, J. L.; Marriner, G. A.; Via, L. E.; Barry, C. E. I.; Caprioli, R. M. *Anal. Chem.* **2016**, *88*, 2392-2398.
(92) Fields, P. G.; Fleurat-Lessard, F.; Lavenseau, L.; Gérard, F.; Peypelut, L.; Bonnot, G. *J. Insect Physiol.* **1998**, *44*, 955-965.
(93) Matsukura, K.; Izumi, Y.; Yoshida, K.; Wada, T. *Freshwat. Biol.* **2016**, *61*, 80-87.
(94) Löscher, W.; Rogawski, M. A. *Epilepsia* **2012**, *53*, 12-25.
(95) La Vecchia, C.; Negri, E. *Eur. J. Cancer Prev.* **2014**, *23*, 1-7.
(96) Schwartz-Porsche, D.; LÖScher, W.; Frey, H. H. *J. Vet. Pharmacol. Ther.* **1985**, *8*, 113-119.
(97) *Guidance for Industry Q2B Validation of Analytical Procedures: Methodology*; U.S. Department of Health and Human Services. Food and Drug Administration (FDA). Center for Drug Evaluation Research (CDER). Center for Biologics Evaluation and Research (CBER): Silver Spring, MD, 1996, p 1-10.
(98) *Analytical Procedures and Methods Validation for Drugs and Biologics Guidance for Industry*; U.S. Department of Health and Human Services. Food and Drug Administration (FDA). Center for Drug Evaluation and Research (CDER). Center for Biologics Evaluation and Research (CBER): Silver Spring, MD, 2015, p 1-18.
(99) Manicke, N. E.; Wiseman, J. M.; Ifa, D. R.; Cooks, R. G. *J. Am. Soc. Mass. Spectrom.* **2008**, *19*, 531-543.
(100) Dill, A. L.; Ifa, D. R.; Manicke, N. E.; Ouyang, Z.; Cooks, R. G. *J. Chromatogr. B Analyt. Technol. Biomed. Life Sci.* **2009**, *877*, 2883-2889.
(101) Eberlin, L. S.; Ferreira, C. R.; Dill, A. L.; Ifa, D. R.; Cooks, R. G. *Biochim. Biophys. Acta* **2011**, *1811*, 946-960.
(102) Eberlin, L. S.; Ifa, D. R.; Wu, C.; Cooks, R. G. *Angew. Chem. Int. Ed.* **2010**, *49*, 873-876.
(103) Woods, A. S.; Colsch, B.; Jackson, S. N.; Post, J.; Baldwin, K.; Roux, A.; Hoffer, B.; Cox, B. M.; Hoffer, M.; Rubovitch, V.; Pick, C. G.; Schultz, J. A.; Balaban, C. *ACS Chem. Neurosci.* **2013**, *4*, 594-600.
(104) Blaževic, I. *J Bioorg & Org Chem.* **2014**, *1*, 1-4.
(105) Gonzales, G. F. *Evid. Based Complement. Alternat. Med.* **2012**, *2012*, 1-10.
(106) Tafuri, S.; Cocchia, N.; Carotenuto, D.; Vassetti, A.; Staropoli, A.; Mastellone, V.; Peretti, V.; Ciotola, F.; Albarella, S.; Del Prete, C.; Palumbo, V.; Esposito, L.; Vinale, F.; Ciani, F. *Molecules* **2019**, *24*, 1981.
(107) Zhou, Y., Li, P., Branter, A., Wang, H., Shu, X., Yang, J., Si, N., Han, L., Zhao, H., Bian, B. *Sci. Rep.* **2017**, *7*, 44660.
(108) Rubio, J.; Caldas, M.; Dávila, S.; Gasco, M.; Gonzales, G. F. *BMC Complement. Altern. Med.* **2006**, *6*, 1-23.
(109) Ai, Z.; Cheng, A.-F.; Yu, Y.-T.; Yu, L.-J.; Jin, W. *J. Med. Food* **2014**, *17*, 535-542.

(110) Gonzales, G. F.; Ruiz, A.; Gonzales, C.; Villegas, L.; Cordova, A. *Asian journal of andrology* **2001**, *3*, 231-233.
(111) Del Prete, C.; Tafuri, S.; Ciani, F.; Pasolini, M. P.; Ciotola, F.; Albarella, S.; Carotenuto, D.; Peretti, V.; Cocchia, N. *Andrology* **2018**, *6*, 351-361.
(112) Zhou, Y.; Li, P.; Brantner, A.; Wang, H.; Shu, X.; Yang, J.; Si, N.; Han, L.; Zhao, H.; Bian, B. *Sci. Rep.* **2017**, *7*, 44660-44660.
(113) Huang, Y., Peng, X., Qiu, M. *Natural Products and Bioprospecting* **2018**, *8*, 405-412.
(114) Bai, N.; He, K.; Roller, M.; Lai, C.-S.; Bai, L.; Pan, M.-H. *J. Agric. Food. Chem.* **2015**, *63*, 2458-2463.
(115) Bennett, R. C., Mellon, F.A, Kroon, P.A. *J. Agric. Food Chem.* **2004**, *52*, 428-438.
(116) De Nicola, G. R.; Nyegue, M.; Montaut, S.; Iori, R.; Menut, C.; Tatibouët, A.; Rollin, P.; Ndoyé, C.; Zollo, P.-H. A. *Phytochemistry* **2012**, *73*, 51-56.
(117) Wittstock, U.; Agerbirk, N.; Stauber, E. J.; Olsen, C. E.; Hippler, M.; Mitchell-Olds, T.; Gershenzon, J.; Vogel, H. *Proc. Natl. Acad. Sci. U.S.A.* **2004**, *101*, 4859.
(118) Ishida, M.; Kakizaki, T.; Ohara, T.; Morimitsu, Y. *Breeding Science* **2011**, *61*, 208-211.
(119) Ifa, D. R.; Srimany, A.; Eberlin, L. S.; Naik, H. R.; Bhat, V.; Cooks, R. G.; Pradeep, T. *Anal Methods* **2011**, *3*, 1910–1912.
(120) Wiseman, J. M.; Ifa, D. R.; Song, Q.; Cooks, R. G. *Angew. Chem. Int. Ed. Engl.* **2006**, *45*, 7188-7192.
(121) Bjarnholt, N.; Li, B.; D'Alvise, J.; Janfelt, C. *Nat. Prod. Rep.* **2014**, *31*, 818-837.
(122) Conceição, R. S.; Reis, I. M. A.; Cerqueira, A. P. M.; Perez, C. J.; Junior, M. C. d. S.; Branco, A.; Ifa, D. R.; Botura, M. B. *Phytochem. Anal* **2020**, *n/a*.
(123) Hemalatha, R. G.; Pradeep, T. *J. Agric. Food. Chem.* **2013** *61*, 7477−7487.
(124) Doheny-Adams, T.; Redeker, K.; Kittipol, V.; Bancroft, I.; Hartley, S. E. *Plant methods* **2017**, *13*, 17.
(125) Belov, M. E.; Ellis, S. R.; Dilillo, M.; Paine, M. R. L.; Danielson, W. F.; Anderson, G. A.; de Graaf, E. L.; Eijkel, G. B.; Heeren, R. M. A.; McDonnell, L. A. *Anal. Chem.* **2017**, *89*, 7493-7501.
(126) Meissner, H. O.; Mscisz, A.; Mrozikiewicz, M.; Baraniak, M.; Mielcarek, S.; Kedzia, B.; Piatkowska, E.; Jólkowska, J.; Pisulewski, P. *International journal of biomedical science : IJBS* **2015**, *11*, 131-145.
(127) Piacente, S.; Carbone, V.; Plaza, A.; Zampelli, A.; Pizza, C. *J. Agric. Food. Chem.* **2002**, *50*, 5621-5625.
(128) Blažević, I.; Montaut, S.; Burčul, F.; Olsen, C. E.; Burow, M.; Rollin, P.; Agerbirk, N. *Phytochemistry* **2020**, *169*, 112100.
(129) Clément, C.; Diaz, D.; Manrique, I.; Avula, B.; Khan, I. A.; Ponce Aguirre, D. D.; Kunz, C.; Mayer, A. C.; Kreuzer, M. *Agron. J.* **2010**, *102*, 431-439.
(130) Clément, C.; Diaz Grados, D. A.; Avula, B.; Khan, I. A.; Mayer, A. C.; Ponce Aguirre, D. D.; Manrique, I.; Kreuzer, M. *J. Sci. Food Agric.* **2010**, *90*, 861-869.
(131) Gonzales, G. F.; Miranda, S.; Nieto, J.; Fernández, G.; Yucra, S.; Rubio, J.; Yi, P.; Gasco, M. *Reprod. Biol. Endocrinol.* **2005**, *3*, 5-5.
(132) Rubio, J.; Qiong, W.; Liu, X.; Jiang, Z.; Dang, H.; Chen, S.-L.; Gonzales, G. F. *Evid. Based Complement. Alternat. Med.* **2011**, *2011*, 1-7.
(133) Rubio, J.; Dang, H.; Gong, M.; Liu, X.; Chen, S.-L.; Gonzales, G. F. *Food Chem. Toxicol.* **2007**, *45*, 1882-1890.

(134) Gonzales, C.; Rubio, J.; Gasco, M.; Nieto, J.; Yucra, S.; Gonzales, G. F. *J. Ethnopharmacol.* **2006**, *103*, 448-454.
(135) Buskov, S.; Hansen, L. B.; Olsen, C. E.; Sørensen, J. C.; Sørensen, H.; Sørensen, S. *J. Agric. Food. Chem.* **2000**, *48*, 2693-2701.
(136) Montaut, S.; Bleeker, R. S. *Carbohydr. Res.* **2010**, *345*, 1968-1970.
(137) Pedras, M. S.; Zheng, Q. A.; Strelkov, S. *J. Agric. Food. Chem.* **2008**, *56*, 9949-9961.
(138) Esparza, E.; Hadzich, A.; Kofer, W.; Mithöfer, A.; Cosio, E. G. *Phytochemistry* **2015**, *116*, 138-148.
(139) Almukadi, H.; Wu, H.; Böhlke, M.; Kelley, C. J.; Maher, T. J.; Pino-Figueroa, A. *Mol. Neurobiol.* **2013**, *48*, 333-339.
(140) Badu-Tawiah, A.; Bland, C.; Campbell, D. I.; Cooks, R. G. *J. Am. Soc. Mass. Spectrom.* **2010**, *21*, 572-579.
(141) Melnikovova, I.; Havlik, J.; Cusimamani, E. F.; Milella, L. *Boletin Latinoamericano Y Del Caribe De Plantas Medicinales Y Aromaticas* **2012**, *11*, 420-427.
(142) Yang, N.-Y.; Yang, Y.-F.; Li, K. *Journal of Pharmaceutics* **2013**, *2013*, 874875.
(143) Cui, B.; Zheng, B. L.; He, K.; Zheng, Q. Y. *J. Nat. Prod.* **2003**, *66*, 1101-1103.
(144) Tsukamoto, S.; Takeuchi, T.; Rotinsulu, H.; Mangindaan, R. E.; van Soest, R. W.; Ukai, K.; Kobayashi, H.; Namikoshi, M.; Ohta, T.; Yokosawa, H. *Bioorg. Med. Chem. Lett.* **2008**, *18*, 6319-6320.
(145) Gross, H.; Kehraus, S.; König, G. M.; Woerheide, G.; Wright, A. D. *J. Nat. Prod.* **2002**, *65*, 1190-1193.
(146) Jin, W., Chen, X., Dai, P., Yu, L. *Phytochemical Letters* **2016**, *17*, 158-161.
(147) Kamdem, D. P.; Gage, D. A. *Planta Med.* **1995**, *61*, 574-575.
(148) Hagan, E. C.; Jenner, P. M.; Jones, W. I.; Fitzhugh, O. G.; Long, E. L.; Brouwer, J. G.; Webb, W. K. *Toxicol. Appl. Pharmacol.* **1965**, *7*, 18-24.
(149) Administration, F. D. *Code of Federal Regulations Title 21. Part 172.* , 2011; Vol. 3.
(150) Pulivarthi, D.; Steinberg, K. M.; Monzote, L.; Piñón, A.; Setzer, W. N. *Nat. Prod. Commun.* **2015**, *10*, 1934578X1501000723.
(151) Chowdury, B. K.; Sethi, M. L.; Lloyd, H. A.; Kapadia, G. *Phytochemistry (UK)* **1976**, *15*, 1803-1804.
(152) Kaler, K. M.; Setzer, W. N. *Nat. Prod. Commun.* **2008**, *3*, 1934578X0800300529.
(153) Custódio, D. L.; Florêncio da Veiga Junior, V. *RSC Advances* **2014**, *4*, 21864-21890.
(154) Zhao, Q.; Zhao, Y.; Wang, K. *J. Ethnopharmacol.* **2006**, *106*, 408-413.
(155) Wan Othman, W. N. N.; Liew, S. Y.; Khaw, K. Y.; Murugaiyah, V.; Litaudon, M.; Awang, K. *Bioorg. Med. Chem.* **2016**, *24*, 4464-4469.
(156) Efferth, T.; Oesch, F. *Semin. Cancer Biol.* **2019**.
(157) Randolph, K. C. *Southeast. Nat.* **2017**, *16*, 37-58.
(158) Eiter, L. C.; Fadamiro, H.; Setzer, W. N. *Nat. Prod. Commun.* **2010**, *5*, 1934578X1000500323.
(159) Chowdhury, B. K.; Sethi, M. L.; Lloyd, H. A.; Kapadia, G. J. *Phytochemistry* **1976**, *15*, 1803-1804.
(160) Ifa, D. R.; Wu, C.; Ouyang, Z.; Cooks, R. G. *Analyst* **2010**, *135*, 669-681.
(161) Paglia, G.; Ifa, D. R.; Wu, C.; Corso, G.; Cooks, R. G. *Anal. Chem.* **2010**, *82*, 1744-1750.
(162) Bagatela, B. S.; Lopes, A. P.; Cabral, E. C.; Perazzo, F. F.; Ifa, D. R. *Rapid Commun. Mass Spectrom.* **2015**, *29*, 1530-1534.

(163) Kato, L.; Moraes, A. P.; de Oliveira, C. M. A.; Vaz, B. G.; de Almeida Gonçalves, L.; EC, E. S.; Janfelt, C. *Phytochem. Anal* **2018**, *29*, 69-76.
(164) Li, B.; Knudsen, C.; Hansen, N. K.; Jørgensen, K.; Kannangara, R.; Bak, S.; Takos, A.; Rook, F.; Hansen, S. H.; Møller, B. L.; Janfelt, C.; Bjarnholt, N. *Plant J.* **2013**, *74*, 1059–1071.
(165) Conceição, R. S.; Perez, C. J.; Branco, A.; Botura, M. B.; Ifa, D. R. *J. Am. Soc. Mass. Spectrom.* **2020**.
(166) Stévigny, C.; Jiwan, J. L.; Rozenberg, R.; de Hoffmann, E.; Quetin-Leclercq, J. *Rapid Commun. Mass Spectrom.* **2004**, *18*, 523-528.
(167) Schmidt, J.; Raith, K.; Boettcher, C.; Zenk, M. H. *European journal of mass spectrometry (Chichester, England)* **2005**, *11*, 325-333.
(168) Quiroz-Carreño, S.; Céspedes-Acuña, C. L.; Seigler, D. S.; Alarcón-Enos, J. *Phytochem. Anal* **2019**, *30*, 635-643.
(169) Wink, M. *J. Plant Physiol.* **2000**, *157*, 591-592.
(170) Frenzel, T.; Zenk, M. H. *Phytochemistry* **1990**, *29*, 3505-3511.
(171) Santos, A. R.; Paz, N. P. *Biodiversity and Chemotaxonomy*, 1st ed. ed.; Springer International Publishing: Springer Nature Switzerland AG, 2019, p 322.
(172) Shim, H. J.; Lee, J. Y.; Kim, B. J.; Hong, J. *Mass Spectrometry Letters* **2013**, *4*, 79–82.
(173) Soares, E. R.; da Silva, F. M.; de Almeida, R. A.; de Lima, B. R.; da Silva Filho, F. A.; Barison, A.; Koolen, H. H.; Pinheiro, M. L.; de Souza, A. D. *Phytochem. Anal* **2015**, *26*, 339-345.
(174) Meyer, G. M.; Meyer, M. R.; Wissenbach, D. K.; Maurer, H. H. *J. Mass Spectrom.* **2013**, *48*, 24-41.
(175) Zhao, Q. Z.; Zhao, Y. M.; Wang, K. J. *Yao Xue Xue Bao* **2005**, *40*, 931-934.
(176) Feng, T.; Xu, Y.; Cai, X. H.; Du, Z. Z.; Luo, X. D. *Planta Med.* **2009**, *75*, 76-79.
(177) Zhi-Xing, Q.; Peng, Y.; Qi, T.; Pi, C.; Xiu-Bin, L.; Ya-jie, Z.; Yi-Song, L.; Jian-Guo, Z. *Curr. Org. Chem.* **2017**, *21*, 1920-1934.
(178) Wink, M. *The Alkaloids: Chemistry and Pharmacology*, 1st ed ed.; Academic Press, 1993; Vol. 43, p 300.
(179) Iwasa, K.; Nanba, H.; Lee, D. U.; Kang, S. I. *Planta Med.* **1998**, *64*, 748-751.
(180) Samanani, N.; Yeung, E. C.; Facchini, P. J. *J. Plant Physiol.* **2002**, *159*, 1189-1196.
(181) Samanani, N.; Facchini, P. J. In *Recent Advances in Phytochemistry*, Romeo, J. T., Ed.; Elsevier, 2006, pp 53-83.
(182) Mohana Kumara, P.; Uma Shaanker, R.; Pradeep, T. *Phytochemistry* **2019**, *159*, 20-29.
(183) Bhandari, D. R.; Wang, Q.; Friedt, W.; Spengler, B.; Gottwald, S.; Römpp, A. *Analyst* **2015**, *140*, 7696-7709.
(184) Facchini, P. J.; Bird, D. A.; MacLeod, B. P.; Park, S.-U.; Samanani, N. In *Recent Advances in Phytochemistry*, Romeo, J. T., Ed.; Elsevier, 2003, pp 143-180.
(185) Baldwin, I. T.; Schmelz, E. A.; Ohnmeiss, T. E. *J. Chem. Ecol.* **1994**, *20*, 2139-2157.
(186) van der Werff, H. *Annals of the Missouri Botanical Garden* **1991**, *78*, 377-387.
(187) Gil Archila, E.; Cuca Suárez, L. E. *Nat. Prod. Res.* **2018**, *32*, 195-201.
(188) Souza Conceição, R.; de, A. C. M. M.; Alves Reis, I. M.; Branco, A.; Curcino Vieira, I. J.; Braz-Filho, R.; Borges Botura, M. *Ticks Tick Borne Dis.* **2017**, *8*, 275-282.
(189) Figueiredo, A.; Nascimento, L. M.; Lopes, L. G.; Giglioti, R.; Albuquerque, R.; Santos, M. G.; Falcão, D. Q.; Nogueira, J. A. P.; Rocha, L.; Chagas, A. C. S. *Vet. Parasitol.* **2018**, *252*, 131-136.

(190) Liu, Y.; Cheng, E.; Rakotondraibe, L. H.; Brodie, P. J.; Applequist, W.; Randrianaivo, R.; Rakotondrafara, A.; Ratsimbason, M.; Rasamison, V. E.; Kingston, D. G. *Tetrahedron Lett.* **2015**, *56*, 3630-3632.
(191) Ballabeni, V.; Tognolini, M.; Giorgio, C.; Bertoni, S.; Bruni, R.; Barocelli, E. *Fitoterapia* **2010**, *81*, 289-295.
(192) Cassiano, D. S. A.; Reis, I. M. A.; Estrela, I. d. O.; de Freitas, H. F.; Pita, S. S. d. R.; David, J. M.; Branco, A. *Comput. Biol. Chem.* **2019**, *83*, 107129.
(193) Newman, D. J.; Cragg, G. M. *J. Nat. Prod.* **2016**, *79*, 629-661.
(194) Khan, R. A. *Saudi Pharmaceutical Journal* **2018**, *26*, 739-753.
(195) Talaty, N.; Takáts, Z.; Cooks, R. G. *Analyst* **2005**, *130*, 1624-1633.
(196) Cheng, S.-C.; Bhat, S. M.; Lee, C.-W.; Shiea, J. *Int. J. Mass spectrom.* **2018**, *434*, 264-271.
(197) Ifa, D. R.; Wiseman, J. M.; Song, Q.; Cooks, R. G. *Int. J. Mass spectrom.* **2007**, *259*, 8-15.
(198) Kennedy, J. H.; Wiseman, J. M. *Rapid Commun. Mass Spectrom.* **2010**, *24*, 1305-1311.
(199) Gocan, S.; Cimpan, G. *J. Liq. Chromatogr. Rel. Technol.* **2004**, *27*, 1377-1411.
(200) Yan, R.; Wang, W.; Guo, J.; Liu, H.; Zhang, J.; Yang, B. *Molecules (Basel, Switzerland)* **2013**, *18*, 7739-7750.
(201) Xu, X.; Sun, C. R.; Dai, X. J.; Hu, R. L.; Pan, Y. J.; Yang, Z. F. *Molecules* **2011**, *16*, 2551-2560.
(202) Singh, A.; Bajpai, V.; Kumar, S.; Singh Rawat, A. K.; Kumar, B. *Journal of pharmaceutical analysis* **2017**, *7*, 77-86.
(203) Garcez, W. S.; Yoshida, M.; Gottlieb, O. R. *Phytochemistry* **1995**, *39*, 815-816.
(204) Cava, M. P.; Venkateswarlu, A. *Tetrahedron* **1971**, *27*, 2639-2643.
(205) Vecchietti, V.; Casagrande, C.; Ferrari, G. *Farmaco Sci.* **1977**, *32*, 767-769.
(206) Vecchietti, V.; Casagrande, C.; Ferrari, G.; Severini Ricca, G. *Farmaco Sci.* **1979**, *34*, 829-840.
(207) Morais, L. C.; Barbosa-Filho, J. M.; Almeida, R. N. *J. Ethnopharmacol.* **1998**, *62*, 57-61.
(208) Zanin, S. M. W.; Miguel, O. G.; Montrucchio, D. P.; Costa, C. K.; Lagos, J. B.; Lordello, A. L. L. *Quim. Nova* **2011**, *34*, 743-747.
(209) Medeiros, M. A.; Nunes, X. P.; Barbosa-Filho, J. M.; Lemos, V. S.; Pinho, J. F.; Roman-Campos, D.; de Medeiros, I. A.; Araújo, D. A.; Cruz, J. S. *Naunyn Schmiedebergs Arch. Pharmacol.* **2009**, *379*, 115-125.
(210) da Silva, I. G.; Barbosa-Filho, J. M.; da Silva, M. S.; de Lacerda, C. D. G.; da-Cunha, E. V. L. *Biochem. Syst. Ecol.* **2002**, *30*, 881-883.
(211) Cava, M. P.; Behforouz, M.; Mitchell, M. J. *Tetrahedron Lett.* **1972**, *13*, 4647-4649.
(212) Franca, N.; Giesbrecht, A. M.; Gottlieb, O. R.; Magalhaes, A. F.; Magalhaes, E. G.; Maia, J. G. S. *Phytochemistry* **1975**, *14*, 1671-1672.
(213) Lee, S.-S.; Lin, Y.-J.; Chen, C.-K.; Liu, K. C. S.; Chen, C.-H. *J. Nat. Prod.* **1993**, *56*, 1971-1976.
(214) Al-Abdulkader, A. M.; Al-Namazi, A. A.; AlTurki, T. A.; Al-Khuraish, M. M.; Al-Dakhil, A. I. *Saudi J. Biol. Sci.* **2018**, *25*, 776-782.
(215) Nuhu, A. A. *ISRN Nutrition* **2014**, *2014*, 384230.
(216) Davis, A.; Gole, T.; Baena, S.; Moat, J. *PLoS One* **2012**, *7*, e47981.
(217) Silva, M. D. C.; Várzea, V.; Guerra-Guimarães, L.; Azinheira, H. G.; Fernandez, D.; Petitot, A.-S.; Bertrand, B.; Lashermes, P.; Nicole, M. *Braz. J. Plant Physiol.* **2006**, *18*, 119-147.
(218) Santos, C.; Leitao, A.; Pais, I.; Lidon, F.; Ramalho, J. *Emirates Journal of Food and Agriculture* **2015**, *27*, 152-163.

(219) Amorim, A. C. L.; Hovell, A. M. C.; Pinto, A. C.; Eberlin, M. N.; Arruda, N. P.; Pereira, E. J.; Bizzo, H. R.; Catharino, R. R.; Morais-Filho, Z. B.; Rezende, C. M. *J. Braz. Chem. Soc.* **2009**, *20*, 313-321.
(220) Garrett, R.; Vaz, B. G.; Hovell, A. M. C.; Eberlin, M. N.; Rezende, C. M. *J. Agric. Food. Chem.* **2012**, *60*, 4253-4258.
(221) Ky, C. L.; Louarn, J.; Dussert, S.; Guyot, B.; Hamon, S.; Noirot, M. *Food Chem.* **2001**, *75*, 223-230.
(222) Jeszka-Skowron, M.; Sentkowska, A.; Pyrzyńska, K.; De Peña, M. P. *Eur. Food Res. Technol.* **2016**, *242*, 1403-1409.
(223) Monteiro, M. C.; Farah, A. *Food Chem.* **2012**, *134*, 611-614.
(224) Farah, A.; de Paulis, T.; Trugo, L. C.; Martin, P. R. *J. Agric. Food. Chem.* **2005**, *53*, 1505-1513.
(225) Smrke, S.; Kroslakova, I.; Gloess, A. N.; Yeretzian, C. *Food Chem.* **2015**, *174*, 637-642.
(226) Abreu, G. F.; Borém, F. M.; Oliveira, L. F. C.; Almeida, M. R.; Alves, A. P. C. *Food Chem.* **2019**, *287*, 241-248.
(227) Barbosa, M. d. S. G.; Scholz, M. B. d. S.; Kitzberger, C. S. G.; Benassi, M. d. T. *Food Chem.* **2019**, *292*, 275-280.
(228) Bertrand, B.; Guyot, B.; Anthony, F.; Lashermes, P. *Theor. Appl. Genet.* **2003**, *107*, 387-394.
(229) Lemos, M. F.; Perez, C.; Pereira da Cunha, P. H.; Filgueiras, P. R.; Pereira, L. L.; Almeida da Fonseca, A. F.; Ifa, D. R.; Scherer, R. *Food Chem.* **2020**, *310*, 125850.
(230) Simone, C.; Daria, P.; Gabriele, S.; Mariarosaria, A. *Curr. Neuropharmacol.* **2015**, *13*, 71-88.
(231) Caporaso, N.; Whitworth, M. B.; Grebby, S.; Fisk, I. D. *Food Res. Int.* **2018**, *106*, 193-203.
(232) Rosa, J. S. d.; Freitas-Silva, O.; Rouws, J. R. C.; Moreira, I. G. d. S.; Novaes, F. J. M.; Azevedo, D. d. A.; Schwab, N.; Godoy, R. L. d. O.; Eberlin, M. N.; Rezende, C. M. d. *Food Res. Int.* **2016**, *89*, 967-975.
(233) Liu, C.; Yang, N.; Yang, Q.; Ayed, C.; Linforth, R.; Fisk, I. D. *Food Chem.* **2019**, *281*, 8-17.
(234) Ciaramelli, C.; Palmioli, A.; Airoldi, C. *Food Chem.* **2019**, *278*, 47-55.
(235) Tran, H. T.; Lee, L. S.; Furtado, A.; Smyth, H.; Henry, R. J. *J. Sci. Food Agric.* **2016**, *96*, 3300-3312.
(236) Alonso-Salces, R. M.; Serra, F.; Reniero, F.; Héberger, K. *J. Agric. Food. Chem.* **2009**, *57*, 4224-4235.
(237) Panusa, A.; Petrucci, R.; Lavecchia, R.; Zuorro, A. *Food Res. Int.* **2017**, *99*, 155-165.
(238) Kitzberger, C. S. G.; Scholz, M. B. d. S.; Pereira, L. F. P.; Benassi, M. d. T. *Pesquisa Agropecuária Brasileira* **2013**, *48*, 1498-1506.

APPENDICES

Appendix A. Supplementary Data for Chapter 2

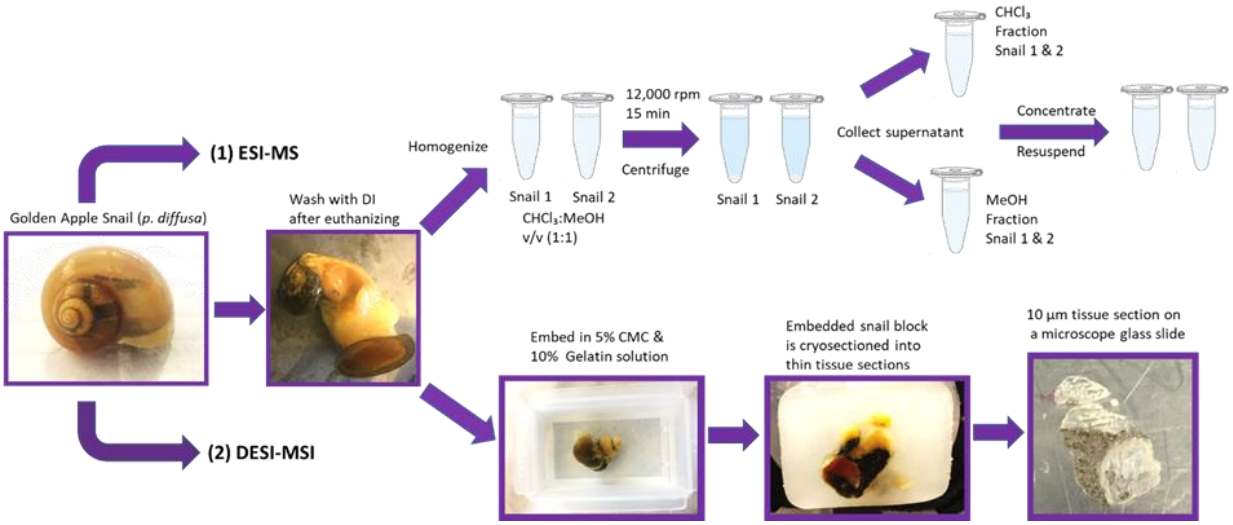

Figure A.1: Sample preparation of (1) the golden apple snail (*p.diffusa*) tissue extracts for ESI-MS analysis. (2) Snail thin tissue sections (10-20 µm) for DESI-MSI analysis.

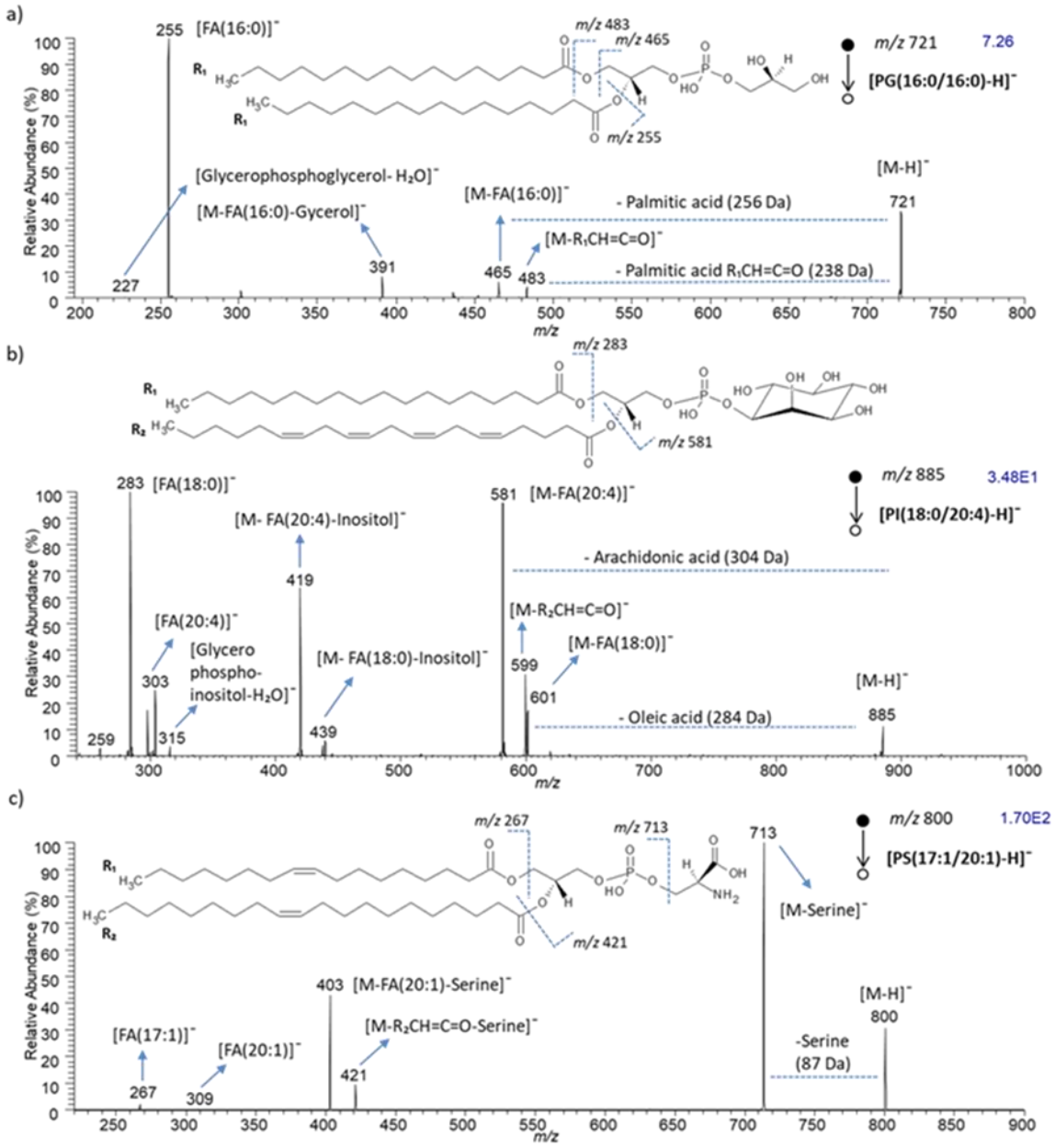

Figure A.2: (-)ESI-MS/MS of the most abundant phospholipids in golden apple snail (*p. diffusa*) in the chloroform fraction of the extract. CID was performed for lipid fragmentation with the isolation window of 1 Da. The lipids were identified as a) Glycerophosphoglycerol $[PG(16:0/16:0)]^-$ of *m/z* 721 with the collision energy of 7 aribitrary units. b) Phosphatidylinositol $[PI(18:0/20:4)]^-$ of *m/z* 885 with the collision energy of 7 aribitrary units. c) Phosphatidylserine $[PS(17:1/20:1)]^-$of *m/z* 800 with the collision energy of 6 aribitrary units. ESI-MS/MS data in combination with LIPID MAPS MS tools was used for the identification of the lipids.

Table A.1: The identification of the most abundant metabolites from the snail (*p.diffusa*) tissue extracts by (-)ESI-MS/MS and tissue sections by (-)DESI-MS/MS

Type of Metabolite	Precursor ion (*m/z*)	CID Energy	MS/MS Fragments (*m/z*)	Tentative Metabolite ID	MS Analysis
Unknown	117	40	**73** (100), 99	-	(-)ESI/DESI
Unknown	125	-	**-**	-	(-)DESI
Unknown	132	65	**86** (100)	-	(+)ESI
Unknown	134	-	**-**	-	(-)DESI
Unknown	147	55	**84** (100), 115, 130, 101	-	(+)ESI
Unknown	156	50	**110** (100)	-	(+)ESI
Unknown	166	40	**120** (100)	-	(+)ESI
Fatty acid	167	25	**123** (100)	Decadienoic acid $[FA(10:2)]^-$	(-)ESI/DESI
Unknown	170	-	**-**	-	(-)DESI
Amino acid	175	40	**116** (100), 60, 130, 140, 158	$[Arginine+H]^+$	(+)ESI
Monosaccharide	179	-	-	$[Hexose-H]^-$/ $[Glu/Gal/Man-H]^-$	(-)ESI/DESI
Monosaccharide	203	30	**158** (100), 116, 88, 172	$[Hexose+Na]^+$/ $[Glu/Gal/Man+Na]^+$	(+)ESI
Monosaccharide	215	20	**169**, 171, 179, 197, 153, 143, 161, 119, 89, 113	$[Hexose+Cl^{35}]^-$/ $[Glu/Gal/Man+Cl^{35}]^-$	(-)ESI
Monosaccharide	217	-	-	$[Hexose+Cl^{37}]^-$/ $[Glu/Gal/Man+Cl^{37}]^-$	(-)ESI
Monosaccharide	219	22	159, 173, 130, 187, 191, 201, 89, 72	$[Hexose+K]^+$/ $[Glu/Gal/Man+K]^+$	(+)ESI
Monosaccharide	221	20	**101** (100), 131, 113, 161	$[Acetylhexose-H]^-$	(-)ESI/DESI
Monosaccharide	225	15	**179** (100)	$[Hexose+COO]^-$ $[Glu/Gal/Man+COO]^-$	(-)ESI
Fatty acid	227	30	**184** (100), 136, 195, 114	Myristic acid $[FA(14:0)-H]^-$	(-)ESI/DESI
Unknown	250	30	235, 220, 205, 191, 168, 139, 97	Unknown	(-)DESI
Fatty acid	253	-	-	Palmitoleic acid $[FA\ (18:1)-H]^-$	(-)ESI/DESI
Fatty acid	255	-	-	Palmitic acid $[FA\ (16:0)-H]^-$	(-)ESI/DESI
Monosaccharide	269	25	**89** (100), 179, 251, 227	$[Monosaccharide+lactate]^-$	(-)ESI/DESI
Fatty acid	277	-	-	α/γ-Linolenic acid $[FA\ (18:3)-H]^-$	(-)ESI/DESI
Fatty acid	279	-	-	Linoleic acid $[FA\ (18:2)-H]^-$	(-)ESI/DESI
Fatty acid	281	-	-	Oleic acid $[FA\ (18:1)-H]^-$	(-)ESI/DESI
Fatty acid	283	-	-	Stearic acid $[FA\ (18:0)-H]^-$	(-)ESI/DESI

Fatty acid	295	18	183, 171, 155, 195, 250, 277	$[FA(19:1)-H]^-$	(-)ESI
Fatty acid	301	-	-	Eicosapentaenoic acid $[FA (20:5)-H]^-$	(-)ESI/DESI
Fatty acid	303	-	-	Arachidonic acid $[FA (20:4)-H]^-$	(-)ESI/DESI
Fatty acid	307	-	-	Unknown	(-)DESI
Fatty acid	309	-	-	Unknown	(-)ESI/DESI
Fatty acid	311	20	**267** (100), 184, 249, 171, 275, 139	Arachidic acid $[FA(20:0)-H]^-$	(-)ESI/DESI
Fatty acid	317	15	**255** (100), 155, 273, 163, 299	-	(-)ESI/DESI
Fatty acid	319	-	**-**	-	(-)ESI
Unknown	325	-	-	Unknown	(-)DESI
Fatty acid	327		299, 283, 249, 229	Docosahexaeonoic acid $[FA (22:6)-H]^-$	(-)ESI/DESI
Unknown	331	-	-	Unknown	(-)DESI
Saccharide	335	12	**273** (100), 219, 317, 299, 255	Unknown	
Saccharide	343	12	**281** (100), 299, 325	Unknown	(-)ESI
Unknown	349	-	-	Unknown	(-)DESI
Unknown	373	-	-	Unknown	(-)DESI
Saccharide	377	15	**161** (100), 179, 221, 263, 281, 341, 143, 113, 119, 256	$[Disaccharide+^{35}Cl]^-$	(-)ESI/DESI
Saccharide	379	-	**-**	$[Disaccharide+^{37}Cl]$	(-)ESI/DESI
Saccharide	341	-	-	$[Disaccharide-H]^-$	(-)ESI
Saccharide	365	15	**203** (100), 305, 185, 245, 275	$[Disaccharide+Na]^+$	(+)ESI
Saccharide	381	-	-	$[Disaccharide+K]^+$	(+)ESI
Saccharide	383	12	**179** (100), 221, 143, 113, 119, 161, 131	$[Acetyldisaccharide-H]^-$	(-)ESI
Saccharide	387	10	**341** (100), 161, 179, 263, 281, 323, 369	$[Disaccharide+COOH]^-$	(-)ESI
Saccharide	391	10	**255** (100), 153	-	(-)ESI
Saccharide	413	8	**377** (100), 360, 215, 198, 167, 293, 395	$[Disaccharide+H_2O+^{35}Cl]^-$	(-)ESI
Unknown	473	15	**205** (100), 189, 267, 251	Unknown	(-)ESI
Saccharide	503	-	-	$[Trisaccharide-H]^-$	(-)ESI
Saccharide	527	10	**365** (100), 347, 467, 407, 305, 203, 185, 509	$[Trisaccharide+Na]^+$	(+)ESI
Saccharide	539	10	**383** (100), 161, 425, 341, 179, 221, 281, 443, 263, 503, 405, 323	$[Trisaccharide+^{35}Cl]^-$	(-)ESI
Saccharide	541	-	-	$[Trisaccharide+^{37}Cl]^-$	(-)ESI
Saccharide	549	-	-	$[Trisaccharide+COOH]^-$	(-)ESI
Saccharide	671	7	**627** (100), 653, 329	Unknown	(-)ESI

Saccharide	701	5	**545** (100), 587, 665, 503, 341, 383, 425, 443, 605, 567, 539, 221, 281, 323, 683, 656	$[Tetrasaccharide-H]^-$	(-)ESI
Saccharide	707	7	**365**	$[Tetrasaccharide+Na]^+$	(+)ESI
Glycerophospholipid (PG)	721	7	**255** (100), 391, 465, 483, 227	$[PG(16/0:16/0)-H]^-$	(-)ESI/DESI
Saccharide	723	-	**-**	$[Tetrasaccharide+K]^+$	(+)ESI
Lipid	778	-			(-)DESI
Lipid	786	-			(-)DESI
Phosphatidylserine (PS)	800	6	**713** (100), 403, 421, 267, 309	$[PS(17:1/20:1)-H]^-$	(-)ESI/DESI
Phosphatidylserine (PS)	810	-	**-**	$[PS (38:4)-H]^-$	
Lipid	826	Unknown			(-)DESI
Lipid	840	Unknown			(-)DESI
Lipid	850	Unknown			(-)DESI
Saccharide	869	6	**527**, 365	$[Pentasaccharide+Na]^+$	(+)ESI
Phosphatidylinositol (PI)	885	6	**283** (100), 581, 419, 599, 303, 601, 439, 315, 259	$[PI(18:0/20:4)-H]^-$	(-)ESI/DESI
Saccharide	885	6	**527,** 365	$[Pentasaccharide+K]^+$	(+)ESI
Saccharide	1047	6	**541** (100), 527, 543	$[Saccharide+H]^+$	(+)ESI

The precursor ions subjected to MS/MS are shown in bold with the relative intensity in brackets.

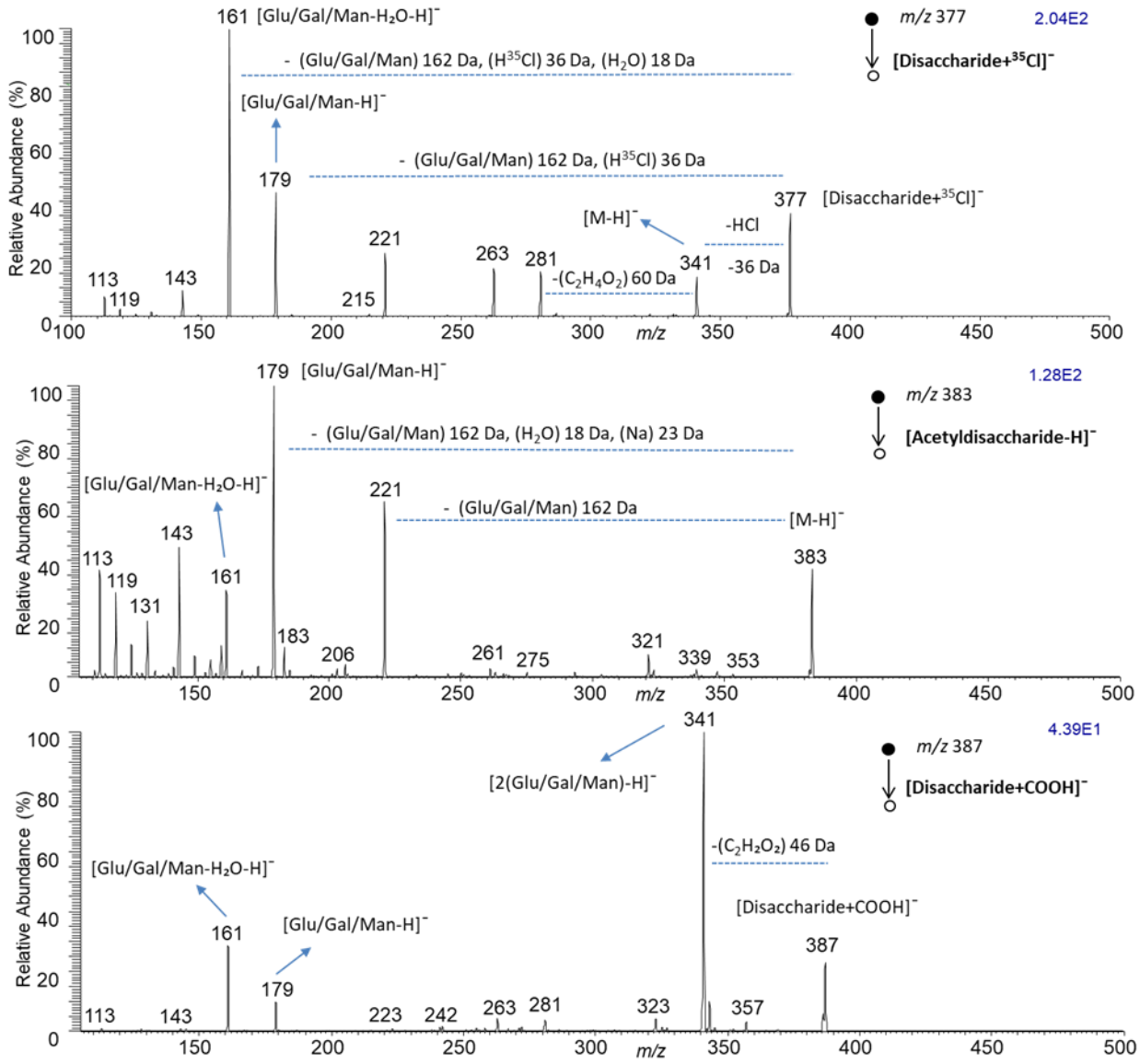

Figure A.3: (-)ESI-MS/MS spectra displaying the fragmentation of disaccharides in the golden apple snail (*p. diffusa).*

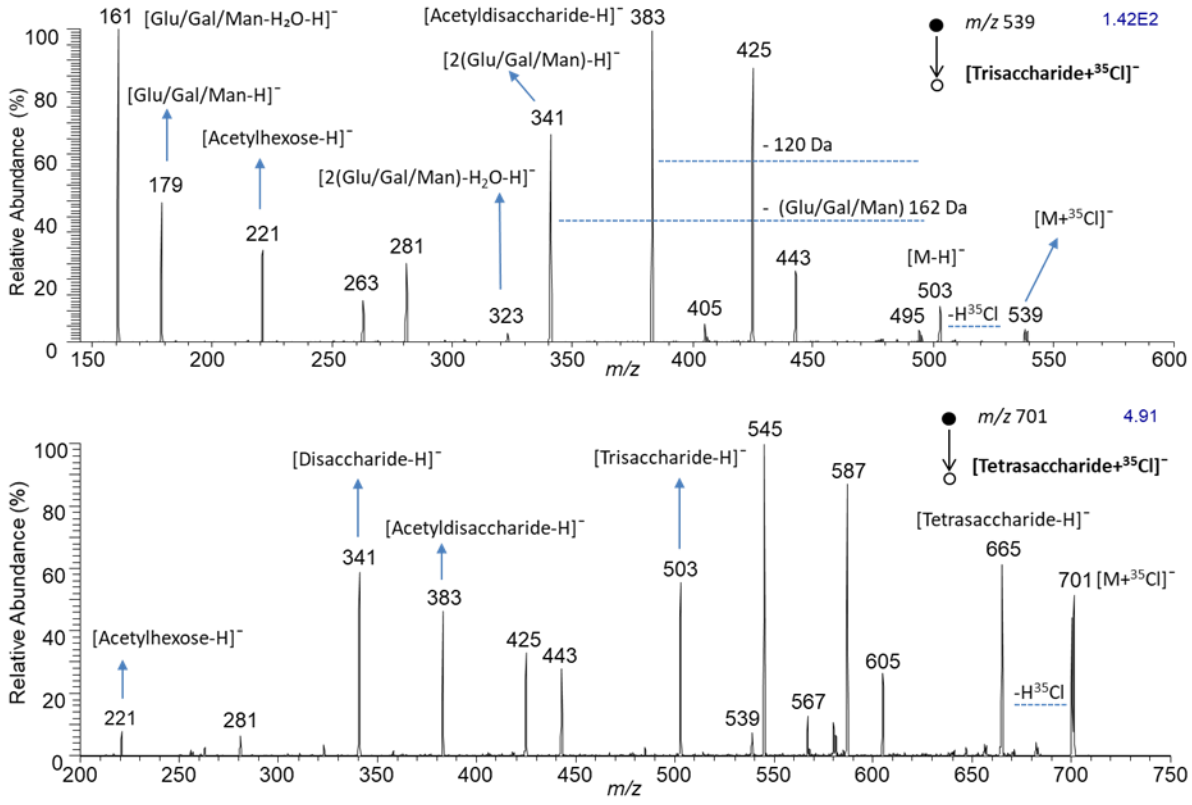

Figure A.4: (-)ESI-MS/MS spectra displaying the fragmentation of polysaccharides in the golden apple snail (*p. diffusa).*

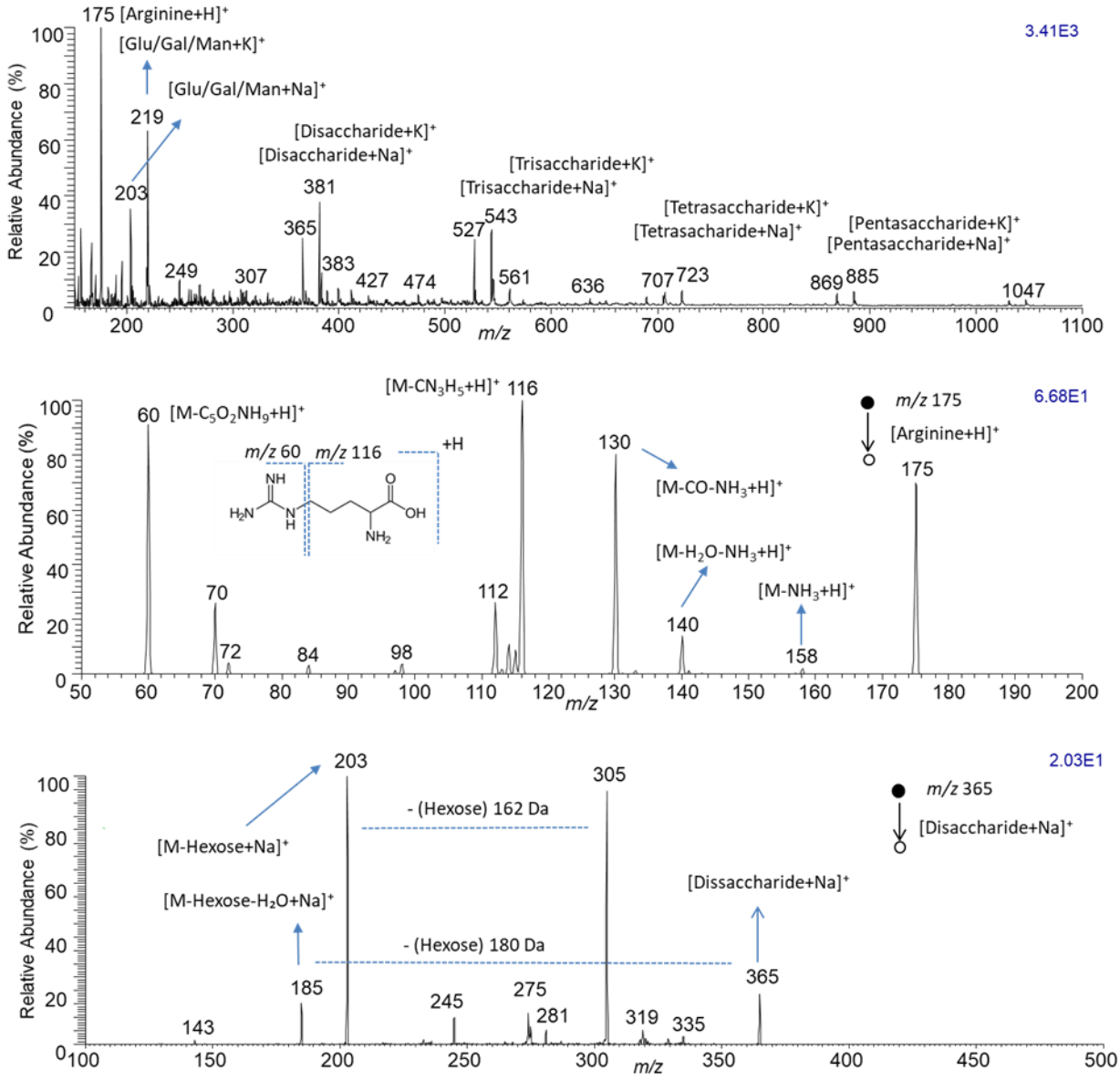

Figure A.5: a) (+)ESI-MS full scan spectra of the methanolic extract golden apple snail (*p. diffusa*). b) (+)ESI-MS/MS spectrum of $[Arginine+H]^+$ of *m/z* 175 fragmented with a colllison energy of 40 (manufacture's unit). c) (+)ESI-MS/MS spectrum of $[Disaccharide+Na]^+$ of *m/z* 365 fragmented with a collision energy of 30 (manufacture's unit).

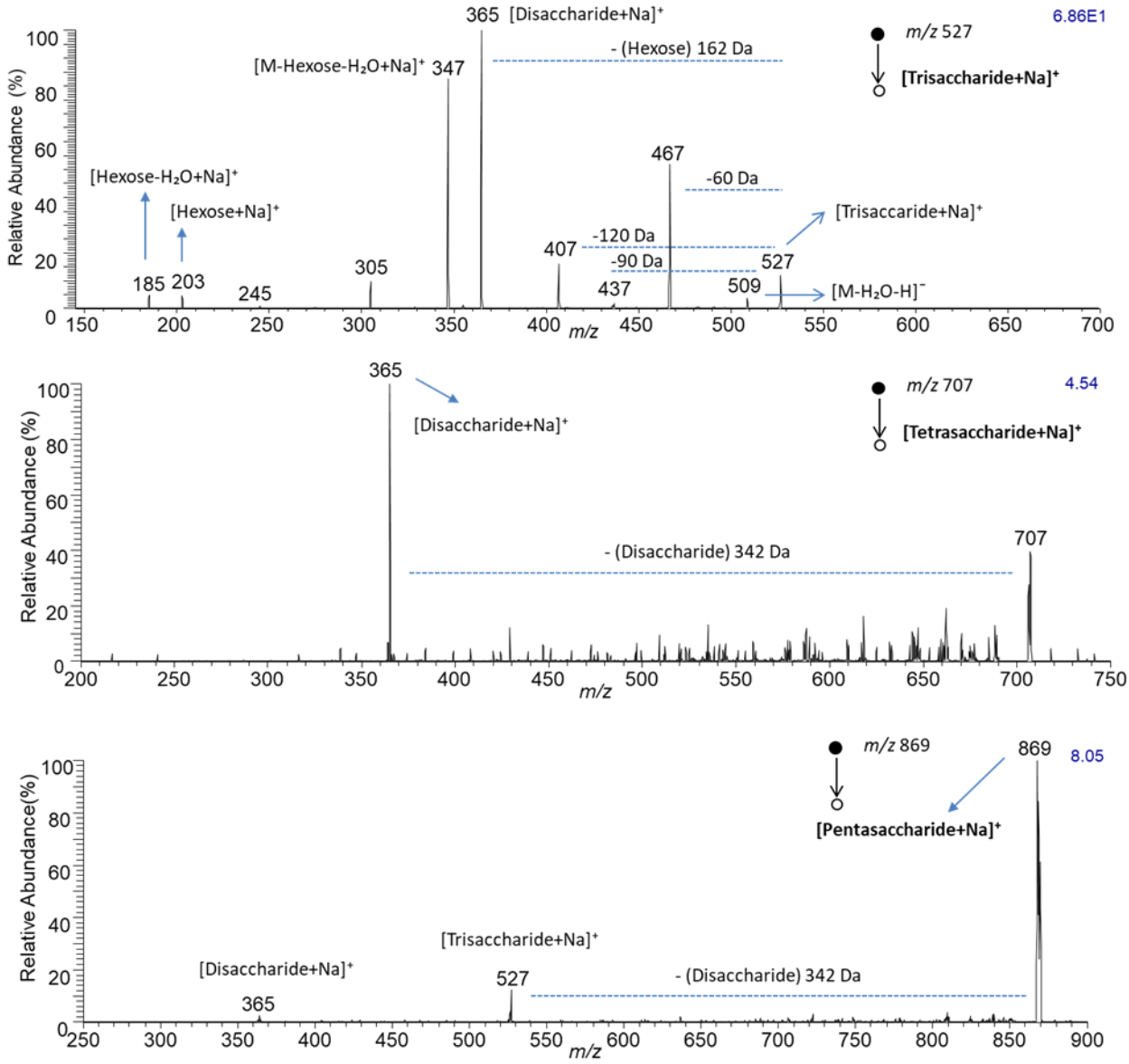

Figure A.6: a) (+)ESI-MS/MS spectra of [Trisaccharide+Na]$^+$ of *m/z* 527. b) [Tetrasaccharide+Na]$^+$ of *m/z* 707. c) [Pentasaccharide+Na]$^+$ of *m/z* 869.

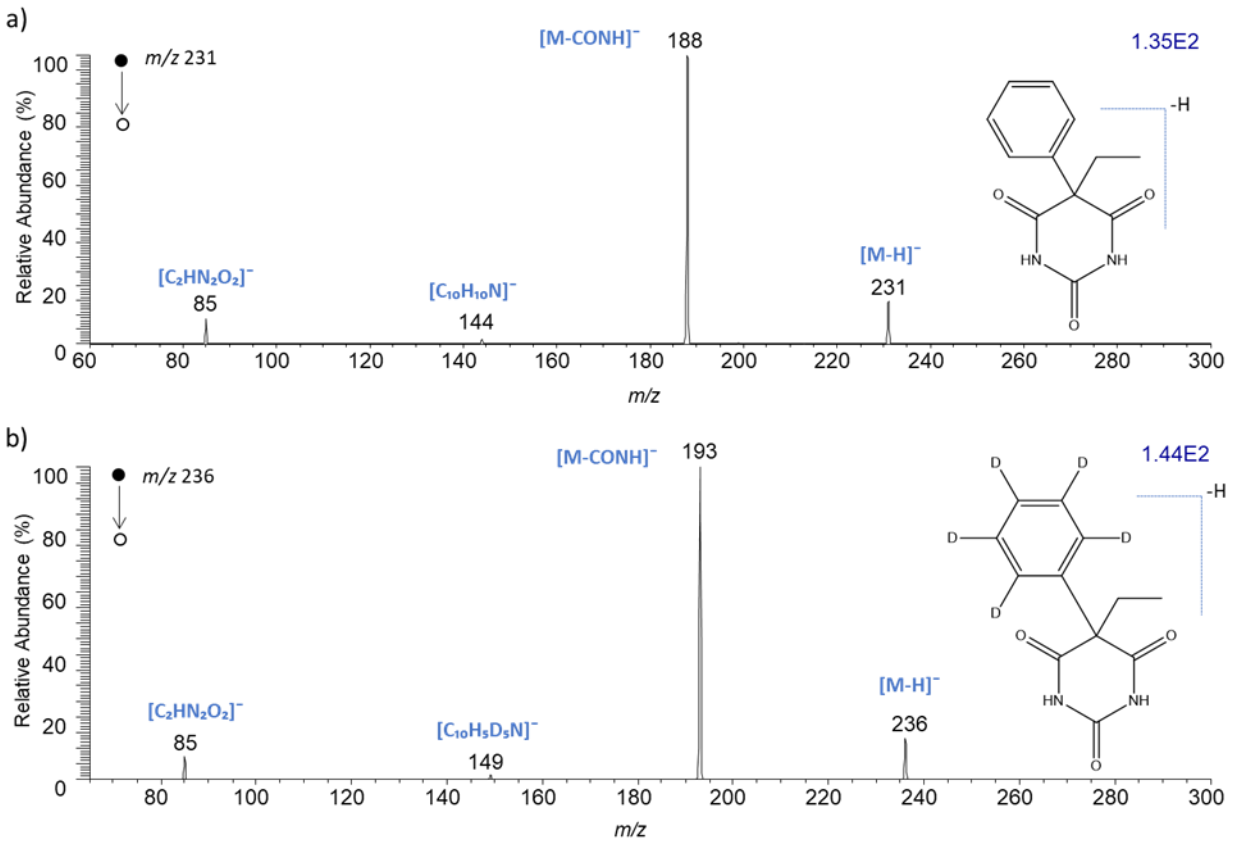

Figure A.7: Average (-)DESI-MS/MS spectra of a) PB (*m/z* 231). b) The isotopically labelled IS, PB-D5 (*m/z* 236) on polytetrafluoroethylene (PTFE) coated microscope glass slides. The MS/MS profiles were collected via CID from 1 µL spots of 100 ng/µL of each standard and fragmented with collision energies of 20 (manufacturer's unit).

Appendix B. Supplementary Data for Chapter 3

Table B.1: (-)ESI-HRMS Analysis of Glucosinolates in Red Maca (*L. peruvianum*) Seeds.

Metabolite	Chemical Formula	Exact mass (*m/z*)	Accurate Mass (*m/z*)	Type of Ion	Mass error (ppm)	R Group
Hexyl-glucosinolate	$C_{13}H_{25}NO_9S_2$	402.08925	402.08708	$[M-H]^-$	-5.4	
Glucotropaeolin	$C_{14}H_{18}NO_9S_2$	408.04230	408.03957	$[M-H]^-$	-6.6	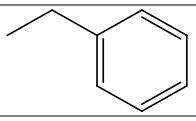
Glucolepigramin	$C_{14}H_{18}O_{10}NS_2$	424.03721	424.03438	$[M-H]^-$	-6.6	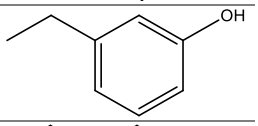
Glucosinalbin						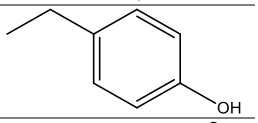
Glucolimnanthin	$C_{15}H_{20}NO_{10}S_2$	438.05287	438.04962	$[M-H]^-$	-7.4	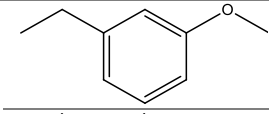
Glucoaubrietin						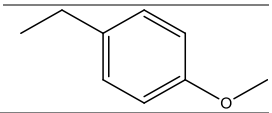
3-hydroxy-4-methoxy benzyl glucosinolate	$C_{15}H_{20}NO_{11}S_2$	454.04778	454.04475	$[M-H]^-$	-6.6	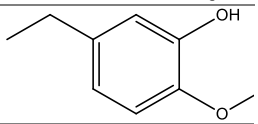

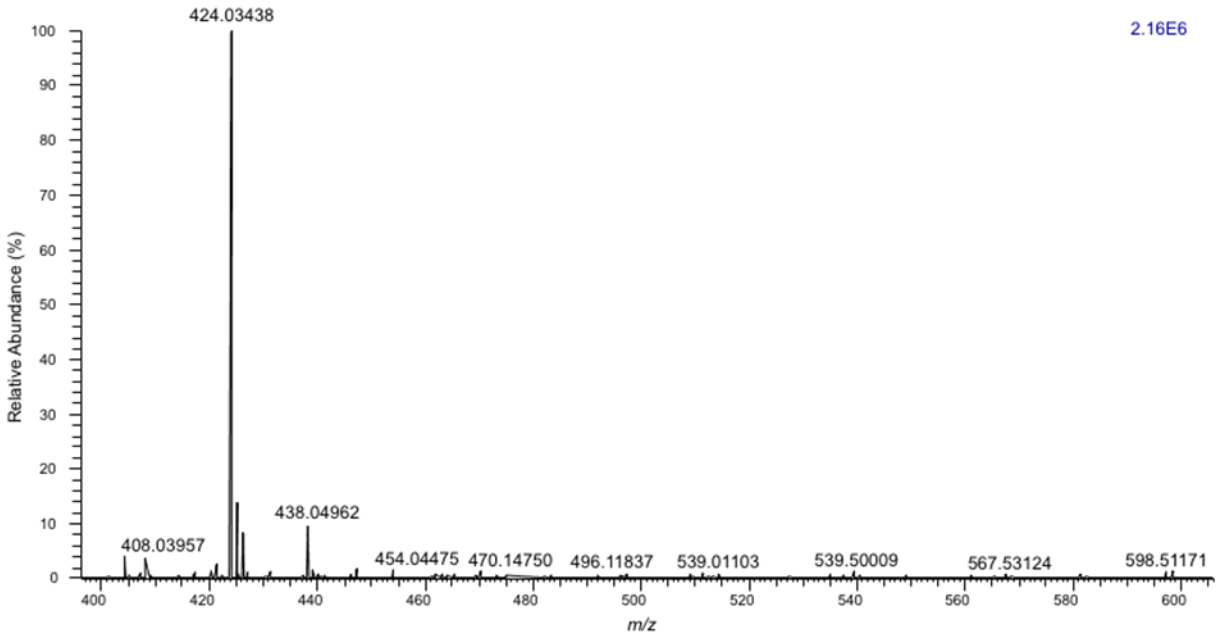

Figure B.1: (-)ESI-HRMS analysis of red Maca (*L. peruvianum*) seeds in the mass range of *m/z* 400-600.